

**Io's Neutral Clouds: From the Atmosphere to the
Plasma Torus**

by

Matthew Howard Burger

M. S., Astrophysical and Planetary Sciences, University of
Colorado

B. A., Physics, Rice University

A thesis submitted to the
Faculty of the Graduate School of the
University of Colorado in partial fulfillment
of the requirements for the degree of
Doctor of Philosophy
Department of Astrophysical and Planetary Sciences

2006

This thesis entitled:
Io's Neutral Clouds: From the Atmosphere to the Plasma Torus
written by Matthew Howard Burger
has been approved for the Department of Astrophysical and Planetary Sciences

Professor Nicholas M. Schneider

Professor Fran Bagenal

Date _____

The final copy of this thesis has been examined by the signatories, and we find that both the content and the form meet acceptable presentation standards of scholarly work in the above mentioned discipline.

Burger, Matthew Howard (Ph. D., Planetary Science)

Io's Neutral Clouds: From the Atmosphere to the Plasma Torus

Thesis directed by Professor Nicholas M. Schneider

Since the discovery of sodium thirty years ago, observations of Io's neutral features have provided essential insight into understanding the relationship between the Io's atmosphere and the Io torus, a ring of plasma encircling Jupiter. In this thesis I use observations and models of Io's corona, extended neutral clouds, and fast sodium jet to probe the interactions between the atmosphere, torus, and neutral clouds.

A corona and neutral cloud model, based on the model of Wilson and Schneider (1999), has been developed to study neutral loss from Io. Neutrals are ejected from Io's exobase and their trajectories followed under the influence of gravity until lost into the plasma torus. I also developed description of the plasma torus based on Voyager and ground-based observations to accurately determine neutral lifetimes.

Mutual eclipsing events between Galilean satellites were used to measure the shape of Io's sodium corona, revealing a corona that is only approximately spherically symmetric around Io. I discovered a previously undetected asymmetry: the sub-Jupiter corona is denser than the anti-Jupiter corona. Modeling implies that sodium source from the sub-Jupiter hemisphere must be twice as large as from the anti-Jupiter hemisphere.

The Galileo spacecraft has imaged a remarkable atmospheric escape process occurring in Io's ionosphere. Electrodynamic consequences of Io's motion through Jupiter's magnetosphere drive mega-amp currents through Io's ionosphere; some sodium ions carrying this current are neutralized as they leave the atmosphere. The Galileo images show that the resulting fast sodium jet removes $\sim 5 \times 10^{25}$ atoms sec^{-1} from Io's atmosphere. The source region of the jet is much smaller than Io itself implying that the ionosphere is densest near Io's equator.

A model-based comparison of the neutral oxygen and sodium clouds details differences in the morphologies and spatial extent of each: sodium extends only 1/4 the way around Jupiter while oxygen forms a complete torus. Sodium emission results from resonant scattering making it relatively easy to determine sodium abundance. The oxygen intensity is highly dependent on the highly variable plasma torus. This complicates the analysis of oxygen observations since the the nature and magnitude of plasma variations has not been well characterized.

Dedication

To Rachel, despite the fact that she made me finish.

Acknowledgements

First let me thank Boulder: if I had to be stuck in grad school for seven years somewhere, Boulder was a good place for it.

Thanks to Nick Schneider for his seven years of advising, guidance, patience, and sending me to the telescope with reasonable regularity.

Thanks to Fran Bagenal for pushing me along and letting me know when it was good enough.

Also, my additional committee members deserve recognition for reading through the whole thing and their insightful comments and questions: Bob Ergun, Mihaly Horanyi, and Ian Stewart (who deserves extra thanks for being a last minute addition to the group). Also thanks to Peter Delamere for agreeing to be on the committee even if his services were not taken advantage of.

I have received observing assistance and data from a number of observers including Imke de Pater, Mike Brown, Antonin Bouchez, Anthony Mallama, Larry Trafton, and Yaron Scheffer all of whom provided me with the mutual event data from Keck and McDonald Observatories. Also, I wish to acknowledge Don Hunten, Ann Sprague, Rik Hill for help and instruction using the LPL Echelle and Coronagraph at Catalina Observatory, as well as their often heroic efforts to repair the instruments during observing runs.

I have received help and guidance from many people through these years from colleagues at other institutions. In particular I'd like to mention Jody Wilson for al-

lowing me to dissect and reassemble his model, as well as an endless enthusiasm for observing sodium. Melissa McGrath has also provided encouragement and support at the times I needed it most.

Thanks to David Brain for seven years of office sharing, protecting my office space while I was off in Virginia, and trying not to wake me up during my many naps of the couch.

And lastly Rachel Osten deserves extra acknowledgment for spending Thanksgiving 1999 and Christmas 2000 alone on a mountain observing with me, reading over the entire thesis, and forcing me to finish it even when I didn't really want to.

Table of Contents

Chapter

1	Introduction	1
1.1	Io's Atmosphere	1
1.2	Observations of the Corona and Neutral Clouds	3
1.3	Neutral Cloud Models	7
1.4	Organization of the Thesis	10
2	Physical Processes Governing Neutrals	13
2.1	Introduction	13
2.2	Emission and Absorption Mechanisms	13
2.2.1	Resonant Scattering: Observing Sodium	14
2.2.2	Electron Impact Excitation: Observing oxygen and sulfur	20
2.3	Creating the neutral clouds: Sputtering	21
2.4	Destruction Physics	25
2.4.1	Electron Impact ionization	26
2.4.2	Charge exchange	28
2.5	Neutral Dynamics	29
2.5.1	Gravity	29
2.5.2	Radiation Pressure	31
2.6	Summary	32

3	Io's Corona: Creation and Destruction	34
3.1	Introduction	34
3.2	Observations	35
3.2.1	Keck Observatory Observations	38
3.2.2	McDonald Observatory Observations	42
3.2.3	Catalina Observatory Observations	43
3.3	Analysis	43
3.4	Discussion	49
3.5	Summary	59
4	Galileo Observations of the Fast Sodium Jet	61
4.1	Introduction	61
4.2	Observations	64
4.3	Analysis	65
4.4	Discussion	66
5	Io's Escaping Neutrals	71
5.1	Introduction	71
5.2	Previous Neutral Cloud Models	73
5.3	A Model of Io's Neutral Clouds	74
5.3.1	Description of the model	74
5.3.2	Treatment of the Io Plasma Torus	77
5.3.3	Neutral Lifetimes in the Inner Jovian System	90
5.3.4	Flux Distributions	97
5.4	Basic Tests of the Neutral Cloud model	99
5.4.1	Effect of Radiation Pressure	99
5.4.2	Testing the model: East/West Sodium Brightness Asymmetry	101
5.4.3	Testing the model: North/South Sodium Brightness Asymmetry	103

5.5	Summary	105
6	Modeling Io's Corona	108
6.1	Introduction	108
6.2	Description and Analysis of Model Runs	110
6.3	Understanding the Shape of the Corona	112
6.3.1	The Average Observed Corona	112
6.3.2	Variations in the Average Corona	120
6.3.3	Building to an Offset Tilted Dipole with an East/West Electric Field	121
6.3.4	Effect of Uniform Variations in the Torus on the Corona	125
6.3.5	Effect of Magnetic Longitude Variations on the Corona	131
6.4	Understanding the Inner/Outer Asymmetry in the Corona	134
6.5	Io's Oxygen Corona	141
6.5.1	Observations	142
6.5.2	The Average Oxygen Corona	144
6.5.3	The Oxygen Asymmetry	148
6.6	Summary	150
7	Io's Extended Neutral Clouds	154
7.1	Introduction	154
7.2	Neutral Cloud Models	155
7.3	Large Scale Features	158
7.3.1	Motions of Neutral Atoms	158
7.3.2	Loss of Neutral Atoms	166
7.3.3	Neutral Cloud Brightnesses	167
7.4	Observations of the Sodium Neutral Cloud	180
7.5	Summary	182

8	Conclusions	184
8.1	Summary of the Thesis	184
8.2	Major Results	186
 Bibliography		190
A	Summary of Eclipse Observations	197
 Appendix		
B	Transformation to the Plasma Coordinate System	202

List of Tables

Table

2.1	Sodium D Line Parameters	17
2.2	Summary of neutral lifetimes for ionization processes	28
2.3	Neutral-Ion charge exchange reactions	30
3.1	Eclipse Parameters	39
6.1	Comparison of corona created with different cross sections, different ejection direction distribution, and different models	116
6.2	Summary of oxygen corona observed by Wolven et al. (2001).	144
7.1	Summary of all available sodium images	181
A.1	Summary of Eclipse Observations	198
A.1	Summary of Eclipse Observations	199
A.1	Summary of Eclipse Observations	200
A.1	Summary of Eclipse Observations	201

List of Figures

Figure

1.1	Discovery of sodium at Io by Brown (1974).	5
1.2	Sunlight available for resonant scattering	9
2.1	Schematic of sodium D resonance line transitions	15
2.2	Curves of growth for sodium D ₂ line	18
2.3	Cartoon of cascade sputtering	22
2.4	Sputtering Flux Distribution	24
2.5	Electron impact ionization cross sections and rate coefficients	27
3.1	Io eclipsing Europa	36
3.2	Removal of solar spectrum	37
3.3	Io's orbital geometry during mutual events	40
3.4	Determination of Impact Parameters	45
3.5	Equivalent widths during mutual events	47
3.6	Determination of corona temperature and column density	48
3.7	Corona column density profile	50
3.8	Mutual event eclipse geometry	53
3.9	Equivalent width vs. Impact parameter	54
3.10	Column density asymmetry in the corona	55
4.1	Cartoon of directional feature geometry	63

4.2	Io's sodium jet through Galileo's clear and green filters	67
4.3	Comparison of Galileo data and modeled jet images	69
5.1	Model Coordinate System	76
5.2	Cartoon of Jupiter's dipole magnetic field	79
5.3	Electron density and temperature in the centrifugal equator	80
5.4	Observations of the Ribbon by Schneider and Trauger (1995)	81
5.5	Illustration of the importance of line-of-sight effects in ground-based observations of the plasma torus	83
5.6	Io's location in the plasma torus at all magnetic and orbital longitudes	85
5.7	Neutral lifetimes in the inner Jovian system for different loss processes	91
5.8	Neutral lifetimes at Io for the basic torus model	93
5.9	Neutral lifetimes at Io for the varying torus model	94
5.10	Comparison of sodium lifetime in the corona predicted by this work with Smyth and Combi (1988b)	96
5.11	Fraction of atoms with escape velocity for different flux distributions.	98
5.12	Effect of radiation pressure on sodium in the cloud and corona.	100
5.13	Model of the East/West Sodium Brightness Asymmetry	102
5.14	Demonstration of the north/south sodium cloud asymmetry	104
6.1	Modeled image of the corona with radial profile	111
6.2	Radially averaged models of a sputtered corona	113
6.3	Radially averaged models of a corona with an exponential source distribution	114
6.4	Motion and ionization of sodium atoms in the corona.	119
6.5	Effects of Jupiter's offset tilted dipole and the east/west electric field on the corona	122

6.6	Demonstration of the effect of the east/west electric field on sodium emission from the corona.	124
6.7	Effect of uniformly varying torus electron density on the sodium corona.	126
6.8	Effect of uniformly varying torus ion temperature on the sodium corona.	129
6.9	Effect of variations in the strength of the east/west electric field on the corona.	132
6.10	Effect of magnetic longitude variations in the torus on the shape of the corona.	133
6.11	Sketch of the regions about Io for discussing the corona asymmetry. . .	136
6.12	Shape of the corona when the source is limited to a single hemisphere. .	137
6.13	Shape of the corona using combinations of sputtering from each side of Io.	138
6.14	Shape of the corona allowing the most probable velocities of each hemisphere to vary independently.	140
6.15	Example of STIS image of Io's atmospheric emissions	143
6.16	Power law slope in the oxygen corona as function of most probable velocity.	145
6.17	Fraction of atoms escaping from Io's corona as function of neutral lifetime and initial velocity.	147
6.18	Effect of electron temperature variations near Io on the coronal oxygen intensity profile.	149
7.1	Examples of modeled oxygen and sodium clouds	157
7.2	Decomposition of model image into observable quantities.	159
7.3	Sample trajectories of neutral atoms ejected from Io	161
7.4	Streamlines of atoms ejected from Io.	162
7.5	Illustration of atoms without escape velocity escaping from Io	163
7.6	Intermediate scale view of neutrals escaping Io	165
7.7	Neutral lifetime as function of the modified L-shell	168

7.8	Examples of modeled neutral cloud brightnesses	169
7.9	Observable changes in the sodium cloud due to Io's motion	171
7.10	Observable changes in the sodium corona due to Io's motion	172
7.11	Comparison between brightness and column density profiles of the sodium neutral cloud.	174
7.12	Effect of the tilt of Jupiter's equatorial plane relative to Earth.	176
7.13	Observable changes in the oxygen cloud due to the changing plasma torus geometry	177
7.14	Variation in oxygen cloud brightness due to torus variability.	178

Chapter 1

Introduction

Io was a simple country nymph who caught Jupiter's eye. Jupiter's wife Juno, suspicious of Jupiter's intentions toward Io, came down to investigate. Jupiter acted quickly by turning Io into a cow. Juno complimented Jupiter on having such a nice cow and asked if she could have it. Because Juno would be suspicious if he refused to give her something so simple as a cow, Jupiter had no choice but to relinquish Io.

Juno was still suspicious of Jupiter and his "cow," so she told Argus, the hundred-eyed creature, to watch over Io. Eventually, Jupiter began to feel guilty about what he had done to Io, so he sent Mercury to kill Argus. Mercury did this, so Jupiter was able to change Io back to her original form.

In this thesis, I use the the watchfulness of Argus and Juno-like models to try to understand the interactions of Io and Jupiter. We must hope that she is revealed before all the observers are gone. (Paraphrased from *Metamorphoses*, Ovid).

1.1 Io's Atmosphere

The first observational evidence of an atmosphere at Io were measurements made by Binder and Cruikshank (1964) who showed an increase in Io's albedo immediately after emerging from eclipse which then decreased to its pre-eclipse value over several hours. This brightening was interpreted as an atmosphere condensing out when solar heating is turned off, creating a reflective surface frost layer that sublimates when the sun

heats the surface after eclipse. Although this observation has only been intermittently repeated since then and remains somewhat controversial, it is now known that Io does in fact have an atmosphere which at least partially condenses when Io goes into eclipse (see reviews by Lellouch (1996); Spencer and Schneider (1996)).

The existence of this atmosphere, however, was still unproven for a decade after Binder and Cruickshank's observations. The Pioneer 10 radio-occultation experiment detected Io's ionosphere (Kliore et al. 1974, 1975), providing more definitive indirect evidence for the atmosphere. At about the same time, sodium emission from Io was discovered by Brown (1974). Sodium has since proved to be minor in abundance but extremely important for studying the dominant species (Section 1.2).

The Voyager flybys of Jupiter propelled Io to a new level of respect in the scientific community with their discovery of the only known extra-terrestrial volcanism. Voyager also made the first direct observation of Io's near-surface atmosphere with a spectrum of SO_2 (Pearl et al. 1979). As only sodium and potassium (discovered by Trafton (1975b)) were known to originate from Io previous to Voyager, and these had been observed in extended clouds extending large distances from Io but not in a near-surface atmosphere, the discovery of this most abundant species in Io's atmosphere provided a new direction for atmospheric studies.

With the passing of Voyager from Jupiter, no detections of Io's atmosphere were made for over a decade Lellouch et al. (1990). The 1980s were spent trying to understand the single SO_2 observation from Voyager. Three classes of models were developed for understanding the atmosphere: buffered models (e.g., Kumar (1982) assume the SO_2 atmosphere is in vapor pressure equilibrium with the surface frost; volcanic models (Ingersoll 1989; Moreno et al. 1991) consider an atmosphere supplied by local volcanic sources; and sputtering models (Sieveka and Johnson 1984) look at an atmosphere created by charged particle impact on the surface.

Observations in the mid-1990s helped to clarify the global extent of the atmo-

sphere. Images of Io passing in front of Jupiter detected absorption by SO_2 and S_2 in a plume silhouetted against Io's disk (Spencer et al. 1997, 2000), proving that the sulfur dioxide is contained in some volcanic emissions. The presence of a global atmosphere has been suggested by observations which detected gaseous SO_2 above three distinct geographical regions on Io's surface (McGrath et al. 2000).

Recently, the *Hubble Space Telescope* has provided an exciting new technique for observing Io's atmospheric SO_2 (Roesler et al. 1999; Feldman et al. 2000). Images of Io's SO_2 distribution are obtained with the Space Telescope Imaging Spectrograph (STIS) by making spatially resolved observations of solar Lyman- α reflected off Io's surface due to attenuation by SO_2 in Io's atmosphere. These images show a global but non-uniform and time-variable atmosphere with SO_2 gas concentrated near Io's equator. Results from the Galileo spacecraft support this suggestion with observations indicating that Io has a global ionosphere (Hinson et al. 1998). Evidence is presented in Chapter 4 that the ionosphere may be denser near the equator.

1.2 Observations of the Corona and Neutral Clouds

The focus of this thesis is not Io's near-surface atmosphere but the features formed from the escape of this atmosphere. Using thirty years of observations, sodium is known to escape through "slow" and "fast" processes. Sputtering of neutrals off the atmosphere and surface form the extended cloud: a banana shaped cloud of slowly escaping neutrals (mean velocity $\sim 2 - 3 \text{ km s}^{-1}$ with a high speed tail extending to $\sim 10 - 30 \text{ km s}^{-1}$) which primarily leads Io in its orbit around Jupiter (Smyth 1992). Similar clouds exist for the more dominant species of sulfur and oxygen (Brown 1981a; Thomas 1996), but have not been well studied since emission from these species are at the limits of what can be observed. There are several mechanisms which result in the escape of fast sodium (velocity $\gtrsim 10 \text{ km s}^{-1}$). Jupiter's magnetic field accelerates sodium ions in Io's collisionally thick ionosphere which are neutralized through charge exchange

to produce fast neutrals (Wilson and Schneider 1999). Sodium ions in the plasma torus can also charge exchange with neutrals to create fast sodium. Similarly, sodium-bearing molecular ions are swept into the torus of plasma which encircles Jupiter and dissociation of these molecules creates a separate fast sodium feature (Wilson and Schneider 1994). Additional fast sodium results from the high speed tail of the sputtering flux distribution (Smyth 1992). A short summary of the observational and modeling efforts to understand Io's neutral features follows.

Since its discovery thirty years ago (Brown (1974),Figure 1.1), sodium has proved itself to be essential for understanding the escape of Io's atmosphere. Despite its small abundance, optical wavelength observations of sodium have several advantages over observations of more abundant species such as oxygen and sulfur. The emission from these species results from electron impact excitation in the plasma torus, so the observed emission is a function of both the neutral density and the electron density and temperature of the plasma, making the neutral density profile difficult to determine from observational data without detailed modeling. Even in regions where the plasma is less important for creating the emission, the lines are weak and at wavelengths inaccessible from the ground. Because the sodium D lines are formed through a resonant transition at optical wavelengths, sodium can be observed at Io in both emission and absorption when in sunlight. Also, sodium emission is much brighter than optical emissions from other atmospheric components.

The observations of sodium made within a few years of its discovery fleshed out the spatial extent and general morphology of the cloud. Using separate spectra of Io's disk and the region near Io's disk, Trafton et al. (1974) demonstrated that the emission originates from an extended region at least $10''$ ($\sim 20 R_{Io}$) in radius around Io. Continued observations of the spatial extent of the cloud detected a partial torus of neutral sodium extending at least one-fifth of the way around Jupiter from Io (Macy and Trafton 1975b). The first two-dimensional images of the cloud (Muench and Bergstrahl

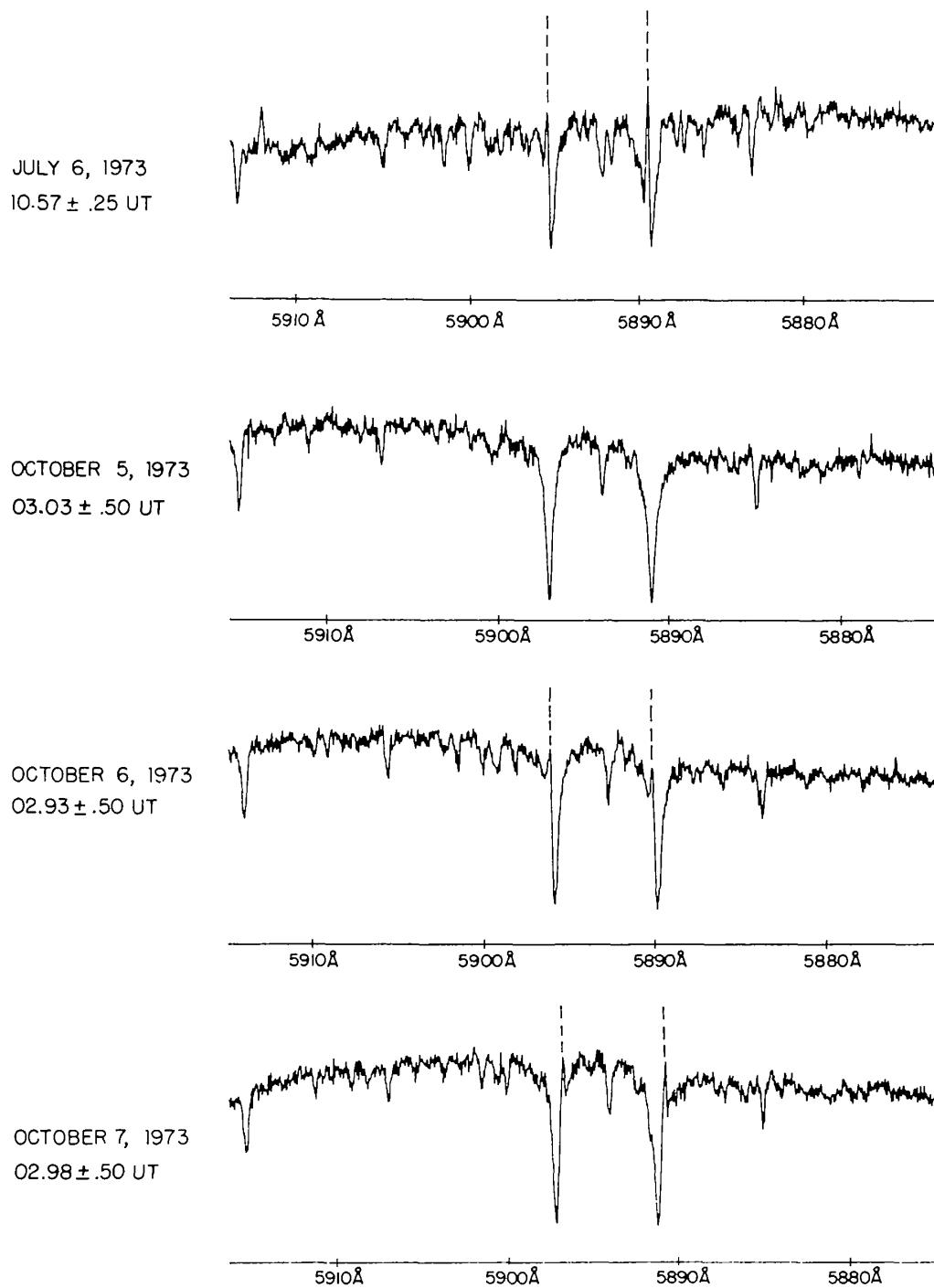


Figure 1.1 The earliest spectra of Io's sodium emission by Brown (1974). Iogenic sodium D lines are indicated with broken lines. These spectra are reproduced from Brown and Chaffee (1974)

1977; Matson et al. 1978; Murcray and Goody 1978) showed the “banana-shaped” cloud primarily leading Io in its orbit.

Because several groups were involved in monitoring programs and other observations of the sodium emission, two asymmetries were discovered even while the general morphology of the cloud was still being determined. Bergstralh et al. (1975, 1977) demonstrated that although on average the sodium emission remains roughly constant from one year to the next, the intensity is about 25% higher when Io is at eastern elongation (orbital phase = 90°) than at western elongation (orbital phase = 270°). This is in addition to an approximately 20% variation in the overall brightness which did not correlate with any known variables (e.g. Io’s magnetic longitude). A north/south asymmetry was discovered by Trafton and Macy (1975): the ratio of the sodium brightness north of Io to that south of Io is a function of Io’s magnetic longitude with the side further from the magnetic equator showing brighter emission. The discovery of the plasma torus by Voyager in 1979 provided an explanation for this asymmetry (Trafton 1980).

Neutral clouds of other species have also been detected. Trafton (1975b) discovered potassium originating from Io with a morphology similar to the sodium cloud. Although oxygen and sulfur are the most abundant species in the cloud, observations of each have been sparse: Oxygen was discovered by Brown (1981b); sulfur by Durrance et al. (1983). Recent years have also seen a monitoring program of optical wavelength emissions of neutral oxygen at 6300 \AA originating near Io’s disk (Scherb and Smyth 1993; Oliverson et al. 2001).

Although spectroscopic and imaging studies were able to study the morphology of the large scale features, it was not possible to observe sodium in Io’s corona close to Io. The corona, or exosphere, is the region within $\sim 6 R_{\text{Io}}$ consisting of bound and escaping atoms which have been lost from Io’s collisional atmosphere but are still in the region where Io’s gravity dominates over Jupiter’s. In general, it is not possible to spatially resolve the region close to Io because of Io’s high geometric albedo and the

effects of atmospheric seeing. Observations of Io eclipsing the other Galilean satellites (Schneider et al. 1987, 1991a) however, has provided a method of determining the radial column density profile of sodium close to Io. Additionally, the HST observations which produced the images of Io’s atmospheric SO₂, have also measured the radial intensity profiles of oxygen and sulfur in Io’s corona for the first time (Wolven et al. 2001).

The early spectra also detected a fast component to the sodium escaping from Io (Trafton 1975a). Sodium has since been observed at speeds of up to 100 km s⁻¹ Brown (1981a). Early imaging studies of the fast sodium features (Goldberg et al. 1984; Pilcher et al. 1984) characterized it as a narrow feature directed away from Jupiter perpendicular to the Jovian magnetic field line through Io. A second fast sodium feature, known as the molecular ion stream, was discovered by Schneider et al. (1991b) and originates in the plasma torus. This feature has been shown to result from dissociation of molecular ions in the torus (Schneider et al. 1991b; Wilson and Schneider 1994).

1.3 Neutral Cloud Models

Modeling efforts to understand Io’s sodium emission began almost immediately after its discovery. These earliest models concentrated on understanding the basic source, loss, and emission mechanisms to great success. Matson et al. (1974) made the first prediction that sodium atoms sputtered are the source of the cloud of sodium around Io.

The first attempt to understand the emission mechanism was made by McElroy et al. (1974) who assumed that Io has a “normal” satellite atmosphere consisting of nitrogen gas with a trace sodium component excited by collisions with N₂. Resonant scattering of sunlight by sodium atoms was initially ruled out due to energy requirements and the assumption that sodium was in a bound surface atmosphere. With the observation that the emission is not confined to Io’s disk, Trafton et al. (1974) and Matson et al. (1974) revived the resonant scattering hypothesis. Definitive proof that

resonant scattering is responsible for the sodium emission was provided by Bergstralh et al. (1975) and Trafton et al. (1974) who demonstrated that the sodium intensity is strongly correlated with Io's orbital phase. This is expected for resonantly excited sodium emission because Io's changing radial velocity relative to the sun Doppler shifts the resonant wavelength in and out of the deep solar Fraunhofer line (Figure 1.2). Additional evidence was provided by Macy and Trafton (1975a) who failed to detect emission from Io while it was in eclipse, implying that solar photons are needed to excite the emission. More recently, sodium emission from electron impact excitation has been detected through ground-based spectroscopy (Bouchez et al. 2000) and Galileo spacecraft imaging (Geissler 1999) of Io in eclipse, although this accounts only for only a small fraction of the total emission when Io is in sunlight.

Sodium loss was first assumed to be due to photo-ionization by solar photons (Macy and Trafton 1975a), although they realized that the photo-ionization lifetime is longer than the lifetime to create a complete neutral torus around Jupiter. This conflicted with their observations limiting the cloud to $\sim 1/5$ the circumference of Io's orbit.

A series of papers beginning with Fang et al. (1976) has built up a neutral cloud model as numerical techniques improved and more detailed observations of sodium and the plasma torus became available. The object of these papers has been to understand the evolution of the sodium cloud from the ejection of neutrals out of Io's atmosphere to their eventual loss by ionization. The first of these papers investigated the creation of a torus of neutral sodium originating from a massless Io (Fang et al. 1976). Smyth and McElroy (1977) improved on this by including Io's gravity and limiting the neutral lifetime for a closer agreement with the observations which suggested that the cloud extends only part way around Jupiter. A subsequent paper (Smyth and McElroy 1978) presented the first detailed comparison between models and imaging data (supplied by Murcray and Goody (1978)). The images showed the asymmetric shape of the

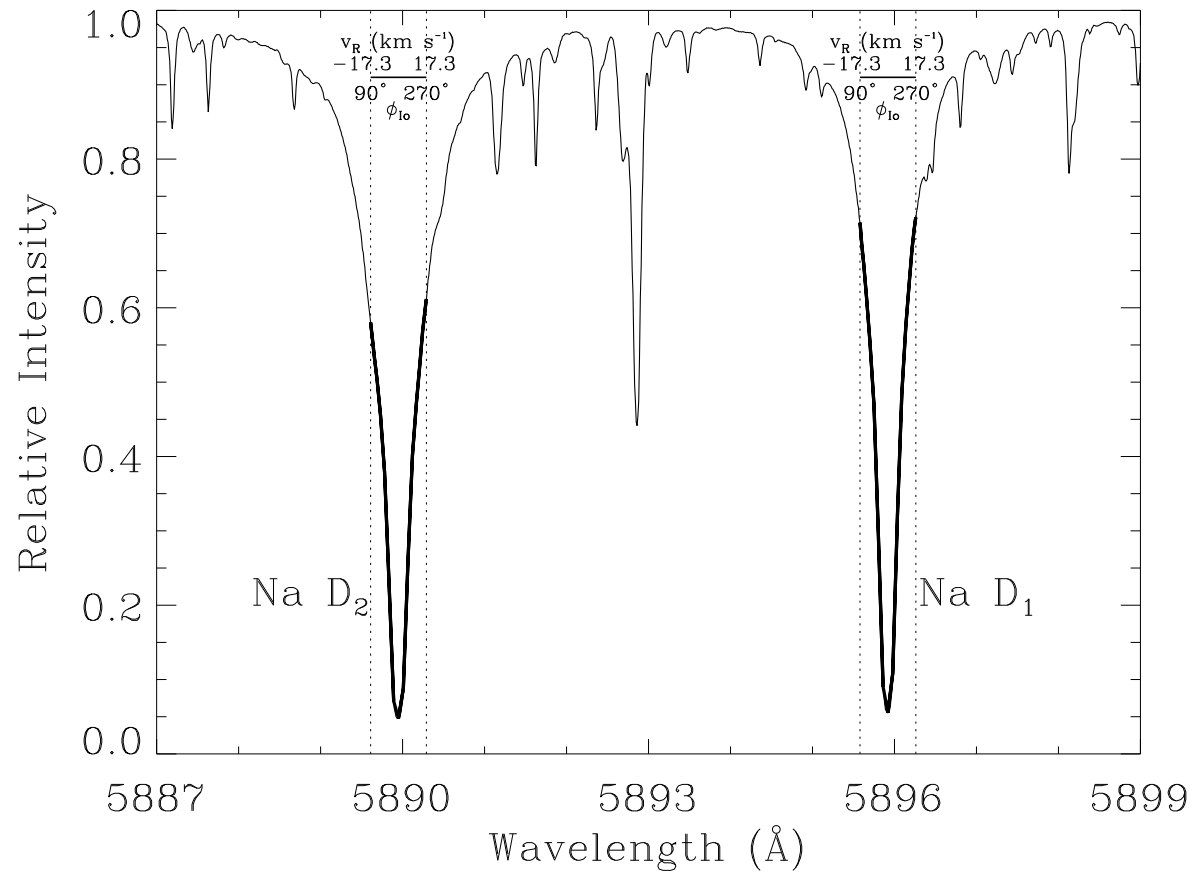


Figure 1.2 The amount of sunlight available for resonant scattering of sunlight by sodium atoms for different Io orbital phases. The intensity of sodium emission is directly proportional to the amount of sunlight at the wavelength of emission in the rest frame of sodium. The radial velocity of Jupiter relative to the sun is taken to be 0 km s⁻¹ here, but must be included when determining actual emission intensity. Scale bars in each line indicate the range of the Doppler shift due to the changes in Io's radial velocity and orbital longitude. This range is also indicated by a heavy line through the part of the solar profile.

sodium cloud: the leading cloud was clearly denser and brighter than the trailing cloud. Assuming a uniform lifetime of $\sim 15 - 20$ hours, they concluded that asymmetric loss from Io could explain the shape of the cloud, noting that ejection of neutrals from the trailing hemisphere primarily populates the forward cloud.

A mechanism for producing the east/west asymmetry (Bergstralh et al. 1975, 1977) in the sodium cloud was explored by Smyth (1979, 1983). The first paper provided a qualitative demonstration that solar radiation pressure on sodium atoms could produce an east/west asymmetry similar to that observed. This work was continued in the second paper with three-dimensional model calculations of the sodium cloud. This work represented a substantial improvement on their ability to model the sodium cloud.

The next major advancement in modeling the neutral clouds came with the development of a general framework for modeling Io's neutral clouds (Smyth and Combi 1988a). The application of this model (Smyth and Combi 1988b) was the first study to include in detail the effects of the plasma torus (although Trafton (1980) had considered the role of the torus in explaining specific observations). These two papers by Smyth and Combi provide the basis for their future work on the neutral clouds and Io's corona: their subsequent work has been applications of this model. These applications include an attempt to use a single source velocity distribution to understand the sodium neutral cloud, the sodium corona, and the fast sodium directional feature (Smyth and Combi 1997) and an application of these results to understanding neutral oxygen observations far from Io (Smyth and Marconi 2000).

1.4 Organization of the Thesis

This thesis is a joint observational and modeling survey of neutral features originating at Io. I concentrate on three distinct but interconnected neutral features: the bound corona, the fast sodium jet, and the extended neutral clouds. Although most of the observations concentrate on sodium due to the relative ease and availability of

observations, I also discuss the physics of oxygen and sulfur lost from Io and compare these species to the well observed sodium features.

The major questions addressed by this thesis are:

(1) Understanding Io's Corona:

- How stable is the corona? Does the corona vary over long time scales?
- Is the corona radially symmetric?
- How does the plasma torus affect the shape of the corona?
- What does the shape of the corona imply about the loss from Io's atmosphere?
- What do morphological differences between the oxygen and sodium coronae imply about loss? Are there differences in the loss mechanisms?

(2) Io's fast sodium jet:

- How large is the source region of the fast sodium jet? Is it a global or narrowly confined region?
- What are the implications of the source size for Io's ionosphere?

(3) The extended neutral clouds:

- Can difference morphological aspects of the clouds be explained through particle motions?
- What effect do the different oxygen and sodium lifetimes have on the neutral clouds?
- How important is the plasma torus in determining the intensity of oxygen? Can column densities be determined without independent measurements of the plasma?

This thesis is organized so as to best answer these questions. In Chapter 2, I discuss the physical processes at work which are common to all three regions. Chapter 3 presents mutual event observations designed to probe the radial structure of the sodium corona. I report the discovery of a previously undetected asymmetry in the column density between the sub-Jupiter and anti-Jupiter hemispheres. Galileo observations of Io's fast sodium jet are described in Chapter 4. These observations are the closest view to date of the source region of the jet. A neutral cloud model based on the model of Wilson and Schneider (1999) and extended for study of sodium cloud to Io is described in Chapter 5. Applications of this model to the corona and extended clouds are presented in Chapters 6 and 7, respectively.

Chapter 2

Physical Processes Governing Neutrals

2.1 Introduction

Multiple physical processes are responsible for the creation, destruction, and visibility of Io's corona and neutral clouds. In this chapter I discuss many of the physical processes that together create the unique neutral clouds observed at Jupiter. In Section 2.2, I describe the processes of resonant scattering, which allows sodium to be observed, and electron impact excitation, the process which dominates the oxygen and sulfur emission. Next I describe sputtering, the main source of neutral escape from Io's exobase. Section 2.4 describes the two processes which limit the size of the neutral clouds: electron impact ionization and charge exchange. The chapter concludes with a summary of the forces which act on the neutrals between their loss from Io (i.e., their entry into the clouds) and their loss by ionization. The specific application of these physical processes to the neutral clouds will be discussed in Chapter 5 where the neutral cloud model is introduced.

2.2 Emission and Absorption Mechanisms

Knowing which microscopic physical processes are responsible for producing the observed radiation from an astrophysical object is a good first step in understanding the properties of the object. This section describes the processes which allow Iogenic neutrals to be observed both in emission and absorption. The first mechanism, resonant

scattering, applies only to sodium and explains why sodium is the most commonly observed neutral at Io. The second mechanism, electron impact excitation, is the main mechanism responsible for emission by oxygen and sulfur. A small component of the sodium emission is due to electron impact excitation of sodium, but since this is small compared to the emission by resonant scattering, it is not included in this work.

2.2.1 Resonant Scattering: Observing Sodium

The sodium observations discussed in this thesis reveal the presence of sodium either through emission or absorption. The same physical mechanism is responsible in each case: the resonant scattering of light by sodium atoms. As sunlight interacts with sodium atoms, photons are absorbed and almost instantly re-emitted (within $\sim 10^{-8}$ sec). Since the incident photons all originate from the same direction (the direction of the sun) and are emitted isotropically, an observer looking along the sun-Io line (with Io between the sun and the observer) will see the intensity of sunlight at the resonant wavelengths diminished; i.e., an absorption line. When observing off the direct line-of-sight to the sun, sodium is observed in emission.

The two main advantages of observing resonantly scattered sodium are that the cross sections for the resonant transitions are large resulting in strong spectral features, and that the intensity depends only on the column density of sodium and the intensity of incident sunlight, not on the state of the plasma flowing through it. It is much easier to derive the sodium density in the neutral cloud than the oxygen density since the intensity of oxygen emission is strongly dependent on the the plasma exciting the emission.

The radiative transfer of the sodium D lines ($3s\ ^2S_{1/2} \rightarrow 3p\ ^2P_{1/2}, 3p\ ^2P_{3/2}$) is discussed here to show how the observed absorption or emission relates to the column density of sodium. The lines connect to the ground state and are excited by absorption of solar photons. Figure 2.1 shows a schematic of these transitions including the hyperfine

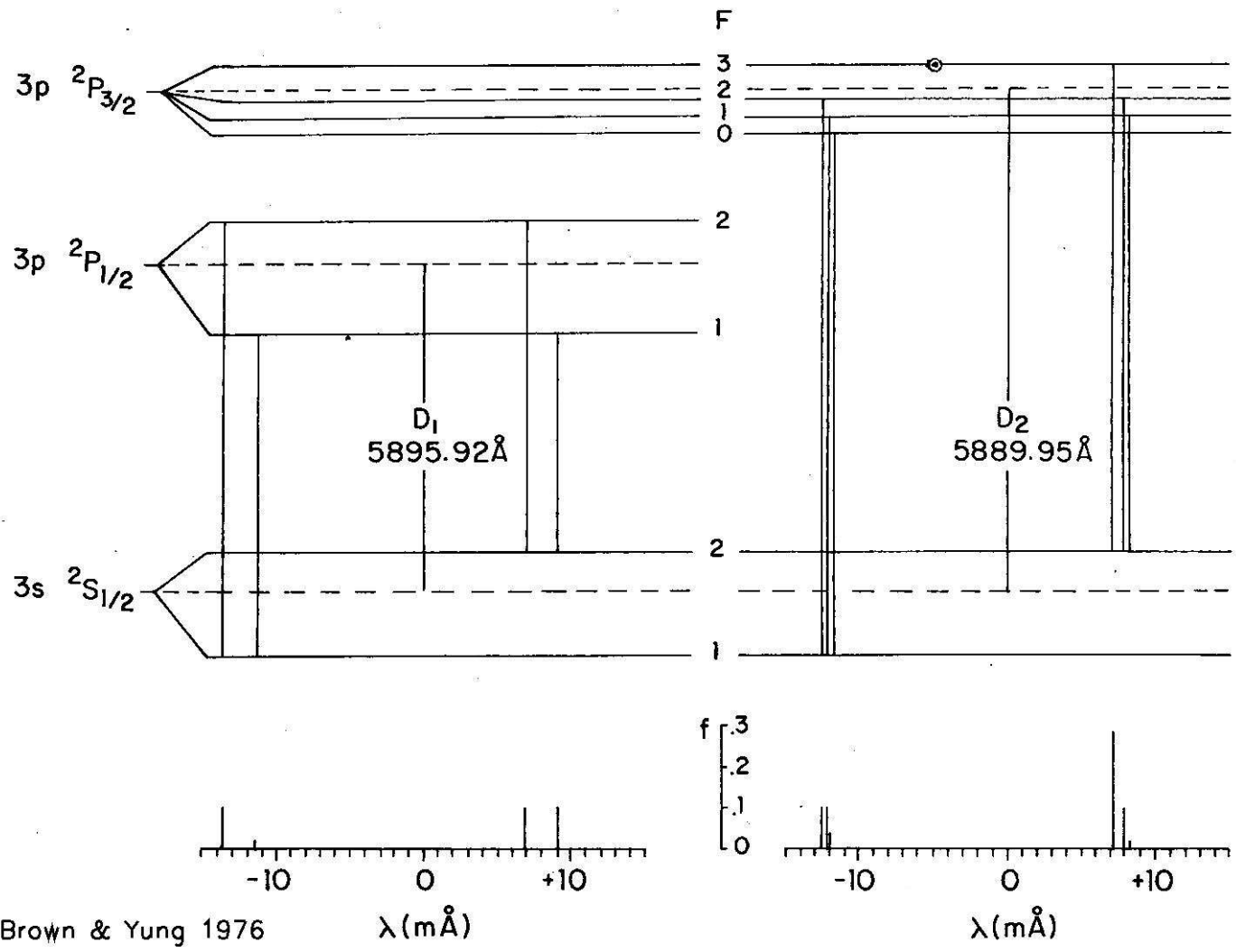


Figure 2.1 From Brown and Yung (1976): Schematic of the sodium D resonance transitions

structure. Hyperfine structure must be included to properly determine the curve of growth (equivalent width vs. column density plot). The following is based on discussions of resonant scattering of sunlight by sodium in Chamberlain (1961) and Brown and Yung (1976).

The fraction of incident sunlight not absorbed by sodium atoms is determined by:

$$T = e^{-\tau} = e^{-\sigma(\lambda)N} \quad (2.1)$$

where $\tau = \sigma(\lambda)N$ is the optical depth through a cloud of sodium atoms with column density N . The wavelength dependent absorption cross section coefficient ($\sigma(\lambda)$) is the sum of the individual Doppler broadened hyperfine line profiles:

$$\sigma = \sum \sigma_i = \sum \sigma_{0i} e^{-\frac{(\lambda-\lambda_{0i})^2}{\alpha_i^2}} \quad (2.2)$$

The cross section at the center of hyperfine line i is given by

$$\sigma_{0i} = \left(\frac{\lambda_{0i}^2}{c\sqrt{\pi}\alpha_i} \right) \left(\frac{\pi e^2}{m_{Na}c} \right) f_i \quad (2.3)$$

The Doppler broadening constant α depends on the temperature according to:

$$\alpha_i = \frac{\lambda_{0i}}{c} \sqrt{\frac{2kT}{m_{Na}}} \quad (2.4)$$

The offsets of each hyperfine line from the central wavelengths ($\Delta\lambda$) and their oscillator strengths (f_i) are listed in Table 2.1.

The measured quantity for an absorption line is the equivalent width, defined as

$$W_\lambda = \int_{-\infty}^{\infty} (1 - T)d\lambda = \int_{-\infty}^{\infty} (1 - e^{-\tau})d\lambda \quad (2.5)$$

and is a function of the sodium column density and temperature. The curves of growth for the D_2 line and the ratio of W_{D_2} to W_{D_1} at several temperatures are shown in Figure 2.2. For optically thin regions ($\tau < 1$) the equivalent width is linear with column density (on the log-log plot) and independent of temperature. When the sodium is optically thick ($\tau \gtrsim 1$), the degeneracy in temperature is lifted and the equivalent width

D ₁ $^2S_{1/2} \rightarrow ^2P_{1/2}$, $\lambda_{D_1} = 5895.92 \text{ \AA}$, $f=0.33$		
Hyperfine Transition	$\Delta\lambda(\text{m\AA})$	f
F=2 \rightarrow F=1	-13.6	0.102
F=1 \rightarrow F=1	-11.4	0.020
F=2 \rightarrow F=2	+6.9	0.102
F=1 \rightarrow F=2	+9.1	0.102
D ₂ $^2S_{1/2} \rightarrow ^2P_{3/2}$, $\lambda_{D_2} = 5889.95 \text{ \AA}$, $f=0.65$		
Hyperfine Transition	$\Delta\lambda(\text{m\AA})$	f
F=2 \rightarrow F=1	-12.6	0.102
F=1 \rightarrow F=1	-12.2	0.102
F=0 \rightarrow F=1	-12.0	0.041
F=3 \rightarrow F=2	+7.2	0.287
F=2 \rightarrow F=2	+7.9	0.102
F=1 \rightarrow F=2	+8.3	0.020

Table 2.1 Sodium D Line Parameters (from Brown and Yung (1976))

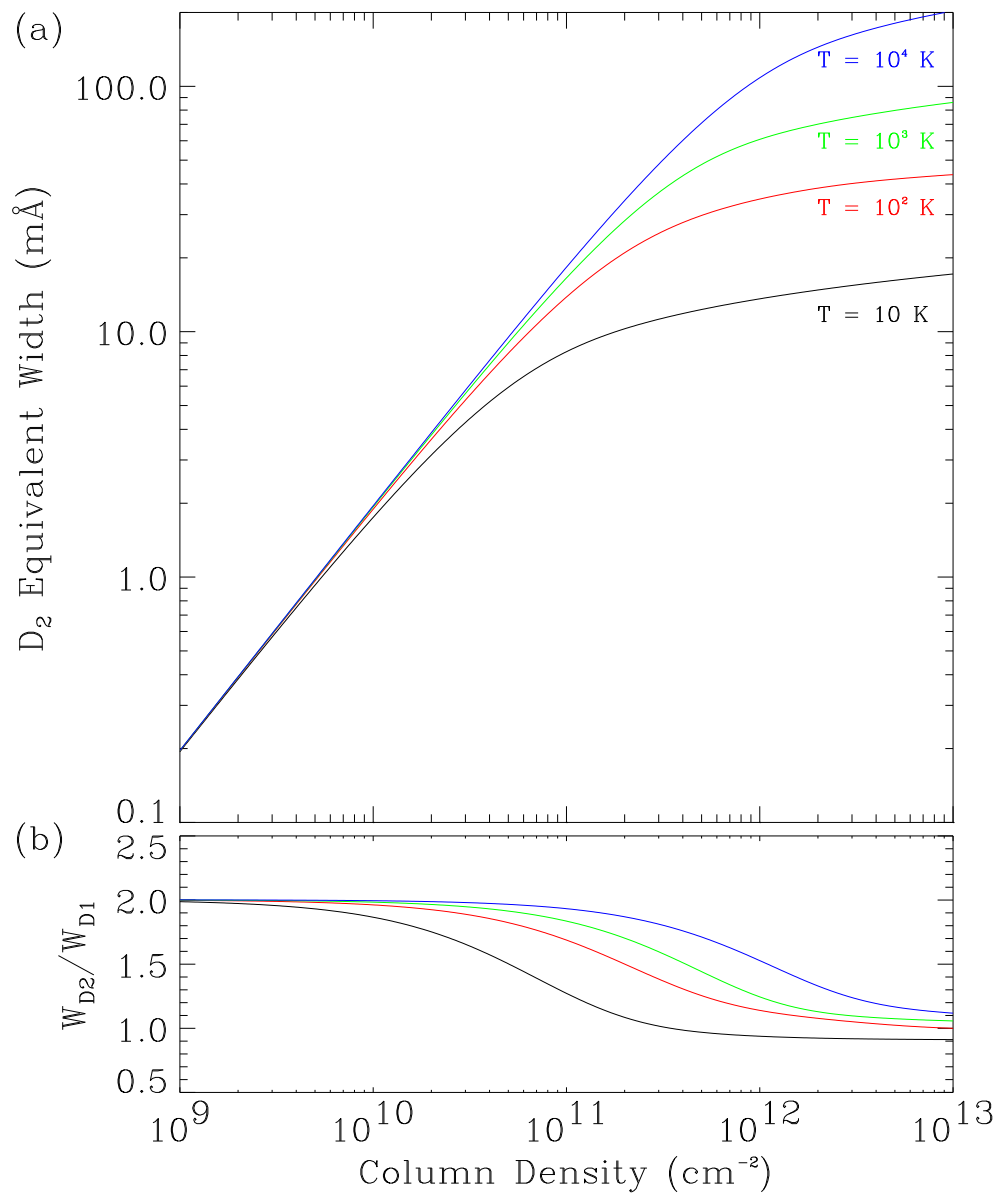


Figure 2.2 (a) Curves of growth for the Na D_2 line at 5890 \AA for four temperatures. (b) Ratio of equivalent widths of D_2 and D_1 lines at the four temperatures in (a). Note that, $W_{D_2}/W_{D_1} = 2$ for low column densities and approaches 1 for high column densities.

increases by $\sqrt{\ln(\sigma N)}$. The transition point between the optically thin and optically thick regimes is a function of temperature. Note that in the optically thin regime, the ratio of W_{D2} to W_{D1} reduces to the ratio of the oscillator strengths of the two lines, in this case, $W_{D2}/W_{D1} \rightarrow 2$ (Figure 2.2b). As the column of absorbing sodium increases, the ratio of equivalent widths approaches 1, providing a simple estimate of the optical depth.

When viewing from a geometry other than directly along the sun-Io line, sodium is seen in emission. The absorbed photons are emitted isotropically (the D₂ line is slightly anisotropic (Parkinson 1975), but for these purposes, it is assumed to be isotropic). The observed sodium intensity coupled with knowledge of the intensity of the solar continuum at sodium D wavelengths directly determines the column density.

When the gas is optically thin, the intensity is given by

$$E = gN \quad (2.6)$$

where N is the column density and the g-factor is the rate of photon absorption per neutral atom defined by

$$g = \left[\gamma \cdot \pi F_{\odot}(5900\text{\AA}) \cdot \frac{\lambda^2}{c} \right] \left(\frac{\pi e^2}{m_e c} \right) f \quad (2.7)$$

The term $\left(\gamma \cdot \pi F_{\odot} \frac{\lambda^2}{c} \right)$ is the total number of photons available for absorption in units of photons cm^{-2} , and $\left(\frac{\pi e^2}{m_e c} f \right)$ is the absorption coefficient in $\text{cm}^2 \text{s}^{-1}$. The solar continuum flux at the sodium D wavelengths is $\pi F_{\odot}(5900\text{\AA}) = 2.02 \times 10^{12} \text{ photons} \cdot \text{cm}^{-2} \cdot \text{\AA}^{-1} \cdot \text{s}^{-1}$. The term $\left(\gamma \cdot \pi F_{\odot}(5900\text{\AA}) \right)$ is the solar flux at the absorption wavelength in Io's rest frame, where γ is the ratio of the solar intensity at the sodium line Doppler shifted to Io's rest frame to the continuum (see Figure 1.2). If Io's radial velocity relative to the Sun is 0 km s^{-1} then for the two Na D lines, $\gamma_{D2} = 0.05$ and $\gamma_{D1} = 0.06$ (Brown and Yung 1976). At Io's maximum radial velocity of $\pm 17.3 \text{ km s}^{-1}$ (corresponding to eastern and western elongation), $\gamma_{D2} = 0.6$ and $\gamma_{D1} = 0.7$. Since the emitted intensity

is directly proportional to γ , there is an order of magnitude change in the brightness of the sodium cloud over Io's orbital period simply because of the change in Io's radial velocity relative to the sun.

Converting Equation 2.6 to the unit of choice for line emission measurements, the Rayleigh ($1Ra = 10^6 \text{ photons} \cdot \text{cm}^{-2} \cdot \text{s}^{-1} \cdot (4\pi \text{ster})^{-1}$), yields:

$$\begin{aligned} E_{D_2} &= (3.9 \times 10^{-7} Ra \cdot \text{cm}^2) \gamma_{D_2} N \\ E_{D_1} &= (2.0 \times 10^{-7} Ra \cdot \text{cm}^2) \gamma_{D_1} N \end{aligned} \quad (2.8)$$

For regions where sodium is optically thick, multiple scatterings become important and a more detailed model of the radiative transfer is needed to correctly determine the column density from the brightness. Since sodium is only optically thick in the corona near Io, where the emission can not easily be observed from Earth, it is not necessary to do this modeling here. A method to determine the column density of sodium from optically thick absorption lines is described in chapter 3.

2.2.2 Electron Impact Excitation: Observing oxygen and sulfur

Oxygen and sulfur are not observed through resonant scattering like the trace constituent sodium. Instead, the emission observed for these neutrals is excited by electron impacts. It is more difficult to determine the column density of the emitting region for electron excited emission due to the fact the the emitted intensity depends not only on the number of neutrals present, but also on the properties of the plasma that bathes the neutrals and which varies considerably along the line of sight. The morphology of the emitting region is therefore sensitive to both the distribution of neutrals and changes in the plasma.

The emission intensity is determined by integrating the volume emission rate ρ_k over the line-of-sight. The volume emission rate in units of $\text{cm}^{-3}\text{s}^{-1}$ is:

$$\rho_k = C_k(n_e, T_e) n_e n_i \quad (2.9)$$

where n_e and T_e are the electron density and temperature of the plasma, C_k is the emission rate coefficient for the observed transition (emission line) and n_i is the density of the neutral atom or ion being excited. C_k is tabulated in the CHIANTI atomic physics database (Dere et al. 1997) as a function of electron density and temperature for the UV lines of sulfur and oxygen that are observed. The emitted intensity of an electron impact excited line is then

$$I = \int_{-\infty}^{\infty} \rho_k dy = \int_{-\infty}^{\infty} C_k(n_e, T_e) n_e n_i dy \quad (2.10)$$

where y is the direction along the line of sight.

2.3 Creating the neutral clouds: Sputtering

The material observed in the corona and neutral clouds all originated at Io: Gases are released from volcanic vents, sublimated from frosty regions of the surface, and sputtered (see below) off the surface by incident charged particles. This material either remains in the atmosphere or snows out farther away from the active volcanic centers. In these regions the atmosphere is maintained by vapor pressure equilibrium with the surface. At the atmospheric exobase, some sputtered atoms escape with ballistic trajectories into the exosphere where there are no collisions or other interactions between neutrals. Below I present the flux speed distribution used to characterize the sputtering process.

Sputtering occurs when an ion striking the surface or atmosphere initiates a cascade of collisions which results in the ejection of a neutral (Figure 2.3, and see Johnson (1990)). I use the modified sputtering flux-speed distribution introduced by Smyth and Combi (1988b) to parameterize the speed distribution of sputtered atoms. The single particle speed distribution function is given by:

$$f(v) \propto \frac{1}{(v^2 + v_b^2)^\alpha} \left[1 - \left(\frac{v^2 + v_b^2}{v_M^2} \right)^{1/2} \right] \quad (2.11)$$

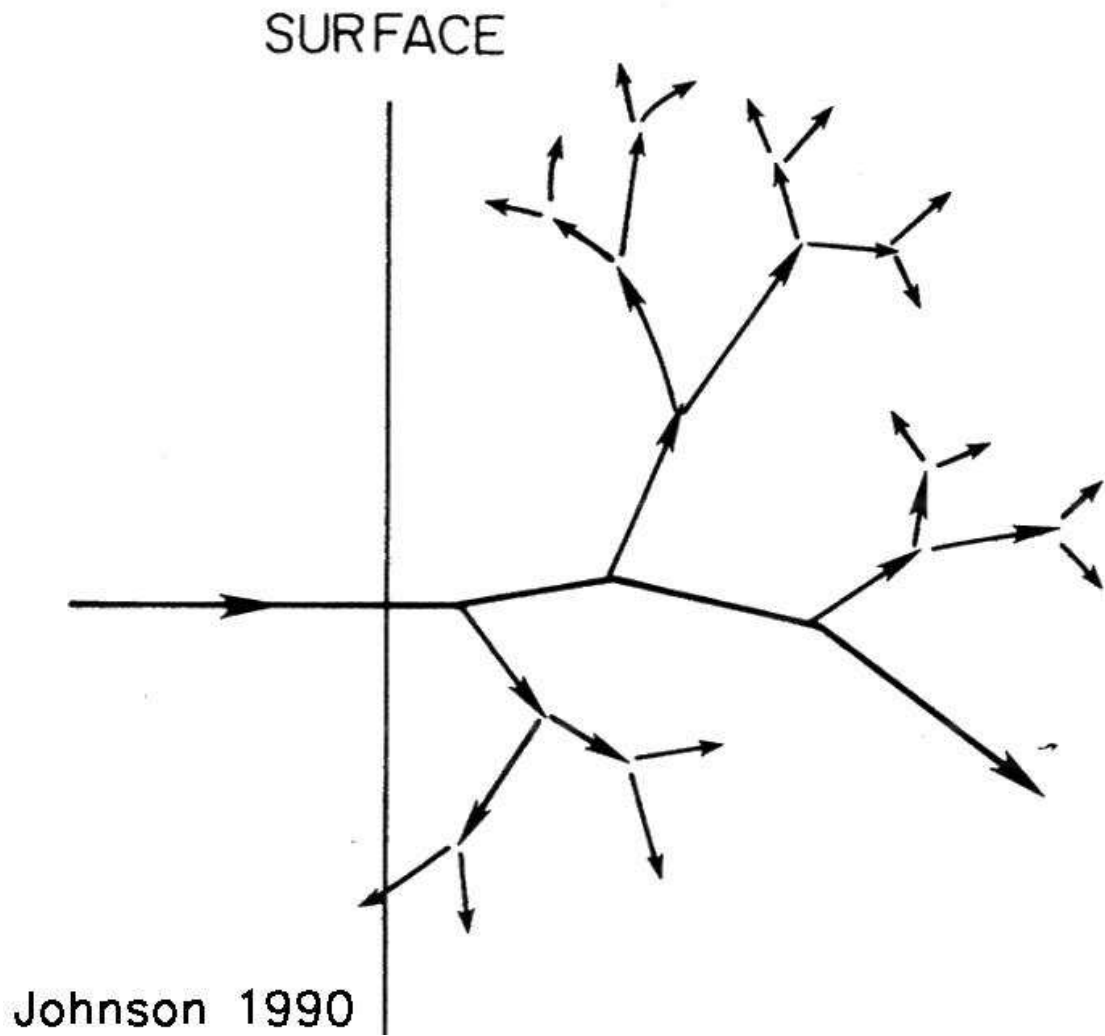


Figure 2.3 Sketch of collisional cascade which results in surface sputtering. Atmospheric sputtering can be represented by a similar sketch with “surface” replaced with “exobase.” Figure from Johnson (1990)

where $v_M = \frac{2m_n}{m_{ion}+m_n}v_R$ is the velocity a sputtered atom would have if the atom were ejected from a single completely elastic collision with a torus ion and represents the high speed cutoff of the distribution. m_{ion} and m_n are the masses of the average torus ion and the sputtered neutral, respectively. v_R is the relative speed between the incident ions, which are assumed to be co-rotating with Jupiter's magnetic field, and Io. v_b is related to the energy required to eject a neutral. For pure surface sputtering, the surface binding energy is $mv_b^2/2$. Because sputtering at Io is a mix of surface and atmospheric sputtering, neither of which are likely to be uniform in composition, the average binding energy is not easily determined. Therefore the speed distributions used in this thesis are described in terms of their most probable speed, v_p , which is a non-linear function of v_b : v_b is chosen such that the speed distribution has the desired most probable velocity. The parameter α regulates the high speed behavior of the distribution. Physically it is related to the relative importance of single- and multi-ejection events. Classical sputtering (described by Sieveka and Johnson (1984)) is described by $\alpha = 3$.

The flux distribution for this process is given by

$$\begin{aligned}\phi(v) &\propto v^3 f(v) \\ &\propto \frac{v^3}{(v^2 + v_b^2)^\alpha} \left[1 - \left(\frac{v^2 + v_b^2}{v_M^2} \right)^{1/2} \right]\end{aligned}\quad (2.12)$$

examples of which are shown in Figure 2.4 for several values of v_p and α . Note that the escape speed from Io's exobase is 2.1 km s^{-1} , so for a low energy sputtering distribution only the high speed tail is important for forming the extended cloud. Panel (a) compares the shapes of sputtering distributions with different values of α . This parameter describes the high speed sputtered material such that the distribution decreases proportional to $v^{3-2\alpha}$ for $v_p < v < v_M$, with a much more rapid drop-off for $v \sim v_M$. The high speed power law drop-off is not affected by the most probable speed as demonstrated in panel (b).

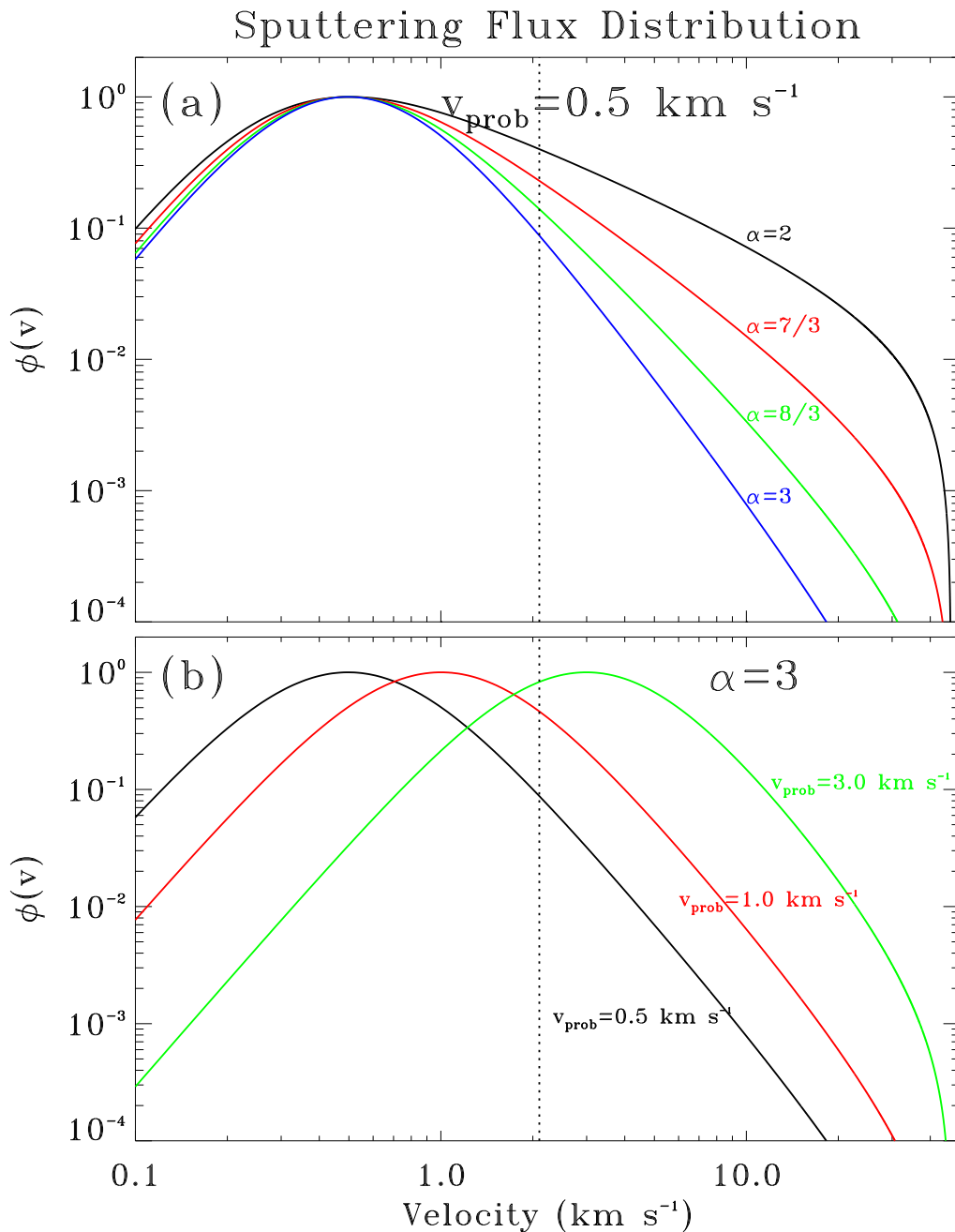


Figure 2.4 Examples of the sputtering flux distribution used as a possible initial flux distribution from Io's exosphere. The normalization is relative to the most probable speed of the distribution. (a) Flux distributions formed by varying α , keeping the most probable speed of the distribution constant at $v_p = 0.5 \text{ km s}^{-1}$. The dotted line shows the escape velocity from Io's exobase ($v_{\text{esc}} = 2.1 \text{ km s}^{-1}$). (b) Flux distributions keeping $\alpha=3$ (classical sputtering) and varying the most probable speed.

2.4 Destruction Physics

All the neutral atoms ejected from Io's exobase are eventually lost from the system. In this thesis, two types of loss will be considered: a neutral can hit a large object and be lost to the system or it can be ionized and swept into the plasma torus. Only two objects are considered as sinks for sodium. A neutral can re-impact Io's atmosphere if it is not ejected with sufficient energy to escape Io's gravitational pull. Neutrals can also hit Io if by chance they re-intersect Io's orbit when Io is there. This is a relatively rare occurrence, but it is taken into account as a possibility when calculating particle trajectories. The other physical sink is Jupiter: occasionally a neutral's trajectory takes it too close to Jupiter and is lost from the system.

The dominant sink for neutrals is ionization caused by interaction with the plasma torus. Ionization of the neutral clouds provides the source for the torus, so that the plasma torus and the neutral clouds are intimately related. The lifetime of a neutral ejected from the exobase is

$$\tau = \left(\sum \nu_i \right)^{-1} \quad (2.13)$$

where ν_i are the ionization rates of each individual process. Two ionizing mechanisms are considered: electron impact ionization and charge exchange. The former is most important for sodium; the latter is the dominant oxygen sink. Both processes are important for sulfur. A brief description of the methods for determining the lifetime of neutrals for each mechanism is given below. The photo-ionization rates for oxygen (~ 38000 hours, Smyth and Marconi (2000)) and sodium (~ 400 hours, Smyth and Combi (1988b)) are significantly longer than either the electron impact or charge exchange ionization rates and are therefore ignored.

2.4.1 Electron Impact ionization

The rate of neutral ionization due to electron impacts is given by:

$$\nu_{EI} = n_e K(T_e) \quad (2.14)$$

where n_e and T_e are the electron density and temperature, respectively, at the location of the neutral atoms and $K(T_e)$ is the rate coefficient. The rate coefficient depends on the cross section for ionization which is determined experimentally. Two published measurements of the sodium cross section are shown in Figure 2.5(a). The older measurement (Zapesochnyi and Aleksakhin 1969) is included to provide consistency with previous neutral cloud models (e.g. Smyth and Combi (1988b)). All modeling results in later chapters use the cross section measured by Johnston and Burrow (1995) except where explicitly stated otherwise. This change in atomic data has an effect on the understanding of the neutral cloud due to the fact that the lifetime of sodium at Io is ~ 1.4 times longer than previously thought. Implications for changing the sodium lifetime are considered when discussing model results in Chapters 6 and 7.

The rate coefficient K is a measure of how difficult it is for a given species to be ionized by plasma of a given temperature. I have determined the rate coefficient as a function of electron energy (temperature) using the method of Arnaud and Rothenflug (1985) who empirically parameterize the cross sections shown in Figure 2.5(a) and integrate over a Maxwellian velocity distribution. The rate coefficients for sodium, oxygen, and sulfur are shown in Figure 2.5(b).

Once the rate coefficient is determined, the lifetime of the neutral follows easily from the product of the local electron density and the temperature dependent rate coefficient. Table 2.2 lists typical lifetimes at Io for sodium, oxygen, and sulfur. Since the lifetimes of all species are strongly dependent on the plasma properties, a further analysis of the lifetime will be presented in Chapter 5 when the implementation of the plasma torus is discussed.

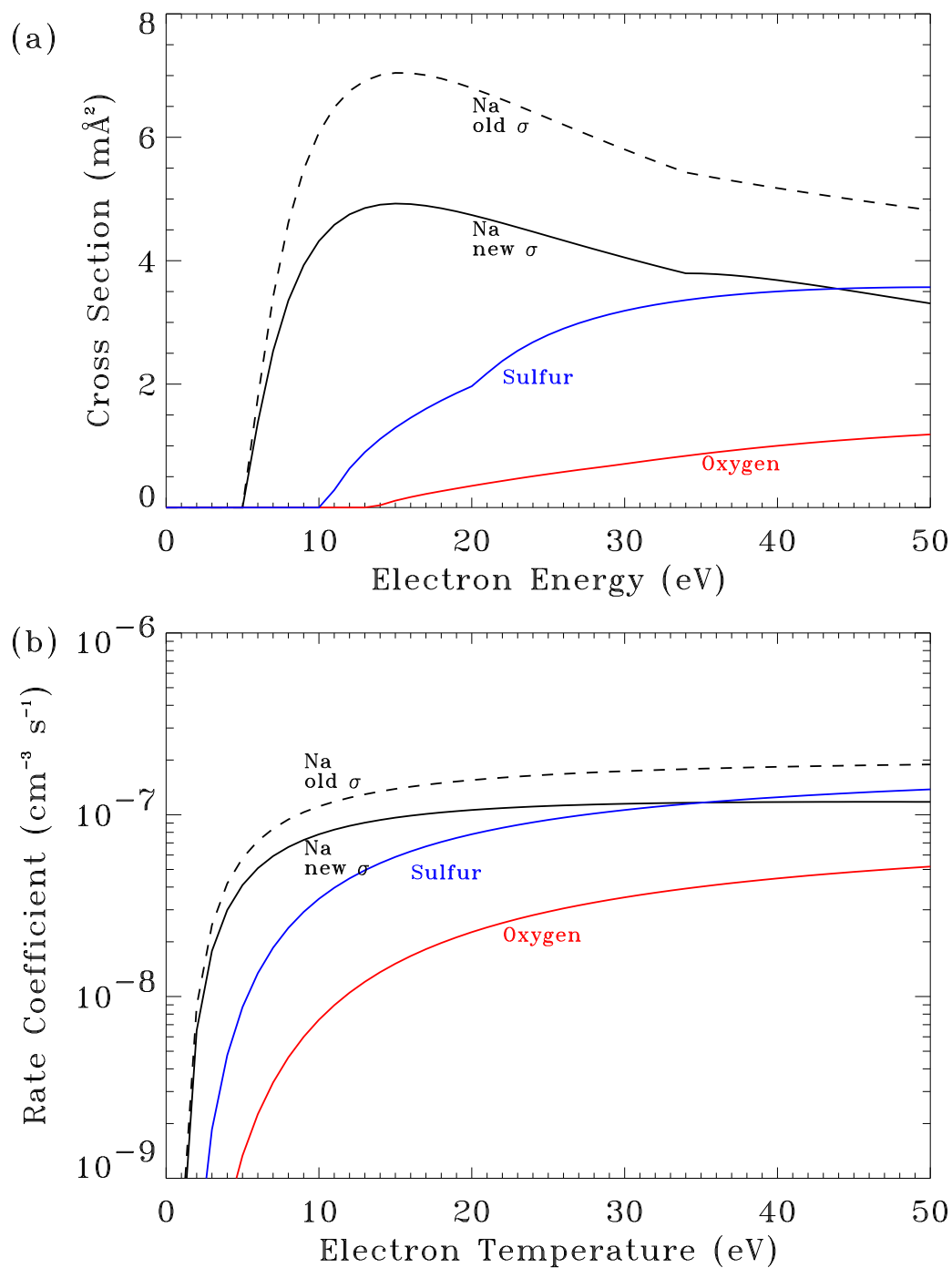


Figure 2.5 (a) Electron impact ionization cross sections. Neutral sodium cross sections determined by Johnston and Burrow (1995) are shown with a solid line. The older measurements of Zapesochnyi and Aleksakhin (1969) are drawn with the broken line. Cross sections for oxygen and sulfur are shown in blue and red, respectively (Arnaud and Rothenflug 1985). (b) Rate coefficients for sodium, oxygen, and sulfur determined from the cross sections in (a).

Species	Electron impact	Charge exchange
Sodium	4 hours	50 hours
Oxygen	150 hours	30 hours
Sulfur	20 hours	30 hours

Table 2.2 Approximate average neutral lifetimes of sodium, oxygen, and sulfur for the processes of electron impact ionization, and charge exchange at Io.

2.4.2 Charge exchange

As seen in Table 2.2, oxygen and sulfur take much longer to be ionized by electron impacts than sodium. For these neutral species, charge exchange with Io torus ions is a significant loss mechanism from the neutral clouds. Charge exchange is a collisional process between two species, at least one of which is ionized, during which the electron clouds of the two species overlap and an electron may be transferred. Loss by charge exchange depends on the densities of the different torus species and is therefore affected by both temporal and spatial variations in the plasma torus.

The ionization rate per neutral due to charge exchange, ν_{CX} , is determined by:

$$\nu_{CX} = \sum_i \nu_i = \sum_i \sigma_i v(\mathbf{r}) n_{ion}(\mathbf{r}) \quad (2.15)$$

where the sum is performed over each possible charge exchange reaction. σ_i is the charge exchange cross section for reaction i , and $n_{ion}(\mathbf{r})$ is the density of the torus ion in reaction i at distance \mathbf{r} from Jupiter. $v(\mathbf{r})$ is the relative velocity of ions and neutrals. Torus ions are assumed to be co-rotating rigidly with Jupiter's magnetic field so that:

$$v_{ion} = \Omega r \quad (2.16)$$

with Ω equal to the angular velocity of Jupiter's magnetic field. The neutral velocity is approximated by the Keplerian velocity appropriate for their distance from Jupiter:

$$v_n = \left(\frac{GM_J}{r} \right)^{(1/2)} \quad (2.17)$$

Therefore, the relative velocity is

$$v(\mathbf{r}) = v_{ion} - v_n = \Omega r - \left(\frac{GM_J}{r} \right)^{(1/2)} \quad (2.18)$$

The important charge exchange reactions for sodium, oxygen, and sulfur are listed in Table 2.3 with their cross sections and rate coefficients at Io's orbit ($k = \sigma v(r = 5.91 R_J)$).

2.5 Neutral Dynamics

Between their ejection into the Jovian system and their eventual loss, Iogenic neutrals are subjected to the relentless forces of gravity and radiation pressure. The positions of particles are determined by solving the equations of motion defined by:

$$m_n \frac{d^2 \mathbf{x}_n}{dt^2} = \sum_i \mathbf{F}_i \quad (2.19)$$

where m_n and $\frac{d^2 \mathbf{x}}{dt^2}$ are the mass and acceleration, respectively, of neutral species n, and \mathbf{F}_i are the individual forces of Jupiter's gravity, Io's gravity, and radiation pressure. The following are brief descriptions of these forces as they relate to neutrals in the inner Jovian system.

2.5.1 Gravity

The classical gravitational force is appropriate for the neutrals leaving Io:

$$\mathbf{F} = -G \frac{M_p m_n}{r_p^2} \hat{r} \quad (2.20)$$

where G is the universal Gravitational constant, M_p is the mass of the object exerting the force (i.e., Jupiter and Io), r_p is the distance from the neutral to that object, and m_n is the mass of the neutral. The acceleration caused by the gravitational force is what is actually important, so:

$$\mathbf{a} = -G \frac{M_p}{r_p^2} \hat{r} \quad (2.21)$$

which is independent of the mass of the neutral being considered. This is important because it means that the neutrals considered in this thesis behave identically when injected into the system when only gravity is considered. Differences in cloud morphologies are due to factors other than their dynamical behaviors when added to the Jovian system.

Reaction	σ (\AA^{-2})	k ($10^{-9} \text{ cm}^3 \text{ s}^{-1}$)
$\text{O} + \text{O}^+ \rightarrow \text{O}^+ + \text{O}$	22	13
$\text{O} + \text{O}^{++} \rightarrow \text{O}^{++} + \text{O}$	9	0.5
$\text{O} + \text{O}^{++} \rightarrow \text{O}^+ + \text{O}^+$	0.9	5
$\text{O} + \text{S}^+ \rightarrow \text{O}^+ + \text{S}$	0.1	0.06
$\text{O} + \text{S}^{++} \rightarrow \text{O}^+ + \text{S}^+$	3.8	2.2
$\text{O} + \text{S}^{+++} \rightarrow \text{O}^+ + \text{S}^{++}$	32	18
$\text{S} + \text{O}^+ \rightarrow \text{S}^+ + \text{O}$	5	3
$\text{S} + \text{O}^{++} \rightarrow \text{S}^{++} + \text{O}$	39	22
$\text{S} + \text{S}^+ \rightarrow \text{S}^+ + \text{S}$	40	23
$\text{S} + \text{S}^{++} \rightarrow \text{S}^+ + \text{S}^+$	0.5	0.3
$\text{S} + \text{S}^{++} \rightarrow \text{S}^{++} + \text{S}$	13	7.4
$\text{S} + \text{S}^{+++} \rightarrow \text{S}^+ + \text{S}^{++}$	22	12
$\text{Na} + \text{O}^+ \rightarrow \text{Na}^+ + \text{O}$	0	0
$\text{Na} + \text{O}^{++} \rightarrow \text{Na}^+ + \text{O}^+$	~ 30	17
$\text{Na} + \text{S}^+ \rightarrow \text{Na}^+ + \text{S}$	0	0
$\text{Na} + \text{S}^{++} \rightarrow \text{Na}^+ + \text{S}^+$	~ 30	17

Table 2.3 Summary of the major charge exchange reactions between neutral oxygen and sulfur atoms and the major torus ions. Cross sections are compiled from McGrath and Johnson (1989) The rate coefficients are calculated at the distance of Io's orbit.

2.5.2 Radiation Pressure

More than just a perturbation, radiation pressure can have a real effect on the dynamics of neutrals ejected from Io. Because the resonant transition of sodium is near the peak of the solar black body continuum, radiation pressure is most important for understanding the evolution of sodium. Oxygen and sulfur have resonant transitions at FUV wavelengths (1304 Å and 1299 Å, respectively) where the solar continuum is very weak, and therefore radiation pressure is not a factor affecting these species.

Radiation pressure is a force exerted on a cloud of atoms due to the absorption and emission of photons by the gas. The isotropic scattering of photons that causes the sodium cloud to be visible also results in a force equal to the rate of change in the net momentum of the absorbed photons:

$$\mathbf{F} = \frac{d\mathbf{p}}{dt} \quad (2.22)$$

Since the photons are all initially incident from the direction of the sun, the magnitude of the momentum of a single photon is

$$p_{phot} = \frac{h}{\lambda} \quad (2.23)$$

where h is Planck's Constant, c is the speed of light, and λ is the wavelength of the absorbed photon. Therefore the net change in momentum of the neutral is equal to the momentum of the incident absorbed photons, i.e.

$$\frac{d\mathbf{p}}{dt} = g \times \mathbf{p}_{phot} \quad (2.24)$$

where g is the rate of photon absorption by a neutral atom given by Equation 2.7.

The acceleration due to the resonant scattering of photons therefore:

$$\begin{aligned}
 a_{rad} &= \frac{F_{rad}}{m_{Na}} & (2.25) \\
 &= \sum_{l=D_1, D_2} \frac{g_l \cdot p_{phot}}{m_{Na}} \\
 &= \sum_{l=D_1, D_2} \frac{1}{m_{Na}} \cdot \left[\gamma_l \cdot \pi F_{\odot} \cdot \frac{\lambda^2}{c} \right] \cdot \left[\frac{\pi e^2}{m_e c} \cdot f_l \right] \left[\frac{h}{\lambda} \right] \\
 &= \left[\frac{\pi F_{\odot} \lambda h}{c m_{Na}} \right] \left[\frac{\pi e^2}{m_e c} \right] [\gamma_1 f_1 + \gamma_2 f_2]
 \end{aligned}$$

Using the values appropriate for sodium, the radiation pressure acceleration is a function only of γ for each line, which in turn is a function of the radial velocity of Io relative to the sun. The radiation pressure term in the equations of motion is therefore:

$$a_{rad} = 0.580 (\gamma_1 + 2\gamma_2) \text{ cm s}^{-2} \quad (2.26)$$

In Io's corona, at $3 R_{Io}$, the acceleration due to Io's gravity on a neutral atom is 20 cm s^{-2} , the centripetal acceleration toward Jupiter of a sodium atom in orbit around Jupiter at Io's orbit is 70 cm s^{-2} , and the acceleration due to radiation pressure of a sodium atom at western elongation, where the radial velocity is maximized, is 1 cm s^{-2} . Although the radiation pressure term is large enough to perturb the orbits of sodium atoms, it is too small to have any observable consequences. The effect of radiation pressure is discussed in more detail in Chapter 5.

2.6 Summary

Each step in the lives of the atoms which make up the neutral clouds can be dominated by no more than two processes. Their birth into the system is represented by ejection from the exobase into the corona. This is dominated by the process of sputtering of Io's atmosphere by the plasma torus. The behavior of the neutrals once they escape from the near-surface atmosphere is governed by the competing effects of Io's and Jupiter's gravitational attraction. In the corona, Io's gravity is the dominant

force; farther out, Jupiter wins out. Atoms are lost from the system by either electron impact ionization or charge exchange with torus ions. The former process dominates the sodium loss from the neutral clouds, although charge exchange near Io's exobase has important observational consequences. Charge exchange is the most important loss mechanism for oxygen. Sulfur is lost through both electron impact ionization and charge exchange.

In the following chapters, different aspects of Io's corona and neutral clouds are described and modeled. All of the features which are discussed result from different combinations of the physical processes discussed here.

Chapter 3

Io's Corona: Creation and Destruction

3.1 Introduction

In this chapter the distribution of sodium in Io's corona is measured using spectra taken of Galilean satellites being eclipsed by Io. Data from 1991 and 1997 are compared with the previous mapping in 1985 by Schneider et al. (1991a) to show that the corona has remained remarkably stable over a period of twelve years. I also present evidence for an apparent column density asymmetry in the corona above Io's sub-Jupiter and anti-Jupiter hemispheres. This chapter has been previously published, in slightly modified form, as Burger et al. (2001). I performed the data reduction for the 1997 Keck Observatory observations as well as the analysis of the combined data sets.

Tracing the distribution of sodium in the corona will help to explain the sources and escape of all coronal species. Although oxygen and sulfur have been detected in the corona (Ballester et al. 1987), the radial density profiles of these species have never been measured due to the difficulties discussed above. Recent observations with the *Hubble Space Telescope* have mapped the intensity profile within $10 R_{\text{Io}}$ (Roesler et al. 1999; Wolven et al. 2001). Saur et al. (2000) have shown that the qualitative features of the bright equatorial emission spots seen in observations of neutral oxygen (OI] 1356 Å) (Retherford et al. 2000) close to Io can be explained through interactions between Io and the plasma torus in a spherically symmetric corona. This is an indication of the difficulties involved in deriving a unique oxygen density profile from remote observations.

Since the sodium abundance is more directly determined from intensity, observations of the sodium corona provide a less ambiguous view of the near-Io environment.

3.2 Observations

Under normal viewing conditions it is not possible to observe sodium close to Io's surface. This is primarily due to two effects. First, Io has a very high geometric albedo. The surface is approximately as bright in backscattered sunlight at 5900 Å as an optically thick sodium atmosphere. Therefore, Io's disk looks the same regardless of how much sodium is present (Brown et al. 1975). Second, the Earth's atmosphere smears the emission on scales of the order of a few Io radii (R_{Io}) in such a way as to significantly alter the observed emission profile (Schneider et al. 1991a).

To circumvent these problems I have taken advantage of mutual eclipsing events between the Galilean satellites following the method of Schneider et al. (1987, 1991a). The plane of Jupiter's satellites crosses the Sun-Jupiter plane twice along Jupiter's twelve year orbit around the Sun. This provides an opportunity to apply a unique method of probing the exospheres of the moons. As the eclipsing moon (e.g. Io as shown in Figure 3.1) passes between the Sun and the eclipsed moon (Europa in Figure 3.1), the light that is not physically blocked by Io's surface passes through its corona. Sodium atoms in this region scatter the solar photons. This light then reflects off Europa and is observed at Earth. Spectra taken of Europa show the sodium absorption feature from Io's corona. A comparison of spectra taken during and outside of eclipse provides a time series of how much absorption took place during different light traversal paths through Io's corona (Figure 3.2).

I use a series of observations of Galilean satellites being eclipsed by Io from the 1997 eclipse season taken at the Keck Observatory in Hawaii and McDonald Observatory in Texas, as well as one event observed from Catalina Observatory in Arizona in 1991. The data sets are discussed in detail below. Table 3.1 lists the events observed for this

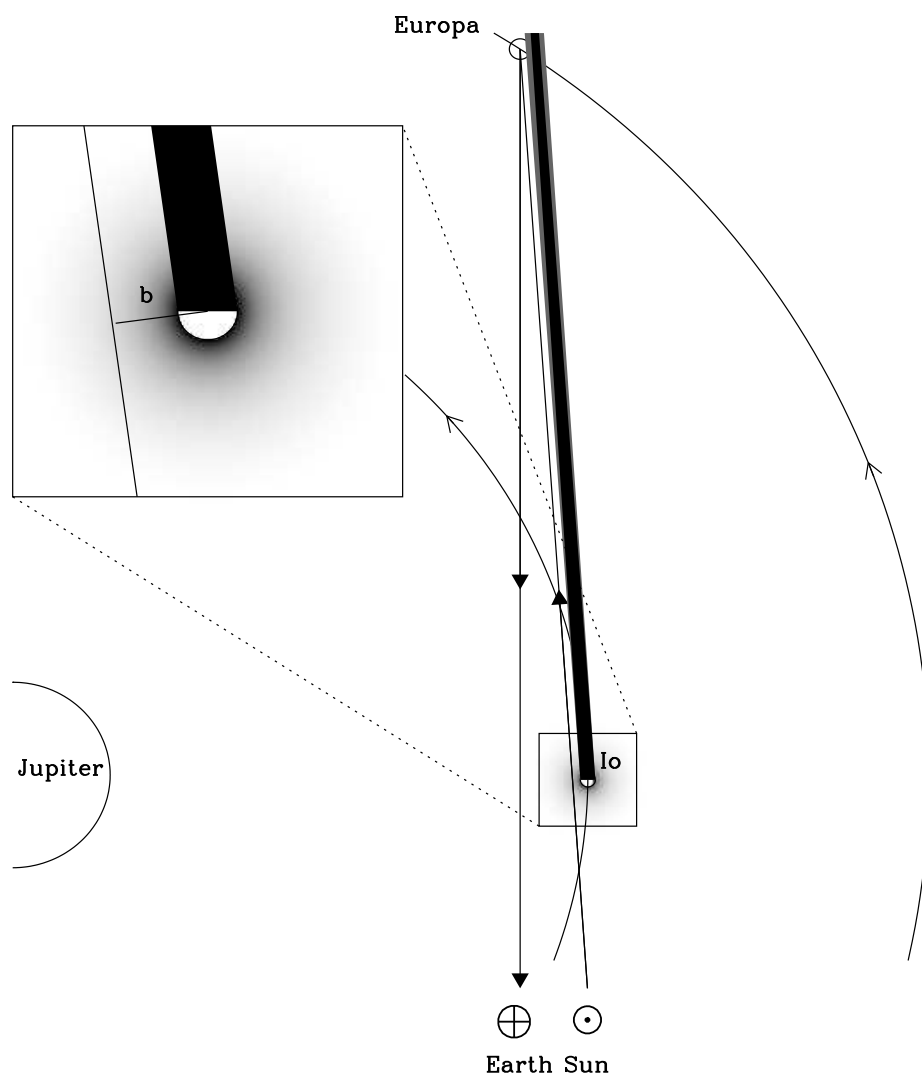


Figure 3.1 Sketch of Io eclipsing Europa. Sunlight passes through the corona, reflects off Europa, and is observed at the Earth. Io's umbra and penumbra are shown falling on Europa. The shaded region surrounding Io represents Io's sodium corona. The extended sodium neutral cloud which leads Io in its orbit is not shown. Io, Europa, and the corona are drawn at three times the scale of Jupiter and the satellite orbits. The direction of satellite motion is indicated, although the magnitude of motion during an observation is not. The insert shows the size of the impact parameter for the observation.

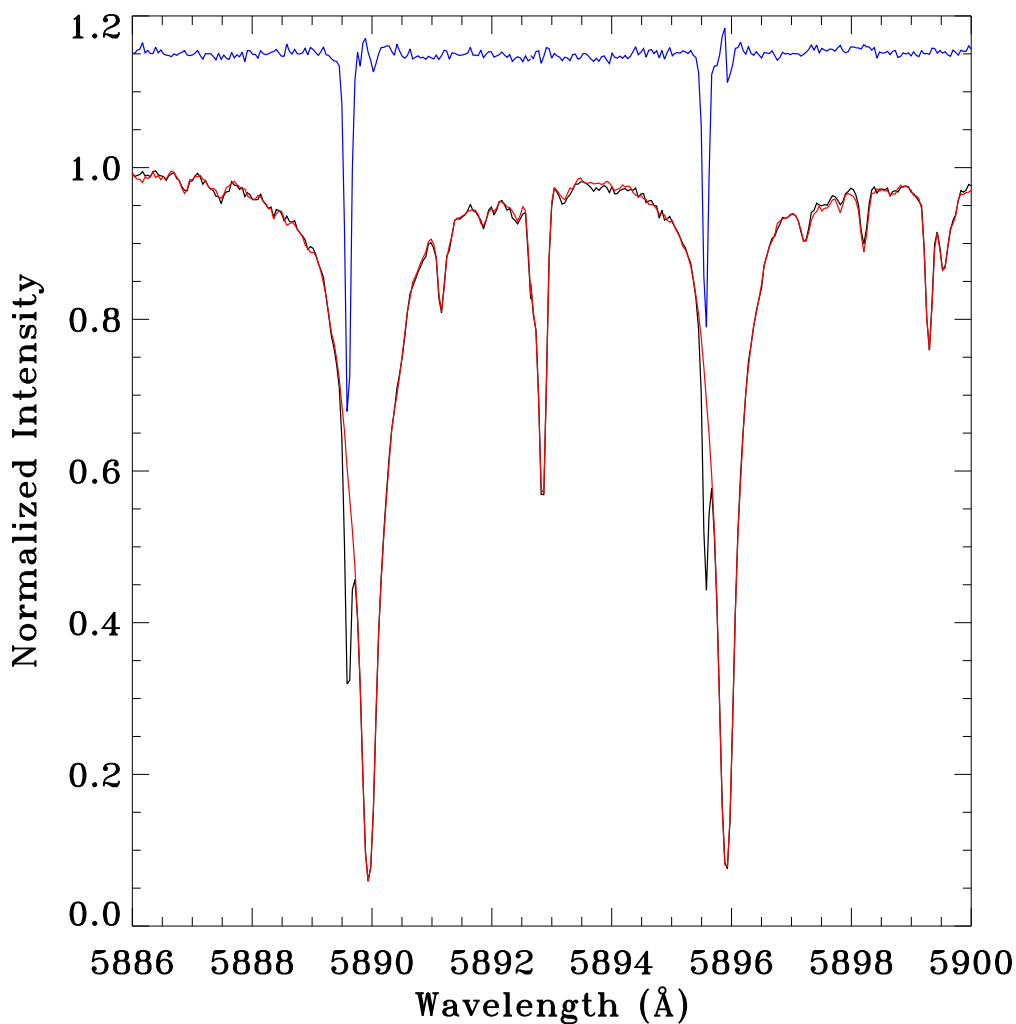


Figure 3.2 Removal of the solar spectrum from an observation from Keck Observatory on 27 August 1997. The black line is a spectrum of Callisto (spectrum #3.10 from Table A.1) during an eclipse showing the absorption from Io's corona. The red line is a spectrum of Callisto out of eclipse (with no absorption at Io). The blue line is the ratio of the two spectra showing a pure Io spectrum. The core of the solar Fraunhofer line is not removed perfectly, but the Doppler shift between the Io sodium absorption line and the solar line is sufficient that the Iogenic absorption is not affected. This line has been shifted up by 0.15 for clarity. Separate corrections are made for the D₂ and D₁ lines. The wavelength calibration is based on the solar rest frame.

analysis. Io's orbital geometry for each observation is shown in Figure 3.3. Although most of the events are clustered near Io's western elongation (orbital phase $\sim 270^\circ$), a variety of orbital geometries are represented. Each event measures a different cut through Io's corona and each observation samples a different section along this trajectory giving us a chance to probe the three-dimensional geometry of the corona. Appendix A lists the location relative to Io of each observation. The determination of the radial distance from Io sampled (the impact parameter, b) is discussed in section 3 below.

3.2.1 Keck Observatory Observations

Three mutual events were observed from the 10-meter telescope at Keck Observatory using the High Resolution Echelle Spectrometer (HIRES) (Vogt 1994), an echelle spectrograph with a cross disperser. At the sodium D line wavelengths ($\sim 5900 \text{ \AA}$) the spectral resolution is $\lambda/\Delta\lambda \sim 67000$ corresponding to a full width at half-maximum (FWHM) for a monochromatic source of 2.0 pixels or 88 m \AA . The signal-to-noise ratio for a 70 second exposure is ~ 450 for the continuum near the sodium D lines, and ~ 115 at the minima of the deep Fraunhofer absorption lines. These observations were made by de Pater, Brown, Schneider, and Bouchez.

The reduction of the spectra proceeded as follows to determine the equivalent widths of the coronal sodium absorption lines: the spectra were first bias subtracted and flat-field corrected in the standard way. Because the light from the observed moon did not cover the entire length of the slit, I was able to subtract background light from the spectra. For each column along the spectral direction, the slice along the spatial direction was approximated by a Gaussian plus a polynomial, with the Gaussian approximating the light from the satellite, and the polynomial the background. I used this primitive fit simply to identify the region of sky along the column and then performed a χ^2 minimization routine to fit a low order polynomial to the sky. By fitting a separate polynomial for each column along the spectral dimension, I subtracted the wavelength-

Ecl. #	Date	UT ^a	Dur ^b	Telescope	Eclipsed Satellite	Min. b ^c	ϕ_{helio}^d	ϕ_{geo}^e	λ_{Io}^f
1	21 Jun 1997	15:32	17.1	Keck	Callisto	2.1	347°	337°	314°
2	27 Aug 1997	8:10	4.5	Keck	Callisto	3.1	233°	235°	162°
3	27 Aug 1997	11:30	13.8	Keck	Ganymede	1.4	261°	263°	256°
4	19 Jun 1997	7:57	6.0	McDonald	Europa	1.2	236°	226°	209°
5	21 Jul 1997	6:24	2.5	McDonald	Europa	2.1	252°	247°	273°
6	20 Aug 1997	8:09	10.6	McDonald	Ganymede	1.6	249°	251°	173°
7	30 Aug 1997	2:35	8.6	McDonald	Europa	1.9	76°	80°	208°
8	3 Oct 1997	1:25	7.6	McDonald	Ganymede	1.6	141°	150°	175°
9	10 Oct 1997	4:15	6.6	McDonald	Ganymede	2.0	149°	159°	242°
10	21 May 1991	3:59 ^g	5.5 ^g	Catalina	Europa	1.2	227°	235°	341°

Table 3.1 Eclipse Parameters. Table notes: (a) Universal time of eclipse midpoint (from Arlot (1996) except as noted) (b) Duration of event in minutes (from Arlot (1996) except as noted) (c) Minimum impact parameter of the event in R_{Io} (see text for details) (d) Io's heliocentric orbital longitude at eclipse midpoint (e) Io's geocentric orbital longitude at eclipse midpoint (f) Io's magnetic (System III) longitude at eclipse midpoint (g) source: Arlot, 1999, personal communication

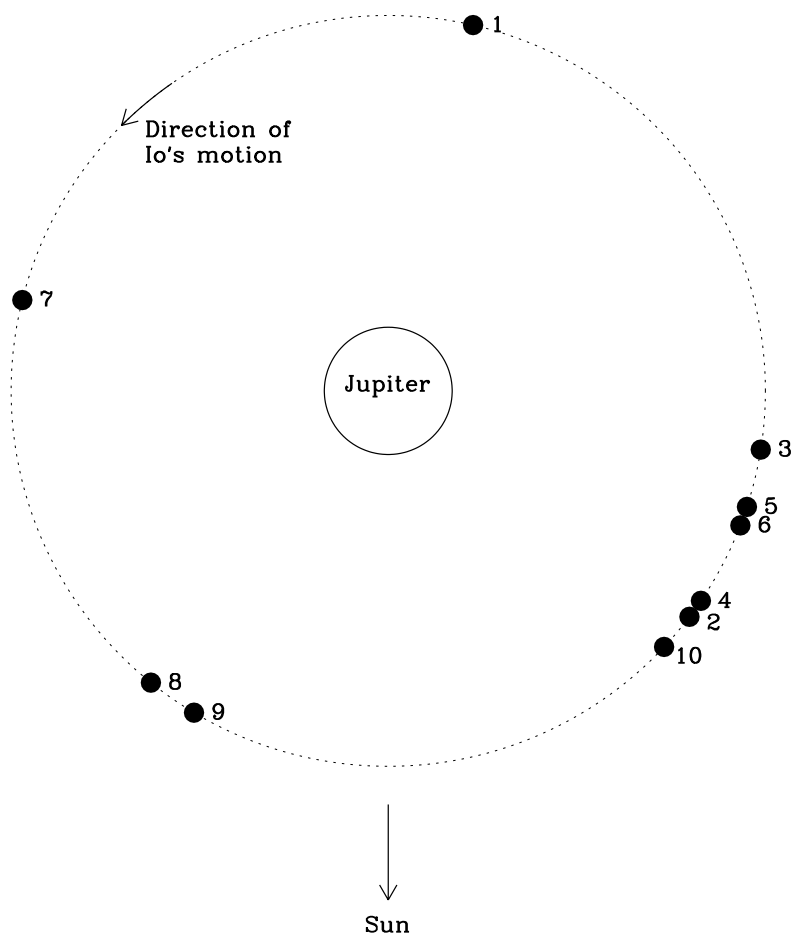


Figure 3.3 Io's orbital geometry for each of the observed mutual events listed in Table 3.1 as observed from the Sun. Io is not shown to scale. Event numbers are indicated. The direction to Earth varies for different observing dates.

dependent background, including the spatially uniform emission from sodium in the Earth's atmosphere. After subtracting the background, the spectra were reduced to one dimension by summing in the spatial direction. This process was performed on all the spectra during the eclipse series plus several spectra taken out of eclipse which were used as solar references to isolate the absorption at Io.

After producing a spectrum, light scattered in the optics of the spectrograph, which fills in the bottom of the Fraunhofer lines, was removed (Vogt 1994). Neglecting this effect underestimates the amount of absorption and therefore the column density of sodium. An empirical correction was performed by matching the spectra to a standard high resolution solar spectrum convolved with the HIRES point spread function. The bases of the solar Fraunhofer absorption lines were 5% of the continuum (Brown and Yung 1976).

The solar spectrum was removed by matching the spectra taken during eclipses with a reference spectrum of the same object taken out of eclipse. The reference was shifted by sub-pixel amounts to account for small wavelength shifts between observations. Dividing an eclipse spectrum by the pure solar spectrum revealed the absorption from sodium in the corona (Figure 3.2). Separate corrections were made to remove the solar spectrum around the D₂ and D₁ lines. Telluric absorptions are negligible in the Keck data near the Iogenic sodium absorption lines, so no further corrections were needed.

A wavelength calibration was made by identification of solar absorption lines (Moore et al. 1966). The resulting calibration gave the wavelengths in the solar rest frame rather than in the observer's rest frame, but allowed for the determination of slight shifts in wavelength between observations. The wavelength calibration is accurate to within 0.05 Å.

3.2.2 McDonald Observatory Observations

Six mutual events were recorded with the 2.7-meter telescope at McDonald Observatory using the 2d-Coudé Echelle Spectrometer by Trafton, Sheffer, and Barker, who also performed the reduction to determine equivalent widths. The events were split evenly between Europa and Ganymede as the eclipsed satellite. Typical spectral resolution attained was $\lambda/\Delta\lambda \sim 60,000$ (as determined from the FWHM of telluric lines in the program spectra). Exposures were 60 seconds in length, yielding signal to noise levels of ~ 100 in the continuum.

Standard reduction and analysis procedures were followed in the IRAF (Image Reduction and Analysis Facility) environment, starting with bias subtraction and flat-field division. The echelle order with the sodium D lines was traced and extracted in order to create a one dimensional spectrum. Due to order spacing constraints it was not possible to distinguish between sky background and scattered light, and these regions toward the ends of the slit were avoided in the 1-d summation. Scattered light in the spectrograph was removed using the method described above for the Keck observations.

McDonald spectra are usually “wet”; i.e., they include an appreciable number of telluric water lines. This contamination was easily removed by a division of all 1-d spectra by a spectrum of a hot star observed on the same night. Despite variations in airmass toward different objects the removal was accomplished by vertically shifting the hot star continuum until an agreement was obtained with line depths of object spectra.

Finally, having produced “dry” spectra of satellites in and out of eclipse, the former were divided by the latter in order to reveal isolated eclipse features produced by Io. Some pronounced residual noise exists at the location of the precise core of the solar sodium lines, but fortunately one can stay clear of these pathological regions since they only affect the very shallow wings of the isolated eclipse features. The signal to noise ratio was determined from continuum regions on both sides of and some 10-30

pixels away from the Fraunhofer core location in each spectrum. Stated as an rms value ($\text{rms} = 1/[\text{SNR}]$), this quantity was used in the computation of 1-sigma error bars for the equivalent width as follows: $\Delta W = \sqrt{n_{pix}} \times \text{rms} \times d\lambda$, where n_{pix} is the base width of the line in pixels and $d\lambda$ is the size of a pixel in the same wavelength unit as that of ΔW .

Thorium lamps have been employed to determine the wavelength calibration. The dispersion is found by a polynomial fit to the positions of identified (i.e., with known laboratory wavelengths) thorium lines.

3.2.3 Catalina Observatory Observations

A single event was observed by Schneider from the Catalina Observatory outside of Tucson, Arizona, using the Lunar and Planetary Laboratory Echelle Spectrometer. The eclipses in 1991 occurred close to Jupiter's solar conjunction making observations extremely difficult. Therefore, although the spectral resolution of the data is quite high ($\lambda/\Delta\lambda \sim 100,000$), these data are of a poorer quality than the other events. Additionally, the 139 second exposures have a lower signal to noise ratio. This event, however, does provide another time period which can be used to search for long term variability in the corona. This data were reduced by Schneider using methods similar to those described above.

3.3 Analysis

Each exposure scanned a different narrow region of Io's atmosphere. To first order, the region can be characterized by the "closest approach distance" between Io and the line connecting the Sun to the eclipsed satellite (commonly called the impact parameter, see Figure 3.1). In reality the sampled region is broadened by the angular size of the Sun, the finite size and visible appearance of the eclipsed satellite, and the motion of the satellite during an exposure. The distribution of impact parameters during an ex-

posure was calculated analytically by Mallama using his method described in Mallama (1991), the G-5 ephemerides (Arlot 1982, 1996), and the satellite limb-darkening model and albedo patterns from Mallama (1991). The distributions are computed for the continuum wavelength bracketing the absorption feature and are independent of the data. Sodium in the corona does not affect these distributions since the absorption feature is narrow and does not significantly change the shape or brightness of the continuum.

Each exposure’s distribution yielded a mean impact parameter and a standard deviation indicative of the width of the distribution during an exposure. The absorption equivalent width of each observation is assigned to the mean impact parameter. The broadening effects listed above can be broken into two categories and quantified. First, instantaneous spreading of light is due to the effects of the finite size of the eclipsed object and the angular size of the sun. Figure 3.4a shows the instantaneous distributions for three times during an eclipse. The amount of spreading is determined by the standard deviation of an instantaneous distribution. The width of the region ($2\times$ the standard deviation) is generally between 0.8 and 1.6 R_{Io} and can vary somewhat during an event. A second effect, smearing during an integration, depends on the relative tangential velocities of the satellites and the exposure times and amounts to ~ 800 km, or 0.4 R_{Io} . Note that these effects do not correspond to the uncertainty in the impact parameter since the distributions themselves are well determined. Figure 3.4b shows the effect of satellite motions during an exposure on the distribution. The similarity between the average distribution (red line) and the instantaneous distribution at the event midpoint (labeled) shows that the smearing due to satellite motion is small compared to the spreading of the light as observed at the Earth.

The timing of each event was determined by Arlot (1996). The uncertainty in the prediction of the event midpoint is 5–15 seconds, corresponding to ~ 150 km in the positions of the satellites (J.-E. Arlot, private communication, 2000). This implies an uncertainty in the prediction of the impact parameter is $\lesssim 0.1 R_{Io}$. The 63 second

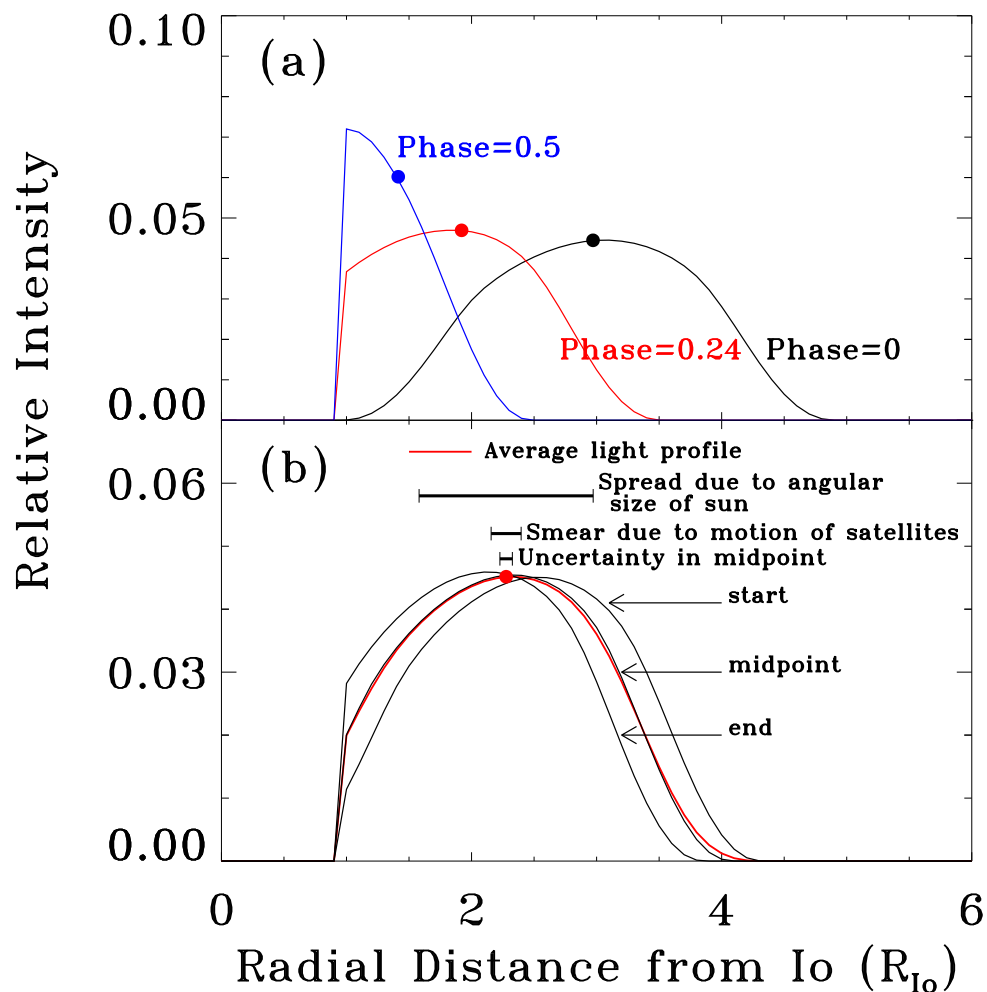


Figure 3.4 Determination of Impact Parameters. (a) Distribution of the light passing Io. Instantaneous distribution of impact parameters near Io at three times (phases) during an eclipse. The point marked on each distribution represents the average distance from Io of the light distribution (the impact parameter) as described in the text. (b) Example of how the impact parameter changes during an observation. Distributions are shown for the beginning, middle, and end of a typical observation. The red profile is the average for the observation. The impact parameter for this profile is marked. Scale bars are given for the uncertainty in the determination of the impact parameter ($2\sigma_b \sim 0.1 R_{Io}$), the amount of smearing due to motion of the satellites during the observation ($\sim 0.2 R_{Io}$ for this observation), and the spread of light due to the sun's angular size ($\sim 1.4 R_{Io}$).

difference between Universal Time (UT) and Terrestrial Dynamical Time (TDT) has been taken into account for comparison of the times of observations and the ephemeris time. Although the strength of the sodium absorption is likely to vary across the eclipsed satellite and during the exposure, departures from linearity are small compared to the error in individual measurements and are therefore neglected.

The column of absorbing sodium was derived by a comparison of the equivalent widths of the sodium D₂ and D₁ resonance lines ($3s^2S_{1/2} \rightarrow 3p^2P_{1/2}, 3p^2P_{3/2}$) at 5889.92 Å and 5895.95 Å respectively. The continuum was determined by fitting a line to the region surrounding the absorption line, and the sum was only performed in the pixel region containing the line. The equivalent widths calculated for each spectrum are given in Appendix A and plotted in Figure 3.5 versus time.

The equivalent width expected for a given value of the column density and the temperature was computed as discussed in Chapter 5. For low column densities (with optical depth $\tau \lesssim 1$ or column density $N \lesssim 10^{11} \text{ cm}^{-2}$) the equivalent width is independent of temperature and depends only on the column density. In this case, the column density listed in Table A.1 is the average of the abundances computed independently for the D₂ and D₁ lines weighted by the uncertainties in the measurements.

The degeneracy in temperature is lifted as the absorbing column increases. Therefore, to determine the column density in the optically thick case, it was necessary to consider the two absorption lines together. For a given pair of D₂ and D₁ equivalent widths, there is a unique column density and temperature which produces the absorptions. These values were computed by plotting curves of the column density required to produce the measured equivalent width versus temperature for each of the measured lines (Figure 3.6). The intersection of the two curves is the unique column density and temperature. The error ellipse in the D₁ vs. D₂ plot was mapped onto the N vs. T plot. The extrema of this ellipse gave the 1- σ errors in temperature and column density listed in Table A.1.

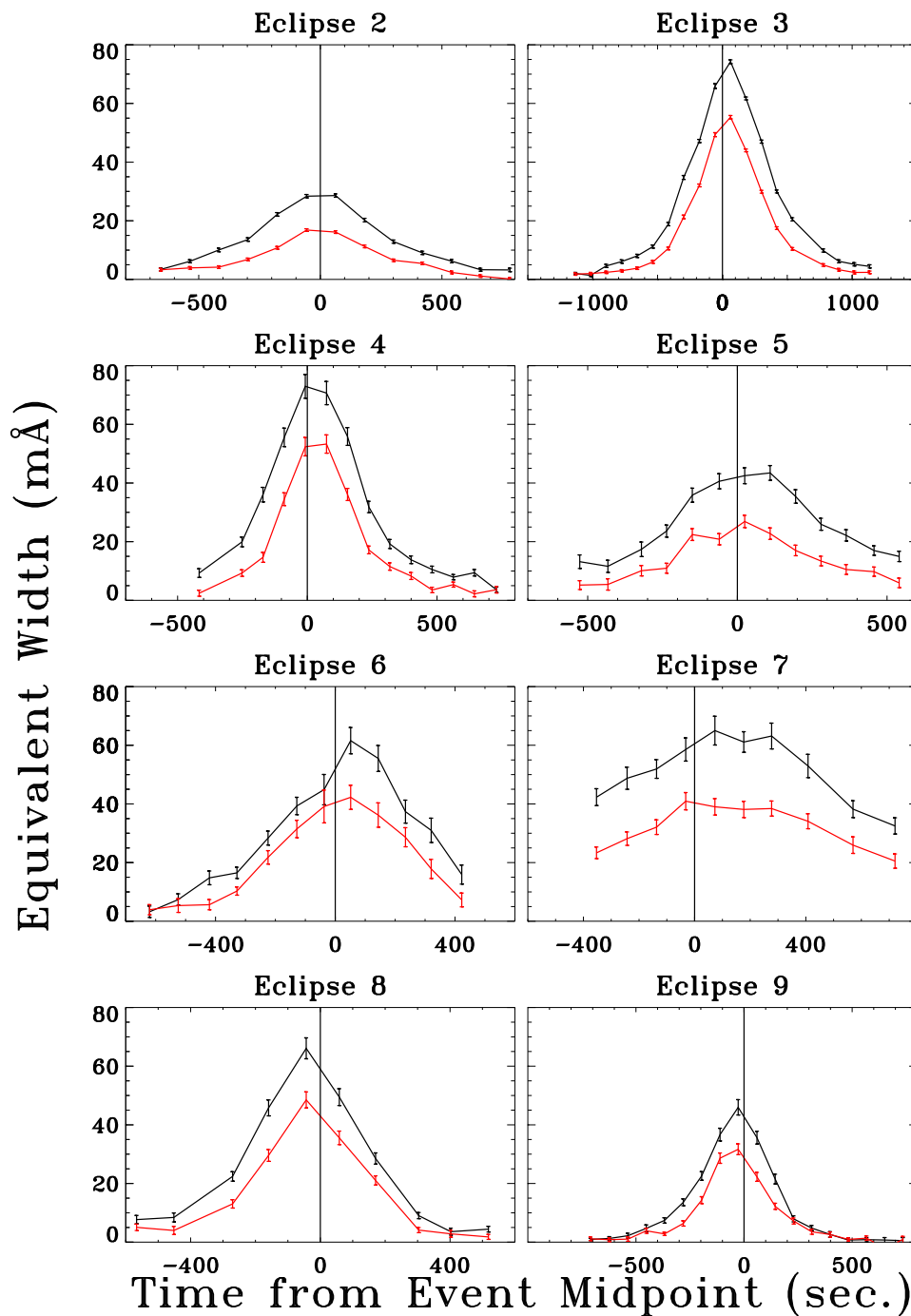


Figure 3.5 Equivalent width versus the time from the event midpoint for the 1997 mutual events. For each event, the black line shows the D₂ equivalent widths and the red line shows the D₁ equivalent widths. Note that events are not symmetric about time = 0, indicative of column density asymmetries in the corona.

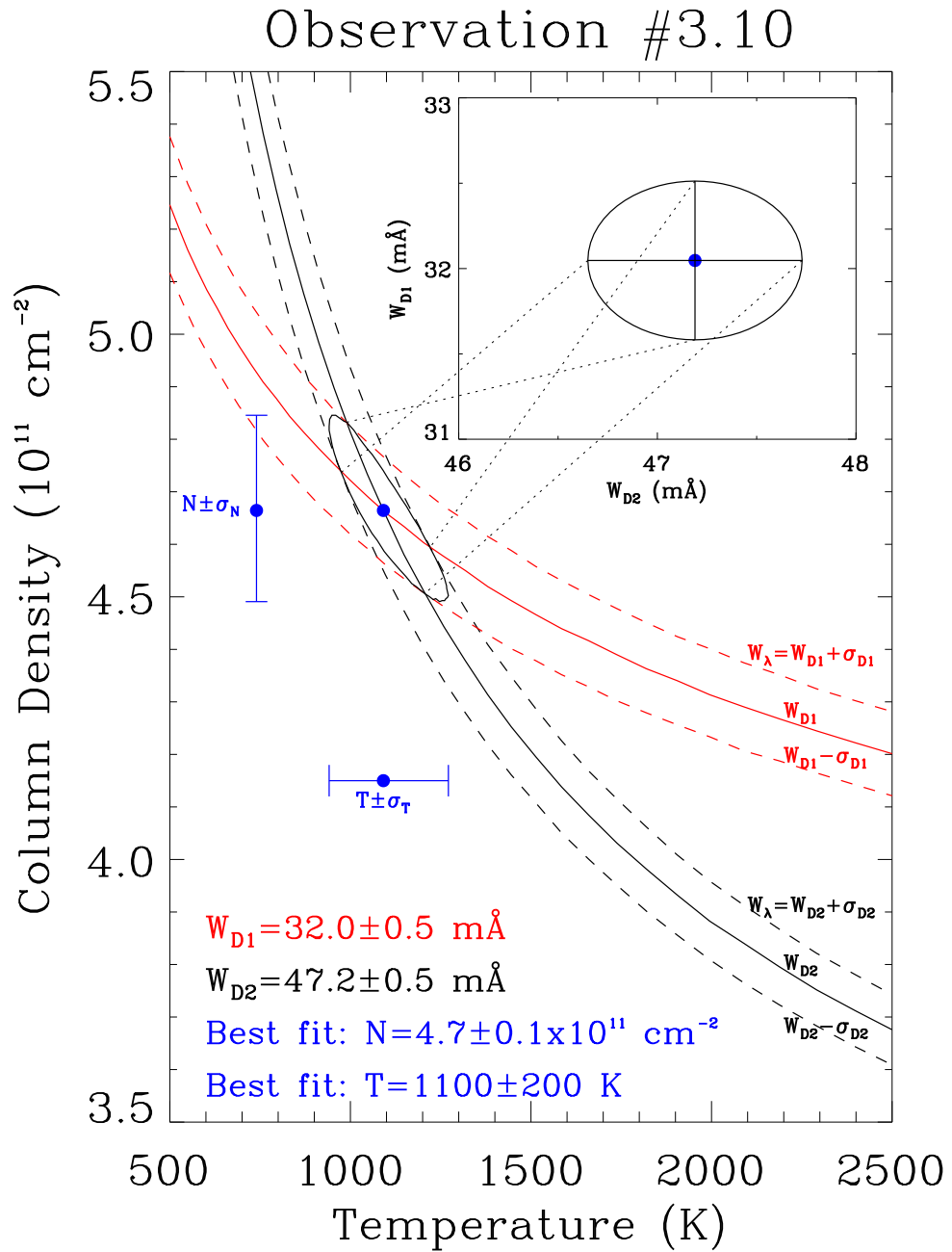


Figure 3.6 Curves of constant equivalent width as a function of temperature and column density. The solid lines show column density vs. temperature for the measured D_2 (black) and D_1 (red) equivalent widths; the broken lines are for the $1\text{-}\sigma$ errors on the equivalent widths. The intersection of the two solid lines gives the unique column density and temperature required to produce absorption lines with the measured equivalent widths. The error ellipse in column density and temperature is shown. The $1\text{-}\sigma$ error bars on N and T are given by the extrema of the ellipse. The insert shows the D_2 and D_1 equivalent widths and their errors for the observation. Dotted lines show how the errors in equivalent width map onto the N vs. T space.

3.4 Discussion

The column densities derived from the comparison of the Na D₁ and D₂ equivalent widths are plotted in Figure 3.7 versus the impact parameter of the observations and listed in Table A.1. Also listed are temperature estimates for observations of optically thick regions of the corona. Plotted over the data in Figure 3.7 are the best fit power law function to all the 1997 data which have an impact parameter less than 5.6 R_{Io} (except as noted below) and the best fit power law from to the data of Schneider et al. (1991a). The outer boundary was chosen to conform with the limits used by Schneider et al. (1991a) who looked at differences between the profile inside and outside of Io's Hill sphere, the effective limit of Io's gravity located at 5.6 R_{Io}. The best spherically symmetric fit to the data is given by:

$$N(b) = 2.2_{-0.7}^{+1.4} \times 10^{12} b^{-2.34_{-0.34}^{+0.27}} \text{ cm}^{-2}. \quad (3.1)$$

Fitting a power law to the data of Schneider et al. (1991a) gives a column density profile of:

$$N(b) = 2.4_{-0.6}^{+1.1} \times 10^{12} b^{-2.48_{-0.32}^{+0.27}} \text{ cm}^{-2} \quad (3.2)$$

which is consistent with the current data within the uncertainty. This indicates that there have been no significant changes in the directionally averaged corona in the twelve years between measurements. However, as discussed below, there are event-to-event fluctuations in the column density profile. Note that outside ~ 6 R_{Io} the corona column density becomes more variable. This is due to a combination of higher noise in the data (due to weaker absorption lines) and real variability in the corona outside of Io's Hill sphere.

An indication that the corona did not vary significantly during the period between the 1985 and 1997 measurements is a mutual event observation from 1991. Only four spectra from the 1991 Catalina Observatory event (event 10) show any measurable

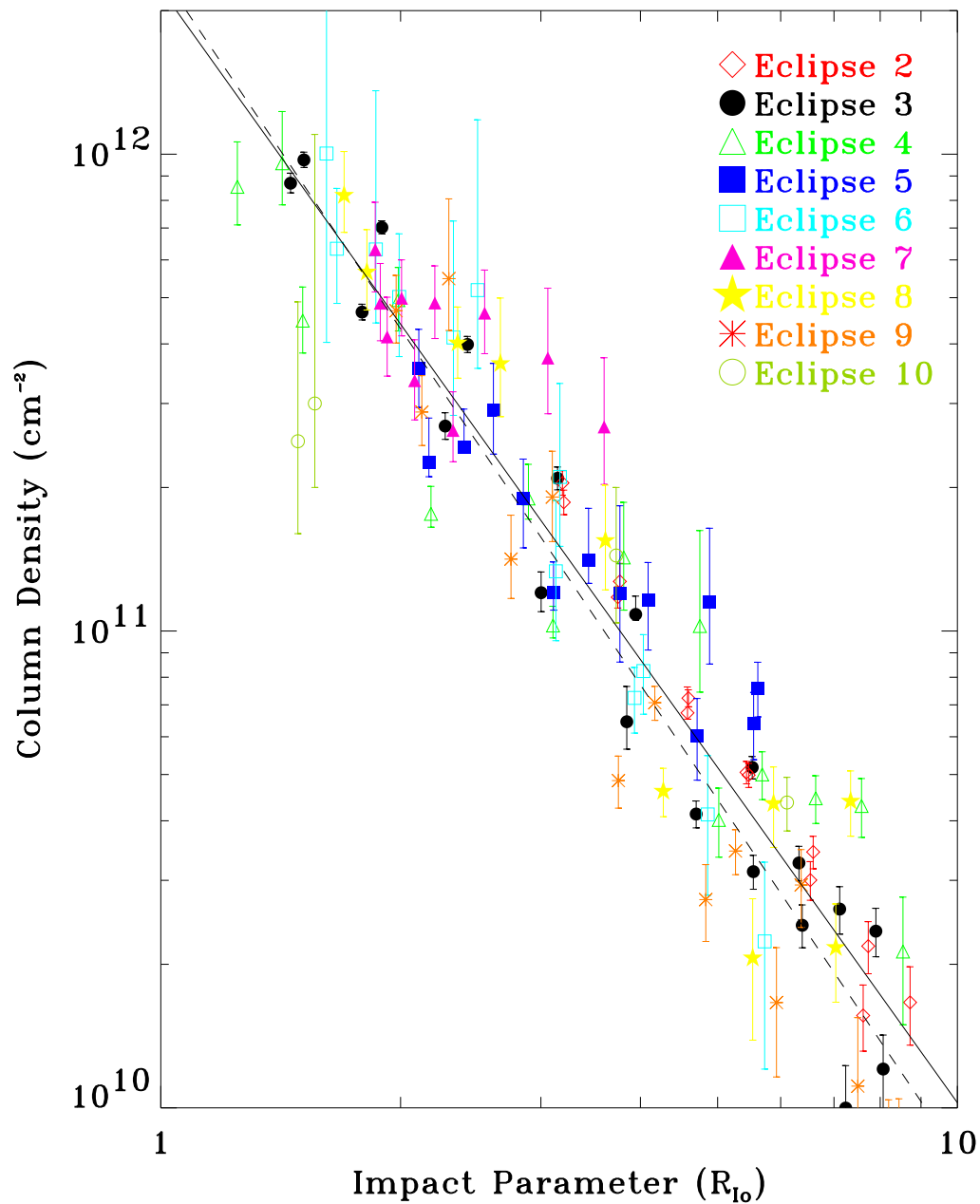


Figure 3.7 Column density versus impact parameter for all the data with measurable equivalent widths. The best fit power law to the all 1997 data within $5.6 R_{i0}$ (equation 2) is plotted with a solid line. The broken line shows the result of Schneider et al. (1991a) (equation 3). Four column density measurements from 21 May 1991 are shown, but are not included in power law fit. Event 1 listed in Table 3.1 is not shown (see text for explanation).

absorption. The column densities determined from this event are shown in Figure 3.7 although they are not included in the fit shown by the solid line. Despite the relatively poor signal to noise of the data, which makes precise column density values difficult to determine, the column densities measured are consistent with those seen in both the 1985 and 1997 data. This is a further indication of temporal stability in the corona, although I was not able use this data to look for spatial asymmetries in the corona. Unfortunately, the observations which measured closest to Io were made when Europa was in Io's umbra, reducing Europa's brightness and, consequently, the signal to noise ratio of the data.

Io was very close to superior heliocentric conjunction for event of 21 June 1997 (event 1) making it difficult to interpret. Because the radial velocity difference between Io and the sun was very small, the resolution of the instrument was not great enough to separate the Iogenic absorption from the solar Fraunhofer line with certainty for most of the observations. However, for some of the observations within $\sim 2.5 R_{\text{Io}}$, where the absorption from the corona is stronger, the equivalent widths were more easily measured. These data are listed in Table A.1. The column densities derived agree qualitatively with the general column density profile in the corona, although the systematic errors introduced in the reduction make quantitative analysis impossible.

The temperature of the corona is estimated to be 1600 K with a $1\text{-}\sigma$ confidence level between 1200 K and 3600 K. The uncertainties in the data are too large to determine a radial temperature profile. Schneider et al. (1991a) measured a temperature of ~ 2000 K. This is consistent with the current measurement, given the wide temperature range estimated from the individual observations as shown in Table A.1. Our measurement is also consistent with previous model predictions for the temperature. Summers et al. (1989) determined that previous observations were consistent with a corona with a temperature of ~ 1000 K, but do not give an upper limit on the temperatures which would be consistent with the data. A model which includes solar heating, plasma heat-

ing, and Joule heating of the atmosphere predicts temperatures ~ 1800 K in the corona (Strobel et al. 1994). Depending on Io’s orbital phase and the solar zenith angle, Wong and Smyth (2000) predict exobase temperatures between 220 K and 2800 K for an SO_2 sublimation atmosphere.

Although I do not see any evidence for long term temporal variability in the corona, I have detected a possible asymmetry in the radial column density profile. Most of the events compare to varying degrees the contrast between Io’s inner (sub-Jupiter) and outer (anti-Jupiter) hemispheres (Figure 3.8a). For seven of the eight events considered, the sub-Jupiter hemisphere is more dense than the anti-Jupiter hemisphere. The two hemispheres had identical column density profiles during event 2. Figure 3.9 shows the D_2 equivalent widths versus impact parameter for eight mutual events. For each event, the red lines show absorption from the sub-Jupiter hemisphere. The blue lines show the anti-Jupiter hemisphere. With the exception of event 2, the spectra from the inner hemisphere show more absorption than the outer hemisphere for measurements at similar radial distances from Io. The D_1 equivalent widths follow a similar trend. Figure 3.10 shows the column density asymmetry between the inner and outer hemispheres of Io. The broken line shows the “average” corona column density on the anti-Jupiter hemisphere; the solid line is a fit to the sub-Jupiter hemisphere. The best fits to the inner and outer coronae are given by:

$$\textit{Sub} - \textit{Jupiter} (\textit{inner}) \textit{ hemisphere} : 3.0_{-0.4}^{+0.9} \times 10^{12} b^{-2.42_{-0.26}^{+0.15}} \textit{ cm}^{-2} \quad (3.3)$$

$$\textit{Anti} - \textit{Jupiter} (\textit{outer}) \textit{ hemisphere} : 1.8_{-0.6}^{+0.8} \times 10^{12} b^{-2.29_{-0.27}^{+0.42}} \textit{ cm}^{-2} \quad (3.4)$$

The anti-Jupiter corona is on average 60% as dense as the corona on the sub-Jupiter side at the same radial distance from Io. The steepness of the column density profiles are similar for the opposite sides of Io. Schneider et al. (1991a) did not detect this asymmetry, although the uncertainties in their data were greater. The uncertainties given in equations 3 and 4 are representative of event-to-event variations in the data.

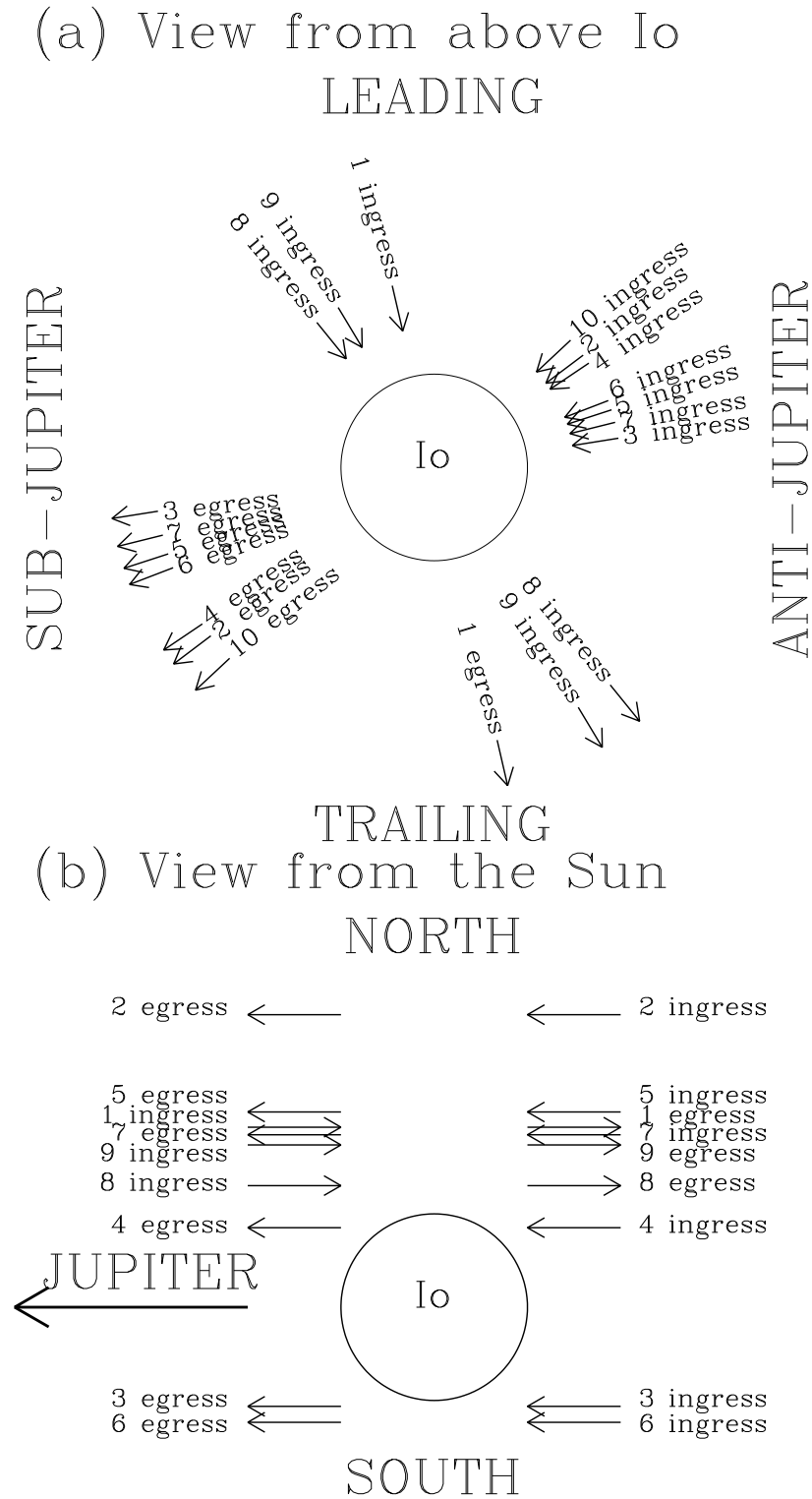


Figure 3.8 Eclipse geometry for each event. (a) Paths of each eclipse in fixed Io coordinates as seen from above Io's north pole. The inbound (ingress) and outbound (egress) portions of each eclipse are shown. Observation lines of sight are perpendicular to the eclipse path in the plane of the page. (b) Paths of each event as seen from the Sun. The lines of sight are perpendicular to the eclipse paths into the page.

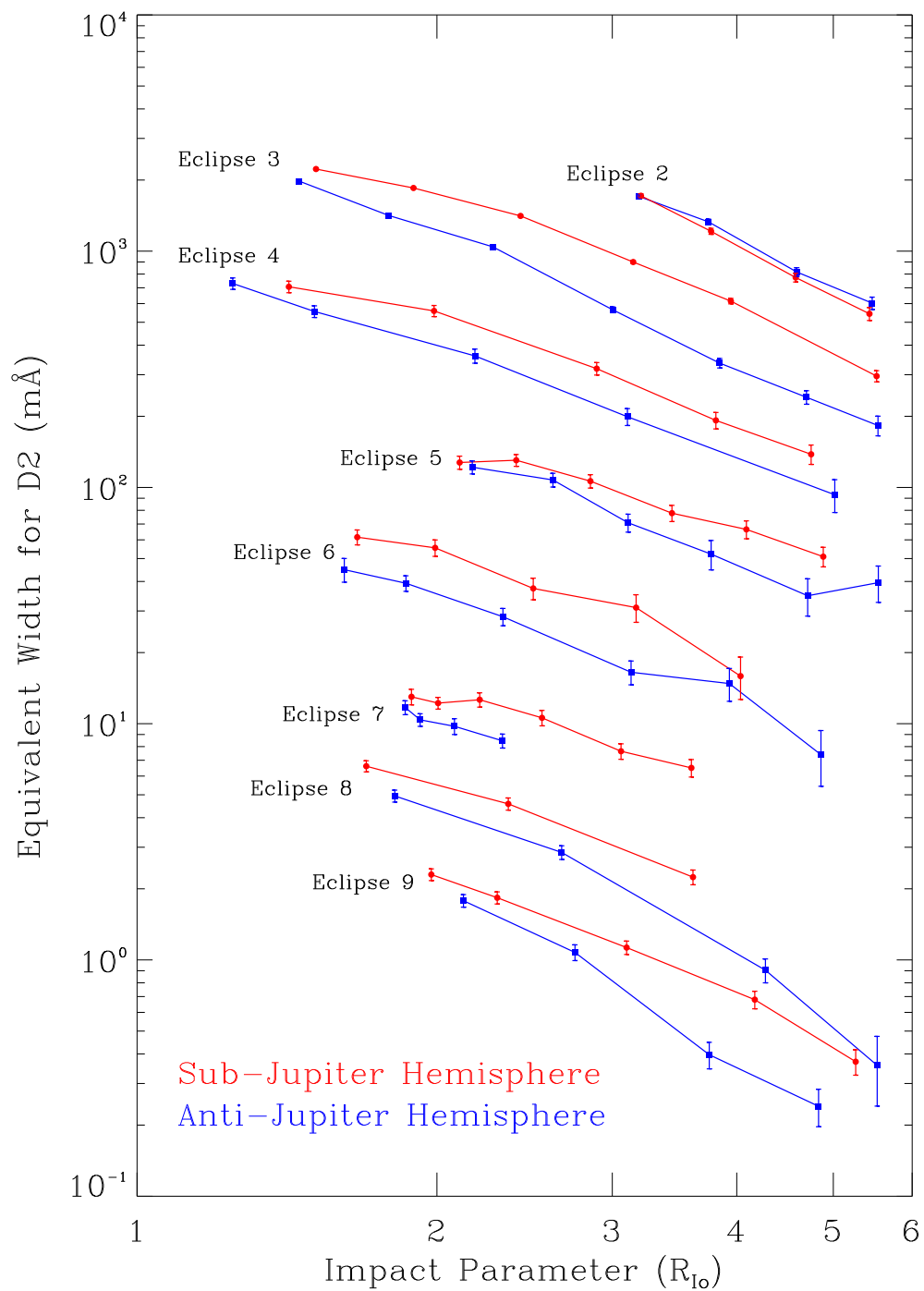


Figure 3.9 Na D₂ equivalent width versus impact parameter for seven of the mutual events observed. For each event, the red line indicates measurements from Io's sub-Jupiter hemisphere; the blue line shows the anti-Jupiter hemisphere. The events have been vertically separated for clarity. Eclipses 2, 3, 4, 5, 7, 8, and 9 have been offset by factors of 60, 30, 10, 3, 1/5, 1/10, and 1/20, respectively. Eclipse 6 has not been shifted.

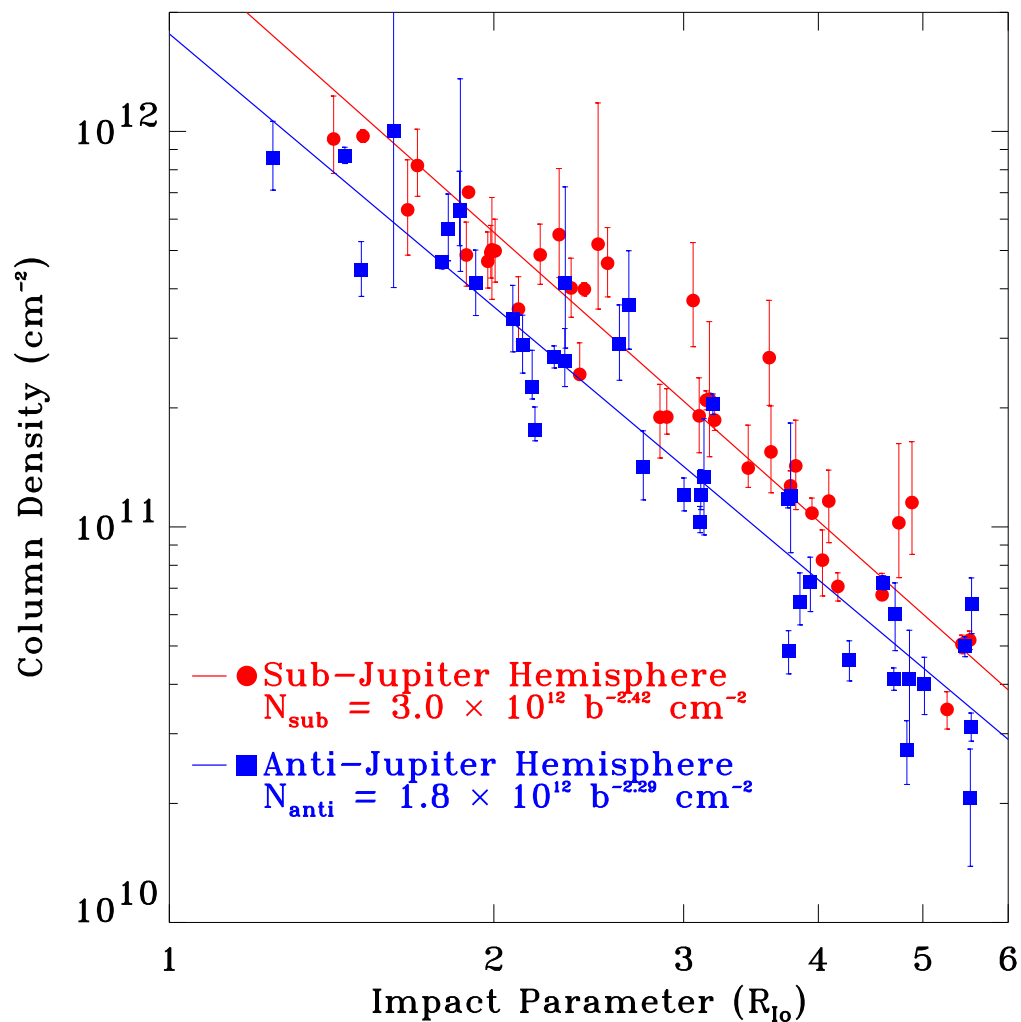


Figure 3.10 Column density versus impact parameter showing the inner/outer column density asymmetry. Red circles denote measurements from Io's sub-Jupiter hemisphere; blue squares show the anti-Jupiter hemisphere. The red line shows a power-law fit to the circles; i.e., the red line is the average coronal column density over the sub-Jupiter hemisphere. The blue line represents the average anti-Jupiter corona. The sub-Jupiter hemisphere is 1.7 times as dense as the anti-Jupiter hemisphere.

Event 7 from McDonald Observatory is unique in that it is the only event which occurred close to Io's eastern elongation. This event shows a similar asymmetry to the other events discussed; namely, the sub-Jupiter hemisphere is more dense than the anti-Jupiter hemisphere. Therefore I conclude that I detect an inner/outer asymmetry rather than an east/west asymmetry. Event 7 is anomalously dense on the sub-Jupiter hemisphere compared to the other events. Since this is the only event observed in this geometry, I cannot determine whether this is a true east/west column density variation or simply representative of short term temporal variability in the corona. This column density anomaly could also be due to an uncorrected systematic error in the data. This would also explain the difficulties in constraining temperature (see Table A.1). However, I still conclude that this event displays an inner/outer asymmetry since the asymmetry is clearly seen in the equivalent widths (Figure 3.9). The asymmetry appears in both the Na D₂ and D₁ equivalent widths. Therefore, despite any possible difficulties in determining the precise column densities for this event, the spectra reveal asymmetric absorption. Although ideally I would like more observations at eastern elongation, the available data better support an inner/outer asymmetry than an east/west asymmetry.

Event 9 is listed in Table A.1 as measuring leading/trailing differences. Although this event occurs close to Io's inferior conjunction (Figure 3.3) and therefore is most suited to measuring differences between the leading and trailing hemispheres (see Figure 3.8a), it does measure some differences between the inner and outer hemispheres and so has been included in this analysis. Similarly, the other events, which primarily compare the inner and outer hemispheres, are also sensitive to leading and trailing asymmetries. The conclusion that I have detected an inner/outer asymmetry rather than a leading/trailing asymmetry is supported by the fact that different events measure different combinations of the regions near Io. For example, event 4 measures the outer/leading hemisphere in the first half of the event and the inner/trailing hemisphere in the second. Event 8 probes the inner/leading hemisphere first and the outer/trailing

last. The inner hemisphere is more dense for each of these events, regardless of whether the leading or trailing hemisphere is also being observed.

I am not able to rule out the possibility of a leading/trailing asymmetry in addition to the inner/outer asymmetry, but there is no clear evidence that this is the case. The two events which best measure leading/trailing differences, events 8 and 9, both show higher column density over the leading hemisphere than the trailing. However, events 3, 4, 5, 6, and 7, which measure leading/trailing differences to lesser degrees, show higher trailing densities. Therefore, it appears that there are no persistent column density differences between the leading and trailing hemispheres. The events which best measure the differences between the inner and outer hemispheres, events 3, 5, 6, and 7, all measure higher column densities above the sub-Jupiter hemisphere than above the anti-Jupiter hemisphere. Unfortunately, the events which best measure differences between the leading and trailing hemispheres occur when the radial heliocentric velocity is lowest and the absorption is most difficult to separate from the solar Fraunhofer line.

Asymmetries in the corona point to asymmetries in the processes which affect slow sodium. These could be related to the creation or loss of neutral sodium in the corona. A density asymmetry would arise if the source rate on the sub-Jupiter side or the loss rate on the anti-Jupiter side is enhanced. Another possibility is that the velocity of escaping neutrals is greater for the anti-Jupiter hemisphere. This would also result in a greater column density of sodium in the sub-Jupiter corona and most likely result in a shallower profile for the anti-Jupiter hemisphere. This change in slope is not seen, although the uncertainties in the determination of the slope may be large enough that a difference in slope between the two hemispheres cannot be seen.

A mechanism for reducing the source rate on the anti-Jupiter hemisphere is suggested by observations of Io's auroral emissions ("equatorial spots"): the anti-Jupiter spot is $\sim 20\%$ brighter than the sub-Jupiter spot (Roesler et al. 1999; Retherford et al. 2000). Saur et al. (2000) have modeled the electron flow past Io to show that the Hall

effect close to Io results in more energy deposited to the anti-Jupiter side than the sub-Jupiter side. In the context of the auroral oxygen emissions, there is more electron impact excitation on the anti-Jupiter side resulting in a brighter equatorial spot. This same effect would result in a greater sodium ionization rate since the ionization potential of sodium is lower than that of oxygen. Since the equatorial spots are observed near Io's surface (within $\sim 1 - 2 R_{\text{Io}}$), only sodium in that region would most likely be affected. Therefore, the amount of escaping neutral sodium would be preferentially reduced on the anti-Jupiter hemisphere, and the column density further out in the corona would be smaller. The slope of the corona, however, would not be affected.

The fast sodium jet observed by Wilson and Schneider (1999) and Burger et al. (1999) (Chapter 4) is most likely not directly responsible for this asymmetry. Fast sodium would show up as a broad, Doppler-shifted feature well below the detection limit. However, it is possible that the escape of fast sodium affects the sputtering rates from Io or the velocity of escaping slow neutrals.

If the corona does in fact have an inner/outer asymmetry then there is a question as to why event 2 appears to be radially symmetric about Io. Understanding this event will require additional observations at large distances from the poles and modeling beyond the scope of this paper. A possible explanation may lie in the fact that this event measures the corona farther above Io's north pole than any of the other events (Figure 3.8b) which might suggest that the processes which cause the asymmetry are acting closer to Io's equatorial region than the polar regions. However, there are other events which measure the corona north of Io, and these events do not support this hypothesis in that I would expect a relationship between the degree of asymmetry and the minimum impact parameter of the event.

There are event-to-event fluctuations in the coronal column density profile. Although the deviations in measured column density are small compared with the mean column density, they are greater than the uncertainties in the individual measurements.

Additionally, as discussed, the inner/outer asymmetry is persistent indicating that when the corona is in a denser state, the column density is increased on both the Jupiter and anti-Jupiter sides. The measured standard deviation in the corona column density at a distance of $3 R_{Io}$ is $\sim 25\%$ of the mean column density at this distance. Above Io's sub-Jupiter hemisphere, the mean column density at $3 R_{Io}$ is $2.3 \times 10^{11} \text{ cm}^{-2}$ with a standard deviation of $0.6 \times 10^{11} \text{ cm}^{-2}$. The variation is proportionately the same above the anti-Jupiter hemisphere: at $3 R_{Io}$ the mean column density is $1.5 \pm 0.4 \times 10^{11} \text{ cm}^{-2}$.

3.5 Summary

This study shows that there have been no significant global changes in Io's sodium corona since the previous study of the column density profile (Schneider et al. 1991a). Measurements of the coronal column density from 1985, 1991, and 1997 all show the same, roughly spherically symmetric sodium corona within 6 Io radii of Io.

The average corona is well described as a spherically symmetric cloud around Io with a column density profile of

$$N(b) = 2.2_{-0.7}^{+1.4} \times 10^{12} b^{-2.34_{-0.34}^{+0.27}} \text{ cm}^{-2}, \quad (3.5)$$

where b is the impact parameter of the observation in Io radii. This corresponds to a radial density profile of

$$n(r) = 6700 r^{-3.34} \text{ cm}^{-3} \quad (3.6)$$

with r the distance from Io in Io radii.

There is evidence however for a persistent asymmetry in the corona. The events which measure nearest Io's equator indicate that the corona above Io's sub-Jupiter hemisphere is ~ 1.7 times as dense as the corona above the hemisphere which faces away from Jupiter. This result may be consistent with the observations of Io's auroral emissions as explained by Saur et al. (2000). Additionally, smaller event-to-event fluctuations of $\sim 25\%$ are seen in the coronal column density.

Theoretical studies of the corona and neutral clouds have always used symmetric loss from Io. Smyth and Combi (1997) modeled the spherically symmetric sodium corona described by Schneider et al. (1991a) with symmetric loss, although they did determine that the corona has an asymmetric density profile when the sodium directional feature is aligned along Io's orbital plane. However, our observing method is not sensitive to an asymmetry caused by the directional feature. Cremonese et al. (1998) found spherically symmetric loss from Io most consistent with the observational data, including the observations of Schneider et al. (1991a) and high resolution spectra of sodium near Io. The data presented here are the highest quality observations made of the sodium column abundance in Io's corona and indicate that the loss from Io may in fact not be as symmetric as previously thought. The origin of this observed asymmetry is presented in Chapter 6.

Chapter 4

Galileo Observations of the Fast Sodium Jet

4.1 Introduction

In this chapter I discuss recent Galileo images of the fast sodium jet at Io. This chapter has been previously published, in somewhat modified form, as Burger et al. (1999). I performed the data reduction and analysis. The modeling in Section 4.4 was a joint effort by myself and J. K. Wilson using the model of Wilson and Schneider (1999). This model is the basis for the neutral cloud model described in Chapter 5.

Since the discovery of the Io sodium cloud more than 25 years ago, planetary astronomers have used imaging and spectroscopic measurements to study the escape of Io's atmosphere (Brown 1974; Trafton et al. 1974). Although only a trace constituent of the material near Io, sodium has proven to be the easiest to observe, with a large cross section for resonant scattering of sunlight and a ground state transition at optical wavelengths (589.0, 589.6 nm). For most atmospheric escape processes, sodium is considered a good tracer of the more abundant species such as sulfur dioxide (Ballester et al. 1994) or its dissociation products oxygen or sulfur.

One escape process, which does not have substantial non-sodium component due to the fact that sodium is the dominant constituent in Io's ionosphere (Wilson and Schneider 1999), offers important insights into the atmosphere of Io and the nature of Io's interaction with Jupiter's magnetosphere. A prominent jet, called the "directional feature," projects roughly radially outward from Jupiter (Goldberg et al. 1984) (Fig-

ure 4.1). It tilts slightly north or south of the equatorial plane depending on the tilt of Jupiter's magnetic field at Io.

Wilson and Schneider (1999) have recently offered a new explanation for the jet. Based on extensive modeling of ground-based images and spectra, they conclude that the jet is a manifestation of ionospheric escape at Io. The escape is driven by the electrodynamic potential of 411 kV induced across Io by its motion through Jupiter's magnetic field (Goldreich and Lynden-Bell 1969; Dessler 1983). The electric field is directed radially outward from Jupiter and perpendicular to the magnetic field. Radio occultations by spacecraft have revealed a global ionosphere capable of conducting mega-ampere currents in response to this potential (Hinson et al. 1998). The dominant ionospheric ion is Na^+ by virtue of sodium's very low ionization potential (Summers and Strobel 1996). Sodium ions are driven by Pedersen currents radially outward from Jupiter. Ions on the sub-Jupiter side of Io are driven to the surface and cannot escape; those on the anti-Jupiter side are not blocked. Some of these escaping ions are neutralized by charge exchange reactions and become fast sodium atoms directed away from Io at velocities of tens of km sec^{-1} . The sodium atoms preserve their ion motion at the moment of charge exchange, which includes a substantial gyrovelocity perpendicular to the local magnetic field. The plane of gyromotion defines the orientation of the jet. Sodium-bearing molecular ions, known to produce fast sodium features farther from Io (Wilson and Schneider 1994), may contribute sodium atoms to the directional feature. Sodium ejected from Io's ionosphere adds to the extended disk of sodium atoms observed as far as 500 Jovian radii from Jupiter (Mendillo et al. 1990). For a more complete explanation of this process, see Wilson and Schneider (1999).

Prior to the Galileo spacecraft observation, only ground-based telescopes had observed the sodium jet. Scattered light from Io prevents measurements much closer than $\sim 0.25 R_J$ and atmospheric blurring limits spatial resolution to about $4 R_{Io}$. Although the Voyager spacecraft carried a narrowband sodium filter, its detector lacked the sensitivity

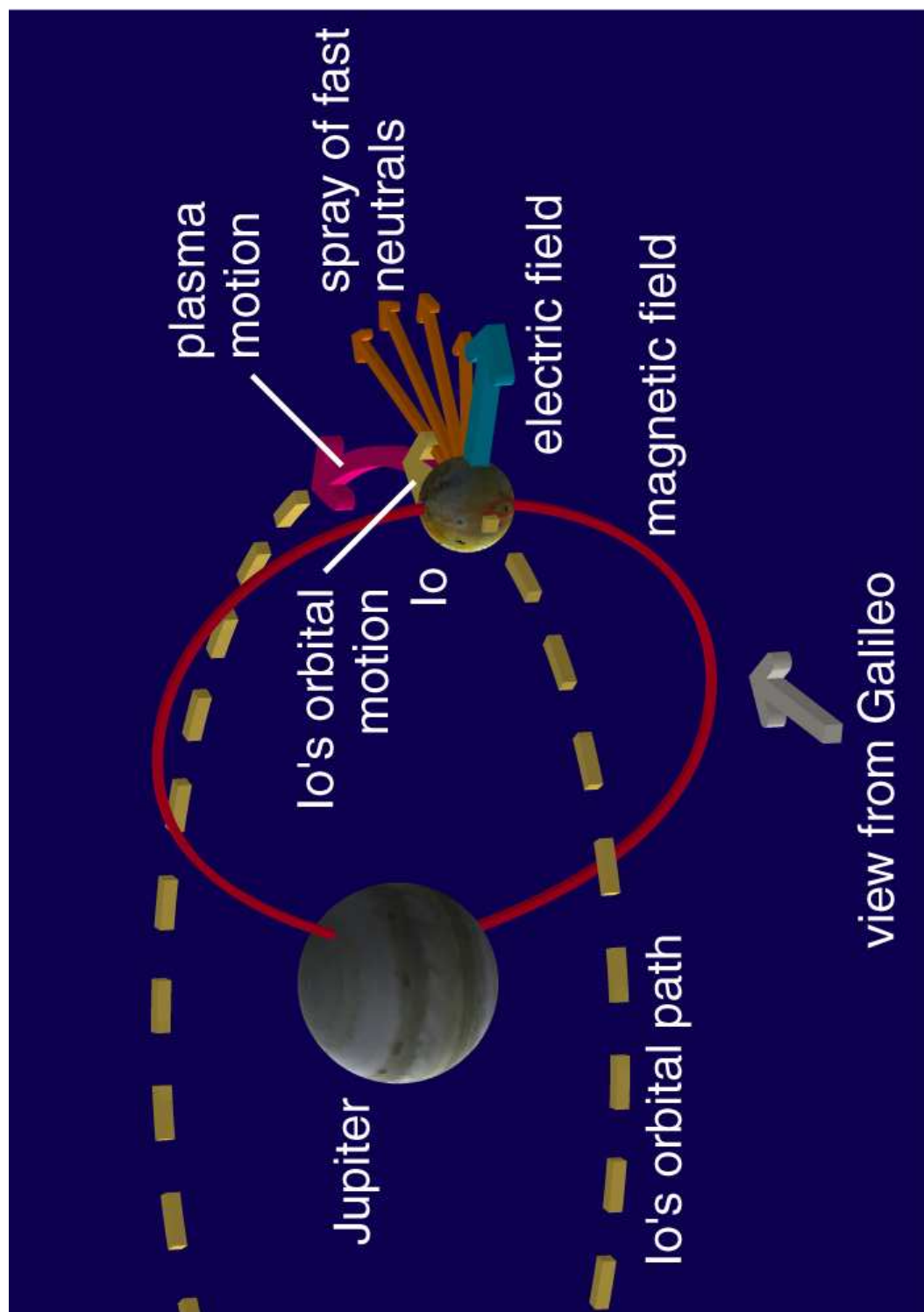


Figure 4.1 The relative directions of the electric field (shown in blue) , magnetic field (red), and motions of ions (pink) and fast neutrals (orange) at Io. Escaping ionospheric sodium creates a spray of fast sodium atoms lying in the plane normal to the Jovian magnetic field line through Io. Galileo viewed the spray almost edge-on giving it the appearance of a jet.

to detect sodium (Goldberg et al. 1980). Galileo therefore offered the first opportunity to trace the jet back to its source region. One of the greatest uncertainties in Wilson and Schneider’s model is the overall size of the source region: does it span Io’s entire disk, or is it confined to more localized regions?

4.2 Observations

The Galileo team faced numerous challenges in designing an appropriate observation to detect faint emission from the sodium cloud so close to Io’s bright disk. Since the sodium cloud glows by resonantly scattering sunlight, it was not possible to image the sodium cloud in Jupiter’s shadow, a technique which has revealed numerous other atmospheric emissions (Geissler 1999). Instead, the observations were optimized for faint emission detection by observing Io’s night side while the Galileo spacecraft lay in Jupiter’s shadow. Io’s disk was placed on the edge of the CCD detector in order to move the small sunlit crescent out of the field of view. A sequence of two 13-second exposures was taken on 9 November 1996 just after the C3 encounter (These images are publicly available through the Planetary Data System Imaging Node). The distance of the spacecraft from Io was 2.1×10^6 km giving a spatial scale of 44 km pixel^{-1} . Io’s magnetic longitude at the time of the observation was $\lambda_{\text{III}} = 34^\circ$.

The image taken by Galileo is a double exposure of Io, with Io repositioned and the filter changed between exposures. The upper image uses a clear filter (effective wavelength = 611 nm, bandpass = 440 nm), and the lower one a green filter (559 nm, bandpass = 65 nm) (Belton et al. 1992). The images were converted from raw counts to intensity units using the GALSOS routine in the VICAR image reduction software package available from the Jet Propulsion Laboratory. Because Na D line emission is at the edge of the green filter bandpass, intensity attributed to sodium must be additionally corrected for the decreased filter efficiency by a factor of ~ 1.6 relative to the peak filter transmission. No such correction was necessary for the clear filter exposure.

4.3 Analysis

Several features appear in the images which complicate the analysis of sodium. The sunlit crescent of Io is just off the frame, and a Jupiter-lit crescent appears in the image. These features are orders of magnitude brighter than any Iogenic emissions and contribute to scattered light in the image. An unfortunate surprise is the volcanic plume Prometheus in full sunlight on Io's day side rising $\gtrsim 75$ km above Io's surface and beyond Io's limb, scattering sunlight directly into Galileo's cameras. Nonetheless, the "directional feature" due to sodium is marginally visible in the raw data.

The relative contributions of scattered light from the sunlit crescent, the plume, and Io's atmosphere itself are difficult to gauge, but can be approximated *in toto* by assuming azimuthal symmetry around Io. We fit this component of the light profile as the sum of two independent power laws centered on the disk of Io in each image; each pixel receives scattered light through both filters due to the double exposure. Stars and other bright spots in the images were removed before fitting, as were the directional features. Light scattered through the broad clear filter dominates most of the field of view. The scattered light falls off as $r_1^{-0.8 \pm 0.2}$, where r_1 is the distance from Io in the clear image. Since the dominant source of error is the non-uniformity of the background, error bars were determined by manually adjusting the fit parameters to minimally acceptable limits. Scattered light centered on the plume in the green image falls off as $r_2^{-1.1 \pm 0.2}$, steeper than in the clear filter. The intensity ratio between the two filters is consistent with the bandpass differences.

The steeper power law observed in the green filter is consistent with the sodium emission expected from Io's extended atmosphere, whose intensity falls off as $r^{-2.3}$ (Chapter 3). Such emission is more likely to be observable through the green filter, whose 7 times narrower bandpass offers better contrast of sodium emission versus scattered light despite the 1.6 times lower filter transmission at the sodium D lines. At the current

level of analysis it is not possible to extract more quantitative information on the sodium corona. Interpretation is complicated, as the corona is optically thick near Io, and Galileo viewed Io’s “night side”. Nonetheless, the ring of emission surrounding Io in both images is clearly Iogenic. The observed intensity is consistent with either continuum scattering by dust around Io or a sodium corona with column density $\gtrsim 6 \times 10^{11} \text{ cm}^{-2}$ at Io’s surface (The lower limit on sodium column density is found by assuming the cloud is optically thin all the way to the surface). As the known sodium corona has a density greater than this, the latter explanation is preferred. We postpone further discussion of this feature to a future paper.

Figure 4.2 shows the image with scattered light subtracted revealing the “jet” originating at Io and extending to the right and slightly downward. The jet appears clearly in both images. The clear filter image has a higher signal to noise ratio (S/N) in regions where contrast against scattered light was not a problem, i.e., far from Io. The green filter provides higher S/N where the reduced sensitivity is not the dominant problem, i.e., closer to Io. The jets cannot be an artifact of the scattered light subtraction, as the background is azimuthally symmetric about the two plumes. These images provide the best spatial resolution ever achieved of the directional feature as well the closest detection to Io. The magnetic field line through Io is shown in figure 2. As predicted by the model of Wilson and Schneider, the orientation of the directional feature is roughly perpendicular to the magnetic field.

4.4 Discussion

Quantitative measurements of the jet properties in the background subtracted image provide key constraints on the escape mechanism. For each radial position along the jet, we extracted an azimuthal profile centered on Io. Near the position of the jet, we fit a linear background to the azimuthal variations in the scattered light profile, and estimated the position, peak brightness and full-width-at-half-maximum (FWHM)

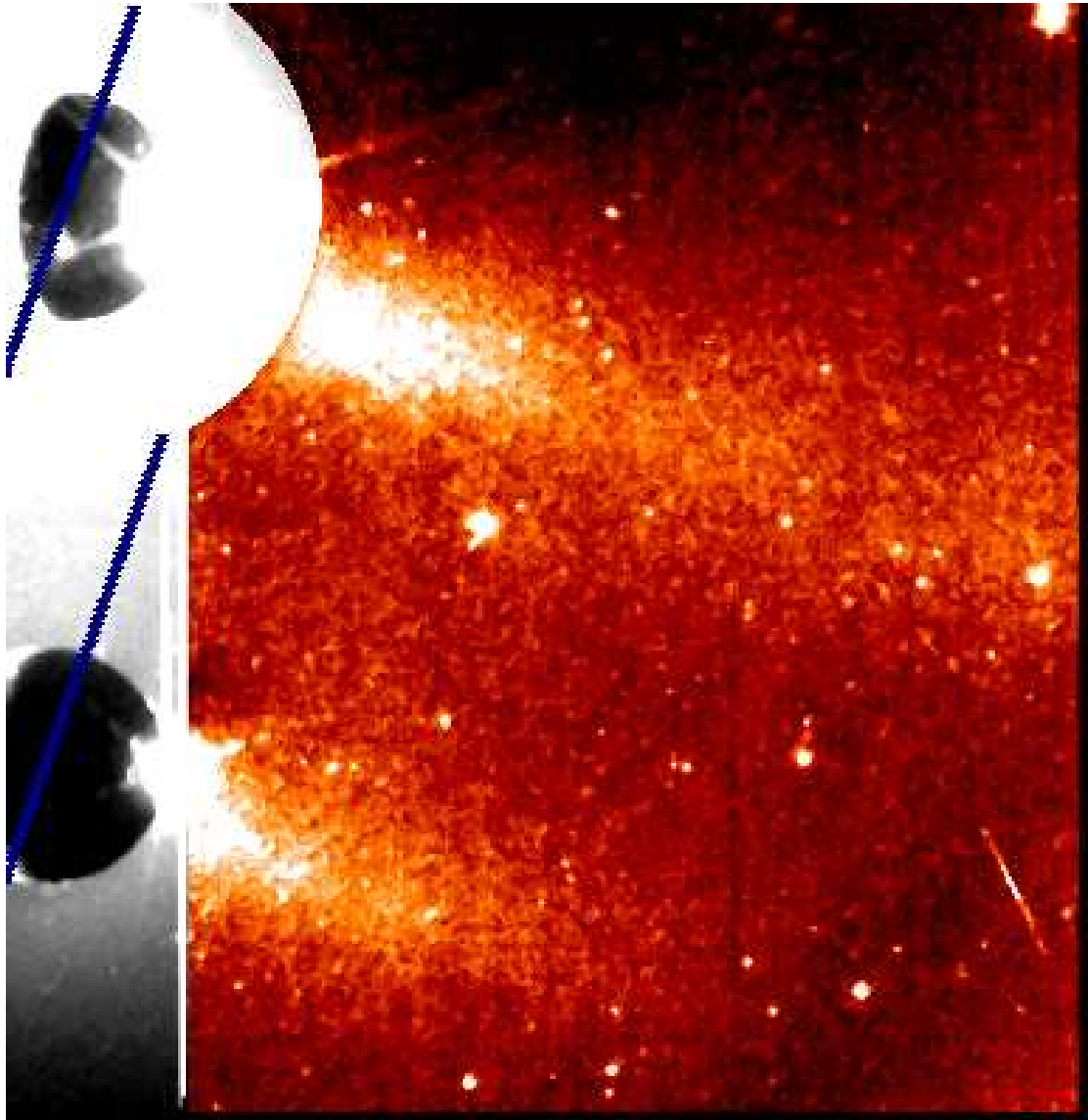


Figure 4.2 The background-subtracted Galileo image showing the fast sodium jet extending down and to the right (false-color red). The top image is primarily through the clear filter; the bottom through the green filter. Io's disk and the region immediately surrounding Io are shown as seen in the raw image using greyscale. Iogenic emission (probably due to sodium, see text) contributes to emission surrounding Io's disk. The bright region at the right edge of Io's disk is due to scattered light from the Prometheus plume. The illuminated crescent on the left edge of Io is sunlight reflected off of Jupiter onto Io. The Pele hot spot can be seen on Io's disk through the clear filter. The fast sodium is brighter in the clear exposure than the green due to the differing filter transmission at 590 nm. The jovian magnetic field line through Io is shown in blue.

of the jet. Errors in these quantities were derived by using the marginally acceptable power-law fits to the residual scattered light background; the derived quantities are not sensitive to the background values chosen. The highest quality measurements were obtained at $3 R_{\text{Io}}$.

Perhaps the most significant measurement is the latitudinal width of the jet. Previous studies of Io's atmospheric loss processes have been divided over whether to consider Io's atmosphere at least as large as Io itself (larger, in the case of an extensive atmosphere with an exobase well above the surface), or significantly smaller than Io (due to a patchy atmosphere concentrated around Io's volcanoes, and absent over the frigid poles) (Spencer and Schneider 1996). The sodium jet is clearly in the latter category. The green filter image offers the best measurement close to Io of $1.1 \pm 0.1 R_{\text{Io}}$ at $3 R_{\text{Io}}$, substantially narrower than Io's diameter. The data are not of sufficient quality to determine how the width changes with distance. Due to the complex velocity structure of the jet close to Io, the supply rate is estimated by comparison of the measured brightness of sodium with simulations of the jet with a known supply rate. The supply rate in the jet is estimated to be $4.8 \pm 1.0 \times 10^{25}$ atoms sec^{-1} , consistent with previous estimates measured farther from Io (Schneider et al. 1991b; Wilson and Schneider 1999).

We can constrain the size of the source region by comparing the Galileo data to profiles simulated using the model of Wilson and Schneider (1999) under the Galileo observing conditions. Figure 4.3a compares the Galileo green filter data with simulated azimuthal intensity profiles at $3 R_{\text{Io}}$ of jets that result from a point source on Io and from an ionosphere covering Io's anti-Jovian hemisphere. Neither model matches the data well. The data are most consistent with an ionosphere concentrated within 35° of the equator (Figure 4.3b). The source region could be even smaller if other processes (such as the bending of magnetic field lines by the Io interaction) are included; such analysis is reserved for a later paper. The present result represents an upper limit on the latitudinal extent of the ionosphere.

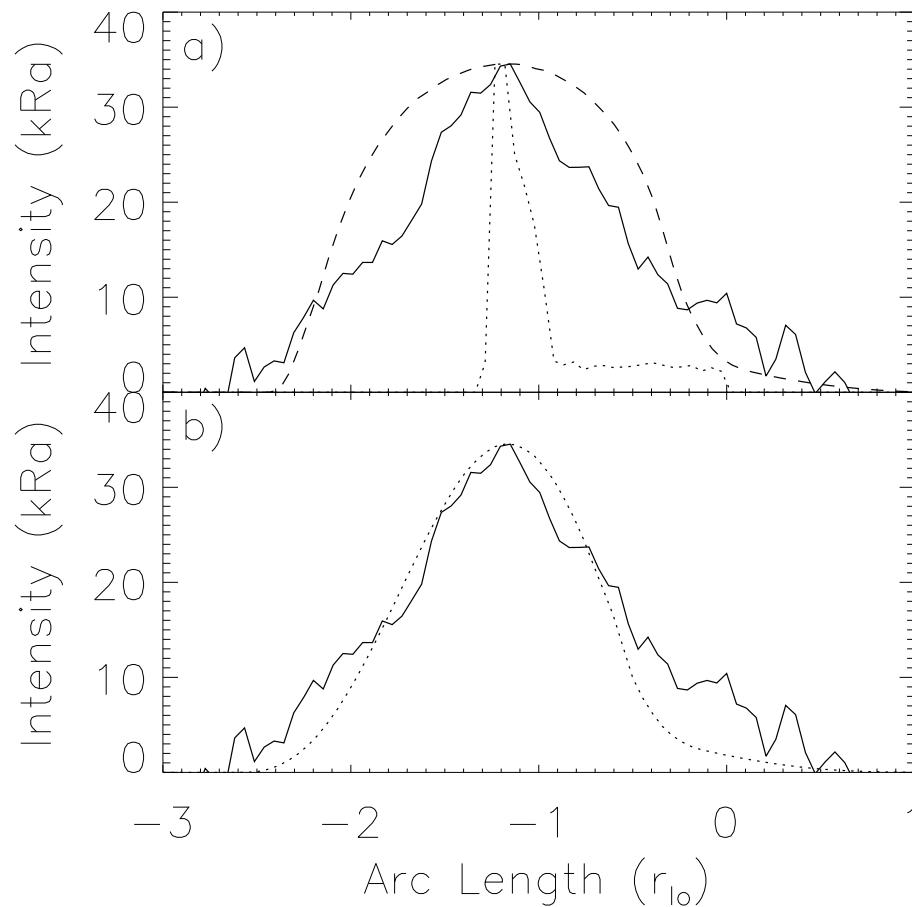


Figure 4.3 (a) Intensity profiles through model images and the green filter data at a constant radial distance of $3 R_{Io}$ from the center of Io. The solid line shows the data (corrected for filter transmission), the dashed line shows a model with a hemispheric source region, and the dotted line shows the jet produced by a point source on Io's anti-Jupiter point. The location of the peaks of the profiles have been adjusted a few tenths of an Io radius so that they are aligned. The cause for this discrepancy is uncertain, but may be related to uncertainties in the subtraction of the sloping background. The full width at half maximum (FWHM) of the data is $1.1 R_{Io}$ compared to $1.7 R_{Io}$ for the hemispheric source and $0.2 R_{Io}$ for the point source, indicating that the source region of the jet is smaller than Io but still covers an extended region. The ionosphere does not extend to the poles. (b) Intensity profiles for the data and the best fit ionospheric distribution. The dashed line shows the intensity resulting from an ionosphere for which the neutral sodium flux at the top of the ionosphere is a Gaussian centered at Io's equator and has a FWHM of 35° . The FWHM of the jet matches the data, showing that Io's ionosphere is concentrated to low latitudes.

Two kinds of source regions are consistent with the observations and the theoretical requirement of a collisionally thick ionospheric layer. The first is an atmosphere concentrated at low latitude (as the model results suggest), expected both due to the preponderance of volcanic outgassing vents there as well as the freezing out of a polar atmosphere. Alternatively, it is conceivable that an individual plume or collection of plumes (and their local atmosphere/ionosphere) could create a large enough ionosphere to create a jet of this size. One possible plume origin is Prometheus, the plume responsible for the scattered light. The Pele eruption (seen in thermal emission near the center of Io's disk through the clear filter) is also a candidate, although its location (just barely on the Jupiter-facing hemisphere) is such that sodium ions created in the plume would most likely not escape Io (Wilson and Schneider 1999).

Further observations of the Io sodium jet are contemplated for future Galileo orbits and the Cassini flyby of Jupiter in late 2000. Without contamination from bright plumes, it may be possible to trace the jet all the way back to its source region in the atmosphere.

Chapter 5

Io's Escaping Neutrals

5.1 Introduction

Observations of Io's extended atmosphere have painted a portrait of a highly dynamic and variable region. The volcanic source processes vary in time, magnitude, and location on Io's surface. Large variations in surface temperature result in the daily collapse of the thin atmosphere. External forces such as Jupiter's rapidly rotating magnetic field and the intense bombardment by plasma torus ions strip the atmosphere away at a rate of a ton per second. Loss of atmospheric neutrals then provides the source regions for the plasma through the formation of Io's corona and extended neutral clouds. Observations of these features provide important insight into the magnitude and variability of this atmospheric loss and the quantity of material available for the formation of the torus. Telescopic observations however are only capable of measuring the line-of-sight integrated column densities and intensities and *in situ* measurements by spacecraft are rare and only measure a single slice through the highly variable plasma. Understanding the details of the escape of Io's atmosphere and the formation of the plasma torus requires a knowledge of the three dimensional distributions of neutrals near Io. This requires a model which can simulate the motions of neutrals to determine probable distributions which can be compared with observations.

Although other authors have published neutral cloud models (e.g. Smyth and Combi (1988a,b)), the development of a new model for understanding Io's neutral fea-

tures is necessary to take advantage of new observations of the neutral clouds and the plasma torus. Recent observations of the Io plasma torus (Schneider and Trauger 1995; Brown 1994) have shown that the intensity and apparent motions of the plasma are extremely variable. In this chapter I describe the neutral cloud model and an empirical treatment of the plasma torus which can reproduce the observed variability in the brightness and morphology of the plasma torus. In chapters 6 and 7 the model is used to investigate in detail the morphologies of Io's corona and extended neutral cloud. The neutral cloud model can also be applied to future studies of Io's neutral features as well as investigations of neutral loss from other solar system objects.

The chapter is organized as follows: In Section 5.2 I discuss the previously published model of Smyth and Combi (1988a,b) with which I will compare the current model. Differences between the two models are discussed in Section 5.3 which is devoted to describing the model in detail. In addition to a description of the approach taken to determine the spatial distribution of neutrals within $\sim 10 R_J$ of Jupiter, I describe the flux distributions of atoms ejected from Io's exobase and my treatment of the plasma torus which governs neutral loss. I have developed a framework for using observations of plasma torus variability to determine the spatially and temporally varying plasma properties. I use this framework to determine characteristics of the lifetime of neutrals as a function of the local time, magnetic longitude, and distance from Jupiter. The chapter concludes in Section 5.4 with several applications of the model to demonstrate that the earliest observations of the sodium neutral cloud can be simulated with this model.

In the following chapters I discuss in detail the comparison between observations reported in this thesis and modeling results of the corona (Chapter 6) and the extended neutral cloud (Chapter 7).

5.2 Previous Neutral Cloud Models

Modeling efforts to understand Io's sodium emission began almost immediately after its discovery. These models are reviewed in Chapter 1. Included here is a description of the model introduced by Smyth and Combi (1988a) as a general model for Io's neutral clouds. This work has continued most recently with several studies of Io's oxygen emissions (Smyth and Marconi 2000; Oliverson et al. 2001).

Smyth and Combi (1988a) developed the framework for a sophisticated neutral cloud model based upon “the conservation in phase space of the one-particle distribution function $f(\mathbf{v}, \mathbf{x}, t)$ for a gas species.” This generalized model was applied to the sodium cloud in a followup paper (Smyth and Combi 1988b). The goals of this study were to explain the physical origin of the predominately forward sodium cloud and the east/west brightness asymmetry in the near Io cloud (Bergstralh et al. 1977). They found that each of these questions could be explained as a consequence of sodium atoms sputtered isotropically from Io's exobase into the radially non-uniform plasma torus. The structure of the torus results in a longer sodium lifetime for atoms which move interior to Io's orbit, which form the leading cloud, than for atoms which move exterior to Io's orbit forming the trailing cloud. The flux distribution from the exobase needed to reproduce adequately the east/west asymmetry was either a classical sputtering flux distribution ($\alpha = 3$ in Equation 2.12) or a Thomas-Fermi-like incomplete collisional cascade sputtering flux distribution ($\alpha = 7/3$); they preferred the latter because of the increased flux of high speed (12–25 km s⁻¹) neutrals which they hypothesized populate the fast sodium directional feature. The work of Wilson and Schneider (1999) and that presented in Chapter 4 show that the sodium directional feature is created through a different mechanism than the slow sodium cloud. Therefore the preference for $\alpha = 7/3$ is not necessary.

Smyth and Combi also introduced a parameterization of the plasma torus in

their second paper which is used in their later work. In the discussion which follows in the this chapter, I compare their treatment of the plasma torus with that I have developed. Although most of the differences between the two methods stem from recent observational results which I have used, I also use a different physical description of the orientation and motions of the plasma torus.

5.3 A Model of Io's Neutral Clouds

5.3.1 Description of the model

The model described here is an extension of the model of Wilson and Schneider (1999) which has previously been used to describe Io's directional feature (see Chapter 4), the molecular ion stream, and the extended sodium disk that is centered on Jupiter and has a radius of $\sim 500 R_J$. The integration algorithm for determining the motions of neutral atoms, which is the basic core of the model, remains unchanged from Wilson's model. However, because the foci of this thesis are Io's corona and extended neutral cloud, several major changes have been made in regard to the lifetimes of neutral atoms within $\sim 8 R_J$ of Jupiter. First, the description of the plasma torus has been refined to include observed variations in brightness and the effects of the east/west electric field. Second, changes have been made in calculating the lifetimes once the local plasma parameters have been determined. The improvement of the sodium electron impact ionization cross sections (Johnston and Burrow (1995), Chapter 2) resulted in a significant change in the sodium lifetime. I have also included charge exchange cross sections of oxygen and sulfur so that these neutral clouds can be modeled. Lastly, I have rewritten much of the model code so that its run speeds are improved allowing the higher spatial resolution simulations which are needed to understand the features close to Io.

In order to simulate the creation of the neutral clouds and their loss into the

plasma torus, a particle approach is used to follow sodium atoms ejected from Io's exobase. I follow packets representing a number of atoms that are subjected to the forces of Io's gravity, Jupiter's gravity, and solar radiation pressure (for sodium only). Ionization reduces the number of atoms that the packet represents. The coordinate system (Figure 5.1) is fixed such that the z-axis is along Jupiter's north-south axis perpendicular to the equatorial rotational plane where the satellites lie. The y-axis is along the sun-Jupiter line with the positive direction pointing radially away from the sun. The x-axis is oriented perpendicular to the y- and z-axes pointing from Jupiter's east (dawn) side to the west (dusk) side.

The gravitational accelerations that packets experience from both Jupiter and Io are calculated:

$$\mathbf{a}_p = \frac{d^2\mathbf{x}}{dt^2} = -\frac{GM_p}{r_p^3} \quad (5.1)$$

where p refers to either Jupiter or Io and r_p is the distance from the packet to the object ($r_p = \sqrt{x_p^2 + y_p^2 + z_p^2}$ with x_p , y_p , and z_p being the differences in the x, y, and z coordinates of the packets and the object p). M_p is the mass of the object and G is the universal gravitational constant.

The acceleration due to radiation pressure, as discussed in Chapter 2, is given by:

$$\mathbf{a}_{\text{rad}} = [a_{x,\text{rad}}, a_{y,\text{rad}}, a_{z,\text{rad}}] = [0, 0.580(\gamma_1 + 2\gamma_2), 0] \quad (5.2)$$

Because the direction from the sun to Jupiter is defined to be the y-axis, radiation pressure always acts in the positive y direction and the force only has one component. This simplifies the calculation of the radiation acceleration since it depends on the radial velocity of the packet relative to the sun, which is simply the velocity in the y direction; i.e., γ_1 and γ_2 are functions of v_y only.

Combining the effects of the three accelerations yields:

$$\mathbf{a} = \mathbf{a}_J + \mathbf{a}_{Io} + \mathbf{a}_{\text{rad}} \quad (5.3)$$

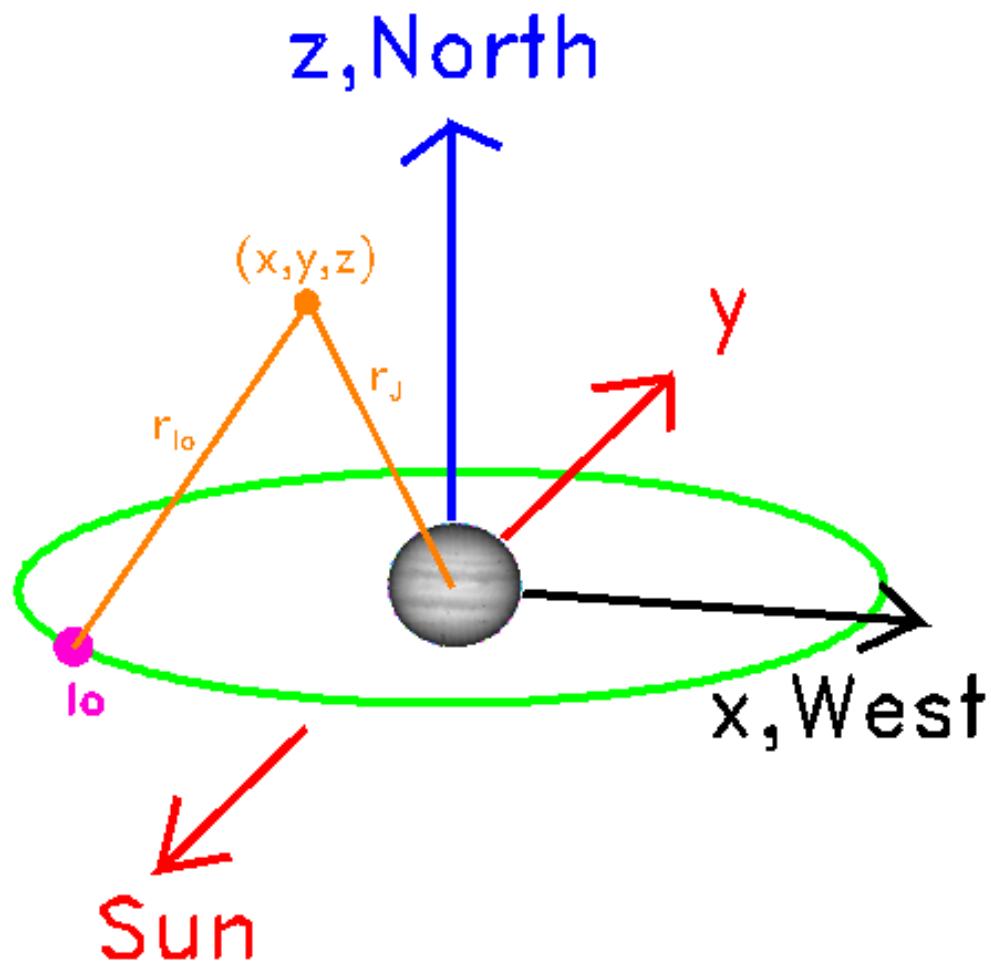


Figure 5.1 Sketch of the coordinate system used in the model. The origin of the coordinate system is fixed at Jupiter's center. The x-axis is direction from east to west. The y-axis is directed radially away from the sun. The z-axis is aligned north along Jupiter's spin axis. Io's orbit is shown in green with Io indicated by the pink dot at orbital phase $\phi = 135^\circ$. A packet is at position (x,y,z) with the distances r_J and r_{Io} labeled.

or

$$\begin{aligned}
\frac{d^2x}{dt^2} &= -\frac{GM_J x_J}{r_J^3} + -\frac{GM_{Io} x_{Io}}{r_{Io}^3} \\
\frac{d^2y}{dt^2} &= -\frac{GM_J y_J}{r_J^3} + -\frac{GM_{Io} y_{Io}}{r_{Io}^3} + 0.580(\gamma_1 + 2\gamma_2) \\
\frac{d^2z}{dt^2} &= -\frac{GM_J z_J}{r_J^3} + -\frac{GM_{Io} z_{Io}}{r_{Io}^3}
\end{aligned} \tag{5.4}$$

The vectors \mathbf{r}_J and \mathbf{r}_{Io} are the instantaneous distances and directions from the packet to Jupiter and Io (see Figure 5.1). These vectors change constantly due to the motion of the packet through the coordinate system and the motion of Io in its orbit around Jupiter. Jupiter is fixed at the origin of the coordinate system. The system of second-order differential equations is solved using a 4th order adaptive step-size Runge-Kutta technique. Io's orbital phase is tracked for each packet for each step in the solver to determine correctly the gravitational acceleration experienced by each packet. The initial starting positions and velocities of the packets are randomly chosen based on distributions which are supplied. Unless specified otherwise, the initial positions are isotropically distributed over Io's exobase. The packets also are ejected isotropically into the hemisphere tangent to the surface at the packets' starting locations. The initial velocity distribution depends on the loss mechanism from the exobase as discussed in Chapter 2. The starting times for packets are uniformly distributed between the beginning and ending times of the model run, simulating a continuous source from the exobase. This creates a realistic cloud made up of neutrals of all ages between the start and finish of the simulation. The total simulated time depends on the species and the region being modeled.

5.3.2 Treatment of the Io Plasma Torus

The instantaneous rate of loss of atoms from each packet and the intensity of observed oxygen and sulfur emission are determined by the local plasma conditions during each time step. Consequently, it is essential to properly determine the location

of the packets in the plasma torus and to understand the structure and variability of the torus to calculate correctly the ionization rate. I will here describe the treatment of the plasma torus used in the model; the ionization rate is discussed in Chapter 2.

Jupiter's magnetic field is approximated as an offset tilted dipole with: a tilt $\alpha_D = 9.8^\circ$ toward the System-III magnetic longitude $\lambda_0 = 200^\circ$, and an offset distance $\delta_D = 0.12 R_J$ toward the magnetic longitude $\lambda_D = 149^\circ$ (Figure 5.2). The centrifugal equator is tilted relative to the equatorial plane by the angle $\alpha_C = \frac{2}{3}\alpha_D = 6.5^\circ$. The plasma torus is aligned along the centrifugal equator parallel to the rotation axis. Therefore the ribbon always appears parallel to the rotation axis and is not perpendicular to the centrifugal equator.

To determine the plasma conditions experienced by a packet, I have developed a transformation to a coordinate system in the rest frame of the plasma torus defined by the coordinates M and ζ in which the ribbon is held fixed at $(M, \zeta) = (5.83 R_J, 0 R_J)$. M is the modified L-shell developed here based on the Voyager *in situ* Plasma Science (PLS) data (Figure 5.3) (Bagenal 1994) and ground-based observations of the local time and magnetic longitude variation in the ribbon location (Schneider and Trauger 1995) (Figure 5.4a). ζ is the distance along the magnetic field line through the packet from the packet to the centrifugal equator. M differs from the true L-shell, which is based on the offset tilted dipole, due to: (1) the inferred presence of an east/west electric field across Jupiter's magnetosphere, and (2) the observation that the ribbon is offset from the center of Jupiter by approximately one-half the offset of the dipole field. The mathematical transformation from the observer's coordinates to the torus coordinates is given in Appendix B.

A comparison of Figure 5.3 and Figure 5.4(a) reveals an apparent, previously unrecognized inconsistency regarding the position of the ribbon. In the former, the dusk ribbon is at a distance of $5.7 R_J$. In the latter, the dusk ribbon oscillates between 5.53 and $5.65 R_J$, a range which excludes the location observed by Voyager. I have

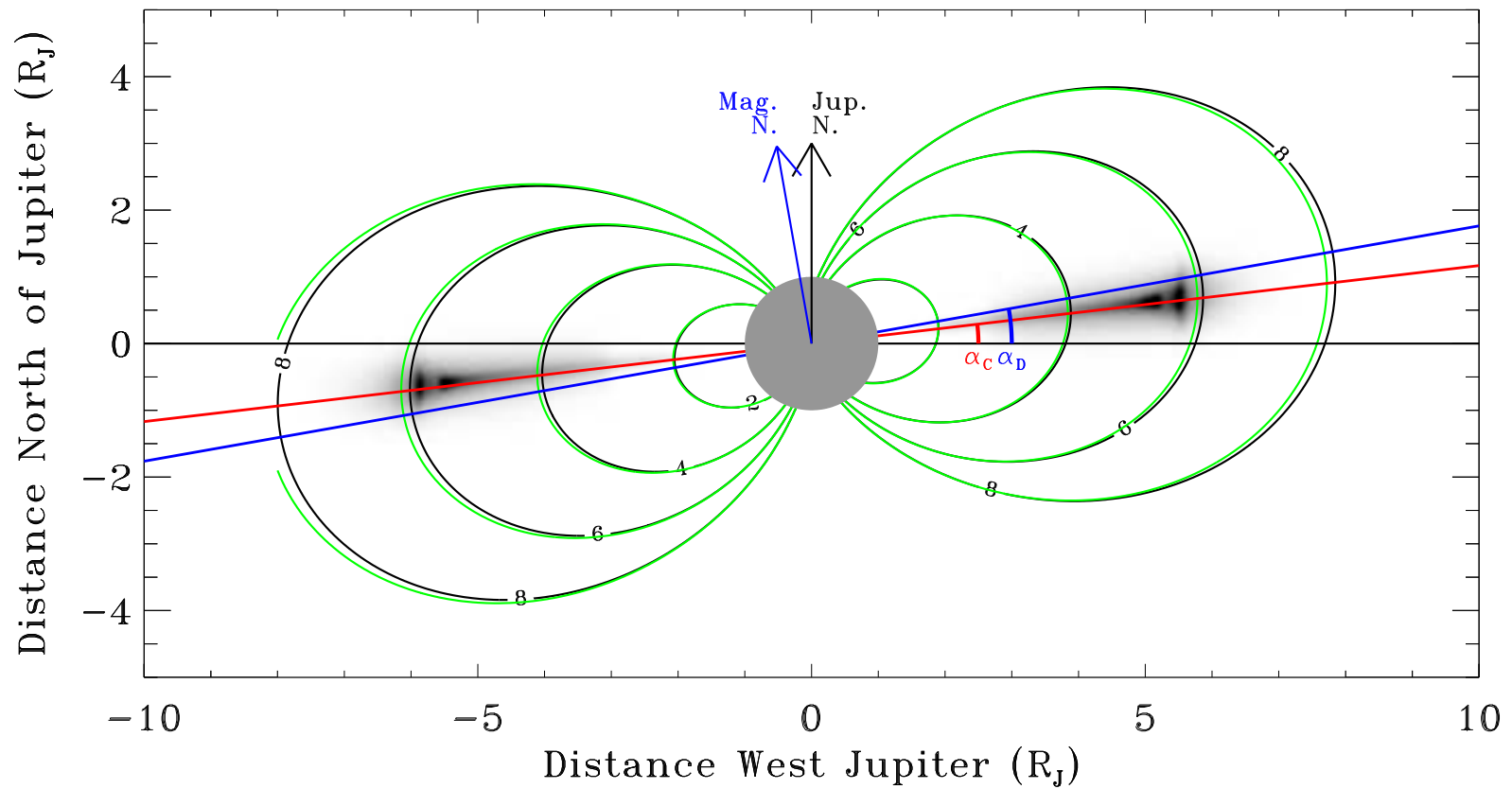


Figure 5.2 Cartoon showing Jupiter's dipole field with the plasma torus aligned along the centrifugal equator. Jupiter's magnetic equator and the direction of magnetic north are shown in blue; the centrifugal equator is shown in red. Jupiter's central meridian longitude (λ_{CML}) in this depiction is 110° . The L value of the field lines are shown in black. The green contours are the modified L-shell, M, used to determine the plasma parameters.

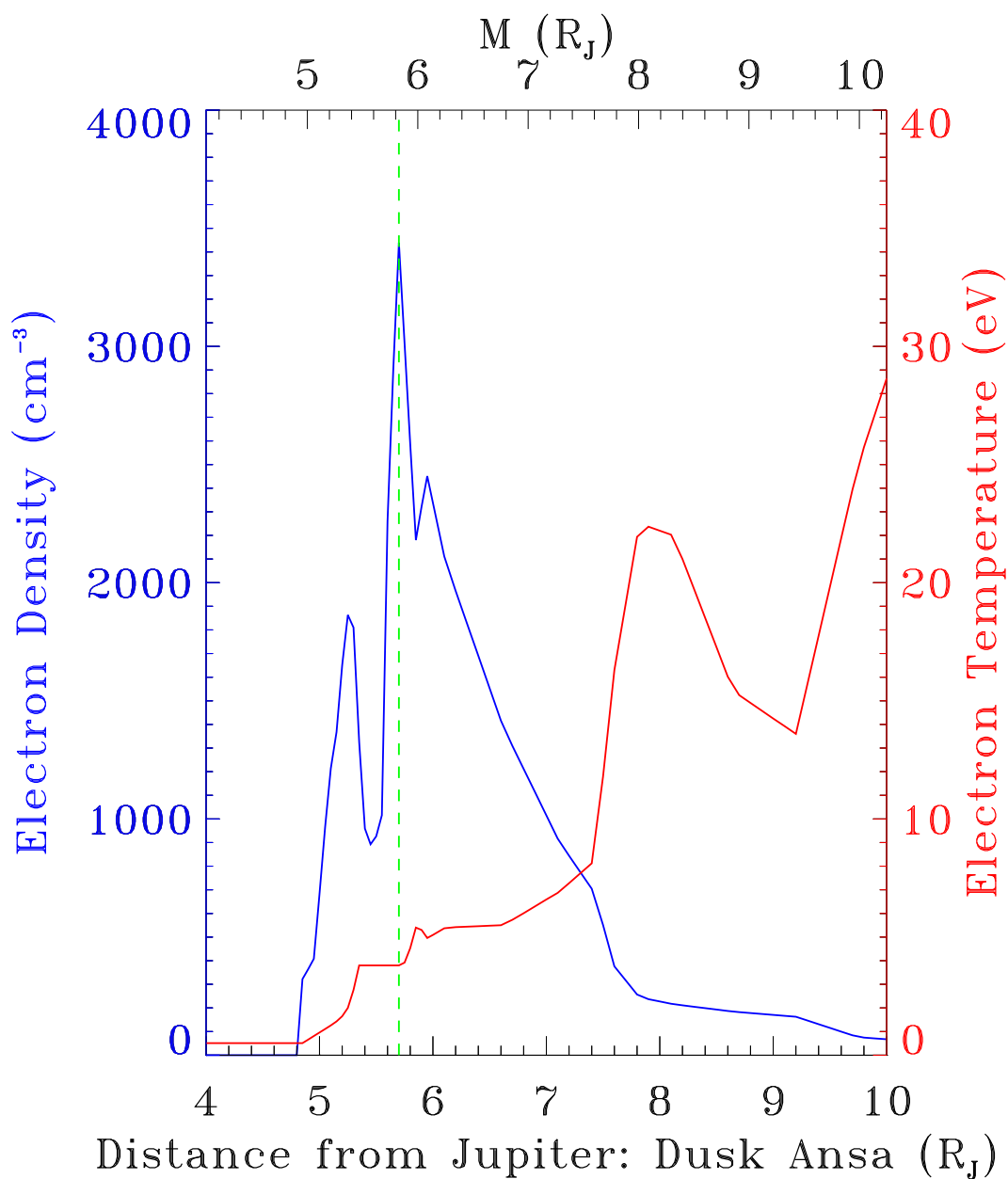


Figure 5.3 The electron density (blue) and temperature (red) in the centrifugal equator measured by the Voyager spacecrafts (Bagenal 1994) are shown as a function of the distance from Jupiter (bottom axis) and the torus M coordinate (top axis) discussed in the text. The broken green line indicates the ribbon observed by Voyager 5.7 R_J from Jupiter and fixed in this coordinate system at $M=5.83 R_J$.

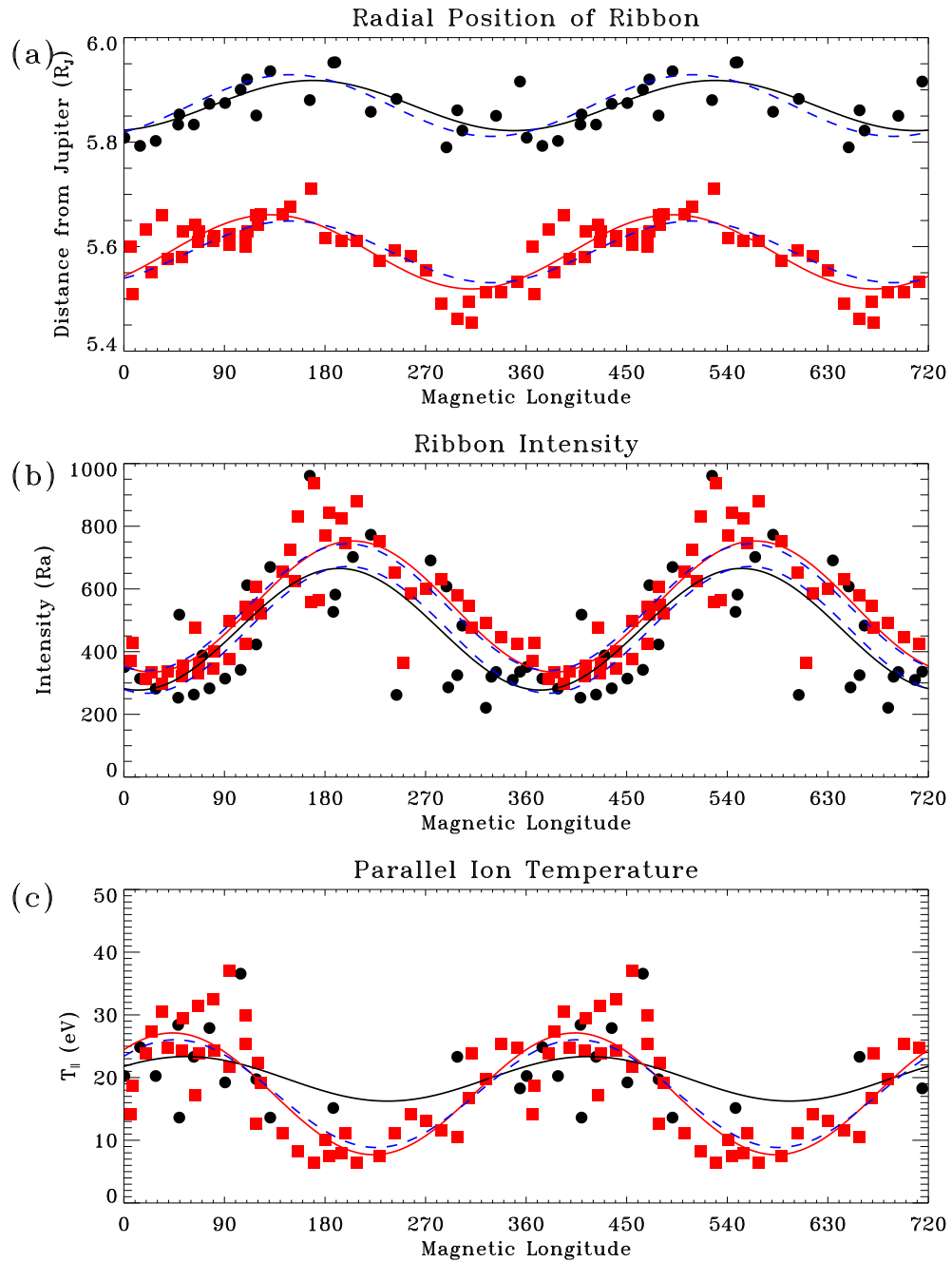


Figure 5.4 Variations in ribbon location, electron density, and parallel ion temperature from observations by Schneider and Trauger (1995). (a) Radial distance of the ribbon from the center of Jupiter as a function of the magnetic longitude of the ansa. Black dots are data from the dawn (eastern) ansa; red squares are from the dusk (western) ansa. The solid black and red lines are fits to the dawn and dusk ansae, respectively. The broken lines show a single sinusoid fit to both ansae. (b) Intensity vs. magnetic longitude. The intensity is proportional to the product of electron density and ion density. Colors as for part (a). (c) T_{\parallel} vs. magnetic longitude. Temperatures are from the modeling by Schneider et al. (1997) based on the observations of Schneider and Trauger (1995). Colors as for part (a).

found that these two data sets do in fact paint a consistent picture. The resolution to the conflict lies in the difference between *in situ* and remote observing. Voyager measured a slice through the three-dimensional plasma. The ground-based observations detect the total integrated flux along the sight line. When line-of-sight effects are taken into account, the Voyager and ground-based data agree. Figure 5.5 shows a simulated image of the plasma torus and the electron density in Jupiter's east/west plane. The maximum electron density, shown by the broken blue lines, on dawn (dusk) side occurs at 6.02 R_J (5.64 R_J). The brightest points in the ribbon (broken red lines), however, are 5.92 R_J at the dawn ansa and 5.56 R_J at the dusk ansa, well inside the distance of maximum electron density and proving that the Voyager and ground-based data are in fact consistent. (The dusk ansa ribbon is not at precisely 5.7 R_J due to the fact that the ribbon moves in and out with an amplitude of ~ 0.06 R_J and depends on magnetic longitude; the central meridian longitude.) Contours of electron density in the centrifugal plane are plotted over the image in green.

The simulated torus images are created by determining the volume emission rate in a grid centered on Jupiter. The plasma electron and ion temperatures and densities are determined by transformation into the plasma coordinate system. The volume emission is then given by:

$$\rho(x, y, z \rightarrow M, \zeta, \phi, \lambda) = C_k(n_e, t_e)n_e(M, \zeta, \phi, \lambda)n_i(M, \zeta, \phi, \lambda) \quad (5.5)$$

in units of photons cm⁻³ s⁻¹. C_k is the emission rate coefficient from the CHIANTI atomic physics database (Dere et al. 1997). The volume emission rate is summed along the line-of-sight to determine the observed emission in photons cm⁻² s⁻¹. The dependence of the plasma densities and temperatures on local time ϕ and magnetic longitude λ is discussed below.

The effect the east/west electric field has is to shift the ribbon east by 0.14 R_J; the amount of shift is proportional to the distance from Jupiter, $\Delta R = \epsilon R_0$ (Barbosa

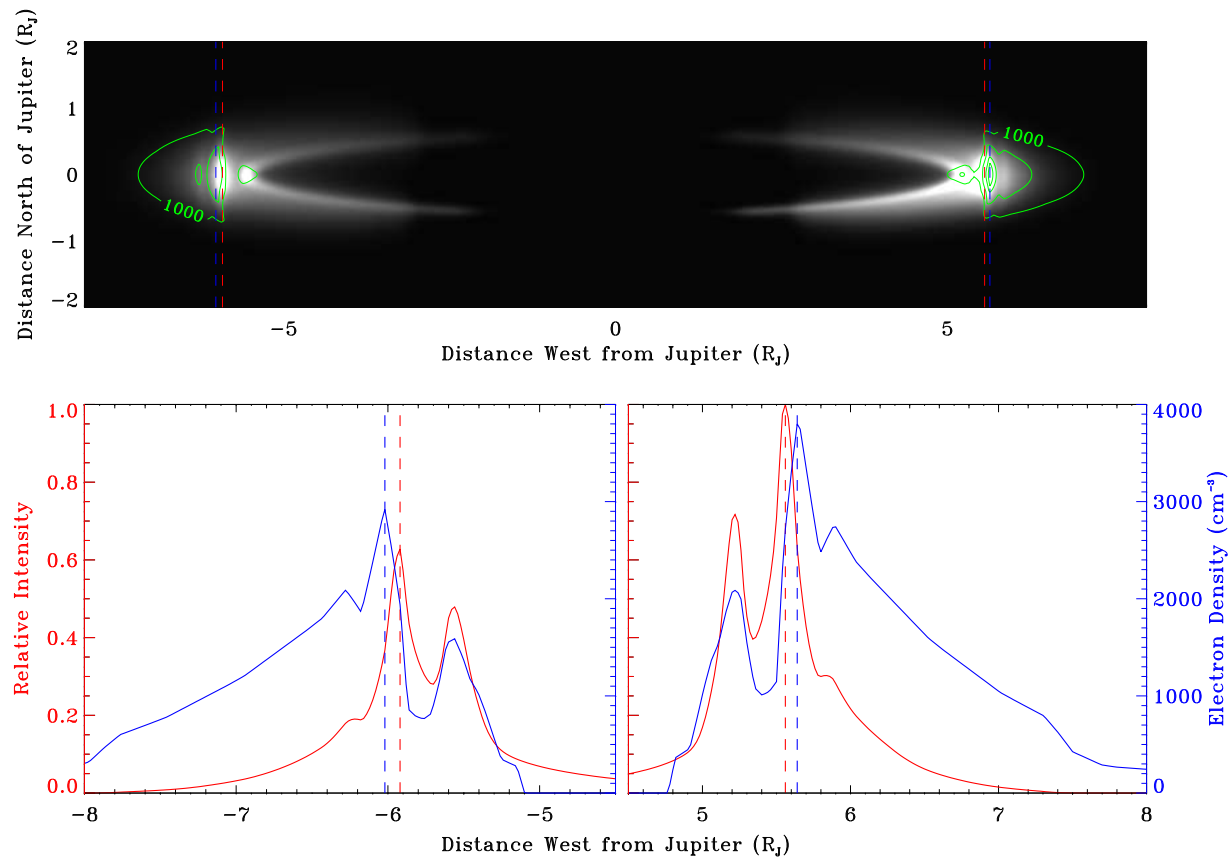


Figure 5.5 Illustration of the importance of line-of-sight effects on Earth-based observations of the plasma torus. (a) A simulated image of singly ionized sulfur. (b) Brightness of the torus (red) and electron density (blue) in the centrifugal plane for the images in (a). The central meridian longitude for this image is $\lambda_{CML} = 20^\circ$.

and Kivelson 1983), where ϵ is the ratio of the inferred east/west electric field to the corotation electric field. The value of ϵ which causes a 0.14 R_J shift at the distance of the ribbon (5.83 R_J) is 0.024. This measured result based on the ground-based observations is consistent with the assumed value used by Smyth and Combi (1988b). The ground-based observations show that the average observed location of the maximum ribbon brightness is 5.87 R_J at the dawn ansa and 5.59 R_J at the dusk ansa. The average distance for all local times is 5.73 R_J . This effect can be simulated with a torus electron profile where the ribbon is at an average distance from Jupiter of 5.83 R_J , shifted 0.14 R_J to the east such that the average observed position of the ribbon as a function of local time can be expressed as $5.83 + 0.14 \sin(\phi)$ where ϕ is the local time (heliocentric orbital phase). The location of the ribbon (i.e., the position of the maximum electron density at a given orbital phase) is fixed in the plasma coordinate system at $(M, \zeta) = (5.83R_J, 0R_J)$.

The local plasma conditions present for each packet depend on the location in the torus (i.e. M and ζ), the local time ϕ and magnetic longitude λ of the packet. All modulations to the radial plasma profile in the torus start from the Voyager PLS data shown in Figure 5.3. These conditions are assumed the average torus at the dusk ansa. Figure 5.6 shows the values of M and ζ as functions of Io's magnetic and orbital longitudes. The variation in these coordinates is indicative of the changing plasma environment at Io. Io is inside the ribbon, demarcated by the broken yellow circle, near eastern elongation when crossing the centrifugal equator.

Based on observations (Schneider and Trauger 1995; Brown 1994) and modeling (Bagenal 1994; Schneider et al. 1997; Barbosa and Kivelson 1983; Ip and Goertz 1983)), I have implemented three types of modulation into the description of the plasma torus:

- (1) Local Time Variations: Barbosa and Kivelson (1983) and Smyth and Combi (1988b) discuss the effects of the global east/west electric field on the plasma

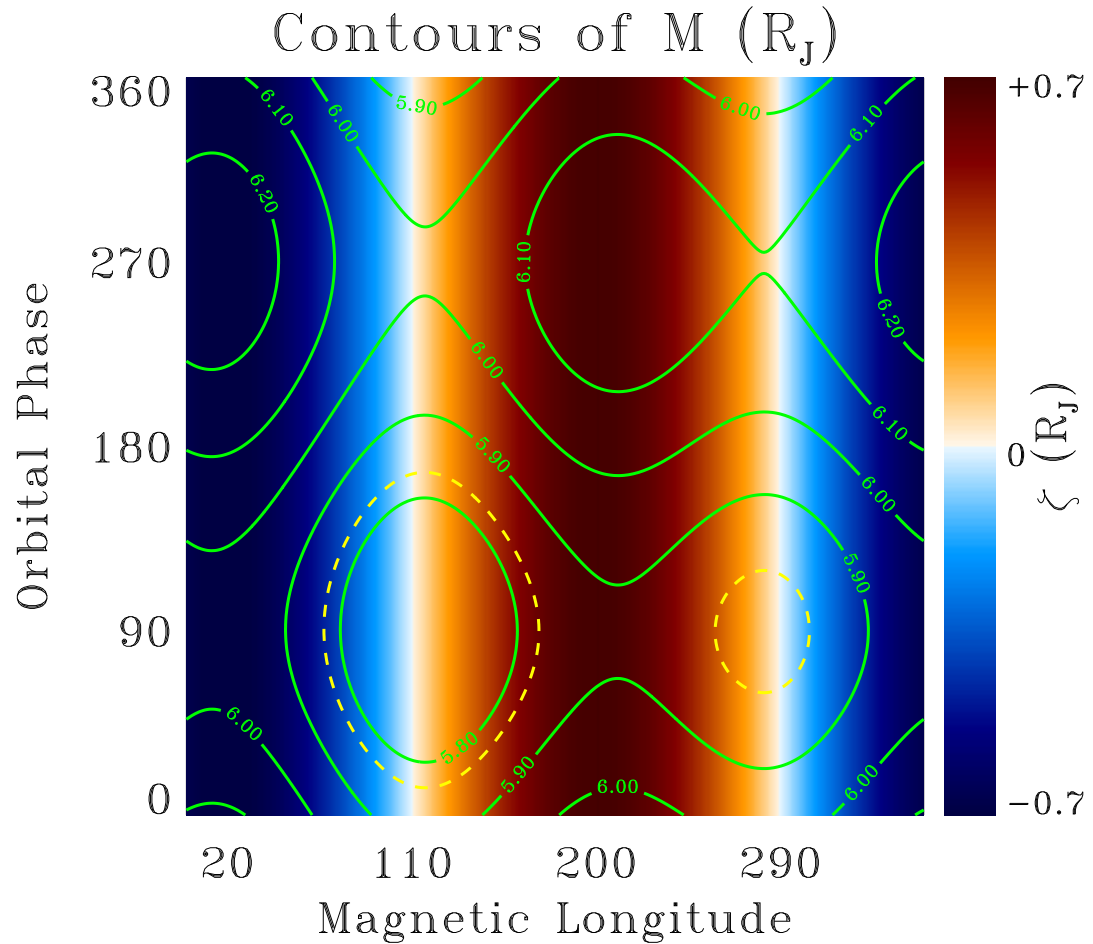


Figure 5.6 Contours of Io's M -value as functions of Io's magnetic and orbital longitudes. The broken yellow circles indicate the location of the ribbon, fixed in this coordinate system at $M=5.83 R_J$. The color indicates Io's ζ value, with darker color indicating that Io is farther from the centrifugal equator. The color is red when Io is north of the torus and blue when Io is south of the torus.

torus. As discussed above, one effect is to shift the torus dawn-ward. The second effect of the electric field is that a torus ion experiences a changing magnetic field as it is swept around Jupiter. This results in a modulation of both the electron density and temperature proportional to $(L(270^\circ)/L(\phi))^2$ where $L(\phi)$ is the L-shell of the torus ion at orbital phase ϕ and $L(270^\circ)$ is the L-shell of the ion at western elongation (Smyth and Combi 1988b). These authors used a theoretical calculation of this variation based on the inferred strength of the east/west electric field and the expected motion of the plasma through the torus. I use instead observations of the eastern and western ansae of the torus to impose an empirical local time variation in the form:

$$C_{LT} = 1 - A_{LT} (1 + \sin \phi) \quad (5.6)$$

where C_{LT} is the local time correction factor as a function of local time (ϕ) and $A_{LT} = (1 - n_{e,east}/n_{e,west})$ is the amplitude of the variation. The value of A_{LT} is determined from observations of ribbon intensity. Schneider and Trauger (1995) measured an east/west intensity ratio in the ribbon of $I_{east}/I_{west} = 0.86$ (Figure 5.4b). Taking into account line-of-sight brightness effects, the east/west electron density ratio in the centrifugal equator is $n_{e,east}/n_{e,west} = 0.94$, or $A_{LT}=0.03$. An additional measurement of the east/west intensity ratio is given by Brown (1994) who took into account line-of-sight effects when determining the intensity ratio in the warm torus. This measured value is $I_{east}/I_{west} = 0.78$, implying $A_{LT} = 0.04$, consistent with that predicted by Smyth and Combi (1988b) based on the inferred magnitude of the east/west electric field and the assumption that the plasma expands in three dimensions as it moves from west to east.

- (2) System-III Variations: The intensity in the plasma torus varies as a function of magnetic longitude (Figure 5.4b). Schneider and Trauger (1995) found that the

intensity in the ribbon varies in the form:

$$I(\lambda) \sim 1 + 0.39 \cos(\lambda - 200^\circ) \quad (5.7)$$

The observations by Brown (1994) were more sensitive to variability in the warm torus and found:

$$I(\lambda) \sim 1 + 0.35 \cos(\lambda - 180^\circ) \quad (5.8)$$

This variation results from a combination of changing electron density and scale height in the torus, as seen in the observations of Schneider and Trauger (1995): when the longitude of the ansa is near 200° , the ribbon is short and bright; at longitudes near 20° , the ribbon is tall and dim. Schneider et al. (1997) suggested that the total flux tube content (the ion column integrated along the field line) may remain constant along a magnetic field line over the period of the magnetic field rotation. The flux tube content can be expressed as:

$$N = \sqrt{\pi} n_0 H \quad (5.9)$$

where n_0 is the electron density on the centrifugal equator. $H = \left(\frac{3kT_{\parallel}}{3m_i\Omega^2}\right)^{1/2} \propto T_{\parallel}^{1/2}$ is the plasma scale height Hill and Michel (1976). Therefore,

$$n_0 \propto \frac{1}{H} \propto \frac{1}{\sqrt{T_{\parallel}}} \quad (5.10)$$

This simplification allows the observed System-III variations in the torus to be expressed as a function of a single parameter: the parallel ion temperature. The variation in T_{\parallel} is expressed as:

$$T_{\parallel}(\lambda) = T_0 + A_{T_{\parallel}} \cos(\lambda - \lambda_{T_{\parallel}}) \quad (5.11)$$

where T_0 is the average ion temperature, $A_{T_{\parallel}}$ is the amplitude of the variation, and $\lambda_{T_{\parallel}}$ is the longitude of maximum temperature. Based on modeling of the images in Schneider and Trauger (1995), Schneider [personal communication]

found that $T_0 = 17.4$ eV, $A_{T_{\parallel}} = 8.5$ eV, and $\lambda_{T_{\parallel}} = 46^\circ$ in the ribbon (Figure 5.4c), and $T_0 = 74.8$ eV, $A_{T_{\parallel}} = 15$ eV, and $\lambda_{T_{\parallel}} = 22^\circ$ in the warm torus. The scale height and electron density can then be expressed as functions solely of the parallel ion temperature:

$$\begin{aligned} H(T_{\parallel}) &= H(T_0) \sqrt{\frac{T_{\parallel}}{T_0}} \\ n(T_{\parallel}) &= n(T_0) \sqrt{\frac{T_0}{T_{\parallel}}} \end{aligned} \quad (5.12)$$

The intensity variations observed by Schneider and Trauger (1995) and Brown (1994) can be simulated with the ribbon temperature results above. The warm torus temperature results produce a lower amplitude variation in the temperature.

Combining these modulations, the electron density and temperature in the torus as functions of M , ζ , ϕ , and λ are given by:

$$\begin{aligned} n_e(M, \zeta, \phi, \lambda) &= n_{e,west}(M) e^{-(\zeta/H(T_{\parallel}(\lambda)))^2} C_{LT}(\phi) \sqrt{\frac{T_0}{T_{\parallel}(\lambda)}} \\ T_e(M, \zeta, \phi, \lambda) &= T_{e,west}(M) C_{LT}(\phi) \\ n_i(M, \zeta, \phi, \lambda) &= n_{i,west}(M) e^{-(\zeta/H(T_{\parallel}(\lambda)))^2} C_{LT}(\phi) \sqrt{\frac{T_0}{T_{\parallel}(\lambda)}} \end{aligned} \quad (5.13)$$

where $n_{e,west}(M)$, $T_{e,west}(M)$, and $n_{i,west}$ are the electron density, electron temperature, and ion density, respectively at western elongation measured by Voyager (shown in Figure 5.3) and the exponential factor takes into account the distance along the field line from the packet to the centrifugal equator. The electron temperature along field lines is constant and therefore does not depend on ζ . C_{LT} is given by Equation 5.6; the parallel ion temperature, T_{\parallel} , depends on λ according to Equation 5.11.

Combining these idealized variations with the observations referred to above, I have developed a “basic torus” and a “varying torus” which I will take as starting points for studies of Io’s corona and extended neutral clouds. The basic torus uses the Voyager

data as its western profile and includes the local time modulation that results from the presence of the east/west electric field. There are no magnetic longitude effects included so that there are no temporal variations in the torus brightness and scale height. The varying torus adds one more layer of complexity by including the System-III variability with the constant flux tube content assumption. In this implementation I use quantities consistent with the observations discussed: the ribbon is offset from the center of Jupiter $0.061 R_J$ toward $\lambda = 149^\circ$. The value of ϵ is 0.24 resulting in a shift of the ribbon east $0.14 R_J$. The radial electron density and temperature profiles used are the Voyager profiles with the following local time and System-III modulations:

$$C_{LT}(\phi) = 1 - 0.03(1 + \sin \phi) \quad (5.14)$$

$$T_{\parallel}(\lambda) = 17.4 + 8.5 \cos(\lambda - 46^\circ) \quad (5.15)$$

The temperature variation is based on the ribbon measurements as they do a better job of replicating the observed brightness variations.

The major strength in the treatment of the torus that I have developed is that it takes into account the theoretical and observational evidence of torus variability. Different ways in which the torus has been observed to vary have been included when determining the neutral lifetimes. This treatment has also been designed with future torus observations in mind: both changes in the magnitudes of the modulations already included as well as any new ways in which the torus might be discovered to vary can easily be included. This is essential since the combined published and unpublished observations of the torus do not show a constant, repeatable set of variations. Instead, the magnitude and form of torus variability is itself variable. An ideal study of the instantaneous state of the neutral clouds would include the instantaneous torus state, which, unfortunately, is not always available. My canonical torus is based on the most comprehensive study of torus variability during a single week. I assume that it is representative of the normal variability. Additionally in the subsequent chapters of this thesis

I impose changes in the torus density and density, the strength of the east/west electric field, and the amplitude of the variations to determine how these different quantities affect the neutrals.

One assumption I have made is that the different regions of the torus do not vary independently. There is no observational or theoretical requirement that the cold torus, ribbon, and warm torus must vary in the same way. To reduce the number of free parameters and make the torus more manageable, there is no radial dependence on the density variations. A more detailed description of the plasma torus can easily be implemented into this neutral cloud model in the future as they become available.

5.3.3 Neutral Lifetimes in the Inner Jovian System

Because the atomic properties of oxygen, sulfur, and sodium are different, the processes responsible for their loss from the neutral clouds are different. As discussed in Chapter 2, the two important loss processes are electron impact ionization and charge exchange. Figure 5.7 shows the lifetimes of each neutral due to both processes in the region of interest for modeling neutral clouds. The plasma conditions used to calculate the lifetimes are those measured by Voyager at western elongation Bagenal (1994); no System-III variability is taken into account. From the top panel it can be seen that the lifetime of sodium is dominated completely by electron impact ionization. For modeling purposes, it is only necessary to consider electron impact ionization of sodium and charge exchange is ignored.

The loss of oxygen, on the other hand, is dominated by charge exchange. The dominant reaction, shown by the broken blue line in Figure 5.7(b) is $O + O^+ \rightarrow O^+ + O$. This reaction dominates due to the combination of high cross section for charge exchange (Table 2.3) and the high abundance of singly ionized oxygen in the torus.

Sulfur presents a mix of charge exchange and electron impact ionization. In the cold torus, within $\sim 5.7 R_J$, the charge exchange reaction $S + S^+ \rightarrow S^+ + S$

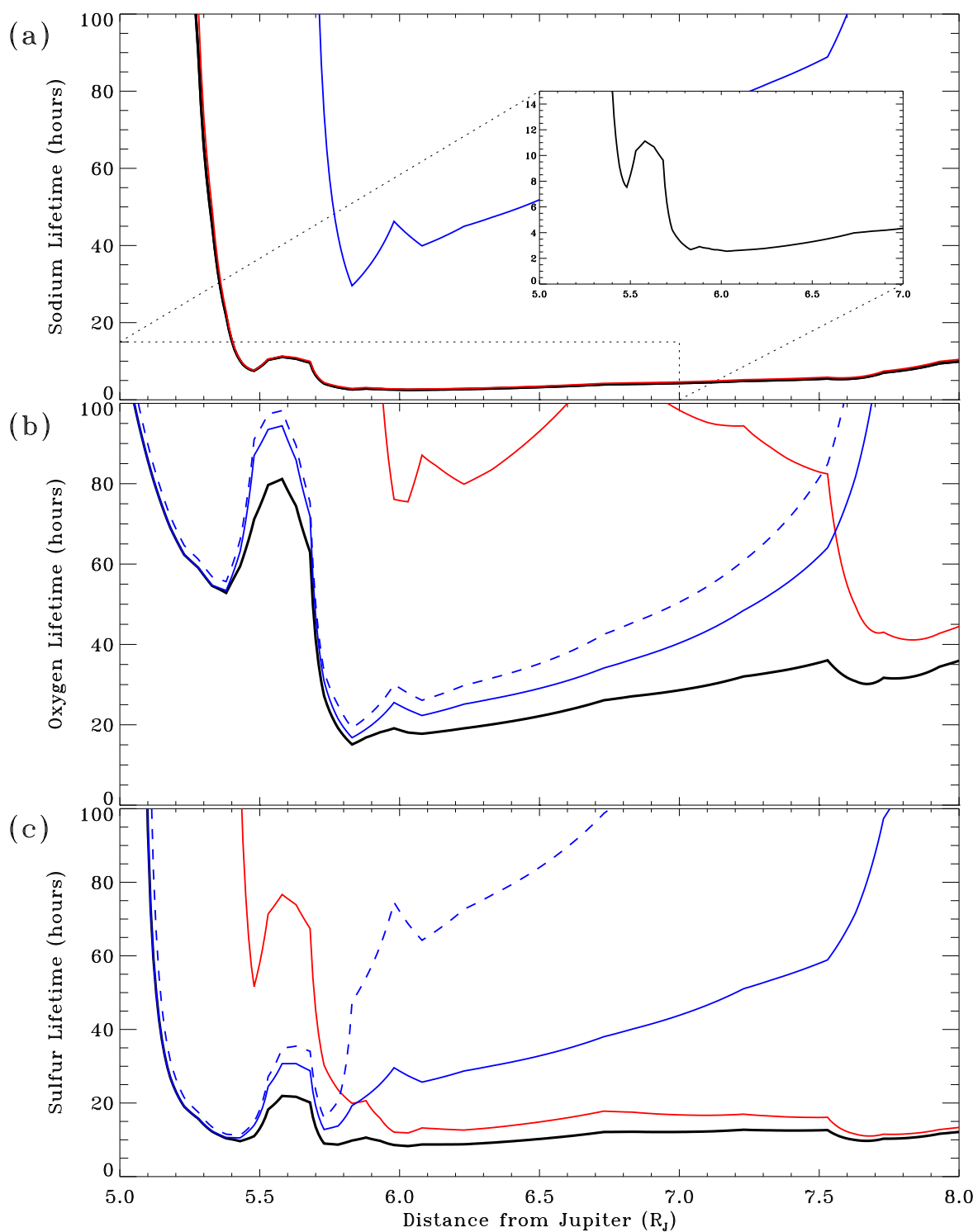


Figure 5.7 Neutral lifetimes in the inner Jovian system for (a) sodium, (b) oxygen, and (c) sulfur due to electron impact ionization and charge exchange. The black lines are the neutral lifetimes, the red lines are the lifetimes if the only active process is electron impact ionization, and the solid blue lines are the lifetimes if only charge exchange is active. The broken blue lines are the lifetimes due to the dominant charge exchange processes (as discussed in the text).

dominates due to the same considerations as the oxygen reaction above. In the ribbon region, the processes undergo a change with electron impact ionization dominating the total ionization in the warm torus. This change takes place because the density of S^+ drops off very quickly outside the ribbon, minimizing the importance of charge exchange. Additionally, the change in electron temperature from the cold torus to the warm torus corresponds to a sharp increase in the rate coefficient of sulfur electron impact ionizations (Figure 2.5) maximizing the importance of electron impact ionization. This switch from one ionization process to the other is not likely to have much impact since both the electron and ion densities vary in the same way off the centrifugal plane and have the same local time and magnetic longitude variations.

The offset and tilt of the dipole along with the east/west electric field cause constant changes in the plasma conditions near Io. Add to this the observed torus variability and it becomes clear that the neutral lifetime in Io's corona is a rapidly changing quantity. Figures 5.8 and 5.9 show the changing lifetimes for each species at Io for the basic and varying tori, respectively.

The lifetimes in the basic, longitudinally symmetric torus are much less variable than in a torus which varies with magnetic longitude. This is of course quite reasonable; Io experiences a much wider range of plasma conditions in the variable torus. One basic trend which holds true for both torus models is that the lifetimes of all species are longer at Io's eastern elongation than at Io's western elongation. This provides the most basic explanation for the observed east/west brightness asymmetry in the sodium cloud near Io (Smyth and Combi 1988b) and is investigated in Section 5.4.2.

Comparison with Smyth and Combi (1988b)

The most complete modeling study of the neutral clouds prior to this work was that of Smyth and Combi (1988b). Significant differences between that work and the current one exist in the treatment of the plasma torus and the determination of neutral lifetimes. Here I discuss several of the strengths of my treatment of these important

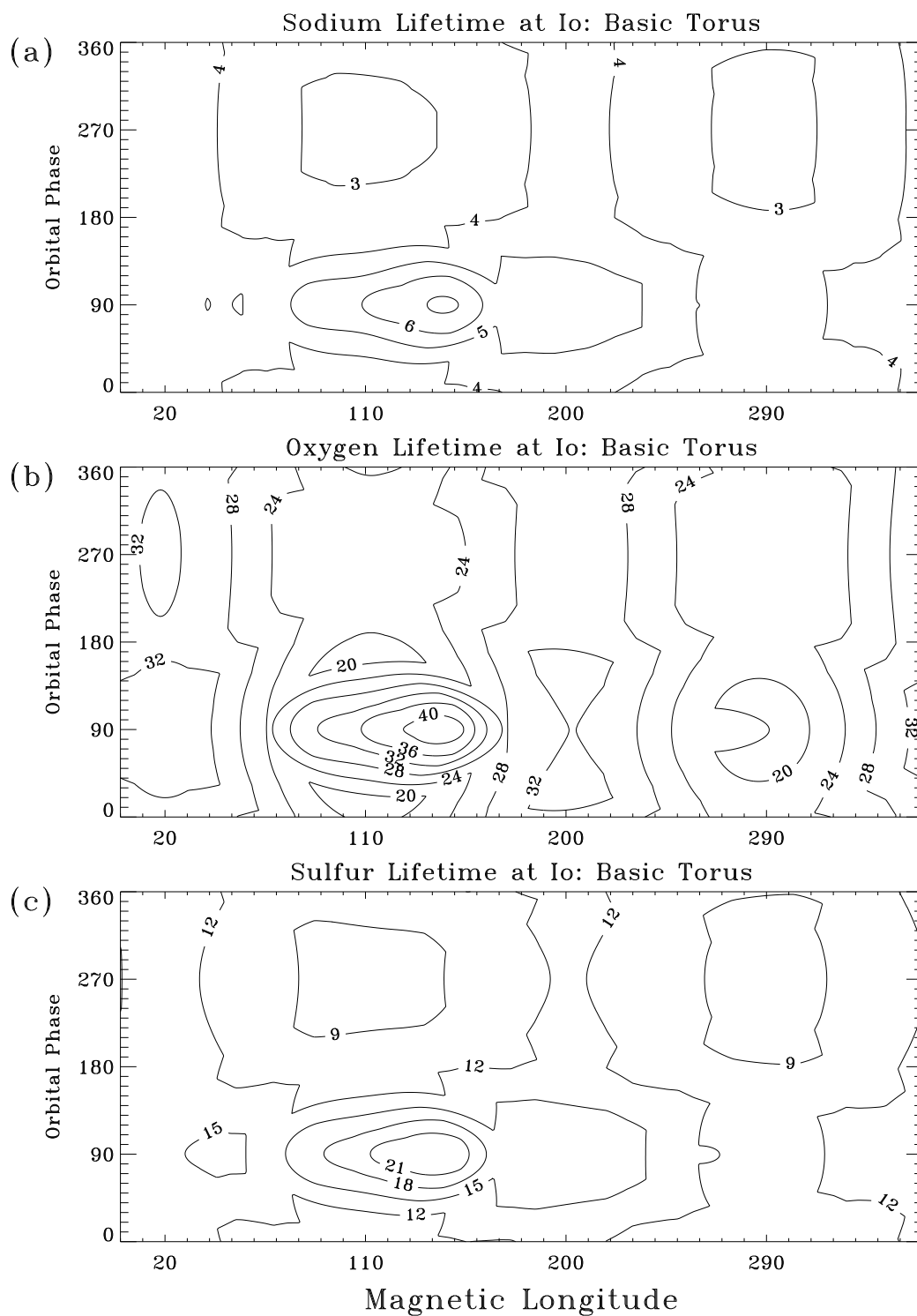


Figure 5.8 Neutral lifetimes in hours for (a) sodium, (b) oxygen, and (c) sulfur at Io as a function of Io's magnetic longitude and local time for a torus which does not vary with magnetic longitude.

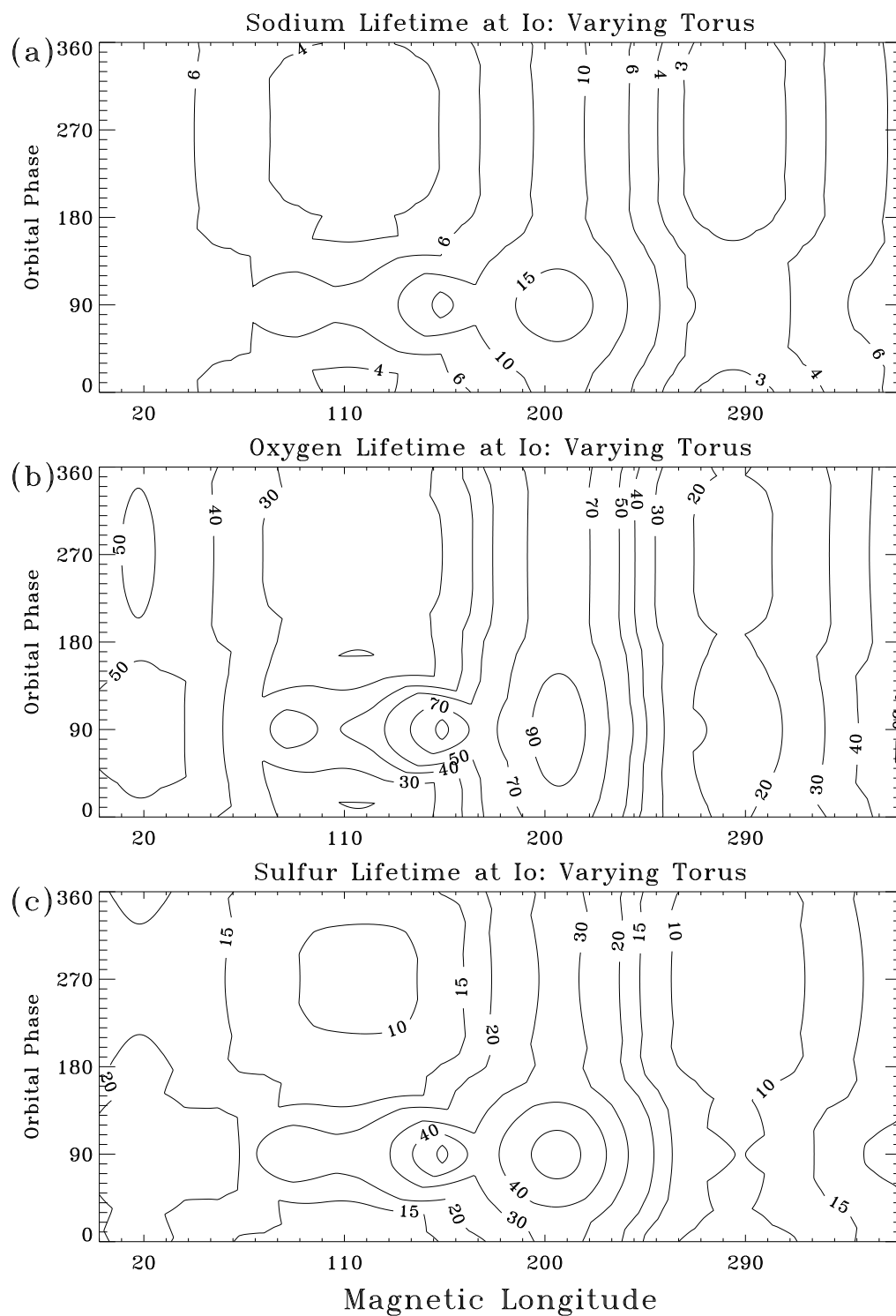


Figure 5.9 Neutral lifetimes in hours for (a) sodium, (b) oxygen, and (c) sulfur at Io as a function of Io's magnetic longitude and local time for a torus which varies with magnetic longitude.

aspects of neutral cloud modeling and contrast it with the previous work.

Two observational results published in recent years have important consequences for the neutral clouds. As discussed in Chapter 2, measurements of the electron impact cross section of neutral sodium (Johnston and Burrow 1995) imply that the sodium lifetime in the torus is ~ 1.4 times longer than previously thought. Consequently, the lifetimes predicted by Smyth and Combi (1988b) are too short and their estimates of the sodium source rate are too high.

The observations of Schneider and Trauger (1995) previously discussed point out two ways in which the plasma torus model used by Smyth and Combi is incomplete. First, the observations show that the brightness and scale height in the torus vary with magnetic longitude. This aspect of the torus was not included in their torus treatment, although these variations are not a first order effect on the shapes of the corona and neutral clouds. A more important difference, however, is the observation that the ribbon oscillates with an amplitude approximately half that of the offset of Jupiter's dipole field. This reduces the range of lifetimes that is experienced in Io's corona because a smaller region of the torus is traversed by Io.

Even taking these differences into account, I predict different sodium lifetimes at Io than Smyth and Combi (Figure 5.10). In panel (b), the lifetimes were computed using the coordinate transformation to the plasma torus described in Section 5.3.2 with the difference that the offset of the ribbon from the center of Jupiter is assumed to be $0.12 R_J$. Additionally, the lifetimes were determined using the older sodium cross sections (Zapesochnyi and Aleksakhin 1969) for consistency with the results of Smyth and Combi which are shown in panel (a). The basic morphologies of the two contour plots in Figure 5.10 are similar: the lifetime is shorter when Io is west of Jupiter than when it is east of Jupiter, and the lifetime extrema occur at approximately the same magnetic longitudes and orbital phases.

The main difference between the two lifetime calculations is the range of lifetimes

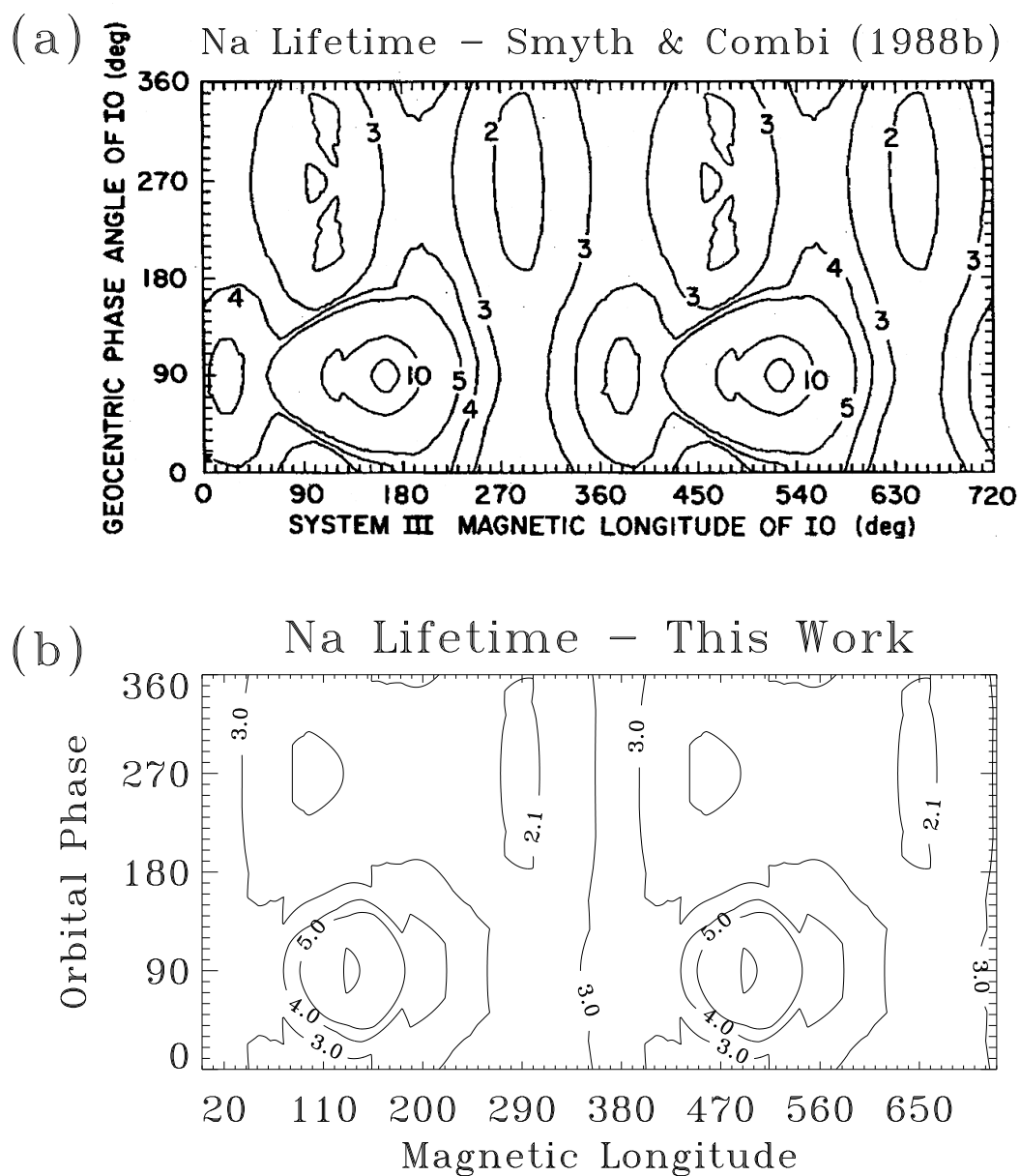


Figure 5.10 Comparison of the sodium lifetime in the corona predicted by (a) Smyth and Combi (1988b) and (b) this work using a similar torus description.

experienced at Io is smaller for my torus parameterization: I calculate a range of 2 to 11 hours compared with Smyth and Combi's range of 2 to 15 hours. This difference arises from differences in the nature of the transformation to the plasma torus coordinate system. Because the torus is aligned along the centrifugal equator, it is always parallel to Jupiter's rotational axis (Figure 5.2). Smyth and Combi, however, assume a torus that is tilted 7° relative to Io's orbital plane. My transformation assumes that the dipole is tilted relative to the plane and the torus is aligned along the centrifugal equator, but extended parallel to the rotation axis which is not perpendicular to the centrifugal equator.

5.3.4 Flux Distributions

The major physical processes which results in neutral ejection from Io's exobase is sputtering as discussed in Chapter 2. The parameter v_b is chosen to give the desired most probable velocity v_p . In the discussion in this chapter and the following chapters, the parameters v_p and α are varied to change the sputtering distribution.

In addition, a general exponential distribution is used as a means to test other speed distributions. This distribution is in the form:

$$f(v) \propto v^\beta e^{-(v/v_T)^2}, \quad v_T = \left(\frac{2kT}{m}\right)^{1/2} \quad (5.16)$$

$\beta = 3$ corresponds to a Maxwell-Boltzmann velocity distribution and $\beta = 5$ corresponds to Jeans escape.

An important consideration when discussing atmospheric escape is that escape from the exobase does not imply escape from Io. For most of the speed distributions which will be discussed in later chapters, the most probable speeds are less than Io's escape velocity from the exobase. This implies that, barring ionization in the corona, most atoms will re-impact the surface. Figure 5.11 gives the fraction of the speed distribution with velocity greater than 2.1 km s^{-1} , the escape velocity from Io's exobase.

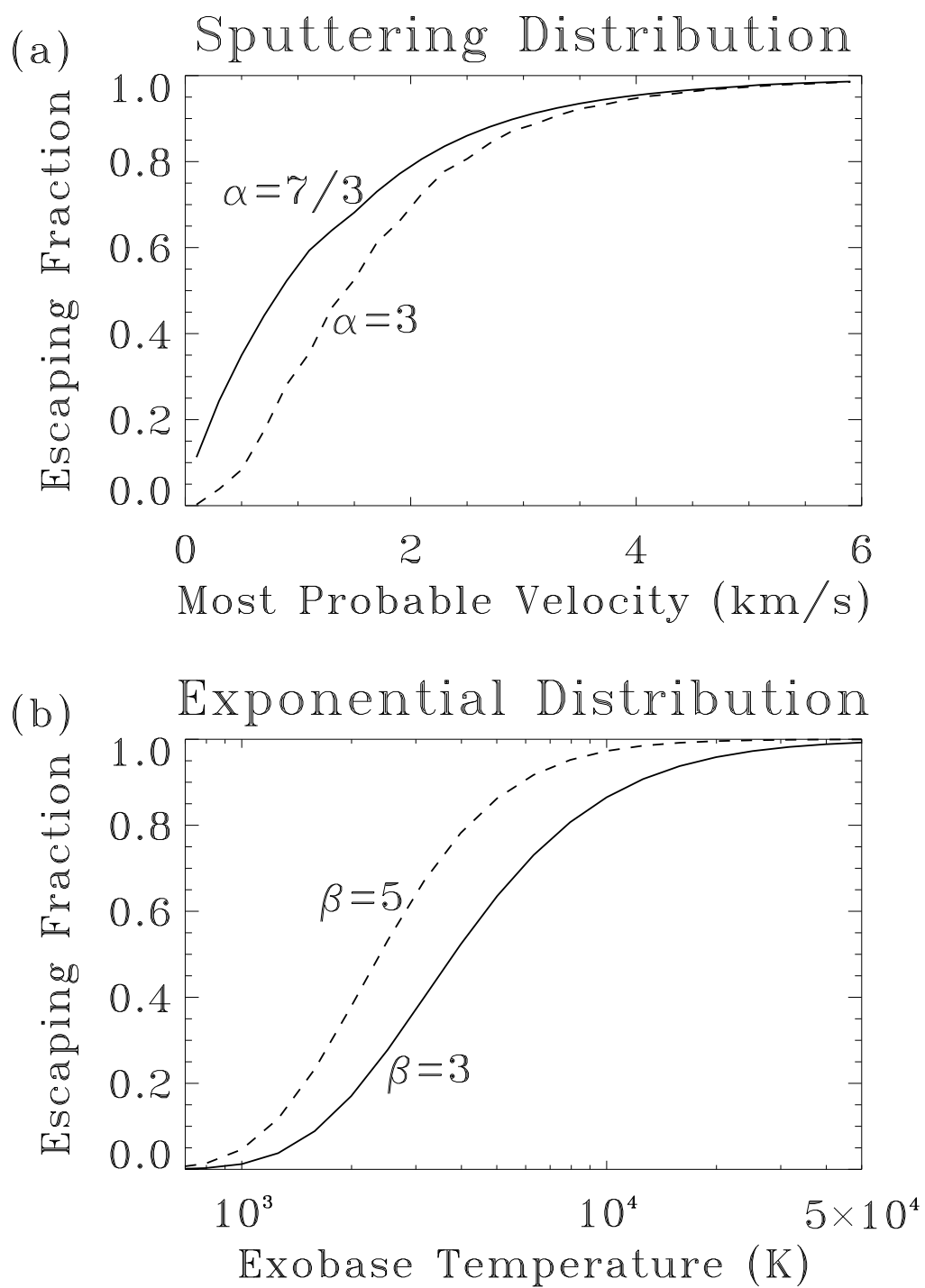


Figure 5.11 (a) Fraction of the atoms escaping from the exobase in a sputtering speed distribution with escape velocity as a function of most probable speed. (b) Same as (a) with an exponential speed distribution from the exobase.

The escaping source rate can be determined from these curves for a stated exobase source rate. For example, with a sputtering distribution with $\alpha = 3$ and $v_p = 0.7 \text{ km s}^{-1}$, 20% of the ejected atoms have escape velocity. The actual percentage of these atoms that escape will depend on the neutral lifetime in the corona.

5.4 Basic Tests of the Neutral Cloud model

In this section I present several basic tests and characteristics of the neutral cloud model. I first discuss the effect of radiation pressure on the sodium agreeing with Smyth and Combi (1988b) who concluded that the effect is small compared to other factors which affect the changing cloud morphology and is not important for defining the large scale sodium cloud morphology. I also use the model to reproduce two previously observed asymmetries in the sodium cloud: the east/west brightness asymmetry (Bergstralh et al. 1975, 1977) and the north/south brightness asymmetry (Trafton and Macy 1975).

5.4.1 Effect of Radiation Pressure

Previous modelers (Smyth 1979, 1983) have determined that the effects of radiation pressure result in an asymmetry between Io's brightness at eastern and western elongation qualitatively similar to that observed by Bergstralh et al. (1975, 1977). Since then, Smyth and Combi (1988b) showed that radiation pressure is a second order effect; the effect of the plasma torus on the east/west asymmetry is more important than radiation pressure. Figure 5.12 demonstrates the effect of radiation pressure on the extended cloud and the corona. In both the large field of view showing the inner Jovian system and the smaller views focusing on Io's corona, changes in the streamlines point to perturbations caused by incident solar photons. However, this effect would be hard to observe due to several considerations. In the corona (Figure 5.12(b)-(c)), radiation pressure "pushes" the corona slightly away from the sun: streamlines of atoms ejected

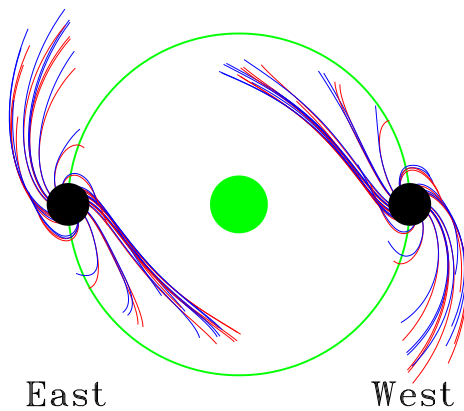
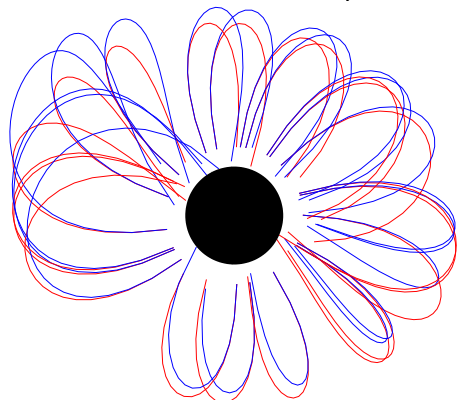
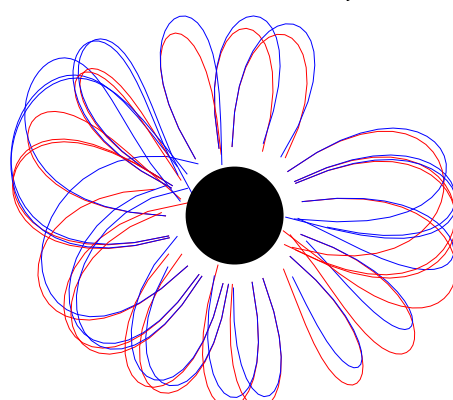
(a) Sodium Cloud, $v=3$ km/s(b) Corona, East
 $v=1.75$ km/s(c) Corona, West
 $v=1.75$ km/s

Figure 5.12 Effect of radiation pressure on neutral sodium atoms in the cloud and corona. The top panel shows twenty hours streamlines of sodium ejected from Io at eastern and western elongation with a velocity of 3 km s^{-1} . The red streamlines show the motion of sodium when radiation pressure is not included; blue streamlines include radiation pressure. The bottom panels show the corona at eastern and western elongation for particles ejected radially with velocity $=1.75 \text{ km s}^{-1}$

toward the sun are slightly compressed and those of atoms ejected away from the sun are slightly elongated. However, there is no east/west effects, so the column density in the corona along the line of sight would not change. In the cloud (Figure 5.12(a)), the effects of ionization by the torus dominate over changes in the trajectories of neutrals (see Chapter 7). The time scale for observable changes due to radiation pressure is greater than the lifetime of the sodium atoms.

5.4.2 Testing the model: East/West Sodium Brightness Asymmetry

In order to demonstrate that the current model can describe the earliest observations of the sodium cloud, I present modeled examples of two asymmetries observed in the sodium emission. The first is the east/west brightness asymmetry reported by Bergstrahl et al. (1977). This study found that the sodium cloud is $\sim 25\%$ brighter at eastern elongation than at western elongation. This difference is not due to radial velocity differences since at elongation the radial velocities are equal in magnitude. The study did correct for Jupiter's radial velocity relative to the sun.

Smyth and Combi (1988b) looked at the effects on sodium lifetime of the Io plasma torus and the east/west electric field which shifts the torus dawn-ward. As can be seen in Figures 5.8 and 5.9, the lifetime of sodium is longer near eastern elongation than western elongation. Since less sodium is ionized east of Jupiter, the density, and subsequently the brightness, is greater. This is demonstrated in Figure 5.13 which shows modeled examples of the east/west asymmetry. The top panel shows the sodium brightness as a function of orbital phase modeled for a single sputtering distribution. The dominant factor on the shape of this curve is the changing value of γ and is discussed in greater detail in Chapter 7. When local time variations in the torus caused by the east/west electric field are not taken into account, the ratio of brightness at $\phi = 90^\circ$ to the brightness at $\phi = 270^\circ$ is ~ 1 (a small deviation from unity results from the slight asymmetry in the D₂ Fraunhofer line). In Figure 5.13, this ratio is ~ 1.22 and

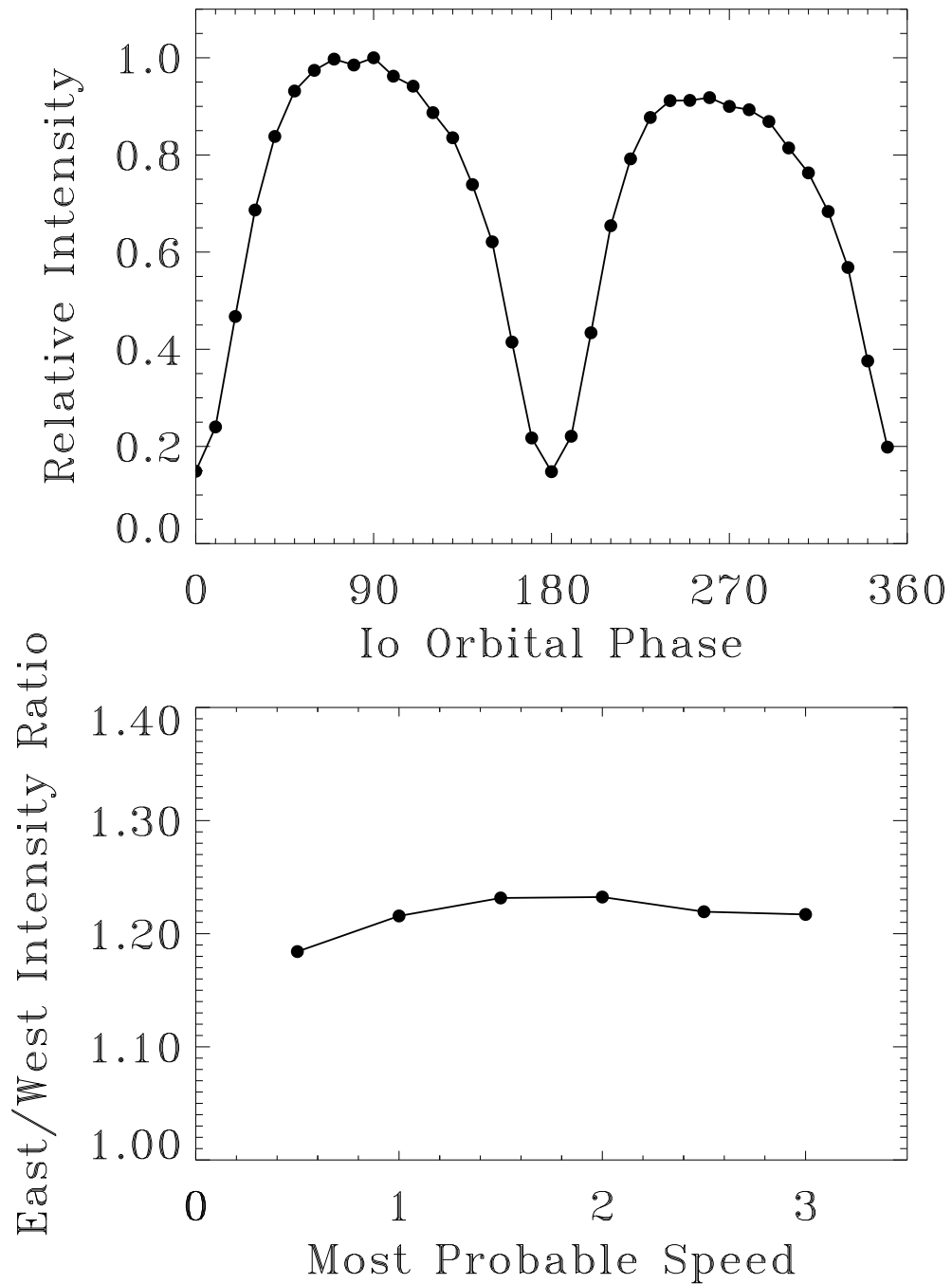


Figure 5.13 Demonstration that the current model reproduces the observed east/west brightness asymmetry in the sodium cloud. (a) The top panel shows the brightness of the sodium cloud as a function of orbital phase for a sputtering distribution with $\alpha = 3$ and $v_p = 3.0 \text{ km s}^{-1}$. (b) Modeled east/west brightness ratio as a function of the most probable speed of the sputtering distribution.

does not vary greatly with most probable speed of the sputtering distribution. The only difference is that the lifetime of sodium near Io is longer on Jupiter's dawn side than on the dusk side so sodium in the corona close to Io is not lost as quickly. The effect of the east/west electric field on the corona is discussed further in Chapter 6.

5.4.3 Testing the model: North/South Sodium Brightness Asymmetry

A second type of asymmetry was discovered in the sodium cloud at about the same time as the first. This is an asymmetry in the spatial distribution of the sodium near Io and is related to the interaction of the neutrals with the plasma torus. Spectra taken by Trafton and Macy (1975) 7.5", 15", and 30" north and south of Io show a correlation between north/south brightness ratio and Io's magnetic latitude. When Io is south of the magnetic equator, the cloud is brighter south of Io than north; similarly, when the cloud north of Io is brighter when Io is north of the magnetic equator. This result was confirmed by Trafton (1977); Trafton and Macy (1977) and Murcay and Goody (1978), the latter of whom examined images of the sodium cloud to detect this asymmetry.

An explanation for this asymmetry came with the discovery of the plasma torus: the neutral lifetime is shorter on the side of Io closer to the centrifugal equator, so the sodium intensity on that side is less (Trafton 1980). This hypothesis can be tested by using the neutral cloud model (Figure 5.14) to simulate images of the sodium cloud at a range of magnetic longitudes. The quantity $(I_N - I_S)/(I_N + I_S)$ was suggested by Murcay and Goody (1978) as a way of removing any calibration differences between their data and Trafton's data. Fits to the two data sets (computed by Murcay and Goody (1978)) are shown over model calculations of the asymmetry 15" north and south of Io. As can be seen, the model successfully predicts a north/south asymmetry that is qualitatively similar to that observed.

The 1980 paper by Trafton suggested that the plasma torus is the source of the

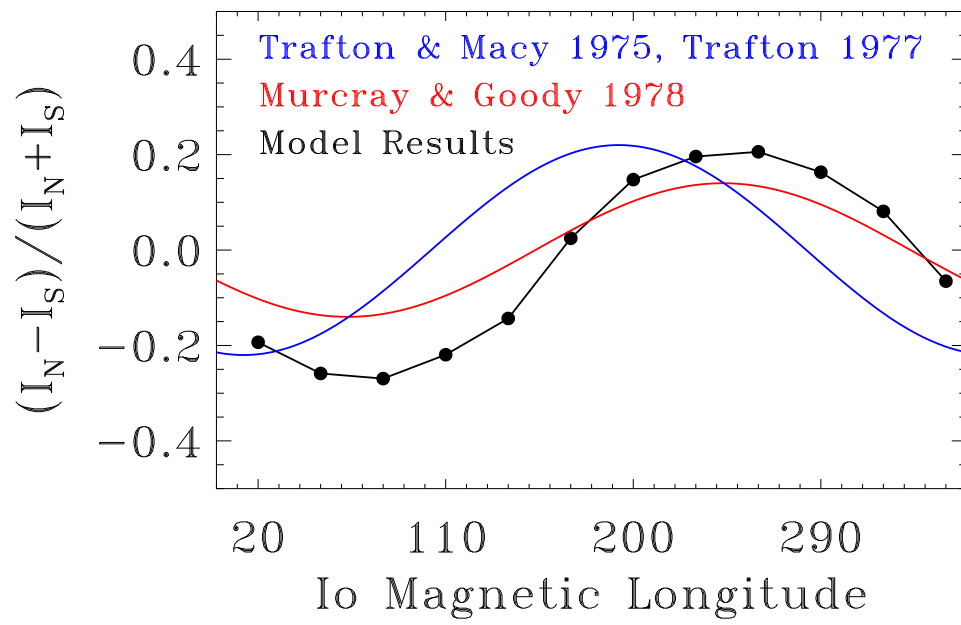


Figure 5.14 Demonstration of the north/south asymmetry in the sodium cloud observed by Trafton and Macy (1975).

north/south asymmetry, but this is the first modeling effort which attempts to explain these observations. There has been comparatively little interest in the north/south sodium brightness ratio, although it is a potential measure of the torus scale height. A comparison of the sodium densities at two points on opposite sides of Io indicates a difference in the neutral lifetimes and the electron densities, which can lead to the scale height in the torus.

5.5 Summary

A model has been developed to study Io's corona and extended neutral clouds. It is an extension of the model of Wilson and Schneider (1999) who have used it to study solar system sodium in all its glory including Io's fast sodium features (the directional feature and molecular ion stream), the extended sodium disk around Jupiter, and the lunar sodium tail. The model calculates the paths of neutral atoms under the influence of gravity and radiation pressure from Io's exobase to their loss by electron-impact ionization, charge exchange, or collision with Io or Jupiter.

The main contributions I have made to this model are the treatment of the Io plasma torus and the calculation of neutral lifetimes. Using observations of the plasma torus (Bagenal 1994; Schneider and Trauger 1995; Brown 1994), I have parameterized several features of the motions and variability the torus is observed to exhibit. Jupiter's dipole axis is tilted relative to its rotational axis; the plasma torus lies along the centrifugal equator, but is oriented parallel to the rotational axis. The dipole offset produces an oscillation of the torus relative to Jupiter: the ribbon is observed to move back and forth with an amplitude of $0.6 R_J$. An additional effect on the position of the torus is caused by the dawn to dusk electric field across the Jovian system. This electric field perturbs the orbits of torus ions such that the entire torus is shifted dawnward. One observational consequence of this shift is that the ribbon feature in the torus appears closer to Jupiter at the western ansa than the eastern ansa.

Observations of the torus have detected variations in the torus intensity as function of both local time and magnetic longitude. The local time variations are a consequence of the east/west electric field Barbosa and Kivelson (1983); Ip and Goertz (1983). The origin of the magnetic longitude variations is not understood, but the observations suggest that the flux tube content along field lines remain constant (Schneider et al. 1997) which simplifies the problem of parameterizing the plasma properties.

I have developed a method for determining the local plasma densities and temperatures for each packet in the model simulations as a function of its location relative to Jupiter and magnetic longitude. The description of the torus includes the effects of the offset tilted dipole, the east/west electric field, and the observed System-III variability. The nominal densities and temperatures of the plasma that are used are the measurements from the Voyager flybys of Jupiter determined by Bagenal (1994). The magnitude of each of deviation from the average state of the torus is based on ground-based observations of the torus (Schneider and Trauger 1995; Brown 1994).

By using the empirical torus parameterization, I have determined the lifetimes of neutral sodium, oxygen, and sulfur in the inner-Jovian system and compared the relative importance of electron-impact ionization and charge exchange for each species. I also compared the current calculation of the sodium lifetime with a previous result by Smyth and Combi (1988b). Although the main differences between the two lifetime calculations result from recent measurements of the sodium electron impact cross section (Johnston and Burrow 1995) and the observations that the amplitude of torus oscillation is only half the magnitude of the dipole offset, Smyth and Combi (1988b) used a torus that is perpendicular to the centrifugal equator rather than the Jupiter's orbital plane.

The chapter concluded with several applications of the model to Io's neutral clouds. First, I demonstrated the effects of radiation pressure previously described by Smyth (1983) and concluded that they are insignificant compared with the larger effects of ionization by the plasma torus. Next, I simulated the east/west brightness asymmetry

measured by Bergstralh et al. (1975, 1977) and confirmed the model results of Smyth and Combi (1988b) which determined that the asymmetry is a result of the effect of the east/west electric field on neutral lifetimes. Lastly, I demonstrated that the magnetic longitude dependence on the ratio of sodium brightness north of Io to the brightness south of Io (Trafton and Macy 1975) is a consequence of non-uniform ionization by the plasma torus as predicted by Trafton (1980).

Chapter 6

Modeling Io's Corona

6.1 Introduction

In Chapter 3 I presented mutual event observations of Io's sodium corona. From these observations I determined the average state of the corona which is formed from the escape of Io's surface atmosphere. It also provides the source for the extended neutral clouds and the plasma torus. Therefore the corona provides a unique link between the the atmosphere and the large scale escape features. To understand the formation of the neutral clouds and the plasma torus it is essential that the processes which create and shape the corona are understood. The key to understanding the relationship between the loss from Io's atmosphere and the creation of the plasma torus is found in the corona. The discovery of a previously undetected asymmetry between the inner and outer hemispheres of the corona points to previously unknown processes at work close to Io's surface which affect the rate at which Io's atmosphere is stripped away and highlights the need for continued study of this region.

The previous chapter described the neutral cloud model which I have helped to develop so that the processes molding the corona can be determined and their implications for Io's atmosphere understood. This chapter applies the model from Chapter 5 to understanding the observations from Chapter 3. I also discuss recent *Hubble Space Telescope* observations of Io's oxygen corona (Roesler et al. 1999; Wolven et al. 2001) which point out several key differences between sodium and oxygen within $6 R_{Io}$ of Io.

I use the neutral cloud model to interpret observational differences between the oxygen and sodium coronae.

The goals for this chapter are:

- (1) Determine the characteristics of the flux distribution of the neutrals escaping from Io's exobase.
- (2) Understand how deviation from the average plasma conditions affects the shape of the corona.
- (3) Study the implications of the observed corona asymmetry on loss from Io's exobase.
- (4) Compare the measured shapes of the oxygen and sodium coronae and determine implications for the sources of each.

In Section 6.2 I discuss the application of the model to the corona and describe the method of comparing the model to observations. Section 6.3 contains the model analysis of flux distributions from Io's exobase which can simulate the average observed corona and discuss how deviation from these flux distributions change the coronal shape. I also describe how the east/west electric field across the inner Jovian system creates the observed east/west sodium brightness asymmetry. The section concludes with an analysis of the effects of uniform variations affecting the entire torus and the observed periodic variations. The implications of the column density asymmetry between Io's inner and outer hemispheres on the spatial distribution of the loss from Io's exobase is described in Section 6.4. I conclude the chapter with a description oxygen corona based on the *HST* observations and the differences between the shapes of the sodium and oxygen coronae, discussing the implications of these differences on the loss from the exobase.

These studies can be combined with future observations of coronal variability to

determine the limits of variability in the torus and to probe the interaction between Io and the surrounding plasma. The coronal asymmetries, variations in the shape of the corona, and the differences between Io’s sodium and oxygen coronae are indicative of spatial and temporal anisotropies in the plasma torus and the loss of neutrals from Io’s exobase. A major focus of this chapter is understanding what produces variations in the shape of the corona allowing interpretation of future observations of these changes.

6.2 Description and Analysis of Model Runs

The mutual event observations discussed in Chapter 3 show that the column density profile in the corona can be described as a power law in the form:

$$N = N_0 b^{-s} \tag{6.1}$$

where b is the impact parameter in Io radii, N_0 is the column density extended to Io’s surface, and s is the power law index. On log-log axes, this relation is linear with y-intercept = $\log(N_0)$ and slope equal to $(-s)$. I will here use the terms “slope” and “power law index” interchangeably to refer to the quantity $(-s)$. When the slope is large, the corona is “steep;” a small slope implies a “shallow” corona.

For the corona models discussed, packets were evenly distributed over Io’s exobase (assumed to be $1.4 R_{Io}$) and ejected isotropically from each point on the sphere surrounding Io with a specified flux speed distribution. The total time of each simulation was 20 hours with packets released at random times throughout the simulation. This duration was chosen such that all neutrals ejected at the beginning of the interval are lost (either by escaping Io, hitting Io’s surface, or ionization) by the end of the simulation. Model images of column density were produced and the radial column density profiles were computed from the positions and un-ionized fractions of the packets remaining at the end of the simulation (Figure 6.1). Power laws functions were fit to these profiles as functions of impact parameter to determine the slopes of the coronae produced with the

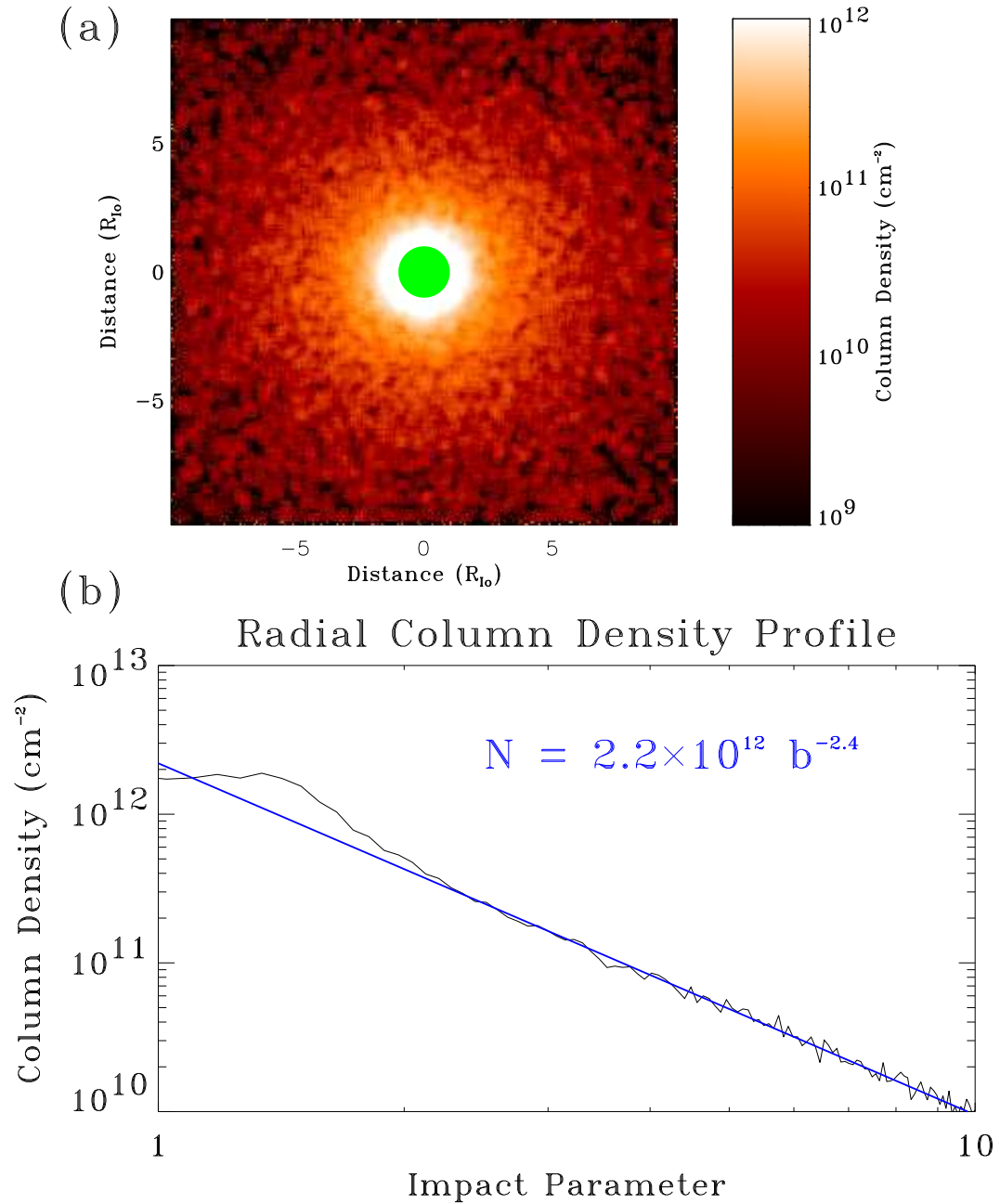


Figure 6.1 (a) Model image of the corona. Scale is logarithmic as indicated by the color scale bar. The image has been scaled such that the column density $1 R_{\text{Io}}$ from the center is consistent with the mutual event observations (Equation 3.5). The green circle of radius $1 R_{\text{Io}}$ represents Io's disk. (b) Radially averaged column density profile of the model image in (a) with best fit power law over-plotted in blue. Note that because the velocity distribution is truncated below 0.75 km s^{-1} , the radial profile does not accurately reflect the corona within $\sim 2 R_{\text{Io}}$.

specified parameters. To save computation time and memory, the speed distributions were truncated below $v = 0.75 \text{ km s}^{-1}$ since packets below that speed do not make it far enough into the corona to affect the column density and could safely be ignored. Outside $\sim 6 R_{\text{Io}}$, Jupiter's gravitational pull begins to dominate over Io's. To avoid artifacts associated with the inner and outer edges, the power laws were fit to the radial profiles between $b=2 R_{\text{Io}}$ and $6 R_{\text{Io}}$, which also corresponds to the regions with the highest quality mutual event data.

6.3 Understanding the Shape of the Corona

The mutual events discussed in Chapter 3 describe a radially averaged corona with the shape:

$$N(b) = 2.2_{-0.7}^{+1.4} \times 10^{12} b^{-2.34_{-0.34}^{+0.27}} \text{ cm}^{-2} \quad (6.2)$$

If sodium escaped freely without ionization or the influence of Io's gravity, the column density in the corona would be proportional to b^{-1} . The significantly faster rate at which the observed corona column density decreases is due to the combined effects of Io's gravity, which slows the escaping atoms, and ionization in the corona. In this section I discuss how this average corona can be created when the velocity distribution of sodium escaping from the exobase can be described by either a sputtering or exponential distribution. I also examine how departure from these parameters affects the corona and look for changes in its shape with orbital phase and magnetic longitude.

6.3.1 The Average Observed Corona

It is possible to adequately model the corona using a range of source distributions, even when using the basic torus model that does not include any System-III variability. Figures 6.2 and 6.3 show how the shape of the corona and the source rate vary with changes in the source flux distribution. The average state of the corona can be modeled using either the sputtering distribution (Equation 2.12) or the exponential distribution

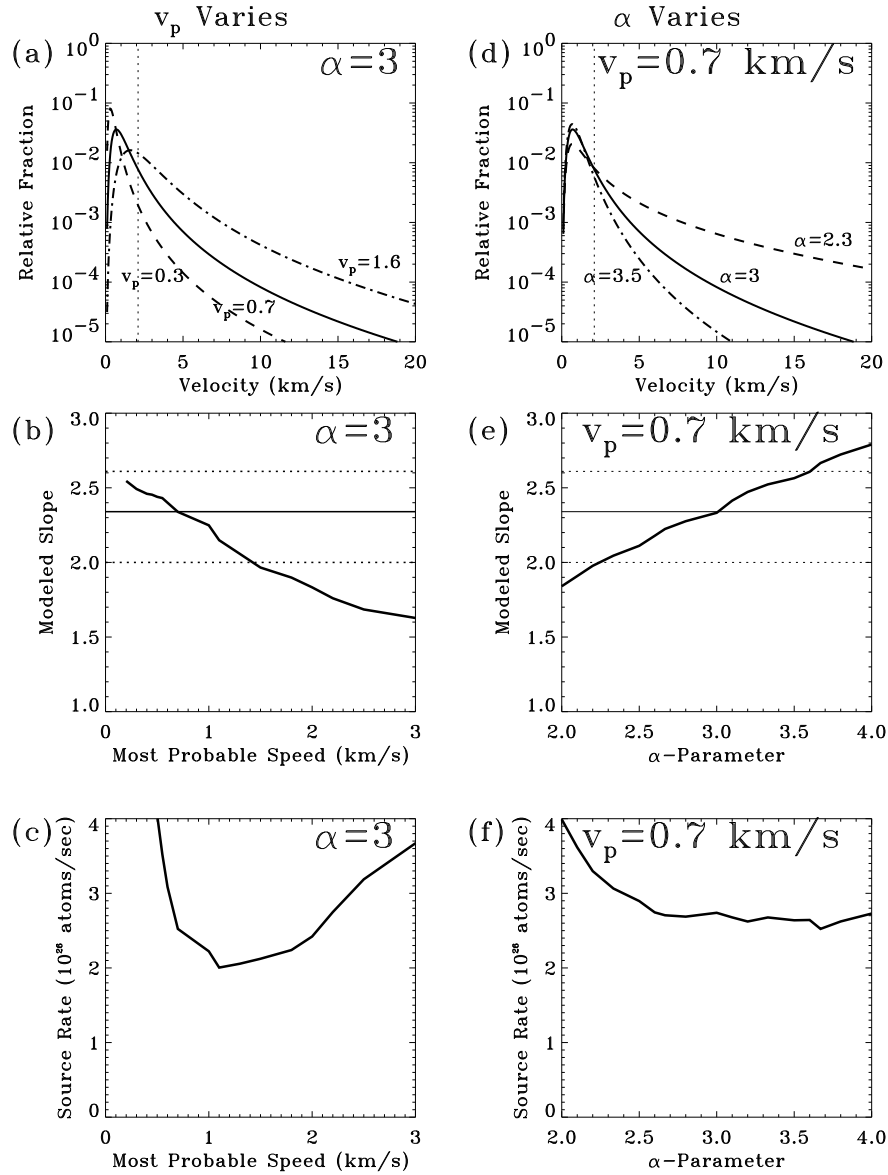


Figure 6.2 Radially averaged models of the observed average sodium corona. (a) Flux distributions at the speeds required to approximate the variability in the corona for the true sputtering case. The dotted line at $v=2.1$ km s $^{-1}$ indicates escape velocity from Io's exobase. (b) Modeled corona slope using a pure sputtering corona ($\alpha = 3$) and varying the most probable speed of the distribution. The solid horizontal line shows the average observed slope; the broken lines show the $1-\sigma$ variation. (c) Source rate needed to match the observed (extrapolated) surface column density of 2.2×10^{12} cm $^{-2}$. (d) Sputtering distributions with the most probable speed held constant and α varied as indicated. (e) Modeled corona slope holding the most probable speed constant at 0.7 km s $^{-1}$ and varying the α -parameter. (f) Modeled source rate for models with $v_p=0.7$ km s $^{-1}$ as function of α .

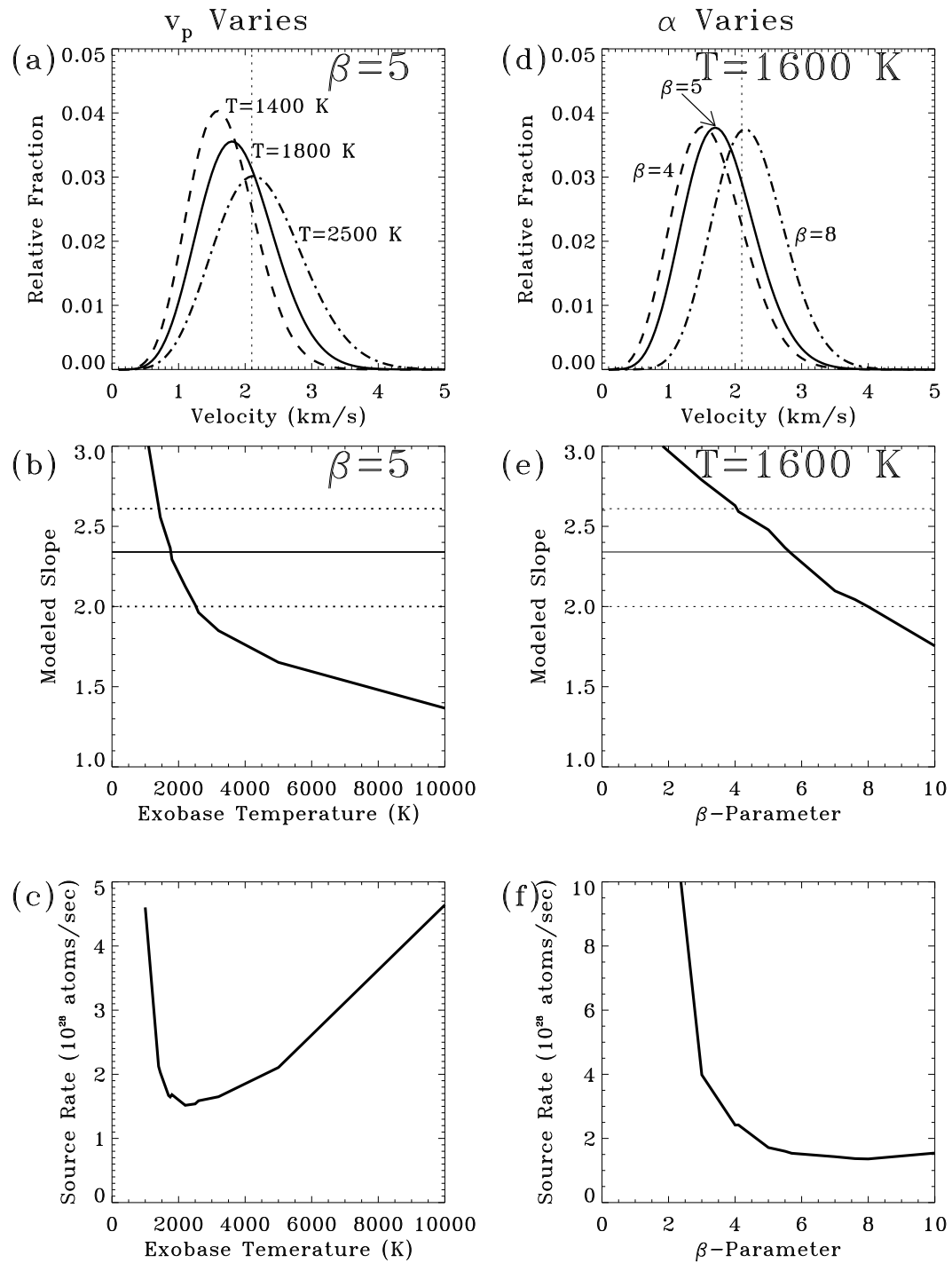


Figure 6.3 Same as Figure 6.2 using a exponential source distribution. In the left panels, the exobase temperature is varied while holding $\beta = 5$ constant, corresponding to a Maxwell-Boltzmann distribution for the escaping sodium. In the right panels, the temperature is held constant while the β -parameter varies.

(Equation 5.16), as discussed below. The torus model used to determine the sodium lifetime for the models in Figures 6.2 and 6.3 is the Basic Torus which does not vary with magnetic longitude. The effects of departures from this torus and of magnetic longitude variations in the torus are examined in the following sections.

The sputtering distribution, as can be seen in Figure 6.2, can create a corona similar to the average corona for a wide variety of parameter choices. The best fit for a pure sputtering distribution ($\alpha = 3$) is with a most probable velocity $v_p \sim 0.7 \text{ km s}^{-1}$ and a source rate of $2.7 \times 10^{26} \text{ atoms s}^{-1}$, somewhat higher than previous results. The slope in the actual corona was found to vary between 2.0 and 2.6. As the most probable speed decreases, the corona becomes steeper. Using the pure sputtering distribution and the average torus conditions, the most probable speed would need to be less than 0.3 km s^{-1} for the corona to drop off as quickly as $b^{-2.6}$. The lower bound of the slope can be achieved by increasing the most probable speed to 1.6 km s^{-1} .

The importance of higher speed sodium on the shape of the corona is examined by varying the α -parameter while holding the most probable speed constant. Decreasing the value of α increases the relative amount of sodium with escape velocity. Figure 6.2(b) shows that varying α between 2.3 and 3.5 captures the full range of variability in the observed slope of the corona. However, these values of α do not actually have any physical significance and should only be viewed as an example of how the speed distribution needs to vary to model the corona, and not as an exact description of escape from Io's exobase.

The right panels of Figure 6.2 show the source rate required to match the observed value of $N_0 = 2.2 \times 10^{12} \text{ cm}^{-2}$ in Equation 6.2, which is the column density of sodium extrapolated to the surface assuming the power law in the corona extends all the way down. The value of N_0 is directly proportional to the source rate so variability in this value unaccompanied by variation in the slope can be interpreted as variations in the rate of neutral sodium atoms escaping from the exobase.

	$v=0.5 \text{ km s}^{-1}$ $\alpha = 7/3$	$v=0.7 \text{ km s}^{-1}$ $\alpha = 3$	$v=1.0 \text{ km s}^{-1}$ $\alpha = 3$
Old σ	$8.1 \times 10^{11} b^{-2.3}$	$1.2 \times 10^{12} b^{-2.7}$	$1.4 \times 10^{12} b^{-2.5}$
Radial Ejection	$2.0 \times 10^{12} b^{-2.5}$		$1.5 \times 10^{12} b^{-2.5}$
New σ	$7.7 \times 10^{11} b^{-2.1}$	$1.2 \times 10^{12} b^{-2.5}$	$1.5 \times 10^{12} b^{-2.3}$
Radial Ejection			
Old σ	$5.6 \times 10^{11} b^{-2.1}$	$8.5 \times 10^{11} b^{-2.6}$	$1.0 \times 10^{12} b^{-2.3}$
Isotropic Ejection			
New σ	$6.3 \times 10^{11} b^{-2.0}$	$8.2 \times 10^{11} b^{-2.3}$	$1.1 \times 10^{12} b^{-2.2}$
Isotropic Ejection			

Table 6.1 Comparison of corona created with different cross sections and different ejection direction distributions. The corona profiles modeled by Smyth and Combi (1988b) are shown in boxes where available. Power law results are the average corona profile assuming a total exobase source rate of 10^{26} atoms s^{-1} .

This average result is similar to that of Smyth and Combi (1997) who determined that an exobase source rate of 1.3×10^{26} atoms s^{-1} for the pure sputtering case with a most probable speed of 1.0 km s^{-1} . These authors preferred $\alpha = 7/3$ because it produced more fast sodium that they believed was needed to explain Io's fast sodium features. Using this value, they found a most probable speed of 0.5 km s^{-1} and exobase source rate of 1.7×10^{26} atoms s^{-1} for this distribution. There are several differences between the current work and the previous results which may help to explain the different results. First, as discussed in Chapter 5, this model uses different sodium electron impact cross sections and a different parameterization of the plasma torus. Second, Smyth and Combi used the mutual event results of Schneider et al. (1991a) which described a somewhat steeper corona with an average slope of ~ 2.5 . Lastly, they assumed that the sodium was all ejected radially from Io's exobase while this work uses an isotropic directional distribution.

Table 6.1 contains a comparison of the different coronae created with the two published cross sections and the corona created with isotropic or radial ejection. Several basic conclusions can be drawn from this the corona profiles listed. First, the old cross section, which predicts a shorter sodium lifetime, results in a steeper corona. This is

because more sodium atoms make it to the outer reaches of the corona when the lifetime is longer, creating a shallow, more extended corona. The dynamics of the atoms' motions are the same, but the change in lifetime changes the shape of the corona. Second, isotropic ejection creates a shallower corona than radial ejection. Isotropic ejection has two effects on the distribution of neutral atoms. First, atoms ejected tangentially to the surface with velocities near the escape speed stay in the corona longer than atoms ejected perpendicular to the surface, since these atoms are more likely to orbit Io before impacting the surface or being ionized. Second, atoms ejected from any point on the exobase can contribute to any part of the corona. This reduces the effects of variations in the spatial distribution of the sputtering. The actual directional distribution is most likely some intermediate between purely radial and purely isotropic ejection. Neutrals can be sputtered in all directions, but the distribution is more concentrated radially outward than tangential to the surface.

The average corona is also well matched using the exponential distribution with $\beta = 5$, corresponding to a Maxwell-Boltzmann speed distribution, with a temperature of ~ 1800 K and an exobase escape rate of 1.8×10^{28} atoms sec^{-1} , which is about two orders of magnitude greater than the estimate for the source rate of sputtered sodium. This is due to the fact that there is very little high speed sodium in this distribution and therefore the source rate must be extremely high to populate the outer regions of the corona. The observed variability in the corona is modeled by varying the temperature between 1400 K and 2500 K. These temperatures are consistent with both the measurements of the coronal temperature (~ 1600 K from Chapter 3) and model estimates for the temperature of the exobase ranging from 200 K to 3000 K (Wong and Smyth 2000).

I have also looked at how changing the shape of the exponential distribution affects the shape of the corona by changing the β -parameter while keeping the temperature constant. For a 1600 K exobase, the observed variation can result from varying

β between 4 and 8. As for the similar exercise discussed above for the sputtering distribution, this does not necessarily have any physical significance but indicates that a significant fraction of the sputtered sodium must have escape velocity to populate the outer regions of the corona.

Apart from reproducing the observed corona, it is instructive to look at how changes in the source distribution affect the shape of the corona. The general trend is that anything which increases the amount of sodium with escape velocity relative to slower, non-escaping sodium, creates a “flatter” corona which extends further from Io. Speed distributions which contain a high percentage of non-escaping sodium create coronae which stay close to Io. This tendency is explained by the fact that little sodium leaving the exobase with escape velocity is ionized before it can escape the corona. Slower sodium, even if it has sufficient velocity to make it to the outer regions of the corona, takes longer to travel that far and is more likely to be ionized and fail to contribute to the neutral component. Sodium leaving the exobase at 3 km s^{-1} takes only 0.9 hours to make it to $6 R_{\text{Io}}$, as opposed to the 2.2 hours it takes for sodium traveling at 2 km s^{-1} . Assuming an approximate lifetime of 4 hours for sodium, 80% of the faster moving sodium survives compared with 58% of the slower sodium (Figure 6.4).

Another interesting result shown in Figures 6.2(e) and 6.3(e) is that the the source rate necessary to match the observations increases for very small and very large most probable velocities. When the most probable speed of the distribution is small, a large fraction of the sodium immediately returns to Io; only the tail end of the distribution is making it into the corona. Therefore the source rate needs to be pumped up to produce the amount of sodium necessary to match the observed N_0 . Since it is only the high speed tail of the distribution which contributes to the density near the exobase, very little sodium makes it farther out into the corona and corona drops off very quickly, creating a corona with a large slope. For speed distributions with higher most probable

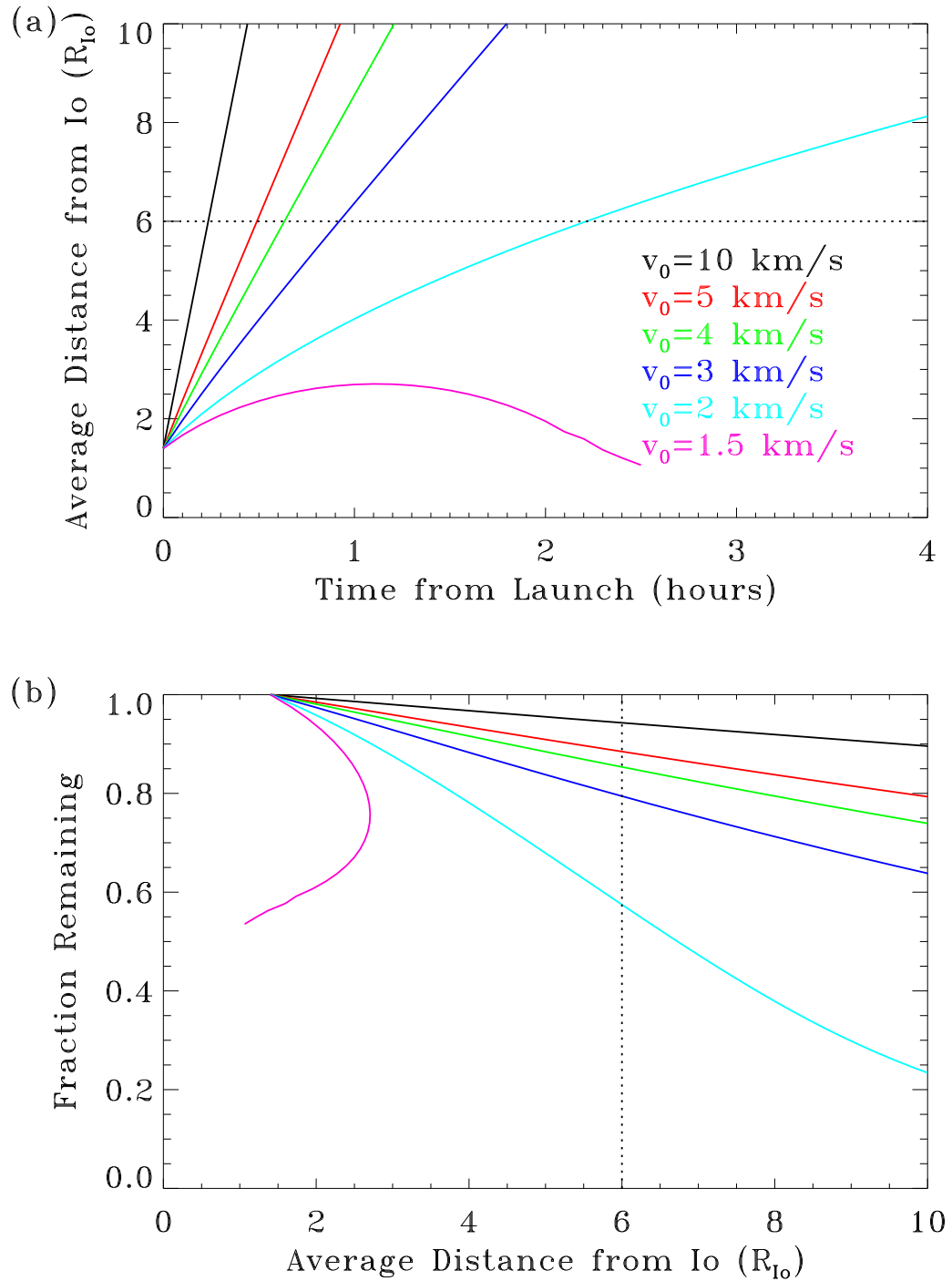


Figure 6.4 (a) Distance from Io of sodium atoms versus time since launch from the exobase. The initial velocity of the atoms is indicated. The dotted at $r=6R_{Io}$ indicates the approximate location of the Hill sphere which corresponds to the outer edge of the corona. (b) Un-ionized sodium fraction versus distance from Io for atoms with the specified initial velocity assuming a constant 4 hour lifetime.

speeds, the source rate increases because less sodium stays near the exobase: the flux through the exobase is high, decreasing the density near Io. The source rate must be increased to offset the effects of the high flux.

6.3.2 Variations in the Average Corona

Variations in the plasma environment at Io affect the lifetime of neutrals in the corona. These variations can be grouped into several categories. First, Jupiter's offset tilted dipole means that the plasma density at Io varies with a period of approximately 10 hours with the electron density being greatest when Io crosses the centrifugal equator ($\lambda_{Io} = 110^\circ$ and 290°). When Io is north or south of the torus, the electron density is lower and the sodium lifetime is greater. Since the time-span between maximum and minimum lifetimes is comparable to the amount of time a neutral sodium atom remains in the corona (~ 2 hours), variations in the corona due simply to the dipole are expected to be small.

The east/west electric field across the Jovian system results in variations with orbital phase in the plasma at Io in two ways: First, the torus is offset from the center of the dipole by an amount proportional to the strength of the electric field, meaning that Io's position relative to the cold torus, ribbon, and warm torus change with Io's orbital phase. Second, as the plasma is swept around Jupiter from west to east, it expands, decreasing the density. This is responsible for the east/west brightness asymmetry near Io (Smyth and Combi (1988b) and see below).

The last type of variability is the observed System-III variability (e.g. Schneider and Trauger (1995)). This variation is treated as variability in the ion temperature, which changes the scale height of the torus and the electron density at the centrifugal equator. This increases both the average sodium lifetime at Io and the range of lifetimes in the corona.

In this section, I explore the effects of each of these three categories of variations

on the shape of the corona using the average sputtering parameters determined above ($\alpha = 3$, $v_p = 0.7 \text{ km s}^{-1}$) as a reference point. Orbital phase effects are measured by looking at the shape of Io's corona at four points in its orbit: when Io is behind Jupiter ($\phi = 0^\circ$), at eastern elongation ($\phi = 90^\circ$), in front of Jupiter ($\phi = 180^\circ$), and at western elongation ($\phi = 270^\circ$). The modeled slope (-s) and the intercept assuming a source rate of $2.7 \times 10^{26} \text{ atoms s}^{-1}$ (N_0) are used to provide a comparison to the observed corona.

6.3.3 Building to an Offset Tilted Dipole with an East/West Electric Field

Three steps were taken to work up to the basic torus described in Chapter 5. First I looked at the corona in a torus centered on Jupiter that is not tilted relative to Jupiter's equatorial plane. The lifetime at Io was a constant 3 hours when using the Voyager torus measurements. The slope remains constant in this case with the coronal column density proportional to $b^{-2.4}$.

A more interesting case is that with Jupiter's offset, tilted dipole, which causes the torus to be inclined relative to Jupiter's equatorial plane. Figure 6.5(a)-(c) shows the effect of the dipole on the sodium lifetime and corona. The shape of the corona was computed as functions of orbital phase and magnetic longitude. The lifetime in this case is constant with orbital phase, since the time-averaged torus has cylindrical symmetry about Jupiter's rotational axis, but varies with magnetic longitude due to both the tilt and offset of the dipole. As shown in panels (b) and (c), the effect of the true dipole is small: there is no appreciable dependence on either orbital phase or magnetic longitude on the shape of the corona. This is due to a combination of factors: first, when the torus is symmetric about Jupiter, the only effect which is asymmetric with respect to Io's orbital phase is radiation pressure, which is too small in magnitude to have any measurable consequences in the corona. Second, the range of lifetimes experienced by sodium atoms is small, diminishing the importance of the changing lifetime. Lastly, the

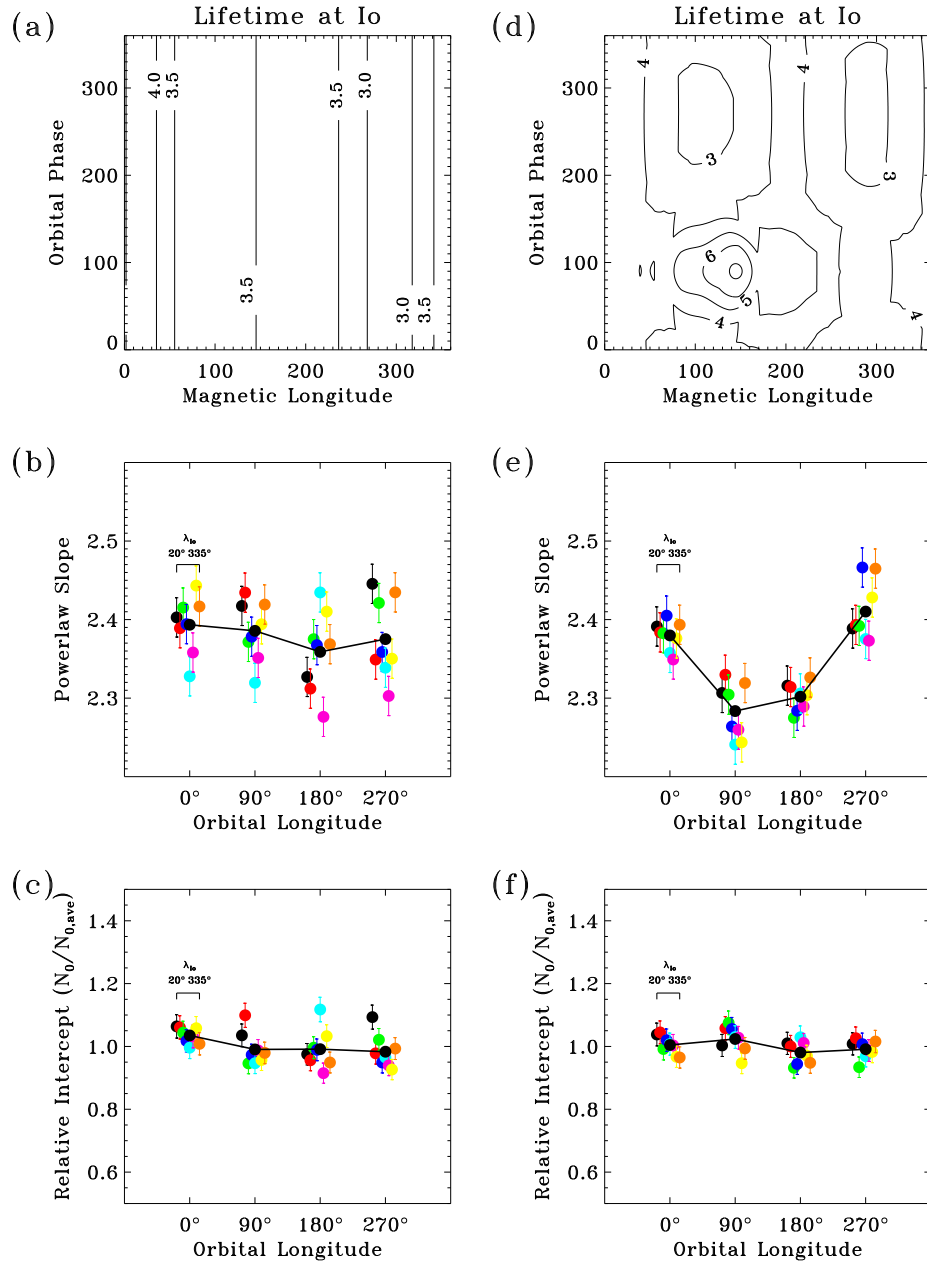


Figure 6.5 The effects of Jupiter's offset tilted dipole and the east/west electric field on the power law fit to the modeled corona. In panels (a)-(c), Jupiter's dipole is included, but the east/west electric field is turned off. In panels (d)-(f) the full offset tilted dipole with the inferred east/west electric field is used. Panels (a) and (d) show contours of the sodium lifetime at Io in hours as a function of the magnetic and orbital longitudes. Panels (b) and (e) show the best fit slope for the corona with uncertainties. Each clump of points shows models for Io at a single orbital location with the magnetic longitude increasing in each clump from left to right. Panels (c) and (f) give the modeled power law intercept relative to the average value of $N_0 = 2.2 \times 10^{12} \text{ cm}^{-2}$.

time scale for these changes is not much longer than the lifetime, so that the average state of the plasma which any individual atom is subjected to does not vary much with magnetic longitude.

The inclusion of the east/west electric field shifts the torus eastward by $0.14 R_J$ at Io's orbit. The consequences of this shift are demonstrated in Figure 6.5(d)-(f). The electric field introduces a strong orbital phase asymmetry in the sodium lifetime which varies on a time scale significantly longer than the average lifetime (40 hours compared to ~ 4 hours). Atoms ejected when Io is east of Jupiter make it farther from Io before ionization resulting in a more extended corona.

Interestingly enough, the intercept does not appear to vary significantly for this same torus implementation. This provides a demonstration of how the east/west electric field produces the local time asymmetry in the sodium cloud (Bergstralh et al. (1975, 1977) and see Section 5.4.2). As demonstrated by Smyth and Combi (1988b), the increase in sodium lifetime near eastern elongation results in increased sodium emission there compared to western elongation. These authors did not discuss how the electric field affects the shape of the corona. When the lifetime is longer, a larger fraction of the sodium sputtered from the exobase can make it to the furthest reaches of the corona before being ionized, thus decreasing the slope and increasing the total number of sodium atoms in the corona. The change in lifetime is sufficient to create the observed sodium brightness asymmetry (Figure 6.6). Without the electric field, the asymmetry disappears. In Figure 6.6, panel (a) shows the total column through the corona both with (blue squares) and without (red circles) the east/west electric field turned on. The total column was determined by creating a model column density image of the corona and totaling all the atoms in the annulus with impact parameter is between 2 and $6 R_{Io}$ and averaged for all magnetic longitudes. The column density without the electric field remains constant with orbital phase; with the electric field, the column density is maximized at eastern elongation. The right panel shows the intensity in the

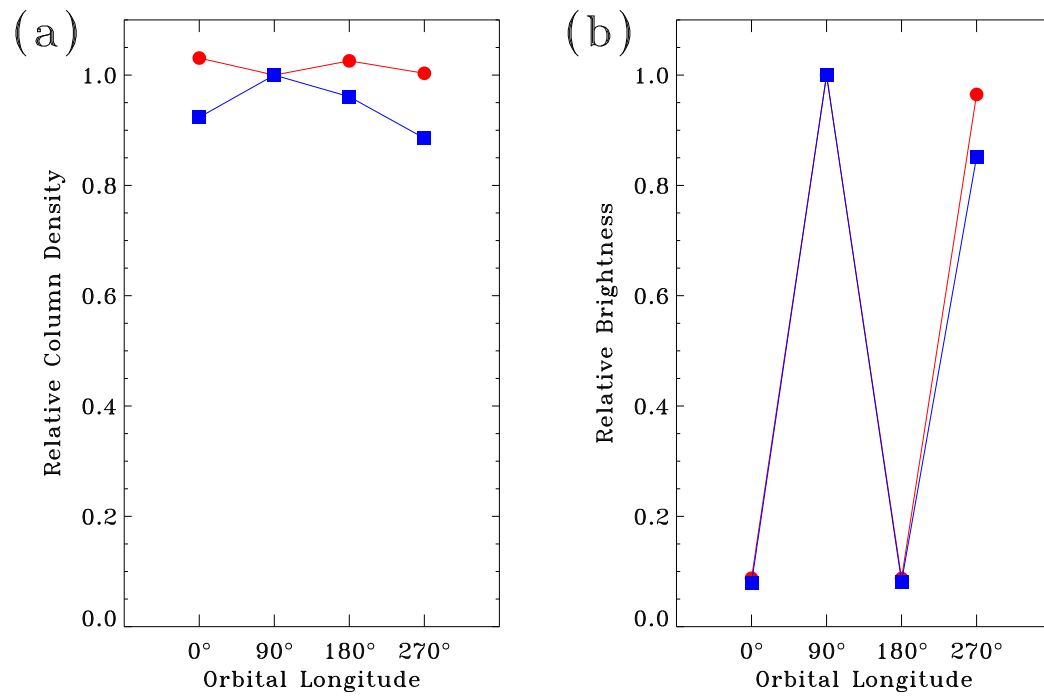


Figure 6.6 A demonstration of the effect of the east/west electric field on the sodium emission from the corona. (a) The total column of sodium atoms in the corona (impact parameter between 2 and 6 R_{I_0} summed along the line of sight) with (blue squares) and without (red circles) the east/west electric field normalized to the value at eastern elongation. (b) Total intensity in the Bergstrahl slit with and without the electric field normalized to the intensity at eastern elongation.

slit of Bergstrahl et al. (1977) (8" by 3" aligned north/south across Io). As expected from the varying radial velocity relative to the sun, the intensity is a strong function of orbital phase (see Chapter 7 for a more complete discussion of this effect). However, the east/west ratio is not constant between the two cases, a consequence of the varying column density shown in the left panel. The east/west asymmetry seen in the case without the electric field is due to the slight asymmetry in the solar D₂ Fraunhofer line.

The mutual event observations cannot confirm or refute the changing shape of the corona between eastern and western elongation. Although no change in slope was detected, the predicted variation is smaller than the event to event fluctuations and only one event was observed near eastern elongation. In addition, this one event (Event #7, Table 3.1) was of lower than average quality. A better sampling of orbital phases is necessary to detect the expected variation in slope with local time.

6.3.4 Effect of Uniform Variations in the Torus on the Corona

Another instructive experiment is to look at the effects of uniform variations in the plasma torus on the neutral clouds; i.e., variations which affect the entire torus in the same way. I discuss here three distinct types of changes in the torus structure: variations in the electron density, variations in the ion temperature, and variations in the inferred strength of the east/west electric field.

Electron density variations have a direct effect on the lifetime of the sodium near Io. Since the ionization rate due to electron impacts is proportional to n_e (Equation 2.14), the lifetime varies inversely with electron density: the lower the electron density, the denser and more extended the corona. Figure 6.7 shows how the shape of the corona varies when the electron density in the torus is uniformly modulated by constant factors of 1/2 and 2 compared to the Voyager measurements. The most prominent feature in the contour plots of sodium lifetime (top three panels) is that the lifetime is longest when the electron density is half that measured by Voyager and shortest when

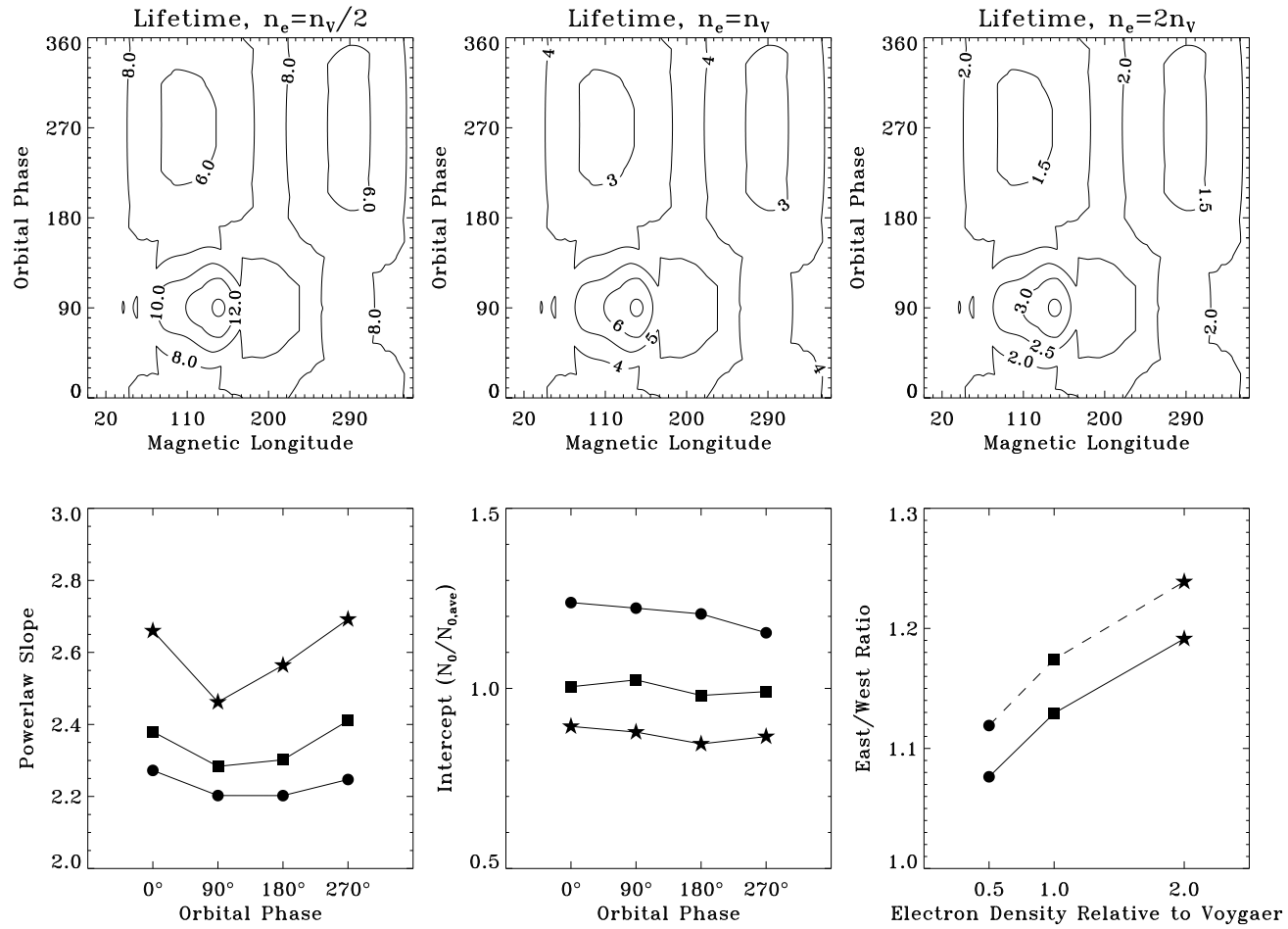


Figure 6.7 Effect of uniformly varying the electron density in the plasma torus on the sodium corona. The top three panels show contours of sodium lifetime at Io when the electron density is half, the same as, and twice that measured by Voyager (n_V), respectively. The bottom left and middle panels give the power law slope and intercept for the three cases as a function of the orbital phase. The circles denote $n_e = n_V/2$, the squares denote $n_e = n_V$, and the stars show $n_e = 2n_V$. Panel (f) shows the modeled east/west density ratio (solid line) and east/west brightness ratio (broken line) for each case.

the electron density is twice the Voyager values. However, the morphology of these contour plots does not change between cases: Jupiter's dipole and the east/west electric field still produce the same effects.

The change in electron density produces large variations in the shape of the corona. As the electron density increases, the power law slope increases and the intercept decreases. The increasing slope implies that the corona is much less extended. The decreasing intercept means that more sodium must be ejected from the exobase to produce the observed N_0 . These are both consequences of the short sodium lifetime: sodium is ionized close to the source so more sodium must be supplied to sustain the corona and this sodium does not make it very far from Io.

Although the intercept is not a strong function of orbital phase for any of the three cases tested here, the steepness of the corona does show an orbital phase modulation which increases in magnitude as the torus electron density increases. This is another effect of the sodium lifetime differences between the three cases. When the electron densities are half the Voyager values, several things happen. First, the lifetime is long enough that more sodium with escape velocity does escape without being ionized. Second, the sodium that does not escape remains in the corona longer and mixes with sodium ejected from a range of orbital phases and magnetic longitudes, reducing the importance of Io's motion. The east/west electric field does still have an effect: the lifetime east of Jupiter is greater than the lifetime west of Jupiter. Therefore, the east/west brightness ratio is greater than one, although damped relative to the the nominal Voyager case. When the electron densities are twice the Voyager values, the orbital phase effect becomes much stronger because there is a larger range in the average lifetime experienced by each atom. Near western elongation, the lifetime is short and atoms are ionized very close to the source creating a steep corona. Near eastern elongation, atoms survive longer and travel farther before ionization creating a shallower corona.

Some of the observed variation in the slope of the corona can result from vari-

ations in the torus electron density. The slope was observed to vary between 2.0 and 2.6 (Chapter 3). Increasing the electron density by 2/3 over the nominal Voyager measurements decreases the sodium lifetime by a sufficient amount to produce a slope of 2.6. However, it is not possible to increase the sodium lifetime enough to create a slope as flat as 2.0 without also changing the initial speed distribution. If the electron density is decreased to zero (i.e., no sodium ionization), then the corona slope is 2.2 when $v_p = 0.7 \text{ km s}^{-1}$. This differs from the b^{-1} dependence of a freely escaping corona due to Io's gravitational force slowing the atoms. Therefore, decreases in torus density alone are not responsible for all of the observed variation in the corona.

The second change in the torus to examine are variations in the ion temperatures. The ion temperature controls the scale height of electrons which in turn affects the lifetime of sodium when Io is off the centrifugal equator. The scale height is proportional to the square root of the ion temperature: when the ion temperature is higher, the torus is “taller” and the range of electron densities is smaller. Therefore, the range of sodium lifetimes is smaller and there is less variability in the corona with magnetic longitude. In practice, the magnetic longitude effect is not very strong – there does not in fact appear to be any significant variation in the coronal density with magnetic longitude, even for the case where the ion temperature is half the Voyager value.

Changing the scale height does have a measurable effect, however (Figure 6.8). When the scale height is large, the electron density remains close to the equatorial value for all Io magnetic latitudes. Therefore the average lifetime is lower (i.e., the average lifetime is closer to the lifetime when Io crosses the centrifugal equator where it is minimized), and the corona is steeper. Shorter lifetime implies that less sodium makes it to the outer edges of the corona. The top three panels in Figure 6.8 show contours of sodium lifetime for ion temperatures equal to half to Voyager values, the Voyager values, and twice what Voyager measured. At magnetic longitudes near where Io crosses the centrifugal equator ($\lambda_{Io} = 110^\circ$ and 290°), the lifetimes do not change

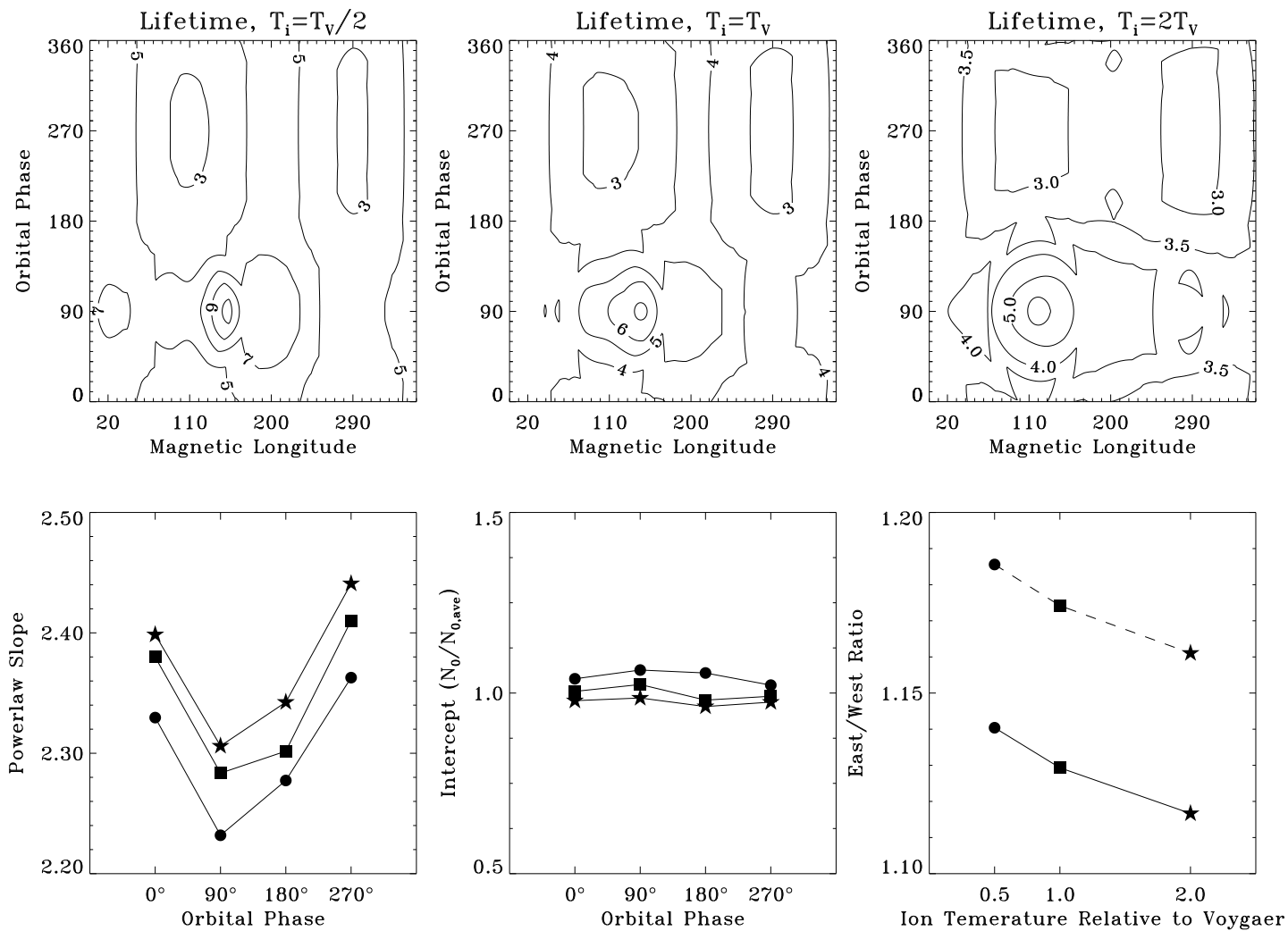


Figure 6.8 Effect of uniformly varying the ion temperature in the plasma torus on the sodium corona. Panels the same as in Figure 6.7 using the ion temperature equal to 1/2, 1, and 2 times the Voyager value. 129

between the three cases since the electron densities at the centrifugal equator do not depend on the ion temperature. The greatest changes occur when Io is at its greatest extent north or south of the torus ($\lambda_{Io} = 200^\circ$ and 20° , respectively). Doubling the ion temperature results in the scale height varying by $\sqrt{2}$; since electron density $\sim e^{\zeta/H}$, changes in the scale height affect the rate at which the electron density, and therefore the sodium lifetime, decreases off the centrifugal equator.

The shape of the corona is not strongly influenced by the changing ion temperatures. There is a trend, however, that can be discerned: as the ion temperature increases, both the slope increases and the intercept decreases. The reasons for this are similar to the reasons for the similar trends seen with increasing electron density discussed above: as the average sodium lifetime decreases, the corona is less extended and the number of atoms supplied to the corona must increase. The changes in each of these quantities are small, comparable to the observational limits of the mutual event observations. Changes in electron density have a much larger effect on the lifetime owing to the fact that the ion temperature variations only affect the lifetime of sodium off the centrifugal equator.

Changes in the ion temperature are not responsible for the observed variation in the slope of the corona: the ion temperature must be increased by an order of magnitude to create a corona as steep as observed. This increases the scale height by a factor of 3 which is large enough that the electron density only varies by 5% due to Io's motion off the centrifugal equator. Similarly, decreasing the scale height to zero, such that the electron density drops to zero immediately off the centrifugal equator, cannot produce a corona as shallow as that observed.

For the third test, I adjusted the strength of the east/west electric field using the parameter ϵ (ϵ is proportional to the strength of the electric field; see Section 5.3.2). The results from the case where the electric field is turned off or at its observed strength are shown in Figure 6.5; a comparison of these cases with that where the field strength is

doubled is given in Figure 6.9. The orbital phase variations of both the power law slope and intercept are strongly influenced by the strength of the electric field, consistent with the previously discussed conclusion that the east/west electric field is responsible for the east/west brightness asymmetry. Doubling the value of ϵ , doubles the offset of the torus to the east and changes the regions of the torus seen by Io. In addition the local time modulation factor is proportional to $(\epsilon/\epsilon_0)^2$, so that both the torus shift and densities are affected and the orbital phase asymmetry becomes even more pronounced.

6.3.5 Effect of Magnetic Longitude Variations on the Corona

The scale height and electron density in the plasma torus have been observed to vary with magnetic longitude (summarized in Chapter 5). This variation is treated as a variation in the parallel ion temperature with λ_{III} according to Equation 5.11. The scale height and electron density vary as described in Equation 5.12 such that the total flux tube content along field lines remains constant as suggested by Schneider et al. (1997). The amplitude of this variation observed by Schneider and Trauger (1995) is $0.5 \times T_0$ where T_0 is the mean ion temperature. In this section I describe the effects of this variation on the shape of the corona.

The variation in corona shape versus System-III longitude is shown in Figure 6.10 for several amplitudes of variation. The model results are fit in the with equations in the form of:

$$y = y_0 + A \cos(2(\lambda - \lambda_0)) \quad (6.3)$$

where y is the power law slope, power law intercept, or the brightness through the Bergstrahl slit. Two wave cycles are fit over the full magnetic field rotation since the torus is symmetric along the field line above and below the centrifugal plane.

There are several important trends seen in these results. First, the magnitude of the variation in the shape of the corona increases with increasing amplitude of the System-III variation in the torus. Simply put, the greater the torus variability, the

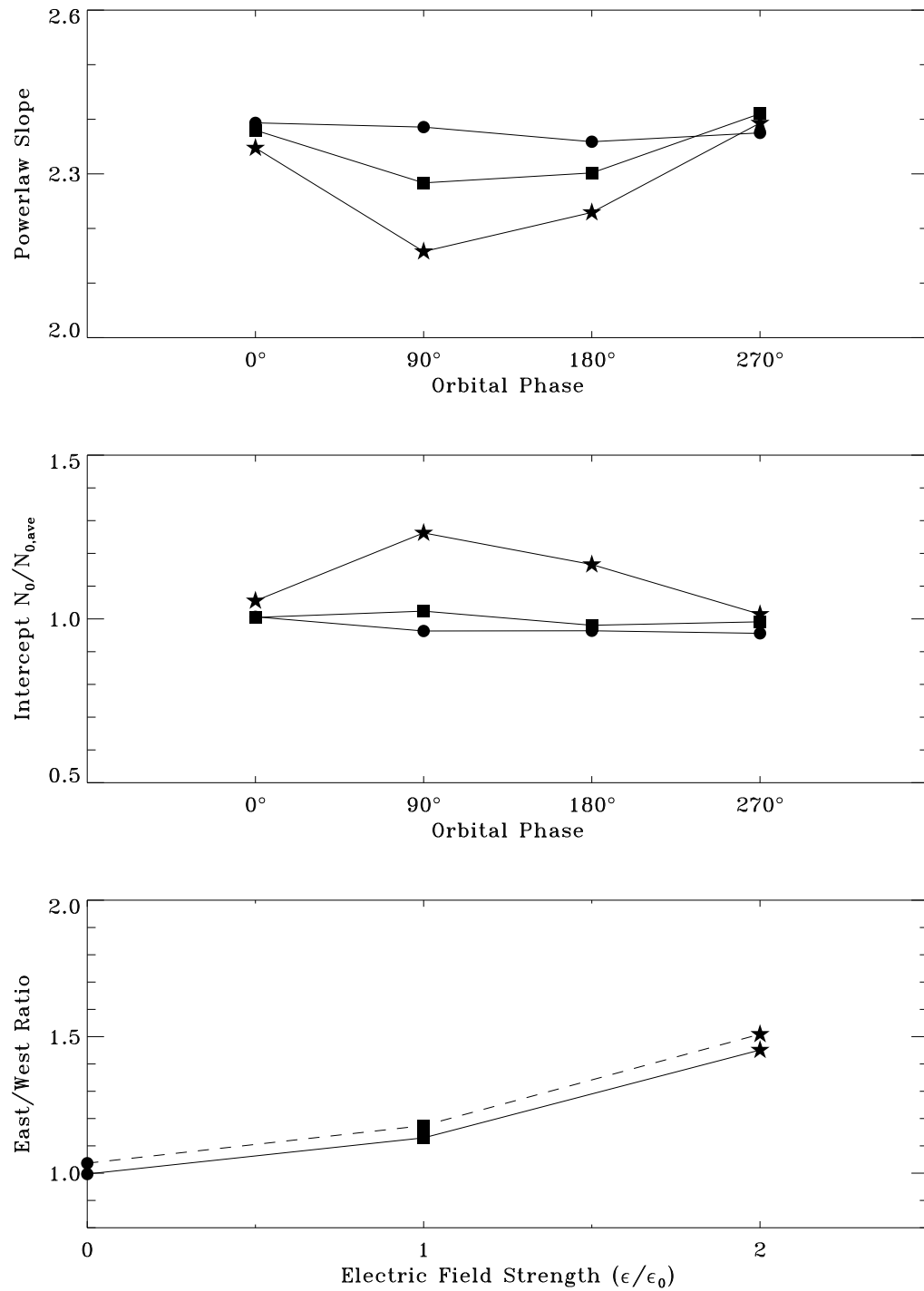


Figure 6.9 Effect of varying the strength of the east/west electric field on the sodium corona. The top panel shows the power law slope as a function of orbital phase; the middle panel shows the power law intercept; and the bottom panel shows the east/west column density ratio (solid line) and brightness ratio (broken line). The circles, squares, and stars represent the cases where $\epsilon = 0, \epsilon_0,$ and $2\epsilon_0$, respectively, with ϵ_0 being the inferred value of ϵ .

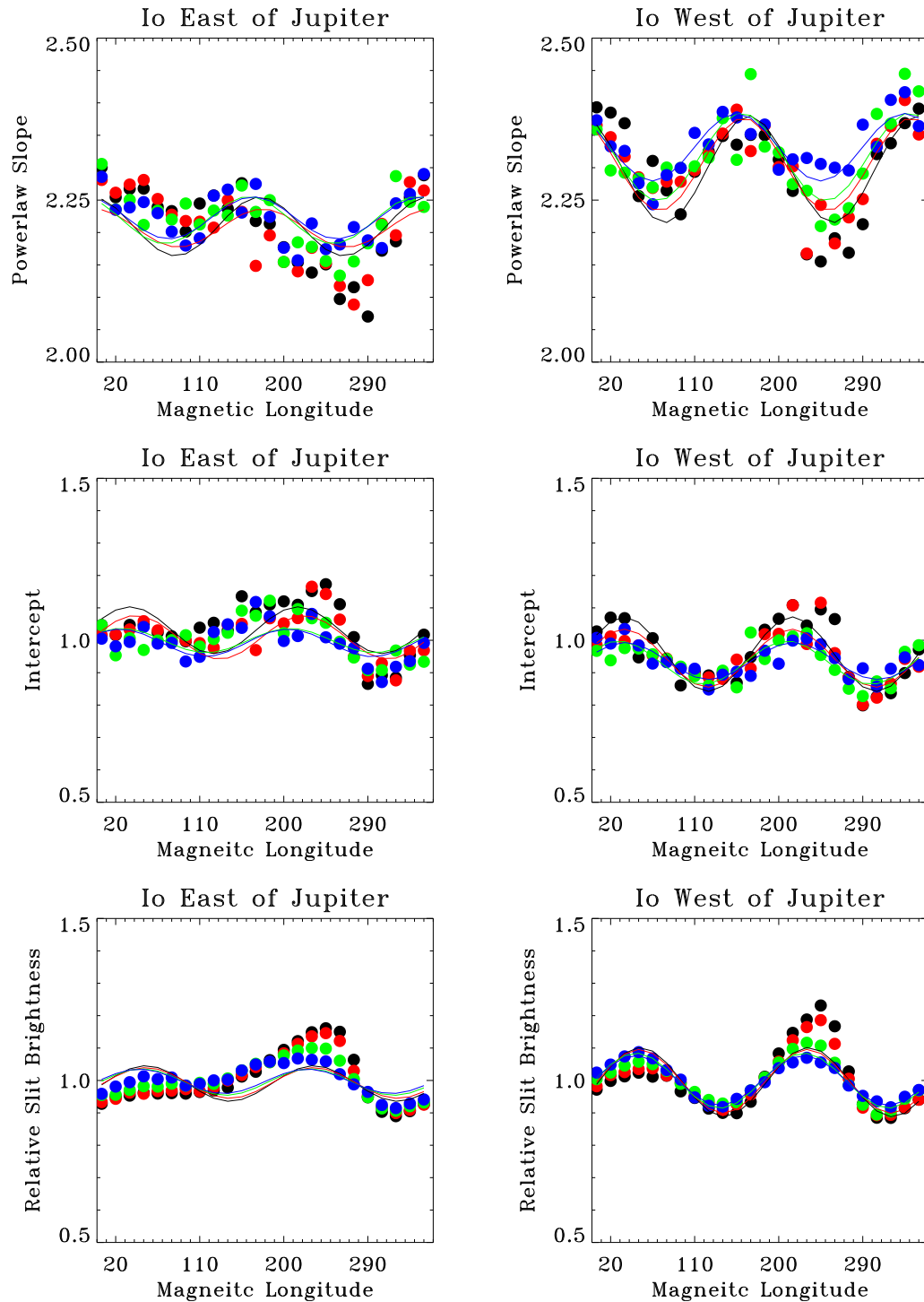


Figure 6.10 Effect of magnetic longitude variations in the plasma torus on the shape of the corona. The left panels show the corona when Io is east of Jupiter; the right panels are when Io is west of Jupiter. The top panels show the slope of the corona, the middle panels show the intercept, and the bottom panels show the relative brightness through the Bergstrahl slit. The amplitudes of the ion temperature variation relative to the mean ion temperature with λ_{III} are 0.0 (blue), 0.5 (green), 0.75 (red), and 0.9 (black). The lines show the sinusoidal fits discussed in the text.

greater the corona variability. There are two peaks in the slit brightness (bottom panels) for Io both east and west of Jupiter: one at $\sim 50^\circ$ and the second at $\sim 230^\circ$. The longitudes of these peaks are determined by maximizing the sodium lifetime. This is a balance of two factors: (a) the greatest extent of Io from the centrifugal equator ($\lambda_{Io} = 20^\circ$ and 200°) and (b) the point of minimum torus scale height ($\lambda_{III} = 226^\circ$). Looking at the case with no System-III variation (blue points), where only the first factor needs to be considered, shows that the peaks are delayed from Io’s maximum extent from the centrifugal equator by 30° to the point where the average lifetime experienced by the atoms is largest. As the amplitude of the torus variation increases, the height of the first brightness peak (at $\lambda_{Io} = 50^\circ$) decreases and the height of the second peak (at $\lambda_{Io} = 230^\circ$) increases. This happens because the sodium lifetime is increased over its previous maximum near the second peak and decreased near the first peak due to the varying scale height in the torus. The magnitude of this effect is small ($\sim 5\%$), but observable with precise photometry over several hours when Io is near elongation.

6.4 Understanding the Inner/Outer Asymmetry in the Corona

As shown in Chapter 3, there is an inner/outer asymmetry in the sodium corona: the inner (sub-Jupiter) hemisphere is consistently denser than the outer (anti-Jupiter) hemisphere. Both sides of the corona, however, drop off at approximately the same rate: i.e., the slopes on the inner and outer sides are the same, but the value of N_0 over the outer hemisphere is approximately 0.6 times N_0 over the inner hemisphere. In this section I discuss possible origins of this asymmetry. Because the regions measured are over the the sub-Jupiter and anti-Jupiter hemispheres, and the source regions are varied over the same hemispheres, I use the following nomenclature in this section: The terms “inner” and “outer” will refer to measurements over the sub-Jupiter and anti-Jupiter hemispheres, respectively. Uses of the terms “sub-Jupiter,” “anti-Jupiter,” “leading,” or “trailing” hemispheres refer to an exobase source confined to that region (Figure 6.11).

Models of the corona created with a source region which is uniform over Io's exobase in a torus that is roughly uniform across the corona are radially symmetric about Io. These are the conditions present for the models thus far discussed in this chapter. A spatially asymmetric corona therefore implies a non-uniformity in either the source or the sink.

To simulate this asymmetry, I divided the exobase into hemispheric regions such that the source could differ between each half of Io. The exobase was divided into either (a) the sub-Jupiter hemisphere (Io surface longitudes between 270° and 90°) and the anti-Jupiter hemisphere (longitudes 90° – 270°), and (b) the leading (longitudes 0° – 180°) and trailing (longitudes 180° – 360°) hemispheres.

Figure 6.12 shows the shape of the corona when the sputtering is confined to either the sub-Jupiter, anti-Jupiter, leading, or trailing hemisphere. Each hemisphere individually can approximately supply the necessary ratio of escaping to non-escaping sodium to produce the observed corona profile over one side of Io, but not over both simultaneously. The slopes on each side are similar to the observed slopes, but the inner/outer ratio is not adequately modeled when the source is limited to a single hemisphere. Sputtering from the sub-Jupiter side primarily supplies sodium to the inner hemisphere and sputtering from the anti-Jupiter side primarily supplies sodium to the outer hemisphere. The leading and trailing hemispheres supply roughly equal amounts to the inner and outer hemispheres; if sputtering were limited to one of these regions, there would not be an observable inner/outer asymmetry.

Since a single hemisphere cannot supply the entire corona in the necessary ratio, I combine hemispheric sources to match the observations. Figure 6.13(a) shows the profiles in a corona formed by adding different proportions of the corona formed from a completely sub-Jupiter sputtering source and a completely anti-Jupiter sputtering source. The shape of the sputtering distribution from each hemisphere is the same; i.e.,

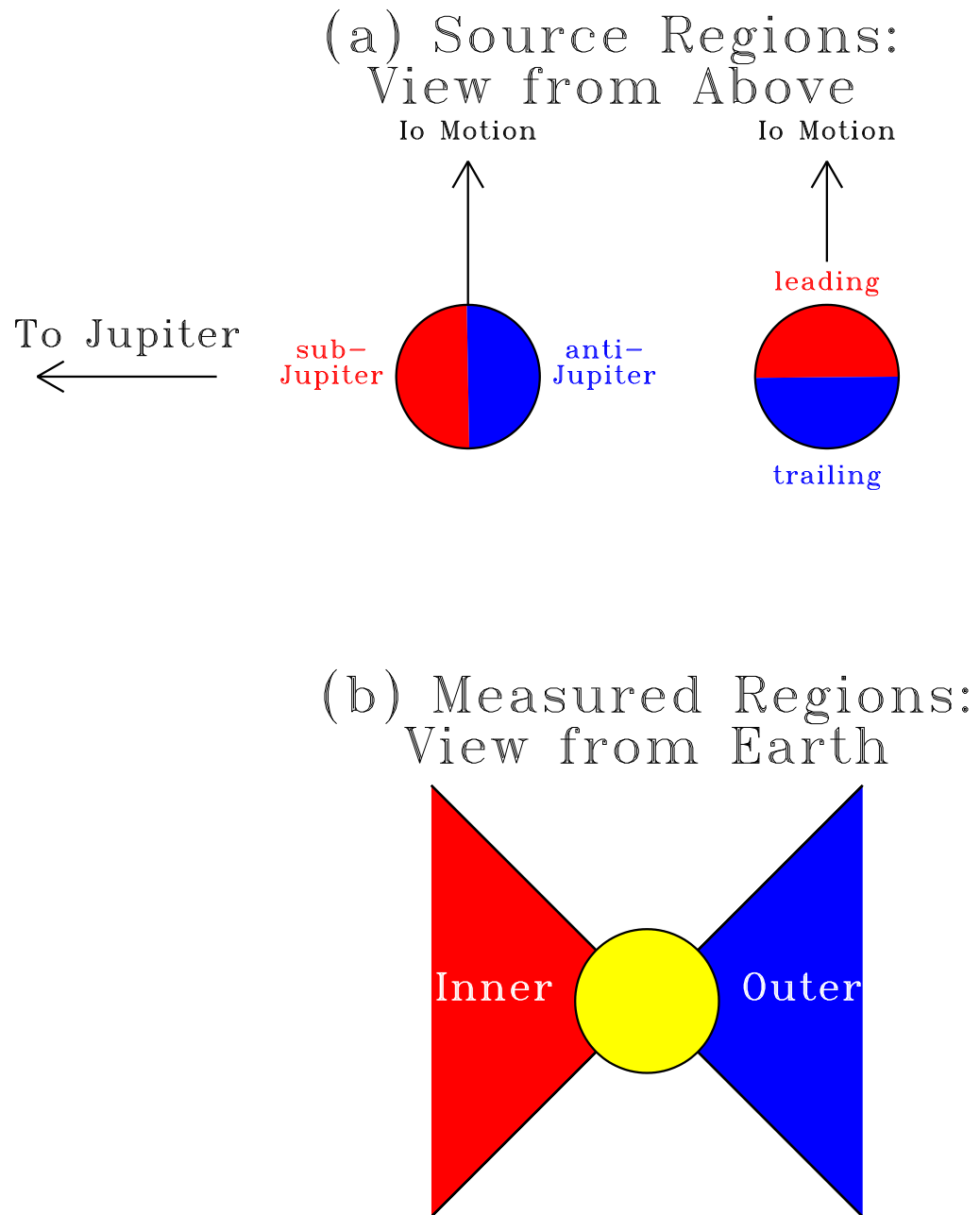


Figure 6.11 Sketch showing the nomenclature used for discussion of the asymmetry in Io's corona.

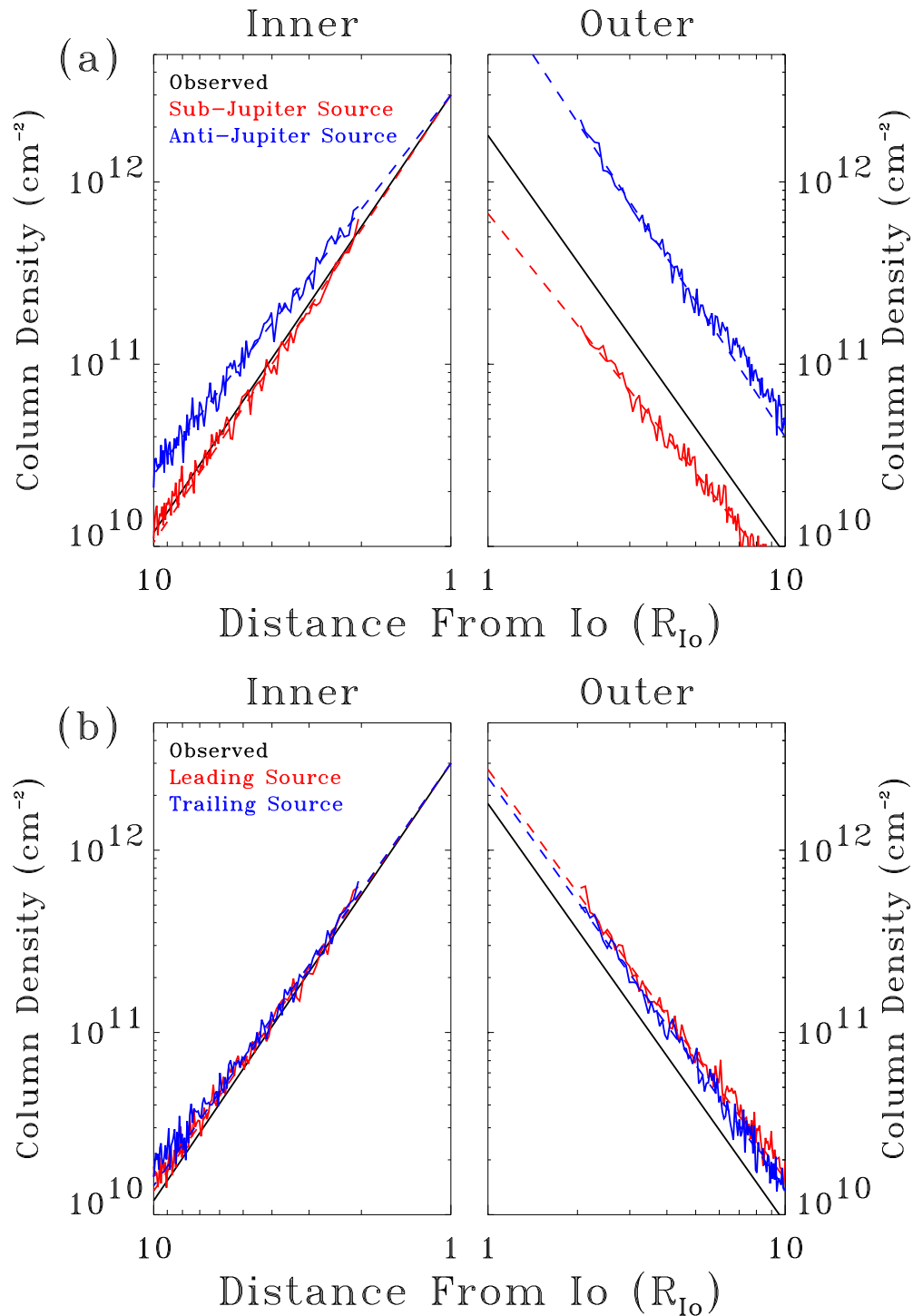


Figure 6.12 Shape of the corona when the source region is limited to a single hemisphere. The black lines in each panel are the observed asymmetric corona. In panel (a), the red lines show the simulated corona when sodium is only sputtered from the sub-Jupiter hemisphere scaled such that the inner modeled profile has the same N_0 value as the inner observed profile. The blue lines represent the corona where the source is limited to the anti-Jupiter hemisphere, similarly scaled to the observed inner corona. The broken red and blue lines are the best fits to the red and blue model profiles extrapolated to the surface. Panel (b) shows the simulated coronae for sodium sources constrained to the leading hemisphere (red) and trailing hemisphere (blue).

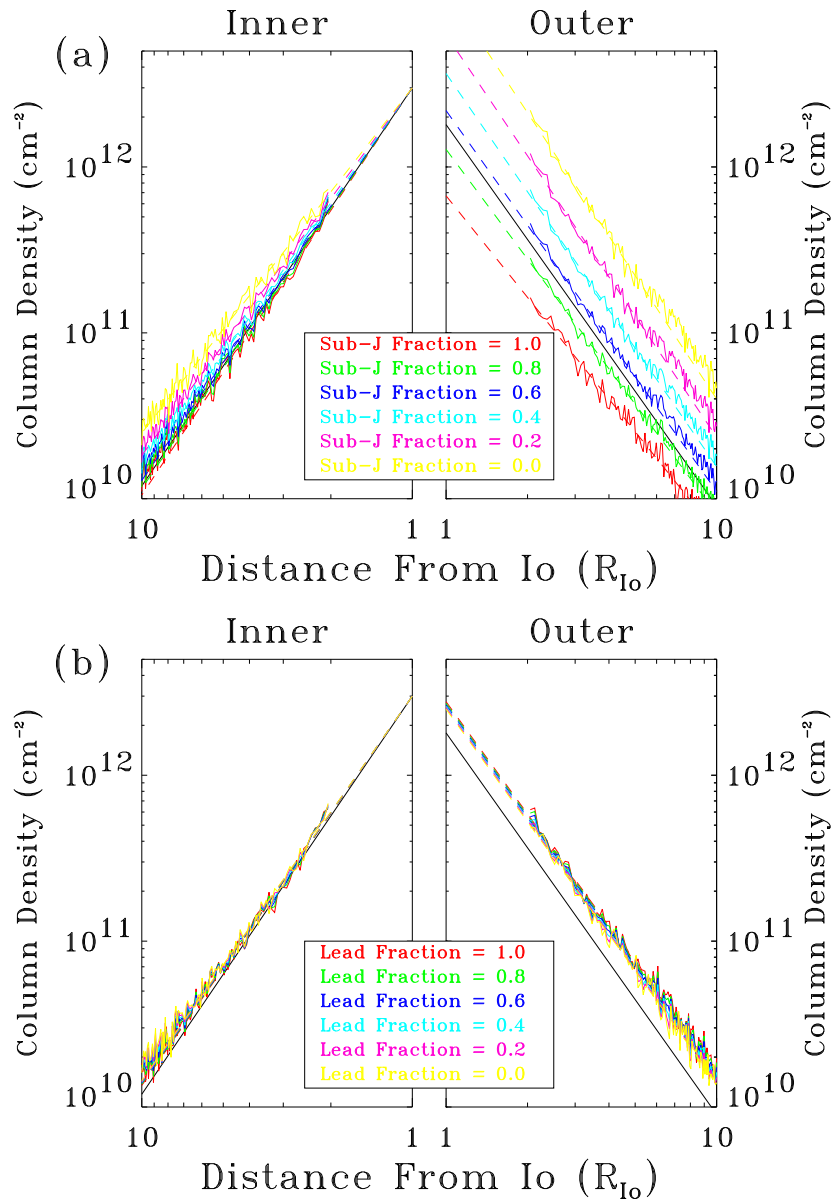


Figure 6.13 (a) Shape of the corona with sodium sputtered from the sub-Jupiter and anti-Jupiter hemispheres mixed. The colors show the fraction of the total source sputtered from each hemisphere. The modeled coronae are scaled such that the surface intercept on the inner hemisphere matches the observations (black lines). The broken colored lines show the fits to the modeled coronae extrapolated to the surface. (b) Shape of corona with sputtering from the leading and trailing hemispheres mixed.

each side has $v_p = 0.7 \text{ km s}^{-1}$. Figure 6.13(b) similarly combines sputtering from the leading and trailing hemispheres.

The first conclusion demonstrated in Figure 6.13 is that the observed corona asymmetry could be created by a sputtering source concentrated on the sub-Jupiter hemisphere: a source with 70% of the total sputtered sodium ejected from the sub-Jupiter hemisphere and 30% ejected from the anti-Jupiter hemisphere reproduces the observations. The observed asymmetry cannot be created by a leading/trailing source asymmetry. Since these hemispheres supply sodium to the inner and outer corona in equal proportions, asymmetric loss from these exobase regions does not create an inner/outer corona asymmetry. It would create a difference between the leading and trailing hemispheres, but no evidence for such an asymmetry was detected (but see below for a discussion of the observed oxygen corona asymmetry).

An inner/outer asymmetry would also be created if the most probable velocities on each side of Io were different. However, the characteristics of an asymmetry formed in this manner are different from that observed. Figure 6.14 shows the consequences of having half the sputtered sodium ejected from each hemisphere but allowing different sputtering distributions from the sub-Jupiter and anti-Jupiter hemispheres. The shape of the corona over one hemisphere is not significantly affected by the sputtering distribution on the opposite hemisphere. Changing the velocity distribution from the sub-Jupiter hemisphere does not affect the corona over the outer hemisphere, and vice-versa. The main effect is that the slope on the opposite side is more or less steep, depending on whether the velocity over that hemisphere is decreased or increased. The slope over a hemisphere is governed by the source distribution on that side; the opposite hemisphere provides sodium, but not enough to affect the shape of the profile. Therefore, the corona asymmetry can not be described simply as a difference in the shape of the sputtering distribution but instead must indicate a difference in the amount of sodium sputtered from each hemisphere. There may be a small difference in the shape

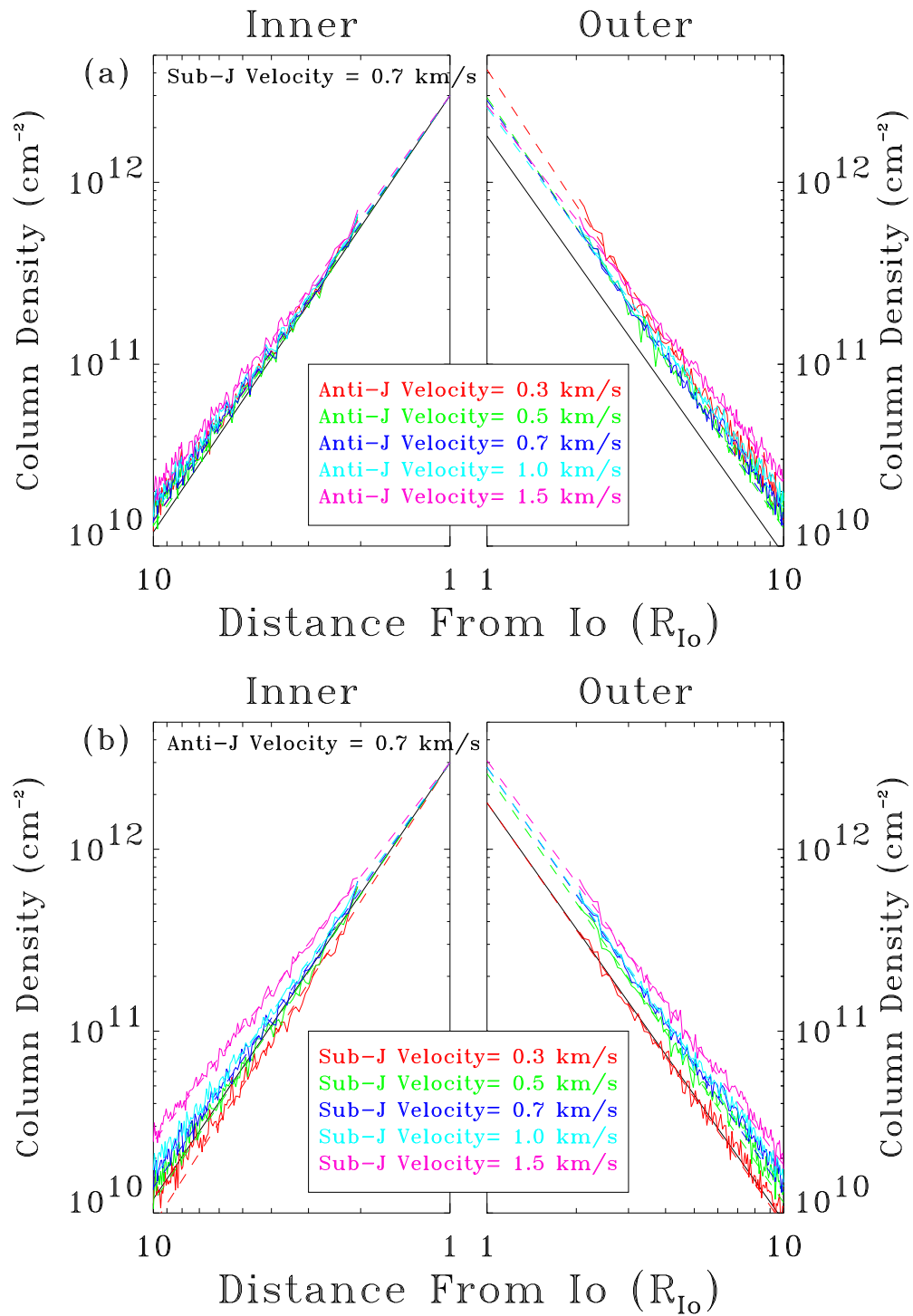


Figure 6.14 Shape of the corona when the most probable velocities of each hemisphere are allowed to vary independently. In panel (a), the velocity is held constant from the sub-Jupiter hemisphere ($v_{\text{sub}} = 0.7 \text{ km s}^{-1}$) and allowed to vary from the anti-Jupiter from $v_{\text{anti}} = 0.3 - 1.5 \text{ km s}^{-1}$. Vice-versa for panel (b). Each hemisphere supplies half the sodium.

of the source distribution implied by the small observed difference in slope measured by the mutual events, but this difference is dominated by the different source rates.

One possible source of this sodium asymmetry is the effect of the electrodynamic interaction caused by Io moving through Jupiter's rapidly rotating magnetic field. Retherford et al. (2000) presented observations of equatorial spot emission near Io's surface. They found that the spot on Io's anti-Jupiter side was consistently brighter than the sub-Jupiter spot. The explanation for this lies in model results that the Io interaction deposits more energy on the anti-Jupiter side than the sub-Jupiter side (Saur et al. 2000). The additional energy is not enough to ionize oxygen, just to excite the emission. Sodium, however, has a lower ionization potential. Therefore energy which excites oxygen can ionize sodium. The equatorial spots are observed close to Io's surface implying that the interaction region is closer to Io than the regions probed by the mutual event observations. The increased sodium ionization would only occur in this region and would reduce the rate at which sodium is released into the corona.

Ionization near the exobase would also likely affect the velocity distribution of the atoms which do escape into the corona. Slower atoms, which spend more time in the interaction region would be preferentially ionized, increasing the most probable speed of the velocity distribution from the anti-Jupiter hemisphere. As seen in Figure 6.14(a), increasing the velocity from the anti-Jupiter hemisphere over that from the sub-Jupiter hemisphere corresponds with a small decrease in the slope from that hemisphere. This is consistent with the mutual event observations which suggested that there is a small difference in the measured slopes, although this difference was within the errors of the measurements.

6.5 Io's Oxygen Corona

Until recently, mutual events provided the only means of measuring the radial profiles of Io's corona. New techniques utilizing FUV observations of Io's emissions with

the *Hubble Space Telescope*, however, have made it possible to obtain spatially resolved images of Io's atmosphere and exosphere (Roesler et al. (1999), Figure 6.15). Besides the obvious advantage that the observations target the most abundant coronal species, the wavelengths observed are in the FUV where the solar continuum is negligible. Therefore the observations can be made any time Io is visible and it is not necessary to wait for the rare mutual events. The disadvantage of this method of observing the corona is that the emission intensity is a function of both the column density of oxygen and the state of the plasma. Therefore, complex modeling of the plasma interaction near Io is needed to truly understand the observations.

6.5.1 Observations

The data used by Wolven et al. (2001) consist of a series of spatially and spectral resolved images of Io's atmospheric and coronal emissions taken between 1997 and 2000. Images of Io's disk at discrete wavelengths are spread out with the wavelength increasing from left to right. Many of the images overlap due to the fact that bright transitions of several of the abundant species in Io's atmosphere and the plasma torus are similar in energy. However, several strong lines from the neutrals are uncontaminated allowing an unambiguous measurement of the intensity. In particular, Wolven et al. (2001) studied a semi-forbidden line of neutral oxygen at 1356 \AA and an allowed transition of neutral sulfur at 1479 \AA . The vertical direction on the detector records emission at constant wavelength. Therefore, Wolven et al. were able to determine the brightness profiles of oxygen and sulfur on opposite sides of Io. Unfortunately, due to the pointing constraints of *HST*, they were not able to align the slit at an arbitrary angle to Io's equatorial plane: the slit was aligned north-east to south-west relative to Jupiter's north pole for all the observations.

Two major differences were detected between the intensity profiles in the oxygen corona and sodium column density measurements. First, the oxygen intensity decreases

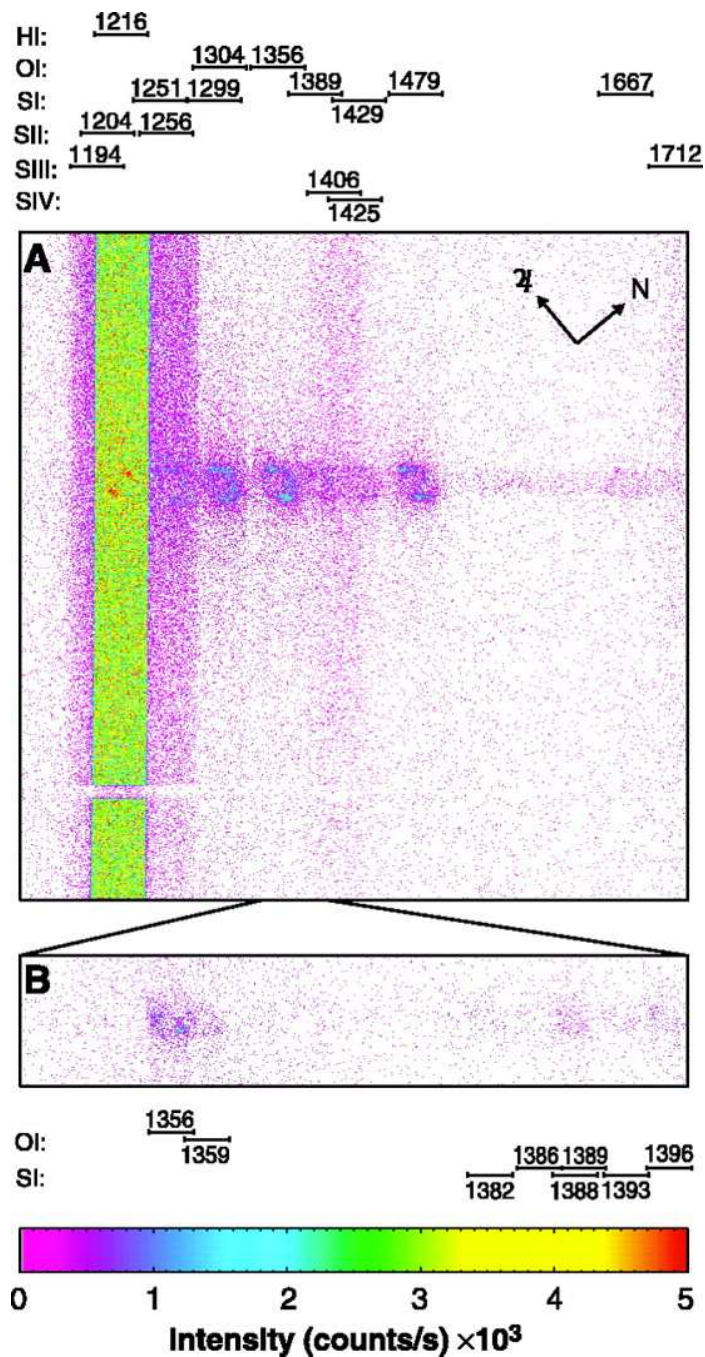


Figure 6.15 Example of STIS image of Io's atmospheric emissions. The circular features in a row just above mid-image are images of Iogenic emission at various O I and S I multiplets; faint, diffuse emission extends above and below the brighter circular features. The vertical green bar is an image of the 52-arc sec by 2-arc sec slit filled with diffuse terrestrial H I Lyman-alpha emission. Also present are several plasma torus lines (vertical bars brighter at the top than the bottom) and the shadow of a 0.5-arc sec fiducial bar in the slit (horizontal band near the bottom). The key above shows the slit positions for various emission wavelengths. The compass shows the directions of Jupiter (east) and jovian north. (From Roesler et al. (1999)).

Location	Measured Profile
Downstream, west:	$I \sim b^{-1.95}$
Upstream, west:	$I \sim b^{-1.76}$
Downstream, east:	$I \sim b^{-1.71}$
Upstream, east:	$I \sim b^{-1.51}$

Table 6.2 Summary of the intensity profiles in the oxygen corona observed by Wolven et al. (2001).

at a slower rate than the sodium. Second, Wolven et al. did not detect an inner/outer oxygen asymmetry. They did however measure a leading/trailing asymmetry: the emissions from the leading (downstream) side of Io were brighter than from the trailing (upstream) side. The following subsections discuss each of these differences and suggest possible reasons why oxygen and sodium do not behavior in the same manner.

6.5.2 The Average Oxygen Corona

The average oxygen profiles measured by Wolven et al. (2001) are summarized in Table 6.2 for the upstream and downstream hemispheres of Io when Io is both east and west of Jupiter. The upstream/downstream asymmetry is discussed in the following subsection. The oxygen corona is substantially flatter and more extended than the sodium corona, which had an average slope 2.3. They attribute the difference in power law slopes to the fact that oxygen has a much longer lifetime than Io.

To test this hypothesis, I have conducted model simulation of Io's oxygen corona (Figure 6.16) producing the average column density profiles. Due to the long oxygen lifetime, there are no variations in the column density with magnetic longitude: the average lifetime that the atoms experience is roughly constant. Because the emission is excited by electron-impacts, the oxygen intensity varies greatly as a function of magnetic longitude. This effect is discussed in greater detail in Chapter 7. Although the value of the intercept is a strong function of magnetic longitude, the slope is not. This is due to the fact the the torus densities and temperatures in this model are roughly constant

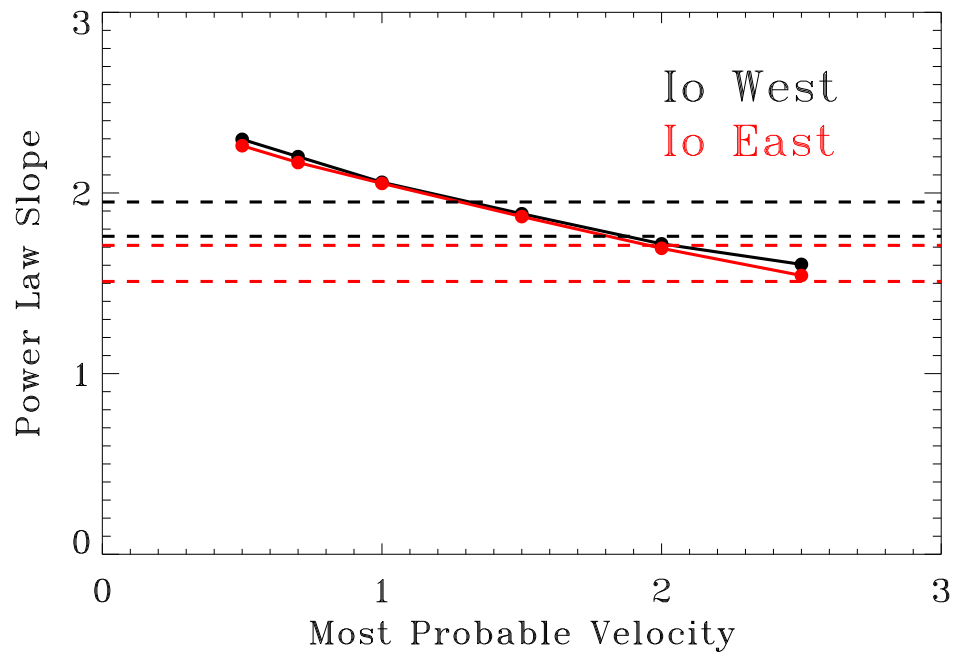


Figure 6.16 Power law slope in the oxygen corona as a function of the most probable speed of the sputtering distribution. The solid black line is the slope when Io is at western elongation; the solid red line is for Io at eastern elongation. The broken lines indicate the average upstream and downstream slopes observed by Wolven et al. (2001) and listed in Table 6.2

across the corona.

I conclude that the longer oxygen lifetime can only partly explain the difference between the shapes of the oxygen and sodium coronae. I found that the average sodium corona with a slope of 2.3 was well modeled with a classical sputtering distribution with a most probable speed of 0.7 km s^{-1} . An oxygen corona with this speed distribution would have a slope of 2.2, similar to the sodium corona although slightly more shallow. The increased lifetime does not have a large effect on the shape of the corona because the atoms which are escaping make it to the outer edge of the corona without much loss to ionization (Figure 6.17). Therefore, although the difference in lifetime is significant, lifetime alone cannot explain the observations.

A shallow oxygen corona would form if the oxygen were ejected from Io with a higher average speed than sodium. In Figure 6.16, the limits set by the average upstream and downstream slopes imply that the most probable speed of the sputtering distribution must be between 1.4 and 2 km s^{-1} . As discussed in Section 6.3, the shape of the corona can be modeled with an initial speed distribution other than the sputtering distribution. Dissociation of the most abundant species in Io's atmosphere, SO_2 , into atomic oxygen and sulfur ($\text{SO}_2 \rightarrow \text{O} + \text{SO}$, $\text{SO} \rightarrow \text{O} + \text{S}$) might be an important source of neutrals in the corona. If the dissociation occurs near Io's exobase, the oxygen might be ejected fast enough to supply a large amount of oxygen to the outer edge of the corona and flatten the profile. It is also possible that there is an unobserved extended SO_2 corona. Dissociation of these molecules far from Io would provide additional oxygen atoms at the edges of the corona and would also create a corona which is less steep than the sodium corona.

An alternative explanation is that the radial profile difference results from a difference in the plasma conditions rather than a difference in the neutral column density. The Voyager flybys detected a decrease in the torus electron temperature near Io (Sittler and Strobel 1987). This variation would result in an apparent flattening of the

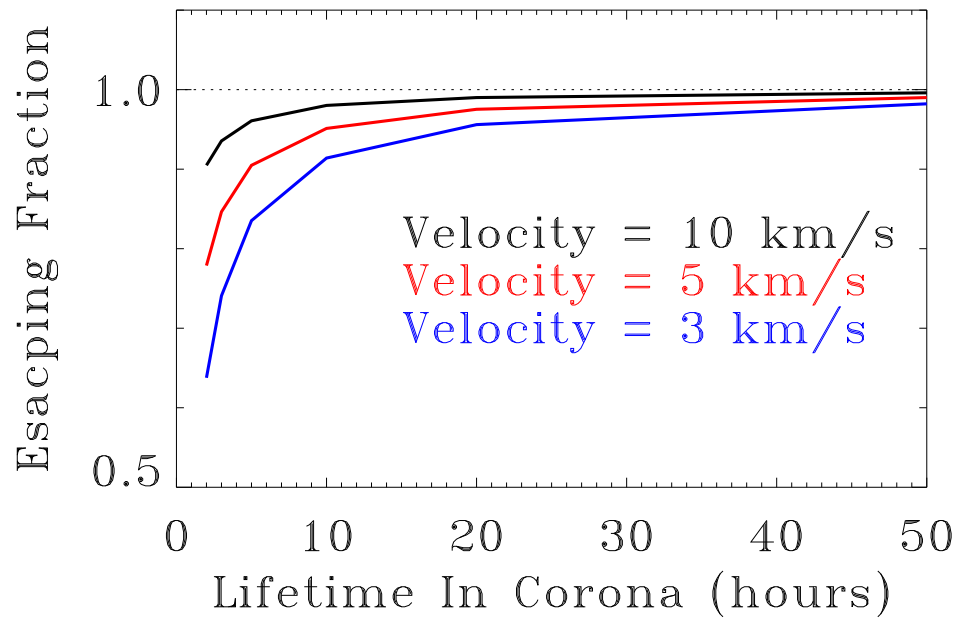


Figure 6.17 Fraction of atoms escaping from Io's corona as a function of neutral lifetime and initial velocity.

radial intensity profile in the corona (Figure 6.18). If the electron temperature near Io's surface is ~ 0.6 the electron temperature $10 R_{\text{Io}}$ from Io, then the modeled radial intensity profile matches the observations assuming that the oxygen is ejected from Io with the same sputtering distribution as sodium. The small dependence of the slope on T_e far from Io is due to non-linearities in the emission rate coefficient.

Wolven et al. noted that the slope of the oxygen corona when Io is east of Jupiter is shallower than when Io is west of Jupiter. Section 6.3.3 described the prediction that the sodium corona would show a east/west difference in slopes as an effect of the east/west electric field. This was shown to be the source of the east/west brightness asymmetry. The models of the oxygen corona however do not predict this asymmetry since any change in lifetime east to west is insignificant: as stated above, very little oxygen is ionized in the corona so changing the lifetime small amount does not have any effect. This difference can be explained by differences in the plasma torus at Io with the T_e decreasing more near Io at eastern elongation than at western elongation.

6.5.3 The Oxygen Asymmetry

Observations of both the sodium and oxygen coronae have detected asymmetries. However, the sodium asymmetry is a column density difference between the inner and outer hemispheres and the oxygen asymmetry is a brightness difference between the upstream and downstream hemispheres. The different natures of these asymmetries suggest that they are formed through different processes. In Section 6.4 I presented the hypothesis that the electrodynamic interaction as described by Saur et al. (2000) between Io and Jupiter's magnetic field decreases the sodium lifetime close to Io's exobase above the anti-Jupiter hemisphere and reduces the number of sodium atoms which can escape into the corona. Because the ionization potential of sodium is less than oxygen, the energy which excites the oxygen emission ionizes sodium. This creates a sodium asymmetry, but does not affect the ionization rate of oxygen resulting in a symmetric

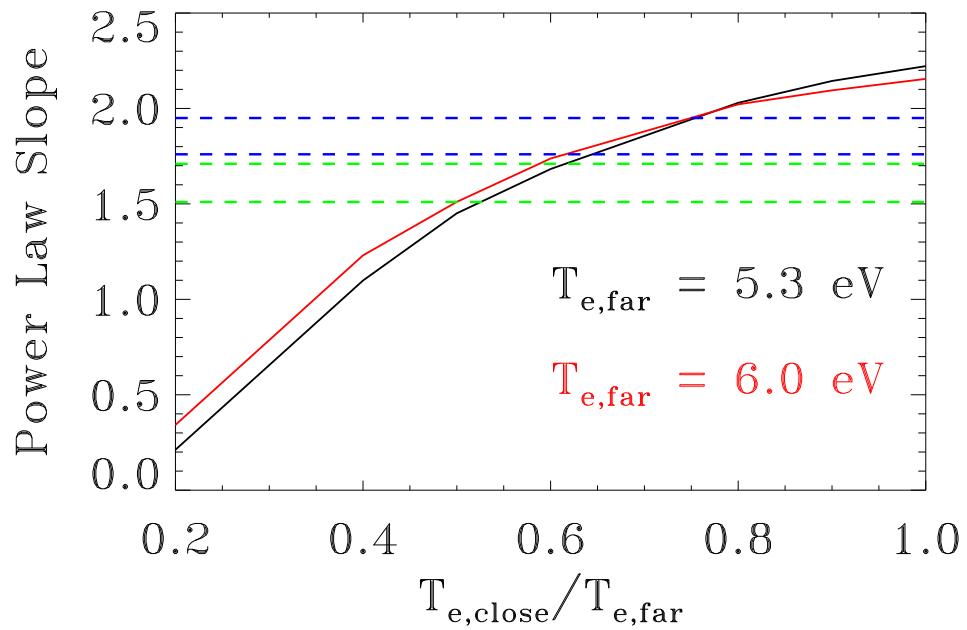


Figure 6.18 Power law slope of emission from the oxygen corona versus ratio of electron temperature at $1 R_{Io}$ ($T_{e,close}$) to electron temperature at $10 R_{Io}$ ($T_{e,far}$). The black line shows the slope for $T_e=5.3 \text{ eV}$ at $10 R_{Io}$; the red line shows the slope for $T_{e,close}=6.0 \text{ eV}$. The blue and green broken lines indicate the observed slopes by Wolven et al. (2001) for western and eastern elongations, respectively.

oxygen corona.

Wolven et al. (2001) attribute the asymmetry they detected to the increased electron density in Io's wake exciting greater emission from the downstream portion of the corona. Because my model of the plasma torus parameters does not include the interaction with Io, I am not able to address this question directly. The models of the sodium asymmetry described previously can be applied to understanding the ejection of neutral oxygen from Io's exobase assuming that the asymmetry is due to column density differences rather than differences in the emission rate. The sodium asymmetry was shown to result from greater sodium ejection from the sub-Jupiter hemisphere than the anti-Jupiter hemisphere. Ejection from either the leading or trailing hemisphere did not produce a difference in inner/outer column density asymmetry. Similarly, a difference between the ejection rates from the sub-Jupiter and anti-Jupiter hemispheres would not create an asymmetry between the downstream and upstream hemispheres. A column density asymmetry between these two regions implies that the source rate of oxygen from the leading hemisphere must be greater than from the trailing hemisphere.

6.6 Summary

The observations of the sodium corona presented in Chapter 3 have successfully been modeled using a classical sputtering source from Io's exobase. Atoms ejected isotropically with a most probable speed of 0.7 km s^{-1} , well below the escape speed from Io of 2.1 km s^{-1} , create a radially symmetric corona about Io which decreases in column density proportional to $b^{-2.3}$. The source rate of sodium necessary to match the observed column density is 2.7 atoms s^{-1} .

I then looked at deviations from the average corona starting with the effect of changing the source flux distribution function. The general trend holds that any change which increases the amount of high speed sodium that is ejected from the exobase creates a shallow, more extended corona. Decreasing the relative amount of sodium with escape

velocity results in a steeper corona which does not extend far from Io.

The state of the plasma in the plasma torus changes on short time scales. Even assuming there are no temporal or magnetic longitude variations in the plasma, Jupiter's rapid rotation rate combined with the offset, tilted dipole and the east/west electric field cause the plasma at Io to vary on rapid time scales. The different reasons for plasma variability at Io each have a different relative importance on the changing shape of the corona.

The most important factor shaping the observed corona is the east/west electric field. Jupiter's offset tilted dipole, without the electric field, does not create a corona which is much different from that which would be created with a torus that is not tilted relative to Jupiter's equatorial plane. This is because the lifetime variation induced by the dipole is too small to have a noticeable effect on ionization in the corona. The inclusion of the east/west electric field, by shifting the torus east more than $0.1 R_J$ at Io's orbit, greatly increases the average lifetime at Io and the range of lifetime experienced by sodium in the corona. The sodium lifetime when Io is east of Jupiter is significantly longer than when Io is west of Jupiter, resulting in a shallower slope to the sodium column density profile east of Jupiter. The increase in slope corresponds with an increase in the total sodium abundance in the corona and therefore Io's sodium emissions are brighter when Io is at eastern elongation than at western elongation. Because the strength of the electric field affects both the slope and the overall column density, the east/west brightness ratio can be used as a probe of electric field strength.

Uniform variations in the electron density also change the shape of the corona. The sodium lifetime is inversely proportional to the electron density. The general trend is that the longer the sodium lifetime, the flatter and more extended the corona. Therefore, increasing the electron density creates a steep corona which remains close to Io. Decreasing the electron density forms a more shallow corona, but the slope only decreases to a point. Without the influence of Io's gravity, neutrals escaping without ion-

ization would have a column density profile proportional to b^{-1} . Io's gravity increases the slope such that for the average modeled flux distribution with $v_p = 0.7 \text{ km s}^{-1}$, the slope with infinite lifetime is ~ 2.2 . To form a more shallow corona, it is necessary to reduce the importance of gravity by increasing the most probable speed of the escaping neutrals.

Changes in the ion temperature only affect the scale height in the corona and therefore do not have as large an effect on the corona as factors which affect the torus at all magnetic longitudes. The main effect is to reduce the System-III variability in the corona, although this variability is not very strong to begin with. Therefore it would be difficult to detect ion temperature variations in the torus by studying the corona. An additional effect of ion temperature increases is that the average lifetime in the corona is slightly longer due to the fact that there is a smaller departure from the maximum electron density. Therefore, the steepness of the corona is a weak function of the ion temperature.

Magnetic longitude variations in the torus have an effect on the coronal shape best seen by looking at the total sodium column through the corona. The brightness modulation is a double peaked function of magnetic longitude. The ratio of the brightnesses of these peaks is a function of the amplitude of the magnetic longitude variations. This a result of the fact that the tilt of torus causes a double peaked variation in the electron density which is modulated by the single peaked magnetic longitude variation. The magnitude of this effect is small, but should be detectable.

The observed inner/outer asymmetry most likely results from asymmetric loss from Io. The effective source rate from the sub-Jupiter hemisphere must account for 70% of the total sodium source. A possible mechanism for creating asymmetric loss from Io's exobase (i.e., an asymmetric coronal source), is an increase in the ionization rate close to the exobase from the interaction between Io and Jupiter's magnetic field. The interaction region is closer to Io than that measured by the mutual events. Increasing

the ionization rate reduces the supply rate of neutral sodium to the outer hemisphere creating the observed asymmetry.

The oxygen and sodium coronae have distinct morphological differences. Both the radially averaged slopes and the nature of their asymmetries are different. The different slopes cannot be explained by the difference in neutral lifetimes between the two species. If the difference in slopes is due to density differences, the shallower oxygen corona implies that the most probable speed of oxygen must be greater than sodium. Assuming a sputtering distribution, the most probable speed must be $\sim 1.4 - 2 \text{ km s}^{-1}$. However, dissociation of SO_2 , a source mechanism available to oxygen but not sodium, could supply faster oxygen near the exobase or resupply the corona farther out. The difference in slopes could also be a result of the fact that oxygen intensity, rather than column density, was observed. An increase in electron temperature with increasing distance from Io, as observed by Voyager, decreases the slope of the radial intensity profile of oxygen.

The mechanism proposed for the sodium asymmetry does not create an inner/outer oxygen column density asymmetry; it does create an asymmetry in the oxygen emission close to Io's surface but not in the corona. The downstream/upstream asymmetry may result from increased electron density in the plasma torus wake (Wolven et al. 2001) or could imply a leading/trailing asymmetry in the oxygen source rates from the exobase. Due to the complex nature of the Io interaction and the strong dependence on the instantaneous state of the plasma on the emission rate it is not possible to distinguish between an emission rate asymmetry and a column density asymmetry.

Chapter 7

Io's Extended Neutral Clouds

7.1 Introduction

The previous chapter discussed neutrals close to Io in the corona. The atoms in the corona are a mix of bound and escaping atoms ejected from Io's exobase. This chapter describes the atoms which escape from the corona; i.e., the atoms sputtered from Io's exobase with escape velocity. This represents the higher speed portion of the distribution, a sufficient number of atoms escape to make the extended and highly photogenic neutral clouds. Understanding the rate and directional distribution of the high speed portion of the sputtered velocity distribution provides details of the interaction between the plasma torus and Io's atmosphere: neutral cloud formation is a direct result of plasma bombardment at Io.

The model developed in Chapter 5 can address several questions regarding the neutral clouds and their changing morphology:

- What are the morphological features in the cloud and how are they explained through the motions of the neutrals?
- What are the significant differences between the sodium and oxygen cloud distributions?
- What effect does the torus have on the shape and extent of the cloud?
- What effect does the torus have on the emission from the oxygen cloud?

Understanding the origins of the morphological features and the complications associated with interpreting images and spectra of the extended neutral clouds are essential for determining the actual distributions of neutrals orbiting Jupiter. This chapter is therefore focused on answering these questions. Section 7.2 discusses the application of the model to the problem of the extended neutral cloud. I also describe the process of extracting measurable quantities from modeled images. In Section 7.3 I describe the morphological similarities and differences between the sodium and oxygen clouds. There are two types of differences: density differences which imply differences in the distributions of the atoms, and brightness differences which result from geometrical parameters specific to observations and peculiarities of the emission mechanisms. I also discuss the effect of the torus on the extent of the clouds. The next section introduces the sodium image archive containing over ten years of imaging data. These images will be essential for the future work with this model. The last section, Section 7.5 summarizes the results and includes a discussion of the joint analysis of the model and data.

7.2 Neutral Cloud Models

The workings of the neutral cloud model has already been described (Chapter 5): packets ejected from Io were tracked under the influence of gravity and lost by electron impact ionization and charge exchange in the plasma torus. Model images were created from the positions and un-ionized fractions of each packet. In Chapter 6, the model runs focused on the region within $\sim 10 R_{\text{Io}}$ of Io as the area of interest was Io's corona. In this chapter, I concentrate on the extended neutral clouds of sodium and oxygen. Therefore, unless otherwise specified, all model images show the region within $10 R_{\text{J}}$ of Jupiter which includes Io's orbit and the outer edges of the neutral clouds. Models of the sodium cloud had a modeled duration of 50 hours, about 1-1/4 Io orbits around Jupiter. Because neutral oxygen has a significantly longer lifetime, the total time of

oxygen simulations was 200 hours. Other specific inputs to the model runs are discussed where appropriate.

The analysis of model images depended on the behavior or features being investigated with the model runs. Two basic methods were employed: (a) qualitative analysis of two-dimensional modeled images, and (b) radial decomposition of images into basic, measurable quantities.

Images of the neutral clouds from above Jupiter's north pole and as observed from Earth allow large structures to be examined (Figure 7.1). Images of this nature allow a qualitative comparison of the neutral clouds under different conditions. The view from above, not available to Earth-bound observers, helps describe the three-dimensional distribution of the neutral atoms. In addition to varying the viewing angle, several choices of the observed quantity are also available. The images in Figure 7.1 show the column density; it is also possible to form images in units of brightness (see Section 7.3.3 below). Column density images, although not of the observable quantities, are not dependent on the peculiarities of the different emission mechanisms. Images in brightness units are strongly dependent on the state of the plasma torus, in the case of oxygen, or the solar Fraunhofer lines, in the case of sodium.

A more quantitative analysis of the images is also possible by performing a radial decomposition to extract several basic quantities. This method allows model images to be compared to other models and provides quantities which can be extracted from images of the neutral clouds (see Section 7.4), making quantitative analysis of the neutral cloud in imaging data possible. The quantities peak intensity, direction, and width of the neutral cloud provide a simple way of describing the complex and asymmetric neutral clouds. Each quantity is measured as a function of distance from Io for the leading and/or trailing clouds. The peak intensity of the the cloud is defined as the maximum intensity along an arc with the constant radius r from Io. The direction is the angle along that arc from some reference point. I measure this angle clockwise from Jupiter

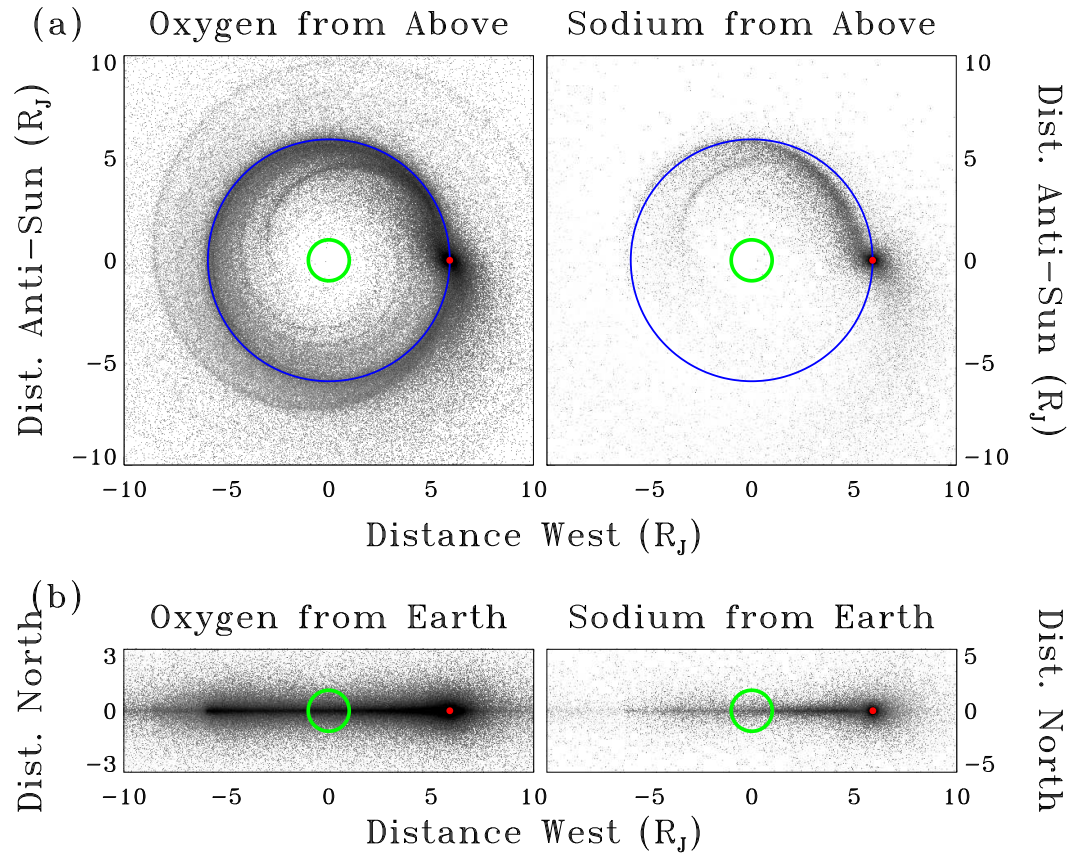


Figure 7.1 Examples of neutral clouds models. The left half shows the oxygen cloud column density from (a) above Jupiter's north pole and (b) Earth. Panels (c) and (d) show the sodium column density from above and Earth, respectively. The green circles indicate the location of Jupiter; the blue circles shows Io's orbit. Io is at western elongation.

north in model images unless otherwise specified. The width is the full width at half maximum measured in radians, for the angular width, or Jupiter radii, for the linear width, with $W_{Rj} = W_{\theta}r$.

To extract these values, the model images are binned into concentric rings about Io with each bin having a constant depth (dr) and width ($d\theta$), both measured in Io radii (Figure 7.2). All the bins in an image have equal area; the number of bins in a ring increases as the distance from Io increases. Plots of an arc at a constant radius (Panel (c)) allow the location of the center of the cloud, the peak intensity of the cloud (Panel (d)), and the full width at half-maximum (FWHM, Panel (e)) to be measured. These quantities are then determined as a function of the distance from Io.

7.3 Large Scale Features

Examples of modeled clouds of oxygen and sodium are shown in Figure 7.1. The column densities are scaled relative to their source rates from Io's exobase; i.e., the greater column density of oxygen is a result of the difference in ionization rates of the two species, not their source rates. Several morphological features can be seen in these images; specifically, the leading sodium cloud interior to Io's orbit, the complete torus of neutral oxygen, and the sharp, well defined edges of the cloud. The following subsections contain discussions of these features and large scale differences between the sodium and oxygen clouds.

7.3.1 Motions of Neutral Atoms

Atoms ejected from Io in the forward direction make up the trailing cloud. These atoms have Io's velocity plus an added velocity which gives them more kinetic energy than Io and orbits with greater semi-major axes. This causes them to move exterior to Io's orbit. As atoms move exterior to Io, they slow down relative to Io, which passes the atoms resulting in a trailing cloud (Figure 7.3). Conversely, atoms ejected in the

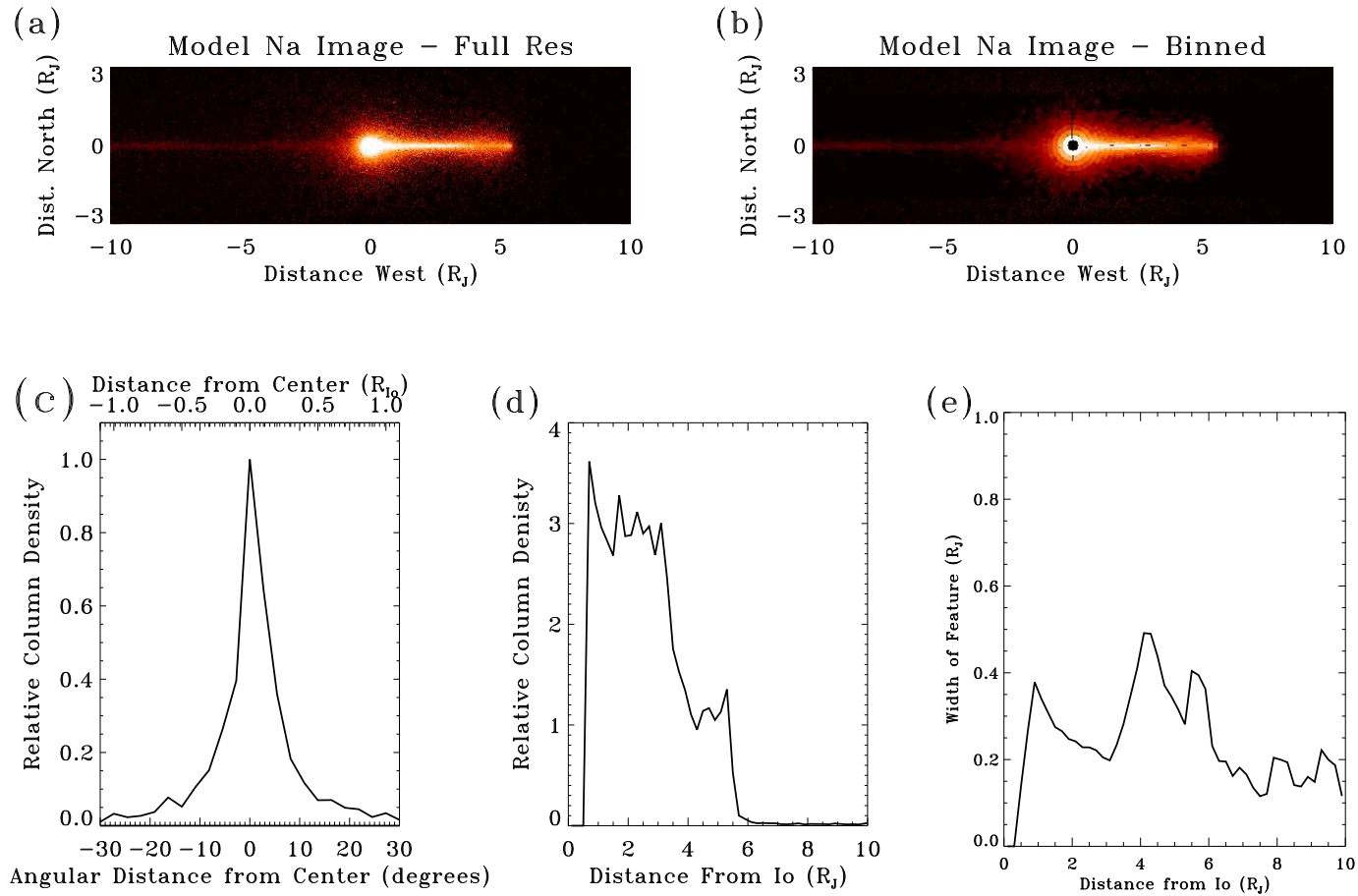


Figure 7.2 Decomposition of a model image into basic observable quantities. (a) Model image at full resolution. (b) Model image binned into concentric circles with each bin having a constant area. (c) Arc through the image at constant distance of $2.1 R_J$ from the center of Io. The angle and distance are measured clockwise from the center of the cloud. (d) Peak intensity versus distance from Io along the forward cloud. (e) Width of the cloud versus distance from Io along the forward cloud.

trailing direction have velocities slightly less than Io's orbital velocity and orbit Jupiter with smaller semi-major axes than Io. These atoms move interior to Io's orbit and will increase their velocities relative to Io forming a leading cloud.

The neutral cloud is composed of atoms with a distribution of initial velocities ejected into all directions. Therefore, understanding these images requires an understanding of how the initial velocity (both speed and direction) and initial location from the exobase affects the course of an atom. Streamlines for atoms as they travel from Io are given in Figure 7.4. In each panel the system is seen from above. Io is at western elongation, east is the negative x (left) direction and the sun is in the negative y (down) direction. The black circles show the location of Io's orbit. Each streamline shows the motion of the atoms relative to Io for 50 hours. Row (1) shows the initial locations and directions of each atom for the column that it heads: column (a) has atoms ejected from the sub-Jupiter point only; column (b) shows ejection from the leading point, column (c) from the anti-Jupiter point, and column (d) from the trailing point. Column (e) shows ejection from all four points together. The following rows each contain atoms ejected with a single velocity: 2.0 km s^{-1} , 2.5 km s^{-1} , 3.0 km s^{-1} , 3.5 km s^{-1} , 4.0 km s^{-1} , 5.0 km s^{-1} , 10.0 km s^{-1} , and 20 km s^{-1} in rows (2)-(9). The actual neutral cloud is made up of superpositions of streamlines of a distribution of velocities that is heavily weighted toward the low speed end of the distribution.

Row (2), which shows atoms with initial velocity 2 km s^{-1} , indicates that atoms with initial speeds less than the escape velocity from the exobase (2 km s^{-1}) contribute to the extended clouds. This is shown in detail in Figure 7.5. . The red streamlines are for the case when Io is a motionless body that is not immersed in Jupiter's gravitational field. In this case, none of the atoms escape from Io. They do, however, travel outside Io's Hill sphere, the effective limit of Io's gravitational domination, before turning around and heading back toward Io. The blue streamlines show the actual situation: Io is orbiting the large planet Jupiter. Under these circumstances, most atoms do escape.

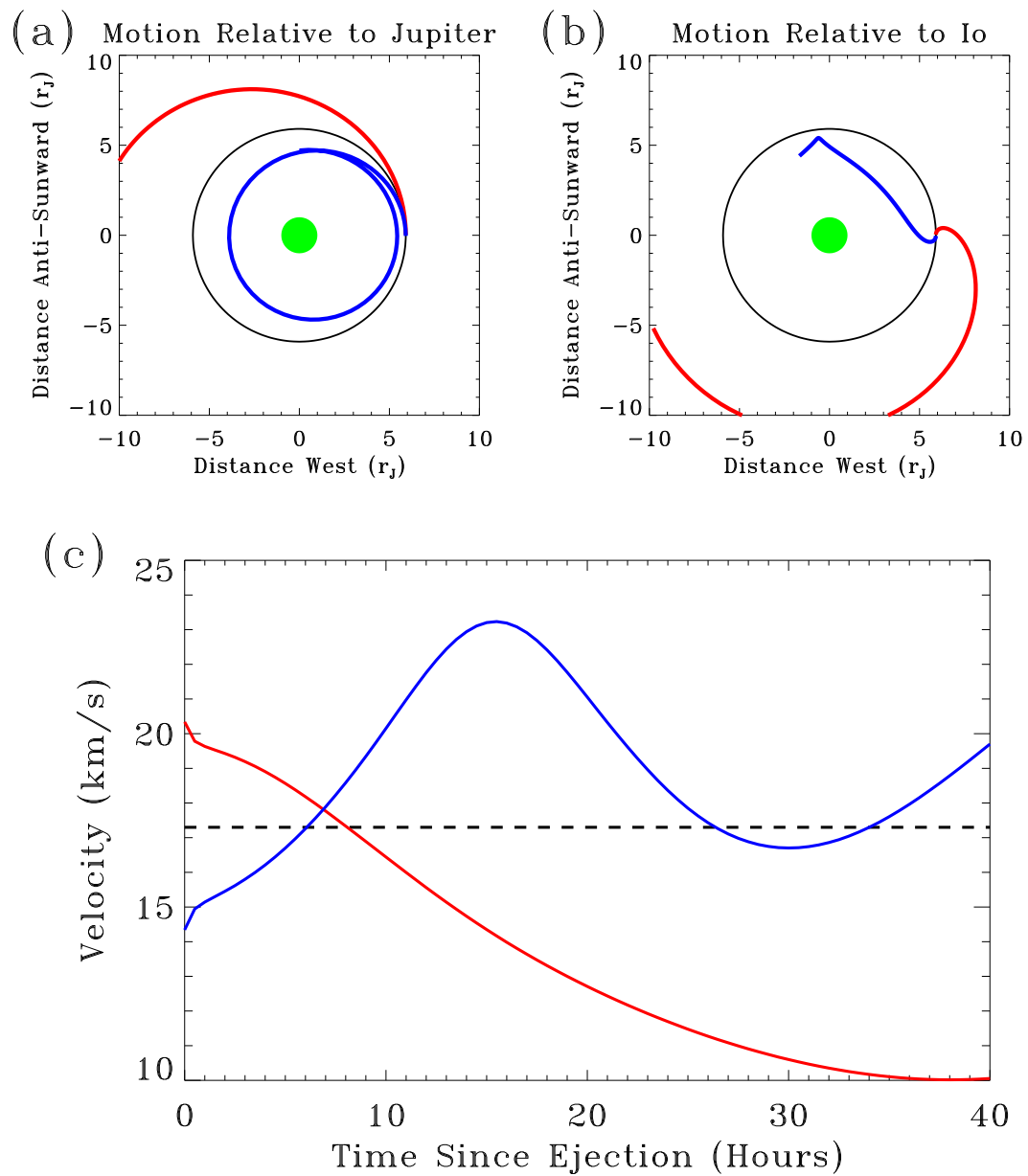


Figure 7.3 Sample trajectories of neutral atoms ejected from Io. The red path shows a sodium atom ejected in the direction of Io's motion; the blue path shows an atom ejected opposite to Io's motion. Both atoms have an initial velocity of 3 km s^{-1} relative to Io. The green filled circles show the location of Jupiter. Io is initially at western elongation; its orbit is shown by the black circle. Panel (a) shows the orbits of the atoms relative to Jupiter as seen from above. Panel (b) shows the motion of the atoms relative to Io. Panel (c) gives the velocity evolution of the atoms relative to Jupiter. The broken black line shows Io's constant orbital velocity.

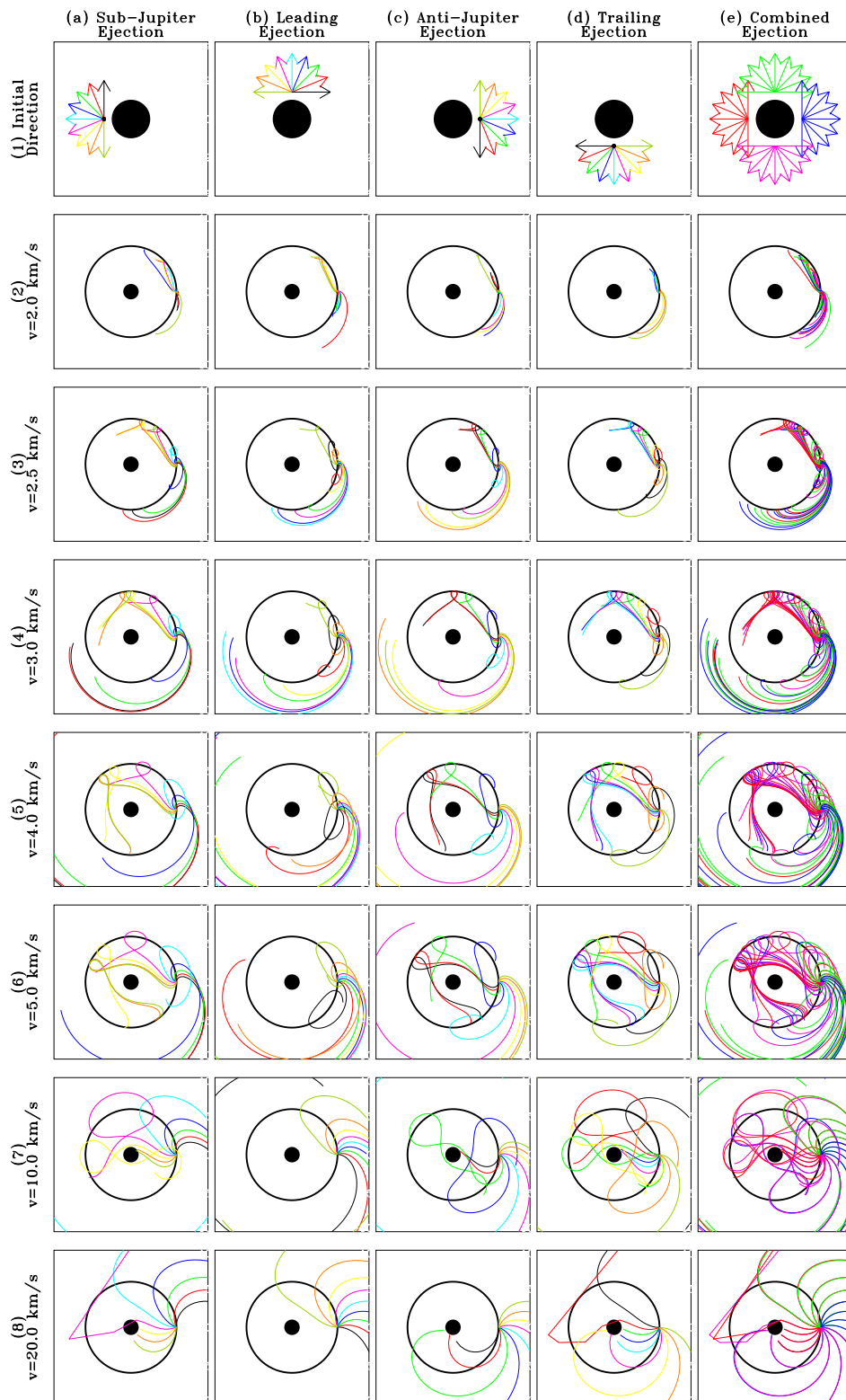


Figure 7.4 Streamlines of atoms ejected from Io with a range of speeds, directions, and location on Io's surface. See discussion in text.

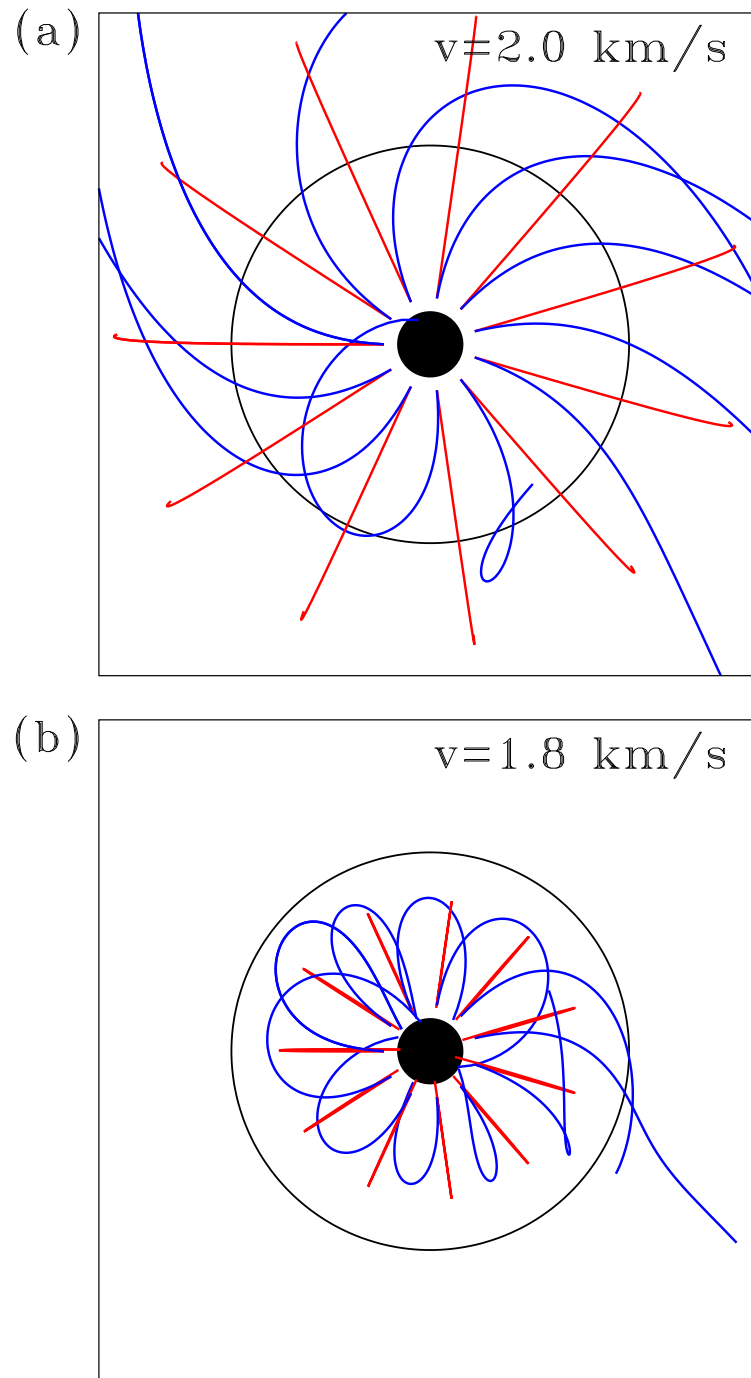


Figure 7.5 (a) Streamlines of atoms ejected from Io with initial velocity of 2 km s^{-1} . The red streamlines show the trajectories when Io is stationary and not immersed in Jupiter's gravitational field. The blue streamlines show their paths when Io is in motion around Jupiter. The black circle at $6 R_{\text{Io}}$ shows the approximate location of Io's Hill sphere. (b) Same as (a) with initial velocity 1.8 km s^{-1} .

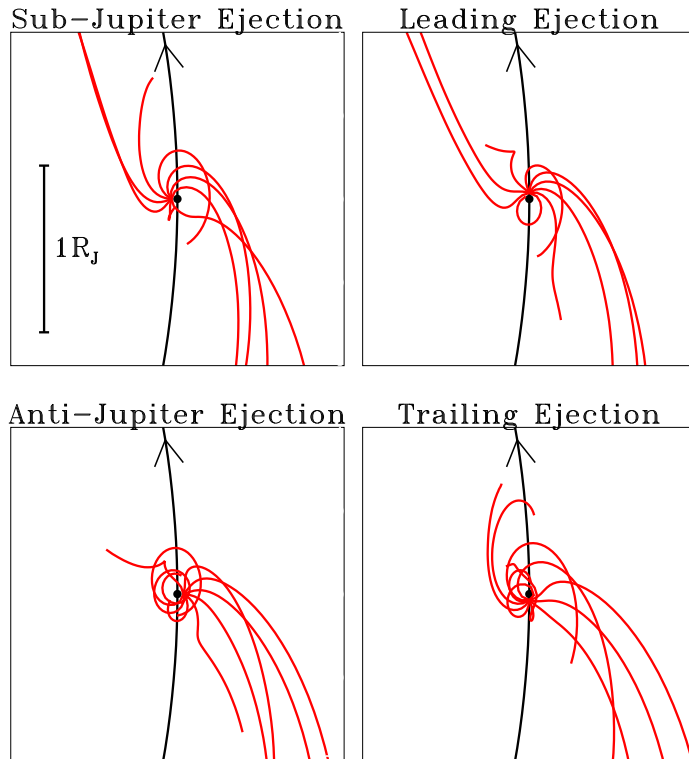
Those that do not are still strongly influenced by Jupiter's gravity: their trajectories are highly perturbed from the Jupiter-less case, but Io is still able to retain control. Panel (b) depicts the same situation for atoms which are not as close to the escape velocity. In this case, the atoms do not make it outside the Hill sphere and their motion is never dominated by Jupiter. The combination of Jupiter's gravity and Io's motion do perturb the streamlines, but in general all of the atoms are bound to Io. A few atoms do escape; conversely, some atoms ejected with greater than escape velocity will not escape.

Another important point is that atoms ejected from any location on the surface can contribute to both the leading and trailing clouds. Atoms with velocities greater than $\sim 2.5 \text{ km s}^{-1}$ are not greatly affected by Io's gravity as they escape the Hill sphere; therefore, the direction the atoms are ejected is the most important factor in determining which part of the extended cloud the atoms join. Atoms in these simulations are ejected isotropically over the hemisphere above each point on the exobase. From each point, some atoms will escape with velocities which puts them into the forward cloud and some with velocities which puts them into the trailing cloud. An intermediate scale view around Io is given in Figure 7.6 to show how atoms from different regions contribute to the extended clouds.

Some of the atoms do in fact hit Jupiter, in which case they are removed from the system. These are the atoms which are ejected in the trailing direction with speed $\sim 17 \text{ km s}^{-1}$. An atom ejected with speed relative to Io that is equal to Io's orbital velocity but in the opposite direction has zero velocity relative to Jupiter and does not orbit; it falls. The atoms with greater speeds can go into retrograde orbit around Jupiter.

The leading cloud shows distinct inner and outer edges. The streamlines in Figures 7.4 and 7.6 help to shed light on the source of these boundaries. The outer edge occurs near Io's orbit at $5.91 R_J$. This is the apojoive of the atoms interior to Io, creating an outer limit to the leading cloud. Because the atoms slow down as they approach

(a) Velocity = 2 km/s



(b) Velocity = 3 km/s

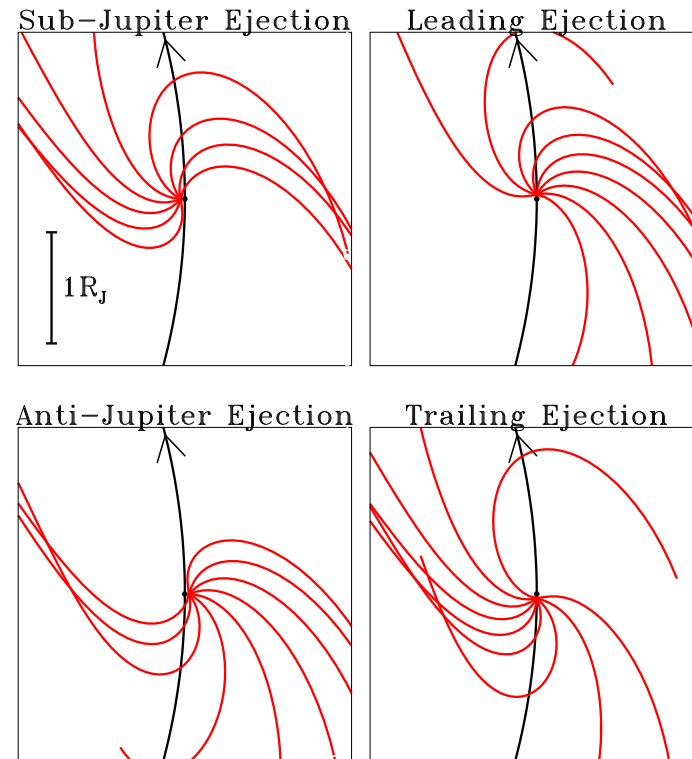


Figure 7.6 Intermediate scale view showing streamlines of atoms from their escape to the exobase into the neutral clouds. In panel (a), all atoms are ejected with an initial velocity of 2 km s^{-1} . In panel (b) the initial velocity is 3 km s^{-1} . The four parts of each panel show escape from four locations on Io as indicated. The angle of escape is distributed over the hemisphere tangent to the surface at the point of escape. The scale of each panel is indicated: panel (a) is a $2 R_J$ by $2 R_J$ square centered on Io (shown to scale by the black filled circle) which is at western elongation, and panel (b) is a $3 R_J$ by $3 R_J$ square. Io's direction of motion is up in the image along its orbit (shown in black).

apojove, a density enhancement is created resulting in the brightening of the outer edge. The inner edge is due to the unequal distribution of streamlines in the leading cloud: ejection over a variety of angles leads to overlapping streamlines and an over-abundance of atoms in the inner edge. Column (e) of Figure 7.4 shows that for velocities between ~ 2 and 4 km s^{-1} , there are more streamlines at the inner edge of the cloud than the outer edge of the cloud creating the density enhancements seen in the model images. In the trailing cloud, the streamlines are more evenly distributed, so there are no density enhancements or sharp, well defined edges.

7.3.2 Loss of Neutral Atoms

Based on these motions, one might expect to see both leading and trailing clouds around Io. Some of the earliest observations of sodium (e.g., Trafton and Macy (1975)), however, showed that the sodium cloud is predominantly a leading cloud: only the portion of the cloud leading Io in its orbit extends around Jupiter. Observations of the oxygen are more difficult, and therefore far fewer in number. The published observations of neutral oxygen outside the corona are inconclusive regarding the angular extent of the oxygen cloud. Brown (1981a) detected oxygen $\sim 180^\circ$ away from Io, but could not determine from this observation if this emission was from the leading edge of the leading cloud or from a complete oxygen torus. More recent spectra (Thomas 1996) concentrated on the leading cloud and did not search for a trailing cloud.

The first attempts to understand the leading sodium cloud assumed non-isotropic ejection of sodium from Io since no mechanism for asymmetric loss was known. The discovery of the plasma torus provided such a mechanism (Trafton 1980; Smyth 1983). The first detailed treatment of the effect of the torus on the sodium lifetime was presented by Smyth and Combi (1988b). The structure of the plasma torus results in a highly non-uniform neutral lifetime. Sodium atoms in the leading cloud, which are interior to Io's orbit, lie mostly in the cold torus where electron temperatures are low and the

lifetime is long ($\gtrsim 7$ hours within $5.7 R_J$). The trailing cloud exterior to Io's orbit is in the warm torus, a region of higher electron temperature and shorter sodium lifetime (~ 3 hours) (Figure 7.7).

The circumstances are similar for oxygen: the neutral lifetime is shorter exterior to Io's orbit than interior. However, this lifetime is significantly longer: the minimum oxygen lifetime in the region near Io's orbit is ~ 20 hours. The sodium lifetime is shorter than this everywhere outside $5.5 R_J$ from Jupiter. Therefore, ionization does not provide such a stringent limit on the size of the cloud and a complete neutral oxygen torus forms rather than a banana-shaped leading cloud. The portion of the cloud trailing Io is made up of atoms ejected in the forward direction which then lag behind Io in its orbit. Because the oxygen lifetime in the warm torus is much longer than the sodium lifetime, oxygen atoms survive long enough to form this additional portion of the neutral clouds. Sodium is ionized too quickly to allow a trailing cloud to be sustained.

7.3.3 Neutral Cloud Brightnesses

The previous sections concern the motions and ionization of neutral atoms and the implications on the column densities of these species. However, remote observations of the neutral clouds are made of line emission brightnesses; column densities must be inferred from the emissions. Figure 7.8 shows brightnesses for the model simulations for which column densities were given in Figure 7.1. The most obvious difference between these figures is that while the oxygen column density is greater and the cloud is more extensive than sodium, its brightness is much less. In this section I discuss some of the some of the factors which must be considered when examining observations. For sodium, the main factors are the effect of the solar Fraunhofer line and the changing viewing geometry from Earth. As oxygen atoms depend on the plasma to excite the emitting electrons, the instantaneous state of the plasma has the greatest effect on the intensity.

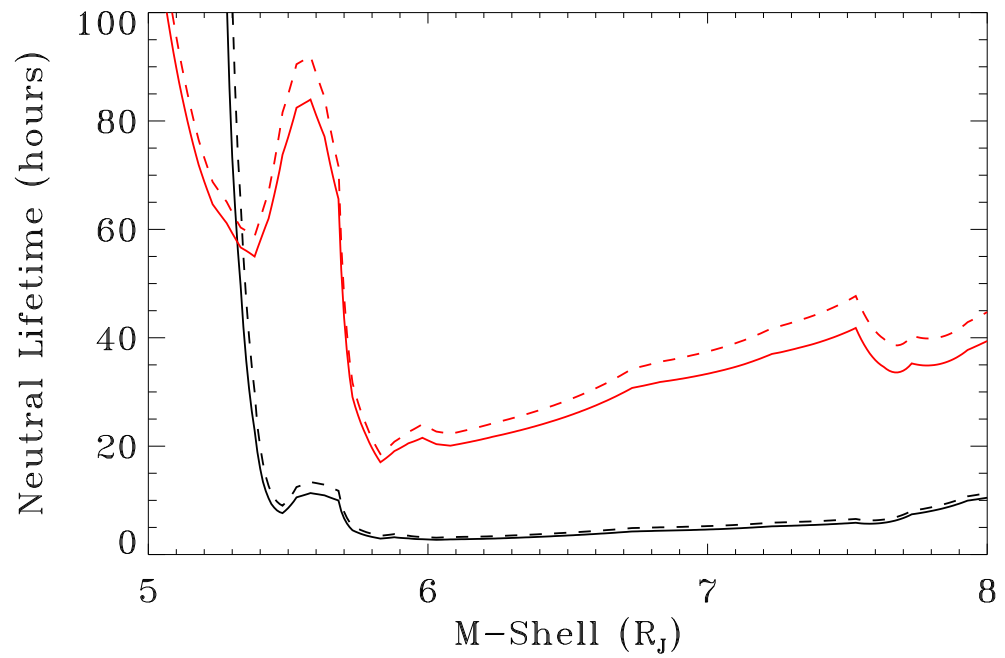


Figure 7.7 Average neutral lifetimes of sodium (black) and oxygen (red) in the torus as function of the modified L-shell parameter M . The solid lines are the lifetimes at western elongation and the broken lines are the lifetimes at eastern elongation.

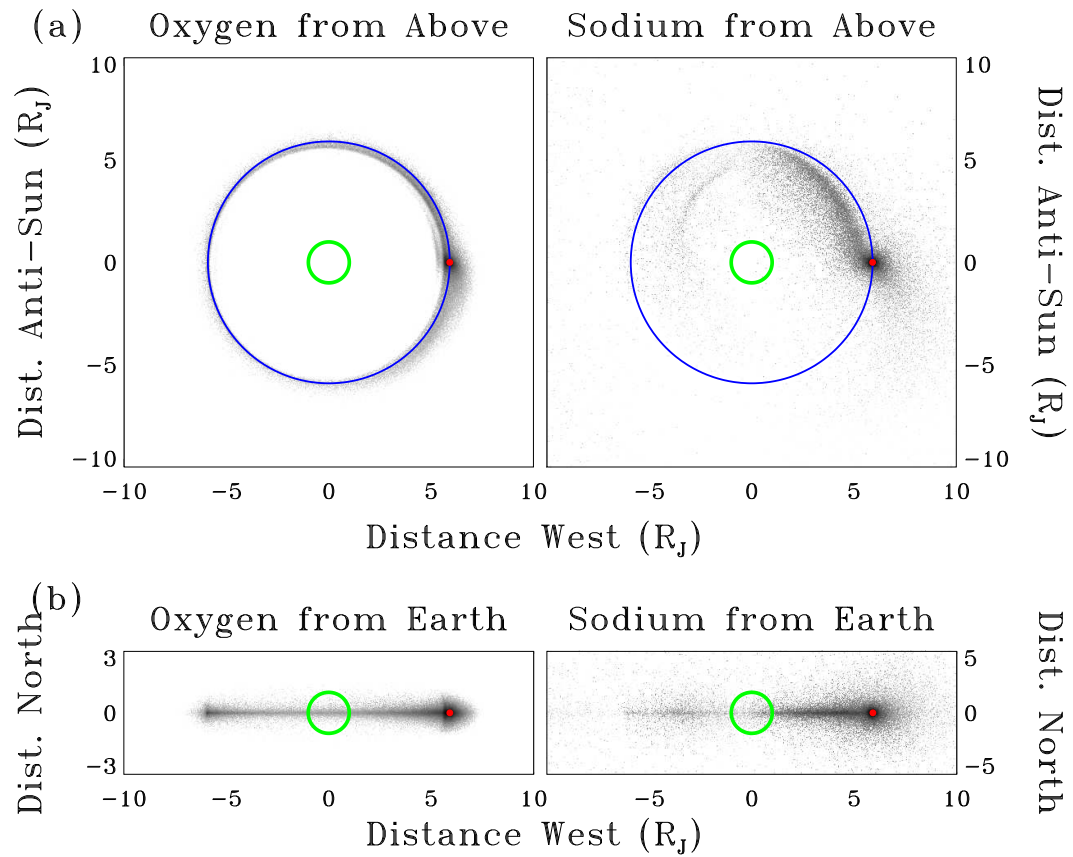


Figure 7.8 Examples of modeled neutral cloud brightnesses. The images were created from the same model runs as the column density images in Figure 7.1.

Factors Affecting Observed Sodium Brightnesses

Io's motion and the motions of the atoms in the cloud result in large variations in sodium intensity which must be understood to determine which brightness variations imply actual changes in the densities of neutral atoms that result from changes in the source or loss rates. Here I will discuss several effects related to the importance of radial velocity relative to the sun and viewing geometry of the sodium cloud on the observed brightness.

The largest factor on the observed intensity and morphology of the neutral cloud far from Io is the changing geometry from which the cloud is viewed as Io orbits Jupiter. Because the cloud is banana shaped and extends along Io's orbit, it looks very different when Io is in front of Jupiter, so that the cloud is seen along its side, than when Io is nearing elongation and the cloud is seen roughly head on. Figure 7.9 shows the cloud as seen at several orbital longitudes assuming it is static as Io moves around Jupiter from superior heliocentric conjunction to eastern elongation. The variations in morphology are due entirely to Io's orbital motion and not any sodium density differences. As can be seen, the brightness of the cloud is extremely variable, but should not be confused with real variations in the distribution of neutrals relative to Io. All the visible changes are due to factors which do not affect the cloud itself, just how the cloud is illuminated and viewed.

Close to Io, the sodium brightness is dominated by Io's changing radial velocity relative to the sun. The deep solar sodium D Fraunhofer lines result from absorption by sodium atoms in the sun's atmosphere. The width of these lines are greater than the range of the Doppler shift of Io caused by Io's motion around Jupiter, implying that sodium near Io never experiences the full brightness of the solar continuum. Because of the steep profiles of the Fraunhofer lines (Figure 1.2), the fraction of the solar intensity available to Io (the γ -factor in Equation 2.9) is a strong function of Io's orbital phase. Figure 7.10 shows how the intensity of sodium in the region near Io (i.e., in the corona)

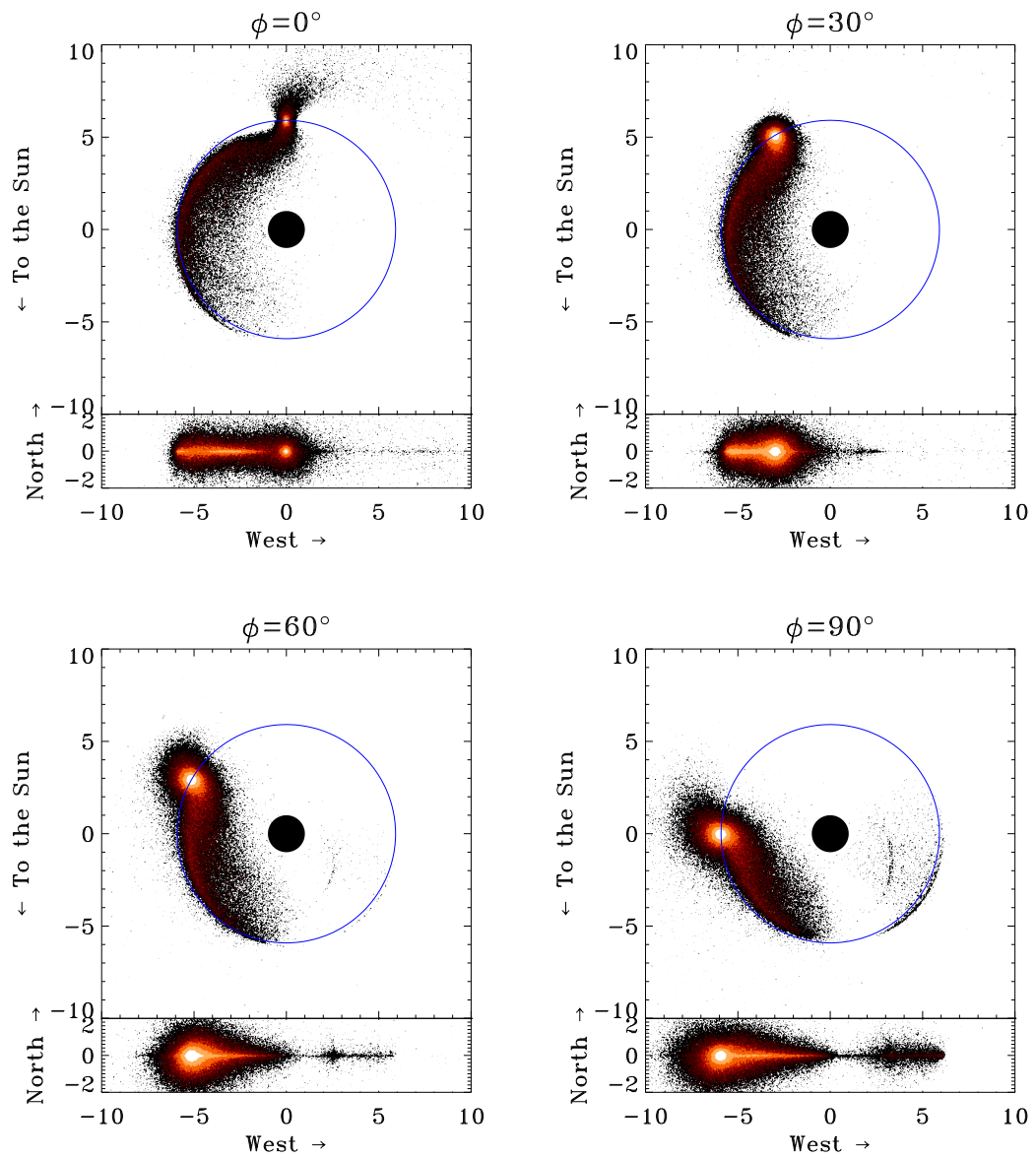


Figure 7.9 The series of images show Io at four orbital phases keeping the sodium cloud densities constant. The Jupiter system is seen from above and from Earth at each location. All differences in morphology are due to the changing viewing geometry and the effects of resonant scattering in the deep solar Fraunhofer lines.

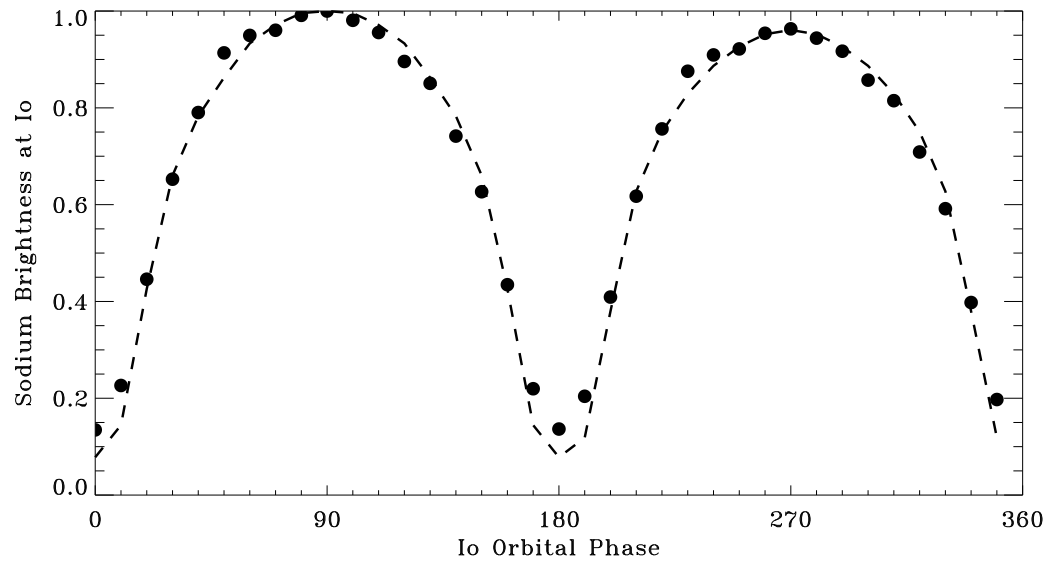


Figure 7.10 Intensity of sodium in Io's corona as a function of orbital phase assuming a static sodium distribution as Io orbits Jupiter. The broken line shows the expected variation in intensity based solely on the changing γ -factor. The intensity is normalized to the brightness at eastern elongation.

varies as Io orbits Jupiter, again assuming that the sodium distribution around Io remains constant. The circles show the relative modeled brightness at Io; over-plotted is the predicted intensity variation based on the changing value of γ . When Io's radial velocity relative to the sun is zero, the intensity of the sodium cloud at Io is $\sim 10\%$ of its peak brightness. Of course, Io cannot be observed at these orbital phases since Jupiter is either blocking Io ($\phi \sim 0^\circ$) or many orders of magnitude brighter ($\phi \sim 180^\circ$), but even for geometries where Io is visible there is a significant change in brightness. The early observations of Io's sodium intensity (Bergstralh et al. 1975; Trafton and Macy 1975) detected these variations as a function of orbital phase and provided the proof that the emission mechanism is resonant scattering. The slight east/west asymmetry in Figure 7.10 stems from an asymmetry in the D₂ Fraunhofer line. The magnitude of this asymmetry is smaller than the observed the east/west asymmetry which is due to asymmetries in the neutral lifetime and represents a physical difference in the corona (Smyth and Combi (1988b) and see Chapter 6).

The large variations in γ also have a significant effect on the the brightness profile of the cloud along its length (Figure 7.11). The column density of sodium along the cloud when Io is at western elongation decreases at a slower rate than the brightness profile because the latter profile combines the effects of the changing density and changing radial velocity. Toward the leading edge of the cloud, the intensity increases despite the fact that the column density is still decreasing. This is because the radial velocity, and therefore γ , is increasing faster than the column density decreases. The rate at which column density decreases slows as the cloud approaches eastern elongation since the cloud turns along the observer's line-of-sight. The cloud brightness however primarily increases due to the additional factor of increasing γ as the radial velocity of sodium increases. The magnitude of this effect is greatest in front of or behind Jupiter where the cloud cannot be observed. However it is important to distinguish which brightening effects on the opposite side of Jupiter from the cloud are due to column density increases

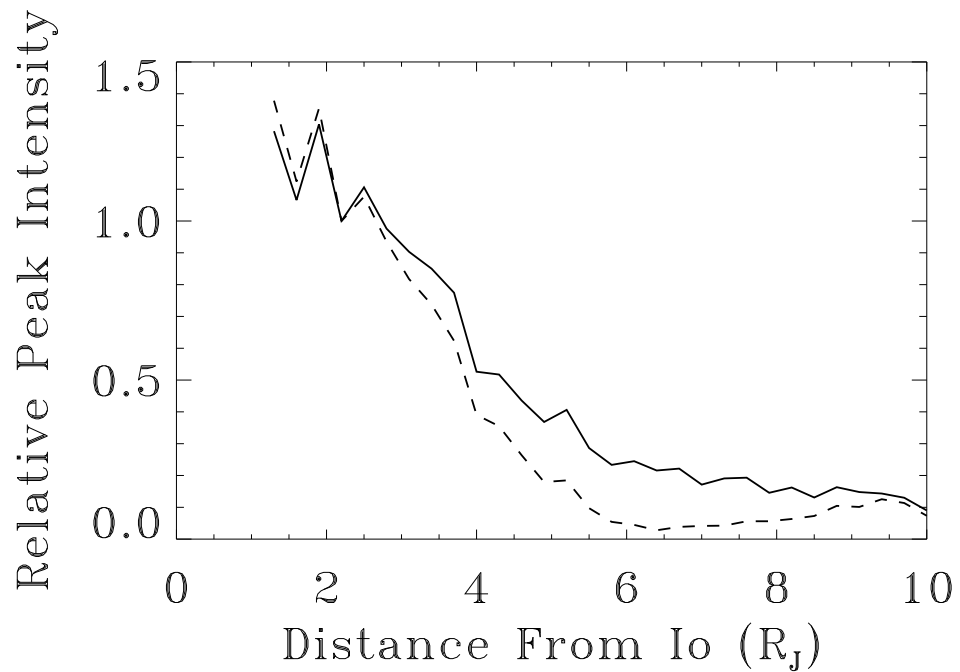


Figure 7.11 A comparison of the column density profile (solid line) and brightness profile (broken line) for the sodium cloud image shown in Figure 7.1. The curves are normalized to unity at 2 R_J from Io. The brightness profile decreases at a faster rate than the column density profile due to the changing value of γ .

along the line-of-sight and which are due to the increasing radial velocity.

A smaller factor also must be considered when comparing the models with data: the angle relative to Io's orbital plane at which Earth-based observers view the sodium cloud varies over the course of Jupiter's twelve year orbit. When comparing images separated by several years, the difference in the sub-Earth latitude of the observer on Jupiter becomes important. Although the emission by sodium and oxygen is isotropic, and is not affected by the direction from which the observations are made, the lines of sight do change and effects the perceived cloud morphology. Figure 7.12 show an example of how the sub-Earth latitude affects the view of the sodium cloud. The effects are most prominent near Io where the densities are the largest. Similarly, phase angle variations over the course of a year change the sight-lines through the cloud and the measured brightnesses.

Factors Affecting Oxygen Brightness

The brightest emission line of neutral oxygen at visible wavelengths ([OI]6300 Å) is excited by electron impacts. Therefore, the intensity of the emission is highly dependent on the state of the plasma torus. Figure 7.13 shows a series of model images of the oxygen cloud where the only parameter which changes between images is Io's magnetic longitude. The shapes and peak intensities of the cloud at greatest elongation from Jupiter are highly variable as a function of the torus orientation (Figure 7.14).

Because the oxygen intensity is such a strong function of the local plasma conditions, it is very difficult to extract the oxygen column density from emission intensity without knowing the state of the plasma torus. The variation in the brightness of the cloud at maximum eastern elongation from Jupiter as several torus parameters vary is shown in Figure 7.14. In the model run from which these images were created, Io is at western elongation, so the intensities are measured 180° away from Io.

Panel (a) shows the variation with magnetic longitude both with and without the effects of the observed System-III variation in the torus. The effect of System-III

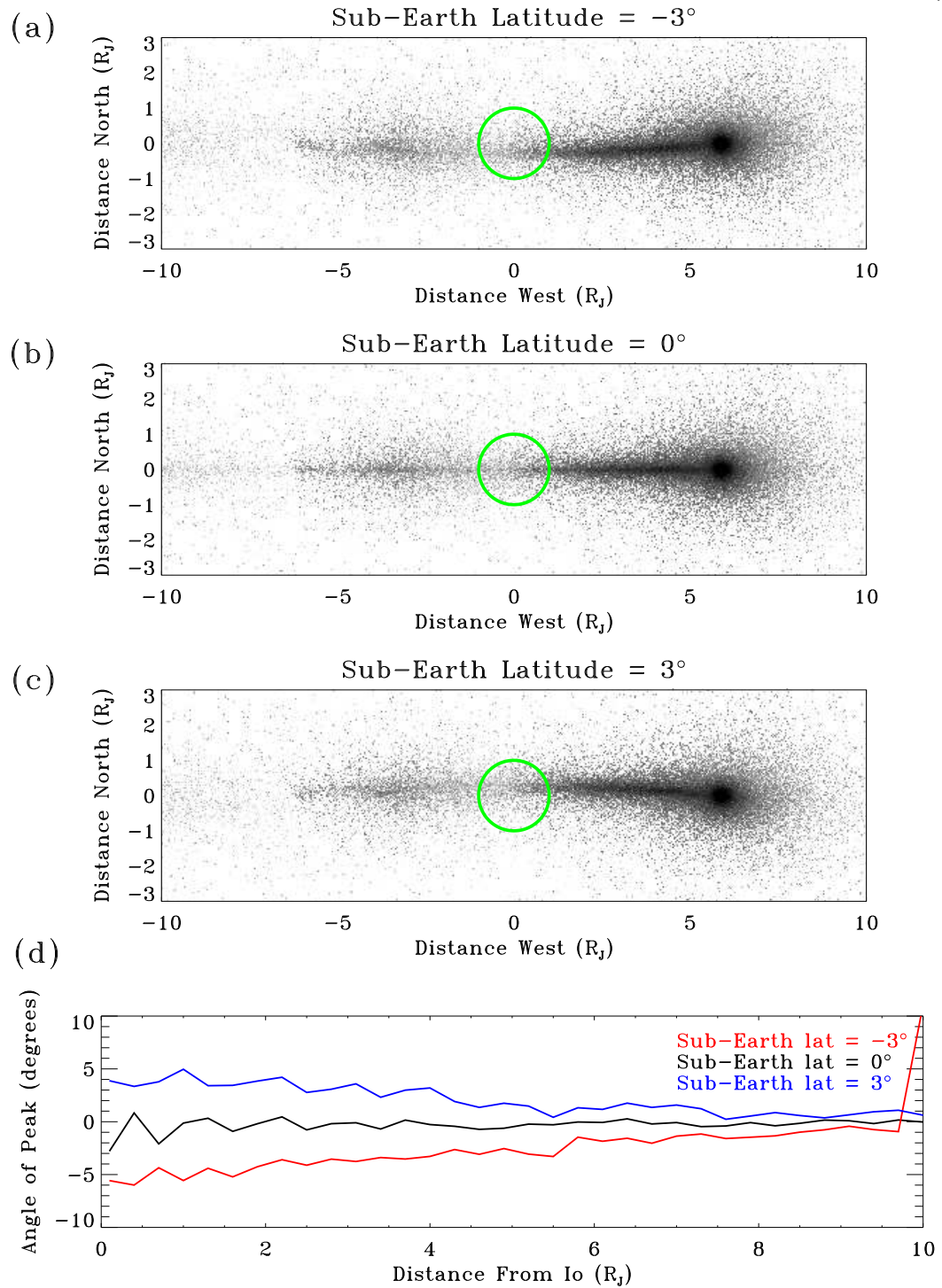


Figure 7.12 The effect of the tilt of Jupiter's equatorial plane relative to Earth. Panel (a) shows the appearance of the cloud when Jupiter's north pole is tilted 3° away from the observer, panel (b) shows no tilt, and panel (c) shows the cloud with Jupiter tilted 3° toward Earth. The green circles show the location of Jupiter in the image. Io is at western elongation. Panel (d) gives the angle of the peak intensity relative to Io's orbital plane for each image. The angle is measured clockwise from East: positive angles indicate that the cloud is rotated north, negative angles are south of the plane.

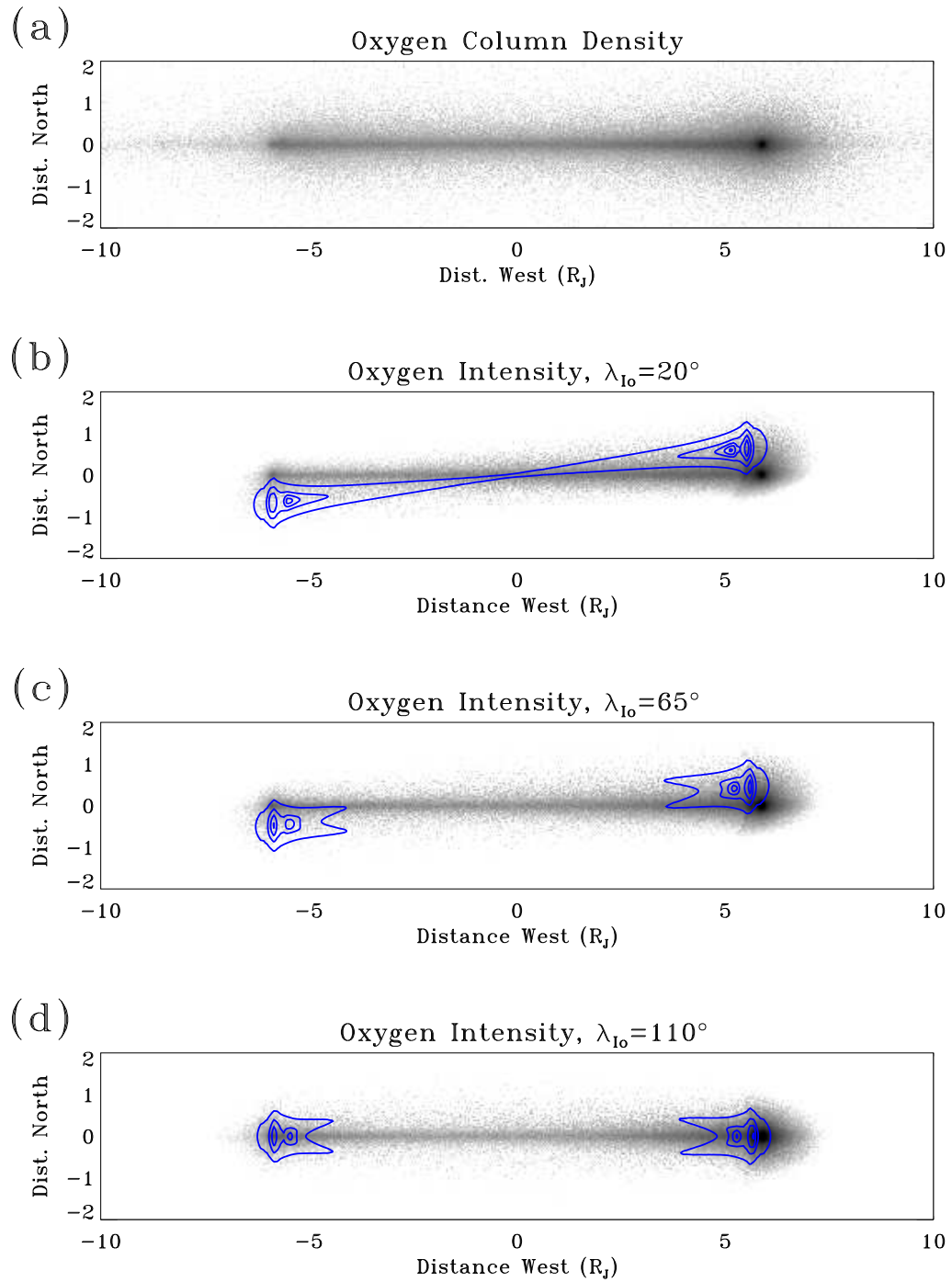


Figure 7.13 (a) Model image showing column density of oxygen as observed from Earth. Io is at western elongation. (b) [OI] 6300 Å brightness for the image in (a) for $\lambda_{Io} = 20^\circ$. The orientation of the plasma torus is shown in blue. (c) Brightness for $\lambda_{Io} = 65^\circ$. (d) Brightness for $\lambda_{Io} = 110^\circ$.

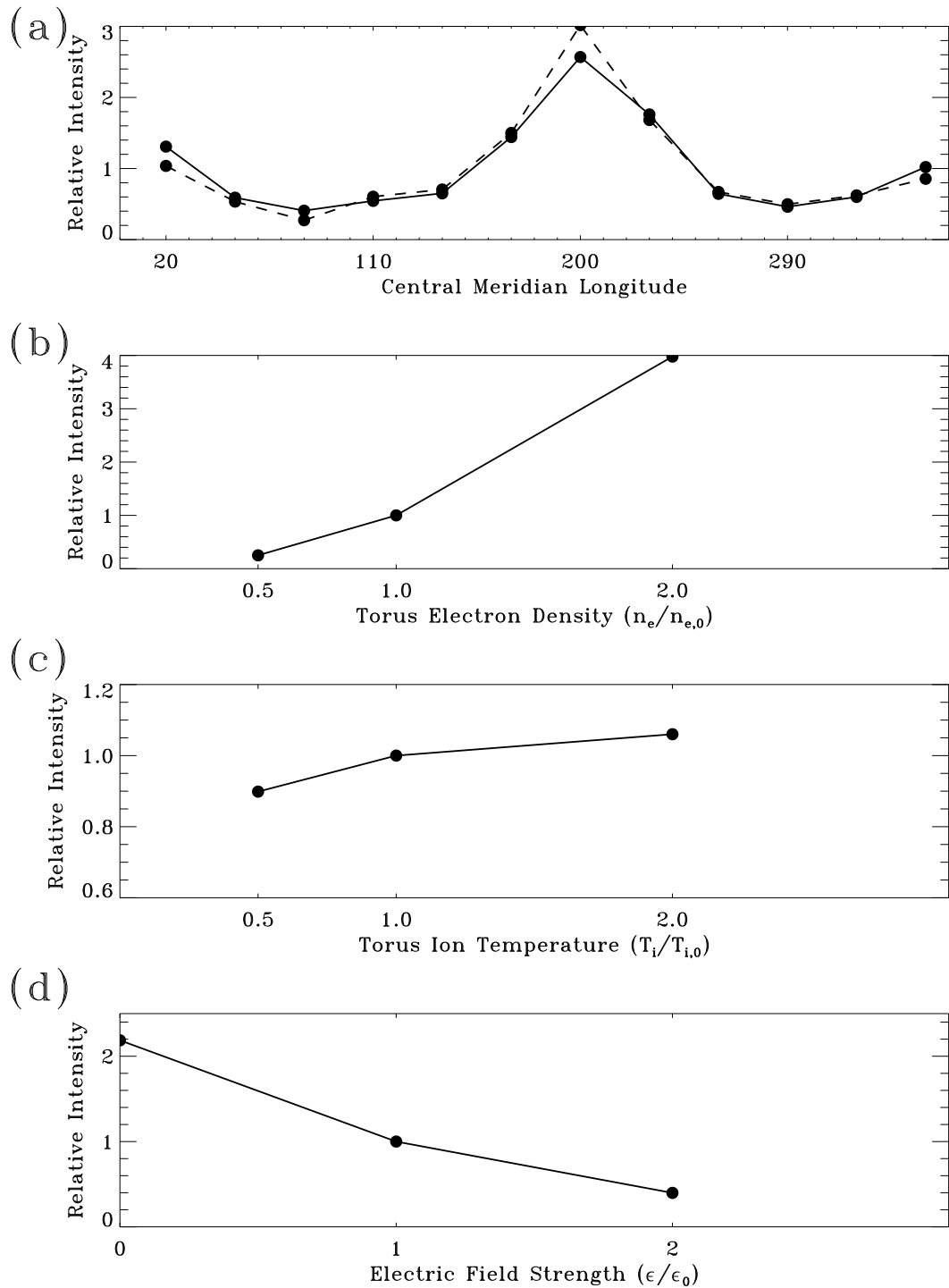


Figure 7.14 Variation in oxygen cloud brightness 180° from Io due to torus variability. Io is at western elongation; brightnesses are measured at eastern elongation at the distance of Io's orbit. (a) Intensity versus CML. The solid line is for a torus has no magnetic longitude variation; the broken line includes the observed variation. (b) Intensity versus torus electron density measured relative to the observed Voyager electron densities. (c) Intensity versus torus ion temperature. (d) Intensity versus east/west electric field strength.

variations are a second order effect on the brightness: the torus geometry is the main factor which determines the brightness. The offset and tilt of the centrifugal equator from the center of Jupiter introduces extreme variability in the intensity despite the fact that the density of oxygen in these images remains constant. Because the magnetic longitude of the observed region is known, it is possible to account for these effects and to coordinate observations with the times of maximum expected emission. Because the System-III variations in the torus have a relatively small effect on the intensity, the uncertainties introduced by this unknown variable are small compared to uncertainties in the overall torus densities and temperatures.

Changes in electron density in the torus (panel (b)) introduce large variability into the oxygen cloud. The emission rate is proportional to the product of the electron density and the emission rate coefficient, which is itself a function of electron density. The result is that relatively small changes in the electron density produce significant changes in intensity. Because the magnitude of the east/west electric field determines the shift of the torus to the east and the amplitude of local time variations in the torus, the intensity is also a strong function of the field strength (panel (d)).

If the electron density and temperature, ion temperature, field strength, and the magnitude of any System-III variability are not known, uncertainties in the column density of oxygen could be as high as an order of magnitude. Therefore determining the densities of oxygen far from Io and using these densities to determine the characteristics of the escape from Io is an uncertain proposition. Observations of oxygen should ideally be coupled with observations of the torus which can determine at least some of these varying parameters so as to reduce the uncertainty in interpreting the oxygen column densities.

7.4 Observations of the Sodium Neutral Cloud

Between 1990 and 2000 a series of observations of neutral sodium and singly ionized sulfur were made from the University of Arizona Catalina Observatory 1.5 meter telescope. Between 1990 and 1994, the JPL Coronagraphic Imager described by Schneider and Trauger (1995) was used. The second set of observations started in 1999 with the LPL coronagraph (Hansell et al. 1995) adapted to observations of Io. Table 7.1 summarizes the observing runs which contributed to the image archive, many of which will be useful for future work on the neutral clouds.

Although the two sets of sodium images from Catalina Observatory used different instruments, the observing techniques were similar. The instruments use coronagraphic optics to reduce Jupiter's intensity and eliminate (or at least minimize) the spikes from Jupiter and the Galilean satellites caused by diffraction off the edges of the secondary mirror and its supports (Lyot 1939). Removing the diffraction features is essential for these observations because the large diffraction spikes off Jupiter in particular can hinder the analysis by obscuring the interesting sodium features. Coronagraphs also provide easy access to the telescope's focal plane. When observing the solar corona, an occulting spot is placed over the sun's disk to observe the much fainter corona. For observations of the inner Jovian system, a neutral density filter is used to cover Jupiter, reducing the planet's intensity by $\sim 10^{-3} - 10^{-4}$ without eliminating it from the images completely. Because Jupiter's intensity is known, it can be used as a standard calibration source present in each image as long as the neutral density filter is calibrated by comparing images of Jupiter with and without the filter in place.

The images were recorded by a CCD which changed between observing runs. The exposure times varied between 120 and 600 seconds. The standard observing strategy was to alternate between exposures through a narrow-band ($\sim 15 \text{ \AA}$) sodium interference filter centered near 5889 \AA and a narrow band interference filter centered on the 6716 \AA

Date	Orbital Coverage	Magnetic Coverage	Number of Images	Lead Observer
10 Jan 1990	136° – 206°	314° – 185°	11	Schneider
11 Jan 1990	334° – 55°	241° – 150°	9	Schneider
12 Jan 1990	174° – 257°	177° – 89°	27	Schneider
7 Feb 1990	92° – 134°	323° – 100°	13	Schneider
8 Feb 1990	270° – 292°	185° – 257°	6	Schneider
10 Feb 1990	314° – 23°	70° – 296°	24	Schneider
30 Jan 1991	24° – 41°	281° – 337°	5	Schneider
31 Jan 1991	170° – 247°	38° – 293°	8	Schneider
1 Feb 1991	16° – 52°	355° – 111°	10	Schneider
2 Feb 1991	217° – 280°	293° – 140°	8	Schneider
4 Feb 1991	260° – 338°	173° – 69°	7	Schneider
5 Feb 1991	100° – 100°	109° – 109°	1	Schneider
6 Feb 1991	305° – 338°	60° – 169°	8	Schneider
21 Feb 1991	126° – 191°	9° – 219°	10	Schneider
22 Feb 1991	323° – 34°	293° – 164°	22	Schneider
23 Feb 1991	221° – 221°	58° – 58°	1	Schneider
24 Feb 1991	64° – 71°	4° – 25°	2	Schneider
25 Feb 1991	207° – 220°	113° – 155°	5	Schneider
26 Feb 1991	69° – 75°	120° – 139°	3	Schneider
5 Feb 1992	232° – 264°	34° – 140°	8	Schneider
9 Feb 1992	309° – 352°	125° – 266°	4	Schneider
26 Mar 1992	289° – 339°	125° – 290°	6	Schneider
30 Mar 1992	23° – 70°	273° – 67°	9	Schneider
31 Mar 1992	228° – 234°	222° – 244°	2	Schneider
10 Feb 1993	74° – 80°	124° – 141°	3	Schneider
14 Feb 1993	175° – 175°	293° – 293°	1	Schneider
24 Jul 1994	30° – 36°	98° – 118°	3	Schneider
25 Jul 1994	219° – 49°	356° – 258°	6	Schneider
26 Jul 1994	52° – 248°	270° – 193°	10	Schneider
27 Jul 1994	255° – 89°	215° – 131°	11	Schneider
28 Jul 1994	101° – 127°	171° – 255°	6	Schneider
30 Jul 1994	148° – 174°	66° – 151°	5	Schneider
11 Oct 1999	151° – 216°	57° – 270°	34	Burger
12 Oct 1999	352° – 54°	354° – 200°	32	Burger
29 Nov 1999	18° – 87°	244° – 110°	34	Burger
30 Nov 1999	225° – 279°	202° – 19°	25	Burger
23 Sep 2000	36° – 67°	89° – 190°	8	Burger
24 Sep 2000	249° – 277°	68° – 159°	9	Burger
25 Sep 2000	80° – 121°	334° – 108°	12	Burger
27 Dec 2000	245° – 312°	292° – 152°	14	Burger
28 Dec 2000	87° – 152°	235° – 85°	20	Burger
29 Dec 2000	289° – 357°	176° – 39°	22	Burger
30 Dec 2000	131° – 196°	116° – 331°	18	Burger

Table 7.1 Summary of all available sodium images

or 6731 Å line of [SII]. These near simultaneous images of Io's neutral sodium features and the plasma torus can be used to look for simultaneous changes in the neutral and plasma environments. In general, the fields of view of the images are large enough to contain the entire inner Jovian system ($\sim 10 R_J$ east and west of Jupiter). Therefore, all the sodium features encircling Jupiter were observed, not simply the sodium near Io. The large field of view in these images has previously been used with great success by Schneider et al. (1991b) who discovered the molecular ion stream on the opposite side of Jupiter from Io. It was also possible to observe both the east and west ansae of the plasma torus simultaneously (Schneider and Trauger 1995). These conclusions drawn from these torus images were used in Chapter 5 to describe the local time and magnetic longitude variations in the plasma torus.

Quantitative measurements of the sodium cloud are difficult since the cloud is not necessarily symmetric and there no obvious shapes to compare with. The basic quantities used to describe the images are the as as those discussed above to describe the models. The method for extracting these quantities was the same as for extracting them from models although the the background subtraction in the images was often not perfectly accomplished, requiring lines to be fit to the background regions of the arc.

7.5 Summary

This chapter describes the basic modeling results of the extended neutral oxygen and sodium clouds. I also discussed many of the difficulties associated with interpreting images and spectra of these species related to the changing viewing geometry, effects of radial motion relative to the sun, and the influence of the plasma torus on the oxygen emission. In addition, the major features in the column density structure were described in terms of the motions of neutral atoms escaping from Io and the ionization of these atoms by the plasma torus.

I also introduced the archive of available sodium images from the Catalina Obser-

vatory which extends back to 1990. Between 1990 and 1994, Schneider et al. obtained data with the JPL Coronagraphic Imager; in 1999 and 2000, I used the LPL Coronagraph to extend this data set. Because the near-simultaneous images were taken of the neutral sodium cloud and the sulfur plasma torus, it will be possible to use this data set in conjunction with the model to better constrain both the variability in the plasma torus and the influence of the plasma torus on the sodium cloud.

Chapter 8

Conclusions

There is something fascinating about science. One gets such wholesome returns of conjecture out of such a trifling investment of fact.

Mark Twain

8.1 Summary of the Thesis

For thirty years observers and modelers have studied the gaseous clouds escaping from Io. The most heavily observed constituent of the clouds, sodium, has continued to demand attention due to the many ways its escape from Io manifests itself, including jets of fast sodium seen escaping from Io's atmosphere and a banana shaped cloud extending close to one million kilometers ahead of Io in its orbit.

The escape of oxygen from Io also exhibits itself in exciting and complex ways. The excitation of its emission by the plasma which acts to ionize it makes the analysis of its brightness morphology both difficult and tantalizing; understanding the distribution of neutral oxygen is intimately coupled with an understanding of the plasma torus. The fact that oxygen is the most abundant species in the neutral clouds and the plasma torus makes the study of oxygen all the more important.

In this thesis I used models and observations of Io's neutral features to study the escape of Io's atmosphere and the source regions of the plasma torus. These studies were complicated by the inherent difficulties involved in studying extremely time-variable phenomena. In spite of these difficulties, I have discovered a new feature of

Io's corona, advanced the understanding of previously observed phenomena with unique observations, helped compile an extensive and unique data set, developed a framework for analyzing future observations, and made predictions of the shape and interactions of the neutral clouds with the plasma torus. Below I summarize the main goals of each chapter. In the following section I describe my success in obtaining these goals and list the major accomplishments of this thesis.

The physical processes which are important for understanding the neutral clouds were reviewed in Chapter 2. The sodium neutral cloud is observed both in emission and absorption through the process of resonant scattering; oxygen line emission is excited by electron impacts which is strongly dependent on the state of the plasma torus. The dominant loss mechanism that forms the corona and neutral clouds is sputtering off the atmosphere and surface by plasma torus electrons. Neutral atoms are lost from the system by ionization. Ionization of sodium atoms occurs primarily through electron impacts. Oxygen is lost mainly by charge exchange with plasma torus ions. Sulfur exhibits a mix of the two mechanisms. Between their ejection from the atmosphere and their loss into the plasma torus, the paths of the atoms are determined by the force of gravity. Sodium atoms also experience a slight perturbation from radiation pressure.

Chapter 3 presented a new series of mutual event observations of Io's sodium corona. Mutual events have been the only method for determining the shape of the sodium corona. Data from three telescopes were analyzed to search for time variability and spatial asymmetries in the sodium corona.

A jet of fast sodium has been observed to extend many Jovian radii from Io (Goldberg et al. 1984; Pilcher et al. 1984). This feature, however, had never been observed close to its source in Io's ionosphere. Galileo observations of this fast sodium jet were presented in Chapter 4. Implications of the observation for Io's ionosphere were discussed.

Chapter 5 contained a description of the neutral cloud model that is used in

Chapters 6 and 7 to study Io's corona and neutral clouds. In addition to describing the model itself, I developed a new method for parameterizing the plasma torus such that the state of the plasma can be described as a function of the position relative to Jupiter and the magnetic longitude. The description relies heavily on observations of the torus (Bagenal 1994; Schneider and Trauger 1995; Brown 1994) and includes the effects of Jupiter's offset tilted dipole field, the dawn-dusk electric field, and observed variability of the torus with magnetic longitude. I also discuss several tests of the model including the first modeling analysis of the observed dependence of the north/south brightness ratio in the sodium cloud with magnetic longitude.

A detailed study of Io's neutral corona is presented in Chapter 6. After first determining the velocity distribution of neutral atoms from the exobase which best models the sodium corona observed in Chapter 3, I describe the effects of variations in the source distribution and in the loss by the plasma torus. I also present a model analysis of the sodium corona asymmetry which I discovered. The chapter ends with a comparison of the oxygen and sodium coronae based on HST/STIS observations of oxygen (Wolven et al. 2001).

Chapter 7 focused on the similarities and differences in the extended neutral clouds of sodium and oxygen. A model analysis was presented to explain morphological features in both the column densities and emission intensities of modeled images. In particular, I discuss the strong dependence on the observing geometry of the clouds, the variations in sodium brightness with orbital phase, and the effects of the plasma torus on oxygen observations. I also present an archive of sodium images which will be used in conjunction with the neutral cloud model to study variability in Io's neutrals.

8.2 Major Results

The modeling and observational studies presented here have yielded answers to several outstanding questions regarding Io's neutral clouds. These results are summa-

rized here for the different regions which I studied:

(1) Io's Corona:

- Comparison of mutual events from 1985, 1991, and 1997 have demonstrated remarkable stability in the sodium corona despite large short term event-to-event variations. This implies that although Io's atmosphere and the plasma torus are both highly variable, on average each remain roughly constant.
- I discovered a previously undetected asymmetry in Io's corona between the sub-Jupiter and anti-Jupiter hemispheres: the corona above the inner hemisphere is denser than above the outer hemisphere. This asymmetry implies asymmetric loss from Io's exobase. Approximately 70% of the source sodium in the corona was ejected from the sub-Jupiter hemisphere.
- The oxygen corona has been observed to be more extended than the sodium corona. If this difference is due to column density differences between oxygen and sodium it implies that oxygen is ejected from Io at a faster average velocity. The longer oxygen lifetime cannot explain the magnitude of the observed difference. The increased velocity may be due to differences in the sputtering of the two species or may indicate that oxygen escapes from Io due to a second mechanism in addition to any loss by sputtering. The difference may also result from the fact that the electron temperature in the plasma torus decreases close to Io as observed by Voyager.
- The mechanism for creating the inner/outer asymmetry in the sodium corona is not responsible for creating an asymmetry in the oxygen column density. It is not possible to distinguish whether the upstream/downstream oxygen asymmetry is a result of differences in the emission rates of oxygen between the two regions or indicative of column density differences without

detailed modeling of the effects of Io's interaction with the torus on the plasma parameters.

- The variable and complex apparent motions and brightness variations of the plasma torus relative to Io cause large variations in the neutral lifetime at Io. These variations affect both the brightness in the the corona and the rate at which the density decreases as a function of distance from Io. The different ways in which the torus changes introduce local time, magnetic longitude, and non-periodic variability in the corona.
- A confirmation of the source mechanism described by Smyth and Combi (1988b) for the east/west brightness ratio in the corona was presented. The explanation for this asymmetry was expanded by showing that the column density at Io's surface does not change as a function of Io's orbital phase and that the asymmetry results from a change in the spatial extent of the corona.

(2) Io's fast sodium jet:

- I presented the first image of Io's fast sodium jet within several Io radii of Io providing support for the resonant charge exchange model of the jet formation described by Wilson and Schneider (1999).
- The jet originates from a region smaller than Io's diameter implying that Io's ionosphere is concentrated near the equator, consistent with observations that the atmosphere is also denser near the equator (Feldman et al. 2000)

(3) Io's extended neutral clouds:

- The plasma torus introduces a magnetic longitude variation in the north/south brightness ratio of sodium in the neutral cloud as predicted by Trafton

(1980).

- The oxygen neutral cloud is significantly larger in extent than the sodium cloud. Observations of oxygen are difficult to make due to the fact that the oxygen emissions are faint compared to scattered light from Jupiter and telluric air glow emissions. In addition, the nature of the emission mechanism makes it difficult to extract column densities from the oxygen intensities without knowledge of the state of the local plasma.
- The large available data set of neutral sodium images combined with the neutral cloud model and near-simultaneous images of the plasma torus will help determine the large term variability in both Iogenic neutrals and plasma.

It is also important to note that although there has been a long history of observing the minor species sodium, new discoveries are still being made. I have presented in this thesis two new observational results based solely on the observations of sodium: the inner/outer asymmetry in the corona and the size of the source region of the sodium jet. Therefore it is essential to study the sodium data set, and other data sets which have not been adequately mined, for the wealth of new results which they should be expected to contain.

Bibliography

- Arlot, J.-E., New constants for Sampson-Lieske theory of the Galilean Satellites of Jupiter, *Astronomy and Astrophysics*, **107**, 305–310, 1982.
- Arlot, J.-E., Predictions of the mutual events of the Galilean satellites of Jupiter occurring in 1997., *Astronomy and Astrophysics*, **314**, 312–314, 1996.
- Arnaud, M., and R. Rothenflug, An updated evaluation of recombination and ionization rates, *Astrophysics and Space Science, Supplement Series*, **60**, 425–457, 1985.
- Bagenal, F., Empirical model of the Io plasma torus: Voyager measurements, *Journal of Geophysics Research*, **99**, 11,043–11,062, 1994.
- Ballester, G. E., H. W. Moos, P. D. Feldman, D. F. Strobel, M. E. Summers, J.-L. Bertaux, T. E. Skinner, M. C. Festou, and J. H. Lieske, Detection of neutral oxygen and sulfur emissions near Io using IUE, *Astrophysical Journal, Letters to the Editor*, **319**, L33–L38, 1987.
- Ballester, G. E., M. A. McGrath, D. F. Stobel, X. Zhu, P. D. Feldman, and H. W. Moos, Detection of the SO₂ atmosphere on Io with the Hubble Space Telescope, *Icarus*, **111**, 2–17, 1994.
- Barbosa, D. D., and M. G. Kivelson, Dawn-dusk electric field asymmetry of the Io plasma torus, *Geophysics Research Letters*, **10**, 210–213, 1983.
- Belton, M. J. S., et al., The Galileo Solid-State Imaging experiment, *Space Science Reviews*, **60**, 413–455, 1992.
- Bergstralh, J. T., D. L. Matson, and T. V. Johnson, Sodium D-line emission from Io - Synoptic observations from Table Mountain Observatory, *Astrophysical Journal, Letters to the Editor*, **195**, L131–L135, 1975.
- Bergstralh, J. T., J. W. Young, D. L. Matson, and T. V. Johnson, Sodium D-line emission from Io - A second year of synoptic observation from Table Mountain Observatory, *Astrophysical Journal, Letters to the Editor*, **211**, L51–L55, 1977.
- Binder, A. B., and D. P. Cruikshank, Evidence for an Atmosphere on Io, *Icarus*, **3**, 299, 1964.
- Bouchez, A. H., M. E. Brown, and N. M. Schneider, Eclipse Spectroscopy of Io's Atmosphere, *Icarus*, **148**, 316–319, 2000.

- Brown, M. E., The Structure and Variability of the io Plasma Torus, *Ph.D. Thesis*, 1994.
- Brown, M. E., Periodicities in the Io plasma torus, *Journal of Geophysics Research*, **100**, 21,683–21,696, 1995.
- Brown, R. A., Optical line emission from Io, in *IAU Symp. 65: Exploration of the Planetary System*, vol. 65, pp. 527–531, 1974.
- Brown, R. A., The Jupiter hot plasma torus - Observed electron temperature and energy flows, *Astrophysical Journal*, **244**, 1072–1080, 1981a.
- Brown, R. A., The Jupiter hot plasma torus - Observed electron temperature and energy flows, *Astrophysical Journal*, **244**, 1072–1080, 1981b.
- Brown, R. A., and F. H. Chaffee, High-Resolution Spectra of Sodium Emission from Io, *Astrophysical Journal, Letters to the Editor*, **187**, L125, 1974.
- Brown, R. A., and Y. L. Yung, Io, its atmosphere and optical emissions, in *IAU Colloq. 30: Jupiter: Studies of the Interior, Atmosphere, Magnetosphere and Satellites*, pp. 1102–1145, 1976.
- Brown, R. A., R. M. Goody, F. J. Murcray, and F. H. Chaffee, Further studies of line emission from Io, *Astrophysical Journal, Letters to the Editor*, **200**, L49–L53, 1975.
- Burger, M. H., N. M. Schneider, and J. K. Wilson, Galileo's close-up view of the Io sodium jet, *Geophysics Research Letters*, **26**, 3333, 1999.
- Burger, M. H., N. M. Schneider, I. de Pater, M. E. Brown, A. H. Bouchez, L. M. Trafton, Y. Sheffer, E. S. Barker, and A. Mallama, Mutual Event Observations of Io's Sodium Corona, *Astrophysical Journal*, **563**, 1063–1074, 2001.
- Chamberlain, J. W., *Physics of the aurora and airglow*, International Geophysics Series, New York: Academic Press, 1961, 1961.
- Cremonese, G., F. Marzari, N. Eccli, and G. Corrain, The Io Sodium Cloud: Comparison between Observations and Numerical Models, *Icarus*, **131**, 138–151, 1998.
- Dere, K. P., E. Landi, H. E. Mason, B. C. Monsignori Fossi, and P. R. Young, CHIANTI - an atomic database for emission lines, *Astrophysics and Space Science, Supplement Series*, **125**, 149–173, 1997.
- Dessler, A. J. (Ed.), *Physics of the Jovian magnetosphere*, 1983.
- Durrance, S. T., P. D. Feldman, and H. A. Weaver, Rocket detection of ultraviolet emission from neutral oxygen and sulfur in the Io Torus, *Astrophysical Journal, Letters to the Editor*, **267**, L125–L129, 1983.
- Fang, T.-M., W. H. Smyth, and M. B. McElroy, The spatial distribution of long lived gas clouds emitted by satellites in the outer solar system, *Planetary Space Science*, **24**, 577–588, 1976.

- Feldman, P. D., et al., Lyman- Alpha Imaging of the SO₂ Distribution on Io, *Geophysics Research Letters*, **27**, 1787+, 2000.
- Geissler, e., P. E., Galileo imaging of atmospheric emissions from Io, *Icarus*, **285**, 870–874, 1999.
- Goldberg, B. A., Y. Mekler, R. W. Carlson, T. V. Johnson, and D. L. Matson, Io's sodium emission cloud and the Voyager 1 encounter, *Icarus*, **44**, 305–317, 1980.
- Goldberg, B. A., G. W. Garneau, and S. K. Lavoie, Io's sodium cloud, *Science*, **226**, 512–516, 1984.
- Goldreich, P., and D. Lynden-Bell, Io, a jovian unipolar inductor, *Astrophysical Journal*, **156**, 59–78, 1969.
- Hansell, S. A., W. K. Wells, and D. M. Hunten, Optical detection of lightning on Venus., *Icarus*, **117**, 345–351, 1995.
- Hill, T. W., and F. C. Michel, Heavy ions from the Galilean satellites and the centrifugal distortion of the Jovian magnetosphere, *Journal of Geophysics Research*, **81**, 4561–4565, 1976.
- Hinson, D. P., A. J. Kliore, F. M. Flasar, J. D. Twicken, P. J. Schinder, and R. G. Herrera, Galileo radio occultation measurements of Io's ionosphere and plasma wake, *Journal of Geophysics Research*, **103**, 29,343–29,357, 1998.
- Ingersoll, A. P., Io meteorology - How atmospheric pressure is controlled locally by volcanos and surface frosts, *Icarus*, **81**, 298–313, 1989.
- Ip, W.-H., and C. K. Goertz, An interpretation of the dawn-dusk asymmetry of UV emission from the Io plasma torus, *Nature*, **302**, 232, 1983.
- Johnson, R. E., *Energetic Charged-Particle Interactions with Atmospheres and Surfaces*, Energetic Charged-Particle Interactions with Atmospheres and Surfaces, X, 232 pp. 84 figs., 28 tabs.. Springer-Verlag Berlin Heidelberg New York. Also Physics and Chemistry in Space, volume 19, 1990.
- Johnston, A. R., and P. D. Burrow, Electron-impact ionization of Na, *Physical Review A*, **51**, 1735, 1995.
- Kliore, A., D. L. Cain, G. Fjeldbo, B. L. Seidel, and S. I. Rasool, Preliminary Results on the Atmospheres of Io and Jupiter from the Pioneer 10 S-Band Occultation Experiment, *Science*, **183**, 323–324, 1974.
- Kliore, A. J., G. Fjeldbo, B. L. Seidel, D. N. Sweetnam, T. T. Sesplaukis, P. M. Woiceshyn, and S. I. Rasool, The atmosphere of Io from Pioneer 10 radio occultation measurements, *Icarus*, **24**, 407–410, 1975.
- Kumar, S., Photochemistry of SO₂ in the atmosphere of Io and implications on atmospheric escape, *Journal of Geophysics Research*, **87**, 1677–1684, 1982.
- Lellouch, E., Urey Prize Lecture. Io's Atmosphere: Not Yet Understood, *Icarus*, **124**, 1–21, 1996.

- Lellouch, E., T. Encrenaz, M. Belton, I. de Pater, and S. Gulkis, Io's atmosphere from microwave detection SO₂, *Nature*, **346**, 639–641, 1990.
- Lyot, B., The study of the solar corona and prominences without eclipses (George Darwin Lecture, 1939), *Monthly Notices of the RAS*, **99**, 580, 1939.
- Macy, W., and L. Trafton, A model for Io's atmosphere and sodium cloud, *Astrophysical Journal*, **200**, 510–519, 1975a.
- Macy, W. W., and L. M. Trafton, Io's sodium emission cloud, *Icarus*, **25**, 432–438, 1975b.
- Mallama, A., Light curve model for the Galilean satellites during Jovian eclipse, *Icarus*, **92**, 324–331, 1991.
- Matson, D. L., T. V. Johnson, and F. P. Fanale, Sodium D-Line Emission from Io: Sputtering and Resonant Scattering Hypothesis, *Astrophysical Journal, Letters to the Editor*, **192**, L43, 1974.
- Matson, D. L., B. A. Goldberg, T. V. Johnson, and R. W. Carlson, Images of Io's sodium cloud, *Science*, **199**, 531–533, 1978.
- McElroy, M. B., Y. L. Yung, and R. A. Brown, Sodium Emission from Io: Implications, *Astrophysical Journal, Letters to the Editor*, **187**, L127, 1974.
- McGrath, M. A., and R. E. Johnson, Charge exchange cross sections for the Io plasma torus, *Journal of Geophysics Research*, **94**, 2677–2683, 1989.
- McGrath, M. A., M. J. S. Belton, J. R. Spencer, and P. Sartoretti, Spatially Resolved Spectroscopy of Io's Pele Plume and SO₂ Atmosphere, *Icarus*, **146**, 476–493, 2000.
- Mendillo, M., J. Baumgardner, B. Flynn, and W. J. Hughes, The extended sodium nebula of Jupiter, *Nature*, **348**, 312–314, 1990.
- Moore, C. E., M. G. J. Minnaert, and J. Houtgast, *The solar spectrum 2935 Å to 8770 Å*, National Bureau of Standards Monograph, Washington: US Government Printing Office (USGPO), 1966.
- Moreno, M. A., G. Schubert, M. G. Kivelson, D. A. Paige, and J. Baumgardner, Io's volcanic and sublimation atmospheres, *Icarus*, **93**, 63–81, 1991.
- Muench, G., and J. T. Bergstralh, Io - Morphology of its sodium emission region, *Publications of the ASP*, **89**, 232–237, 1977.
- Murcray, F. J., and F. Goody, Pictures of the Io sodium cloud, *Astrophysical Journal*, **226**, 327–335, 1978.
- Oliversen, R. J., F. Scherb, W. H. Smyth, M. E. Freed, R. Carey Woodward, M. L. Marconi, K. D. Retherford, O. L. Lupie, and J. P. Morgenthaler, Sunlit Io atmospheric [O I] 6300 Å emission and the plasma torus, *Journal of Geophysics Research*, **106**, 26,183–26,194, 2001.

- Parkinson, T. D., Excitation of the sodium D line emission observed in the vicinity of Io, *Journal of Atmospheric Sciences*, **32**, 630–633, 1975.
- Pearl, J., R. Hanel, V. Kunde, W. Maguire, K. Fox, S. Gupta, C. Ponnampereuma, and F. Raulin, Identification of gaseous SO₂ and new upper limits for other gases on Io, *Nature*, **280**, 755–758, 1979.
- Pilcher, C. B., J. H. Fertel, W. H. Smyth, and M. R. Combi, Io's sodium directional features - Evidence for a magnetospheric-wind-driven gas escape mechanism, *Astrophysical Journal*, **287**, 427–444, 1984.
- Retherford, K. D., H. W. Moos, D. F. Strobel, B. C. Wolven, and F. L. Roesler, Io's equatorial spots: Morphology of neutral UV emissions, *Journal of Geophysics Research*, **105**, 27,157–27,166, 2000.
- Roesler, F. L., et al., Far-Ultraviolet Imaging Spectroscopy of Io's Atmosphere with HST/STIS, *Science*, **283**, 353+, 1999.
- Saur, J., F. M. Neubauer, D. F. Strobel, and M. E. Summers, Io's ultraviolet aurora: Remote sensing of Io's interaction, *Geophysics Research Letters*, **27**, 2893+, 2000.
- Scherb, F., and W. H. Smyth, Variability of (O I) 6300-Å emission near Io, *Journal of Geophysics Research*, **98**, 18,729+, 1993.
- Schneider, N. M., and J. T. Trauger, The Structure of the Io Torus, *Astrophysical Journal*, **450**, 450+, 1995.
- Schneider, N. M., D. M. Hunten, W. K. Wells, and L. M. Trafton, Eclipse measurements of Io's sodium atmosphere, *Science*, **238**, 55–58, 1987.
- Schneider, N. M., D. M. Hunten, W. K. Wells, A. B. Schultz, and U. Fink, The structure of Io's corona, *Astrophysical Journal*, **368**, 298–315, 1991a.
- Schneider, N. M., J. K. Wilson, J. T. Trauger, D. I. Brown, R. W. Evans, and D. E. Shemansky, Molecular origin of Io's fast sodium, *Science*, **253**, 1394–1397, 1991b.
- Schneider, N. M., M. H. Taylor, F. J. Crary, and J. T. Trauger, On the nature of the $\lambda_{\text{SUB}i\text{III}i}/\text{SUB}i$ brightness asymmetry in the Io torus, *Journal of Geophysics Research*, **102**, 19,823–19,834, 1997.
- Sieveka, E. M., and R. E. Johnson, Ejection of atoms and molecules from Io by plasma-ion impact, *Astrophysical Journal*, **287**, 418–426, 1984.
- Sittler, E. C., and D. F. Strobel, Io plasma torus electrons - Voyager 1, *Journal of Geophysics Research*, **92**, 5741–5762, 1987.
- Smyth, W. H., Io's sodium cloud - Explanation of the east-west asymmetries, *Astrophysical Journal*, **234**, 1148–1153, 1979.
- Smyth, W. H., Io's sodium cloud - Explanation of the east-west asymmetries. II, *Astrophysical Journal*, **264**, 708–725, 1983.

- Smyth, W. H., Neutral cloud distribution in the Jovian system, *Advances in Space Research*, **12**, 337–346, 1992.
- Smyth, W. H., and M. R. Combi, A general model for Io's neutral gas clouds. I - Mathematical description, *Astrophysical Journal, Supplement Series*, **66**, 397–411, 1988a.
- Smyth, W. H., and M. R. Combi, A general model for Io's neutral gas clouds. II - Application to the sodium cloud, *Astrophysical Journal*, **328**, 888–918, 1988b.
- Smyth, W. H., and M. R. Combi, Io's Sodium Corona and Spatially Extended Cloud: A Consistent Flux Speed Distribution, *Icarus*, **126**, 58–77, 1997.
- Smyth, W. H., and M. L. Marconi, Io's oxygen source: Determination from ground-based observations and implications for the plasma torus, *Journal of Geophysics Research*, **105**, 7783–7792, 2000.
- Smyth, W. H., and M. B. McElroy, The sodium and hydrogen gas clouds of Io, *Planetary Space Science*, **25**, 415–431, 1977.
- Smyth, W. H., and M. B. McElroy, Io's sodium cloud - Comparison of models and two-dimensional images, *Astrophysical Journal*, **226**, 336–346, 1978.
- Spencer, J. R., and N. M. Schneider, Io on the Eve of the Galileo Mission, *Annual Review of Earth and Planetary Sciences*, **24**, 125–190, 1996.
- Spencer, J. R., P. Sartoretti, G. E. Ballester, A. S. McEwen, J. T. Clarke, and M. A. McGrath, Pele plume (Io): Observations with the Hubble Space Telescope, *Geophysics Research Letters*, **24**, 2471, 1997.
- Spencer, J. R., K. L. Jessup, M. A. McGrath, G. E. Ballester, and R. Yelle, Discovery of Gaseous S₂ in Io's Pele Plume, *Science*, **288**, 1208–1210, 2000.
- Strobel, D. F., X. Zhu, and M. F. Summers, On the vertical thermal structure of Io's atmosphere, *Icarus*, **111**, 18–30, 1994.
- Summers, M. E., and D. F. Strobel, Photochemistry and Vertical Transport in Io's Atmosphere and Ionosphere, *Icarus*, **120**, 290–316, 1996.
- Summers, M. E., D. F. Strobel, Y. L. Yung, J. T. Trauger, and F. Mills, The structure of Io's thermal corona and implications for atmospheric escape, *Astrophysical Journal*, **343**, 468–480, 1989.
- Thomas, N., High resolution spectra of Io's neutral potassium and oxygen clouds., *Astronomy and Astrophysics*, **313**, 306–314, 1996.
- Trafton, L., High-resolution spectra of Io's sodium emission, *Astrophysical Journal, Letters to the Editor*, **202**, L107–L112, 1975a.
- Trafton, L., Detection of a potassium cloud near Io, *Nature*, **258**, 690–692, 1975b.
- Trafton, L., Periodic variations in Io's sodium and potassium clouds, *Astrophysical Journal*, **215**, 960–970, 1977.

- Trafton, L., An explanation for the alternating north-south asymmetry of Io's sodium cloud, *Icarus*, **44**, 318–325, 1980.
- Trafton, L., and W. Macy, An oscillating asymmetry to Io's sodium emission cloud, *Astrophysical Journal, Letters to the Editor*, **202**, L155–L158, 1975.
- Trafton, L., and W. Macy, Io's sodium emission profiles - Variations due to Io's phase and magnetic latitude, *Astrophysical Journal*, **215**, 971–976, 1977.
- Trafton, L., T. Parkinson, and W. Macy, The Spatial Extent of Sodium Emission around Io, *Astrophysical Journal, Letters to the Editor*, **190**, L85, 1974.
- Vogt, S. S., *UCO/Lick Observatory Tech. Rep. 67, HIRES Users Manual*, 1994.
- Wilson, J. K., and N. M. Schneider, Io's fast sodium: Implications for molecular and atomic atmospheric escape, *Icarus*, **111**, 31–44, 1994.
- Wilson, J. K., and N. M. Schneider, Io's sodium directional feature: Evidence for ionospheric escape, *Journal of Geophysics Research*, **104**, 16,567–16,584, 1999.
- Wolven, B. C., H. W. Moos, K. D. Retherford, P. D. Feldman, D. F. Strobel, W. H. Smyth, and F. L. Roesler, Emission profiles of neutral oxygen and sulfur in Io's exospheric corona, *Journal of Geophysics Research*, **106**, 26,155–26,182, 2001.
- Wong, M. C., and W. H. Smyth, Model Calculations for Io's Atmosphere at Eastern and Western Elongations, *Icarus*, **146**, 60–74, 2000.
- Zapesochnyi, I. P., and I. S. Aleksakhin, , *Soviet Physics-JETP*, **28**, 41, 1969.

Appendix A

Summary of Eclipse Observations

This appendix contains a summary of all the eclipse data described in Chapter 3. For each event, all the relevant parameters are listed.

Table A.1. Summary of Eclipse Observations

Obs. # ^a	Phase ^b	b (R _{Io}) ^c	Location ^d	W _{D₂} (mÅ)	W _{D₁} (mÅ)	N (cm ⁻²)	T (K) ^e
1.0	0.2	2.5	L,N	14 ± 2	6 ± 2	7 ± 1 × 10 ¹⁰	<i>thin</i>
1.1	0.2	2.4	L,N	9 ± 2	17 ± 4	6 ± 2 × 10 ¹⁰	<i>thin</i>
1.2	0.3	2.2	L,N	13 ± 4	9 ± 2	1.3 ^{+0.5} _{-0.3} × 10 ¹¹	<i>undetermined</i>
1.3	0.3	2.2	L,N	20 ± 4	25 ± 2	2 ± 1 × 10 ¹¹	<i>undetermined</i>
1.4	0.4	2.1	L,N	24 ± 4	26 ± 2	2 ± 1 × 10 ¹¹	<i>undetermined</i>
1.5	0.5	2.1	N	25 ± 4	17 ± 5	2.6 ^{+1.5} _{-0.8} × 10 ¹¹	< 1200
2.0	-1.9	7.7	A,L,N	3.4 ± 0.5	3.3 ± 0.5	2.2 ± 0.3 × 10 ¹⁰	<i>thin</i>
2.1	-1.5	6.6	A,L,N	6.2 ± 0.5	3.9 ± 0.4	3.4 ± 0.3 × 10 ¹⁰	<i>thin</i>
2.2	-1.1	5.5	A,L,N	10.0 ± 0.6	4.2 ± 0.5	5.0 ± 0.3 × 10 ¹⁰	<i>thin</i>
2.3	-0.6	4.6	A,L,N	13.6 ± 0.6	6.8 ± 0.5	7.2 ± 0.3 × 10 ¹⁰	<i>thin</i>
2.4	-0.2	3.7	A,L,N	22.2 ± 0.6	10.8 ± 0.5	1.18 ± 0.06 × 10 ¹¹	<i>undetermined</i>
2.5	0.3	3.2	A,L,N	28.4 ± 0.6	16.9 ± 0.4	2.04 ± 0.12 × 10 ¹¹	900 ⁺⁷⁰⁰ ₋₄₀₀
2.6	0.7	3.2	J,T,N	28.6 ± 0.6	16.1 ± 0.4	1.86 ± 0.11 × 10 ¹¹	2000 ⁺²²⁰⁰ ₋₉₀₀
2.7	1.2	3.8	J,T,N	20.2 ± 0.6	11.2 ± 0.5	1.27 ^{+0.12} _{0.10} × 10 ¹¹	1100 ⁺⁴⁰⁰⁰ ₋₈₀₀
2.8	1.6	4.6	J,T,N	12.9 ± 0.6	6.5 ± 0.4	6.7 ^{+0.9} _{-0.2} × 10 ¹⁰	<i>undetermined</i>
2.9	2.1	5.4	J,T,N	9.1 ± 0.6	5.4 ± 0.4	5.1 ± 0.3 × 10 ¹⁰	<i>thin</i>
2.10	2.5	6.5	J,T,N	6.2 ± 0.6	2.4 ± 0.5	3.0 ± 0.3 × 10 ¹⁰	<i>thin</i>
2.11	2.9	7.6	J,T,N	3.3 ± 0.5	1.1 ± 0.4	1.6 ± 0.2 × 10 ¹⁰	<i>thin</i>
2.12	3.3	8.7	J,T,N	3.2 ± 0.6	0.2 ± 0.4	1.7 ± 0.3 × 10 ¹⁰	<i>thin</i>
3.0	-1.2	> 10	A,S	1.0 ± 0.4	1.4 ± 0.4	6.7 ± 2.4 × 10 ⁹	<i>thin</i>
3.1	-1.1	> 10	A,S	1.7 ± 0.4	2.0 ± 0.4	1.1 ± 0.2 × 10 ¹⁰	<i>thin</i>
3.2	-0.9	8.1	A,S	2.0 ± 0.4	1.8 ± 0.4	1.2 ± 0.2 × 10 ¹⁰	<i>thin</i>
3.3	-0.7	7.2	A,S	1.4 ± 0.4	2.0 ± 0.4	1.0 ± 0.2 × 10 ¹⁰	<i>thin</i>
3.4	-0.6	6.4	A,S	4.6 ± 0.5	2.4 ± 0.4	2.4 ± 0.2 × 10 ¹⁰	<i>thin</i>
3.5	-0.4	5.5	A,S	6.1 ± 0.6	3.0 ± 0.4	3.1 ± 0.3 × 10 ¹⁰	<i>thin</i>
3.6	-0.3	4.7	A,S	8.0 ± 0.5	3.8 ± 0.4	4.1 ± 0.3 × 10 ¹⁰	<i>thin</i>
3.7	-0.1	3.8	A,S	11.2 ± 0.5	6.0 ± 0.5	6.5 ^{+1.2} _{-0.8} × 10 ¹⁰	<i>undetermined</i>
3.8	0.0	3.0	A,S	18.8 ± 0.5	10.6 ± 0.5	1.20 ^{+0.13} _{-0.11} × 10 ¹¹	700 ⁺²⁷⁰⁰ ₋₅₀₀
3.9	0.1	2.3	A,S	34.8 ± 0.7	21.3 ± 0.6	2.69 ^{+0.18} _{-0.17} × 10 ¹¹	1100 ⁺⁶⁰⁰ ₋₄₀₀
3.10	0.3	1.8	A,S	47.2 ± 0.5	32.0 ± 0.5	4.66 ^{+0.18} _{-0.17} × 10 ¹¹	1100 ± 200
3.11	0.4	1.5	A,S	65.9 ± 0.8	49.4 ± 0.7	8.69 ^{+0.43} _{-0.40} × 10 ¹¹	1700 ± 200
3.12	0.6	1.5	J,S	74.2 ± 0.6	55.3 ± 0.6	9.72 ^{+0.37} _{-0.35} × 10 ¹¹	2300 ± 200

Table A.1 (cont'd)

Obs. # ^a	Phase ^b	b (R _{Io}) ^c	Location ^d	W _{D₂} (mÅ)	W _{D₁} (mÅ)	N (cm ⁻²)	T (K) ^e
3.13	0.7	1.9	J,S	61.7 ± 0.5	44.0 ± 0.5	7.02 ^{+0.23} _{-0.22} × 10 ¹¹	1800 ⁺²⁰⁰ ₋₁₀₀
3.14	0.9	2.4	J,S	47.0 ± 0.5	29.9 ± 0.5	4.00 ^{+0.16} _{-0.15} × 10 ¹¹	1800 ⁺⁴⁰⁰ ₋₃₀₀
3.15	1.0	3.1	J,S	30.0 ± 0.5	17.5 ± 0.4	2.09 ^{+0.12} _{-0.11} × 10 ¹¹	1300 ⁺⁹⁰⁰ ₋₅₀₀
3.16	1.2	3.9	J,S	20.5 ± 0.5	10.4 ± 0.4	1.08 ^{+0.10} _{-0.03} × 10 ¹¹	> 3 × 10 ³
3.17	1.4	5.5	J,S	9.9 ± 0.5	4.9 ± 0.4	5.2 ± 0.3 × 10 ¹⁰	<i>thin</i>
3.18	1.6	6.3	J,S	6.2 ± 0.5	3.3 ± 0.4	3.3 ± 0.3 × 10 ¹⁰	<i>thin</i>
3.19	1.7	7.1	J,S	5.1 ± 0.6	2.4 ± 0.5	2.6 ± 0.3 × 10 ¹⁰	<i>thin</i>
3.20	1.9	7.9	J,S	4.4 ± 0.6	2.4 ± 0.4	2.3 ± 0.3 × 10 ¹⁰	<i>thin</i>
3.21	2.0	> 10	J,S	3.9 ± 0.5	2.2 ± 0.5	2.1 ± 0.3 × 10 ¹⁰	<i>thin</i>
4.0	-0.7	5.0	A,L,N	9.3 ± 1.5	2.4 ± 1.0	4.0 ± 0.6 × 10 ¹⁰	<i>thin</i>
4.1	-0.2	3.1	A,L,N	19.9 ± 1.6	9.3 ± 1.1	1.03 ^{+0.10} _{-0.06} × 10 ¹¹	<i>undetermined</i>
4.2	0.0	2.2	A,L,N	36.0 ± 2.5	14.6 ± 1.7	1.76 ^{+0.25} _{-0.11} × 10 ¹¹	<i>undetermined</i>
4.3	0.3	1.5	A,L,N	55.5 ± 3.2	34.5 ± 2.2	4.48 ^{+0.79} _{-0.65} × 10 ¹¹	3300 ⁺⁵⁴⁰⁰ ₋₁₇₀₀
4.4	0.5	1.2	N	73.0 ± 4.0	52.4 ± 3.1	8.5 ^{+2.1} _{-1.4} × 10 ¹¹	2600 ⁺¹⁷⁰⁰ ₋₁₀₀₀
4.5	0.7	1.4	J,T,N	70.7 ± 4.0	53.3 ± 3.1	9.6 ^{+2.7} _{-1.7} × 10 ¹¹	2000 ⁺¹¹⁰⁰ ₋₇₀₀
4.6	0.9	2.0	J,T,N	55.9 ± 3.0	36.1 ± 2.1	4.94 ^{+0.84} _{-0.68} × 10 ¹¹	2400 ⁺²⁶⁰⁰ ₋₁₁₀₀
4.7	1.2	2.9	J,T,N	31.8 ± 1.9	17.2 ± 1.3	1.89 ^{+0.34} _{-0.18} × 10 ¹¹	> 10 ³
4.8	1.4	3.8	J,T,N	19.2 ± 1.5	11.5 ± 1.3	1.43 ^{+0.43} _{-0.32} × 10 ¹¹	< 10 ⁴
4.9	1.6	4.8	J,T,N	13.8 ± 1.3	8.3 ± 1.2	1.02 ^{+0.60} _{-0.28} × 10 ¹¹	<i>undetermined</i>
4.10	1.8	5.7	J,T,N	10.5 ± 1.1	3.5 ± 0.9	5.0 ± 0.6 × 10 ¹⁰	<i>thin</i>
4.11	2.1	6.6	J,T,N	7.9 ± 0.9	5.4 ± 0.9	4.5 ± 0.5 × 10 ¹⁰	<i>thin</i>
4.12	2.3	7.6	J,T,N	9.4 ± 1.1	2.2 ± 1.0	4.3 ± 0.6 × 10 ¹⁰	<i>thin</i>
4.13	2.5	8.5	J,T,N	3.6 ± 0.9	3.6 ± 1.1	2.1 ± 0.6 × 10 ¹⁰	<i>thin</i>
5.0	-3.0	5.5	A,N	13.2 ± 2.3	5.2 ± 1.5	6.4 ± 1.0 × 10 ¹⁰	<i>thin</i>
5.1	-2.4	4.7	A,N	11.6 ± 2.1	5.4 ± 1.9	6.0 ± 1.2 × 10 ¹⁰	<i>thin</i>
5.2	-1.7	3.8	A,N	17.4 ± 2.5	10.1 ± 1.8	1.20 ^{+0.63} _{-0.34} × 10 ¹¹	<i>undetermined</i>
5.3	-1.1	3.1	A,N	23.6 ± 2.1	10.9 ± 1.7	1.21 ^{+0.19} _{-0.10} × 10 ¹¹	> 10 ³
5.4	-0.5	2.6	A,N	35.8 ± 2.4	22.4 ± 2.0	2.91 ^{+0.74} _{-0.56} × 10 ¹¹	900 ⁺³⁸⁰⁰ ₋₇₀₀
5.5	0.1	2.2	A,N	40.6 ± 2.6	20.8 ± 1.9	2.26 ^{+0.54} _{-0.15} × 10 ¹¹	> 3 × 10 ³
5.6	0.7	2.1	J,N	42.5 ± 2.7	26.9 ± 2.1	3.55 ^{+0.74} _{-0.61} × 10 ¹¹	1400 ⁺³³⁰⁰ ₋₉₀₀
5.7	1.2	2.4	J,N	43.4 ± 2.5	22.7 ± 2.0	2.43 ^{+0.49} _{-0.07} × 10 ¹¹	> 3 × 10 ³
5.8	1.8	2.9	J,N	35.4 ± 2.3	17.0 ± 1.8	1.89 ± 0.40 × 10 ¹¹	> 8 × 10 ³

Table A.1 (cont'd)

Obs. # ^a	Phase ^b	b (R _{Io}) ^c	Location ^d	W _{D₂} (mÅ)	W _{D₁} (mÅ)	N (cm ⁻²)	T (K) ^e
5.9	2.4	3.4	J,N	25.9 ± 2.0	13.4 ± 1.6	1.41 ^{+0.40} _{-0.15} × 10 ¹¹	<i>undetermined</i>
5.10	3.0	4.1	J,N	22.0 ± 1.9	10.5 ± 1.7	1.16 ^{+0.23} _{-0.25} × 10 ¹¹	> 10 ³
5.11	3.6	4.9	J,N	17.0 ± 1.6	9.8 ± 1.6	1.15 ^{+0.49} _{-0.30} × 10 ¹¹	<i>undetermined</i>
5.12	4.2	5.6	J,N	15.0 ± 1.7	6.0 ± 1.6	7.6 ± 1.0 × 10 ¹⁰	<i>thin</i>
6.0	-0.5	5.7	A,S	3.2 ± 1.9	3.9 ± 1.7	2.2 ± 1.0 × 10 ¹⁰	<i>thin</i>
6.1	-0.3	4.9	A,S	7.4 ± 2.0	5.3 ± 2.3	4.1 ± 1.3 × 10 ¹⁰	<i>thin</i>
6.2	-0.2	3.9	A,S	14.8 ± 2.3	5.6 ± 1.7	7.2 ± 1.1 × 10 ¹⁰	<i>thin</i>
6.3	0.0	3.1	A,S	16.5 ± 1.9	10.3 ± 1.4	1.33 ^{+0.54} _{-0.38} × 10 ¹¹	< 8 × 10 ³
6.4	0.1	2.3	A,S	28.4 ± 2.4	21.8 ± 2.3	4.1 ^{+3.1} _{-1.3} × 10 ¹¹	100 ⁺¹⁰⁰ ₋₄₀
6.5	0.3	1.9	A,S	39.3 ± 3.0	31.5 ± 3.0	6.3 ^{+7.3} _{-1.9} × 10 ¹¹	200 ⁺³⁰⁰ ₋₁₀₀
6.6	0.4	1.6	A,S	44.9 ± 5.2	39.1 ± 5.6	1.0 ^{+inf} _{-0.6} × 10 ¹²	< 10 ³
6.7	0.6	1.7	J,S	61.6 ± 4.5	42.3 ± 4.1	6.3 ^{+2.1} _{-1.5} × 10 ¹¹	2100 ⁺³⁵⁰⁰ ₋₁₁₀₀
6.8	0.7	2.0	J,S	55.5 ± 4.4	36.2 ± 4.1	5.0 ^{+1.8} _{-1.3} × 10 ¹¹	2300 ⁺⁷⁵⁰⁰ ₋₁₄₀₀
6.9	0.9	2.5	J,S	37.4 ± 3.9	28.6 ± 3.3	5.2 ^{+6.6} _{-1.6} × 10 ¹¹	200 ⁺⁶⁰⁰ ₋₁₀₀
6.10	1.0	3.2	J,S	30.9 ± 4.1	17.8 ± 3.3	2.1 ^{+1.2} _{-0.6} × 10 ¹¹	<i>undetermined</i>
6.11	1.2	4.0	J,S	15.9 ± 3.2	7.3 ± 2.3	8.2 ± 1.6 × 10 ¹⁰	<i>thin</i>
7.0	-0.2	2.3	A,N	42.3 ± 2.8	23.3 ± 2.0	2.64 ^{+0.54} _{-0.37} × 10 ¹¹	> 10 ³
7.1	0.0	2.1	A,N	48.7 ± 3.8	28.1 ± 2.3	3.35 ^{+0.73} _{-0.58} × 10 ¹¹	<i>undetermined</i>
7.2	0.2	1.9	A,N	51.9 ± 3.2	32.1 ± 2.5	4.14 ^{+0.87} _{-0.71} × 10 ¹¹	2900 ⁺⁷³⁰⁰ ₋₁₆₀₀
7.3	0.4	1.9	A,N	58.6 ± 4.0	40.9 ± 2.9	6.3 ^{+1.6} _{-1.2} × 10 ¹¹	1700 ⁺¹⁸⁰⁰ ₋₈₀₀
7.4	0.6	1.9	J,N	65.0 ± 4.9	39.0 ± 2.8	4.9 ^{+1.0} _{-0.8} × 10 ¹¹	6300 ⁺²⁴⁵⁰⁰ ₋₃₈₀₀
7.5	0.8	2.0	J,N	61.1 ± 3.5	38.1 ± 2.8	5.0 ^{+1.0} _{-0.8} × 10 ¹¹	3900 ⁺⁷³⁰⁰ ₋₂₀₀₀
7.6	1.0	2.2	J,N	63.2 ± 4.4	38.4 ± 2.5	4.87 ^{+0.96} _{-0.77} × 10 ¹¹	≲ 10 ⁴
7.7	1.3	2.5	J,N	52.9 ± 3.9	34.1 ± 2.6	4.6 ^{+1.1} _{-0.8} × 10 ¹¹	2200 ⁺⁴³⁰⁰ ₋₁₃₀₀
7.8	1.6	3.1	J,N	38.2 ± 2.9	25.9 ± 2.8	3.7 ^{+1.5} _{-0.9} × 10 ¹¹	500 ⁺¹⁷⁰⁰ ₋₃₀₀
7.9	1.9	3.6	J,N	32.5 ± 2.8	20.5 ± 2.4	2.7 ^{+1.1} _{-0.6} × 10 ¹¹	600 ⁺⁵⁹⁰⁰ ₋₄₀₀
8.0	-0.8	7.3	L,J,N	7.7 ± 1.4	5.0 ± 1.1	4.4 ± 0.7 × 10 ¹⁰	<i>thin</i>
8.1	-0.5	5.9	L,J,N	8.4 ± 1.5	4.0 ± 1.4	4.3 ± 0.8 × 10 ¹⁰	<i>thin</i>
8.2	-0.1	3.6	L,J,N	22.4 ± 1.6	13.0 ± 1.4	1.55 ^{+0.47} _{-0.33} × 10 ¹¹	< 5 × 10 ⁴
8.3	0.1	2.4	L,J,N	45.8 ± 2.7	29.6 ± 2.0	4.02 ^{+0.76} _{-0.63} × 10 ¹¹	1400 ⁺²³⁰⁰ ₋₈₀₀
8.4	0.4	1.7	L,J,N	66.0 ± 3.6	48.5 ± 2.7	8.2 ^{+1.9} _{-1.3} × 10 ¹¹	1800 ⁺¹¹⁰⁰ ₋₇₀₀
8.5	0.6	1.8	T,A,N	49.5 ± 2.9	35.6 ± 2.3	5.7 ^{+1.3} _{-0.9} × 10 ¹¹	900 ⁺⁸⁰⁰ ₋₄₀₀

Table A.1 (cont'd)

Obs. # ^a	Phase ^b	b (R _{Io}) ^c	Location ^d	W _{D₂} (mÅ)	W _{D₁} (mÅ)	N (cm ⁻²)	T (K) ^e
8.6	0.9	2.7	T,A,N	28.5 ± 1.9	21.0 ± 1.5	3.6 ^{+1.4} _{-0.8} × 10 ¹¹	120 ⁺¹²⁰ ₋₄₀
8.7	1.2	4.3	T,A,N	9.0 ± 1.0	4.1 ± 0.9	4.6 ± 0.5 × 10 ¹⁰	<i>thin</i>
8.8	1.4	5.5	T,A,N	3.5 ± 1.2	2.8 ± 1.2	2.1 ± 0.7 × 10 ¹⁰	<i>thin</i>
8.9	1.6	7.0	T,A,N	4.4 ± 1.0	1.8 ± 0.8	2.2 ± 0.5 × 10 ¹⁰	<i>thin</i>
9.0	-1.7	> 10	L,N	0.9 ± 0.4	1.6 ± 0.6	5.9 ± 3.4 × 10 ⁹	<i>thin</i>
9.1	-1.5	> 10	L,N	0.6 ± 0.5	2.7 ± 0.5	7.8 ± 3.1 × 10 ⁹	<i>thin</i>
9.2	-1.3	9.1	L,N	0.9 ± 0.4	1.1 ± 0.6	5.5 ± 3.4 × 10 ⁹	<i>thin</i>
9.3	-1.1	8.4	L,N	1.3 ± 0.6	0.8 ± 0.6	6.8 ± 3.6 × 10 ⁹	<i>thin</i>
9.4	-0.9	7.5	L,N	2.1 ± 0.8	1.0 ± 0.7	1.1 ± 0.4 × 10 ¹⁰	<i>thin</i>
9.5	-0.7	6.4	L,N	4.7 ± 1.2	3.9 ± 0.9	2.9 ± 0.5 × 10 ¹⁰	<i>thin</i>
9.6	-0.4	5.3	L,N	7.4 ± 0.9	2.8 ± 0.5	3.5 ± 0.4 × 10 ¹⁰	<i>thin</i>
9.7	-0.2	4.2	L,N	13.6 ± 1.2	6.4 ± 0.9	7.1 ± 0.6 × 10 ¹⁰	<i>thin</i>
9.8	0.0	3.1	L,N	22.6 ± 1.5	14.3 ± 1.2	1.91 ^{+0.47} _{-0.37} × 10 ¹¹	200 ⁺⁸⁰⁰ ₋₁₀₀
9.9	0.2	2.3	L,N	36.7 ± 2.2	28.6 ± 1.7	5.5 ^{+2.6} _{-1.2} × 10 ¹¹	200 ⁺²⁰⁰ ₋₁₀₀
9.10	0.4	2.0	L,N	46.0 ± 2.6	31.7 ± 1.8	4.69 ^{+0.87} _{-0.68} × 10 ¹¹	900 ⁺¹⁰⁰⁰ ₋₄₀₀
9.11	0.7	2.1	T,N	35.6 ± 2.2	22.3 ± 1.5	2.88 ^{+0.55} _{-0.43} × 10 ¹¹	900 ⁺²⁴⁰⁰ ₋₆₀₀
9.12	0.9	2.8	T,N	21.5 ± 1.7	12.2 ± 1.0	1.41 ^{+0.33} _{-0.24} × 10 ¹¹	< 6 × 10 ⁴
9.13	1.1	3.8	T,N	7.9 ± 1.0	7.2 ± 1.0	4.9 ± 0.6 × 10 ¹⁰	<i>thin</i>
9.14	1.3	4.8	T,N	4.8 ± 0.9	3.6 ± 0.9	2.7 ± 0.5 × 10 ¹⁰	<i>thin</i>
9.15	1.5	5.9	T,N	2.6 ± 0.9	2.6 ± 0.8	1.7 ± 0.5 × 10 ¹⁰	<i>thin</i>
9.16	1.7	7.1	T,N	0.7 ± 0.7	0.9 ± 0.5	5.6 ± 3.3 × 10 ⁹	<i>thin</i>
9.17	1.9	8.2	T,N	0.8 ± 0.7	1.3 ± 0.7	6.2 ± 4.2 × 10 ⁹	<i>thin</i>
9.18	2.2	8.9	T,N	0.7 ± 0.8	-2.0 ± 0.9	3.7 ^{+4.3} _{-3.7} × 10 ⁹ <i>x</i>	<i>thin</i>
9.19	2.4	9.4	T,N	0.5 ± 1.0	0.9 ± 1.0	3.6 ^{+6.0} _{-5.0} × 10 ⁹	<i>thin</i>
10.1	-0.9	6.1	A,L,S	8.3 ± 1.0	< 5	4.4 ± 0.6 × 10 ¹⁰	<i>thin</i>
10.2	-0.3	3.7	A,L,S	17.8 ± 1.5	11.1 ± 1.5	1.44 ^{+0.56} _{-0.40} × 10 ¹¹	< 10 ⁴
10.3	0.2	1.6	A,L,S	39.4 ± 4.0	24.3 ± 10.0	3 ⁺⁸ ₋₁ × 10 ¹¹	<i>undetermined</i>
10.4	0.7	1.5	J,T,S	21.8 ± 4.0	15.7 ± 2.0	2.5 ^{+2.4} _{-0.9} × 10 ¹¹	< 10 ³

^aObservation number is in the form X.Y where X is the eclipse number as given in Table 3.1 and Y is the number of the spectrum taken in the event series.

^bThe eclipse phase of an observation is defined as the fraction of the event completed at the midpoint of the observation. Negative eclipse phase refers to observations made before penumbral contact; phases greater than 1 refer to observations after final contact.

^cThe uncertainties in the impact parameter are $\lesssim 0.1 R_{Io}$.

^dLocation sampled relative to Io. L=leading hemisphere, T=trailing hemisphere, J=sub-Jupiter hemisphere, A=Anti-Jupiter hemisphere, N=North of Io, S=South of Io

^eApproximate coronal temperature. *thin*=optically thin, no temperature estimate possible, *undetermined*=optically thick, but no temperature estimate possible due to poor data quality

Appendix B

Transformation to the Plasma Coordinate System

The following is a description of the transformation from the observer's coordinate system to the plasma torus coordinate system used for determining the local plasma state.

- (1) The transformation is from the observer's coordinates (x_0, y_0, z_0) to the plasma torus coordinates (L, ζ) where the observer's frame is in heliocentric Jupiter centered coordinates with the positive y axis directed along the sun-Jupiter line away from the sun, the positive x axis is directed from east to west, and the z axis positive in the direction of Jupiter north. The Plasma torus frame is defined by the two coordinates M, the M-shell (modified L-shell) of an atom, and ζ , the distance along the field line from the centrifugal equator to the atom
- (2) Local time of each packet (i.e. heliocentric phase angle)

$$\phi = \tan^{-1} \left(\frac{x}{y} \right) \quad (\text{B.1})$$

- (3) Initial centrifugal radius:

$$r_0 = (x^2 + y^2)^{1/2} \quad (\text{B.2})$$

- (4) Angle from the orbital equator to the magnetic equator:

$$\alpha = -\eta_{\text{tilt}} \cos(\lambda - \lambda_0) \quad (\text{B.3})$$

(5) Angle from orbital equator to the centrifugal equator:

$$\beta = -\frac{2}{3}\eta_{tilt} \cos(\lambda - \lambda_0) = \frac{2}{3}\alpha \quad (\text{B.4})$$

(6) Angle from centrifugal equator to magnetic equator:

$$\theta = \beta - \alpha = -\frac{1}{3}\alpha \quad (\text{B.5})$$

(7) The L-shell of the packet is determined using an offset tilted dipole magnetic field model with the dipole tilted an angle η_{tilt} toward $\lambda_{III} = \lambda_0$ and shifted δ_D towards $\lambda_{III} = \lambda_D$ in the equatorial plane

(8) Offsets in x and y of dipole center from the center of Jupiter

$$\Delta_x = -\delta_D \cos((\lambda - \lambda_D) \sin \phi - \delta_D \sin(\lambda - \lambda_D) \cos \phi \quad (\text{B.6})$$

$$\Delta_y = \delta_D \cos(\lambda - \lambda_D) \cos \phi - \delta_D \sin(\lambda - \lambda_D) \sin \phi \quad (\text{B.7})$$

(9) Centrifugal distance of packet from dipole axis:

$$r_D = ((x - \Delta x_D)^2 + (y - \Delta y_D)^2) \quad (\text{B.8})$$

(10) Angle each point makes with the orbital equator:

$$\gamma_D = \tan^{-1} \left(\frac{z}{r_D} \right) \quad (\text{B.9})$$

(11) Magnetic latitude of each packet:

$$\ell = \gamma_D - \alpha \quad (\text{B.10})$$

(12) L-shell of each packet:

$$L = \frac{(r_D^2 + z^2)}{\cos^2 \ell} \quad (\text{B.11})$$

(13) Distance of the point where the magnetic field line through the packet crosses the centrifugal equator from Jupiter:

$$L' = L \cos^2 \theta \quad (\text{B.12})$$

(14) The M-shell is determined from observations of the ribbon. M is the distance from Jupiter in the centrifugal plane of a packet with its position modulated by the observed changes in the distance of the ribbon from Jupiter. The effect of a purely East-West electric field is also included. The ribbon is assumed offset from the center of Jupiter a distance δ_R towards in the direction $\lambda_{III} = \lambda_R$ in the centrifugal plane

(15) Observed offsets in ribbon position:

$$\Delta x_M = [-\delta_R \cos(\lambda - \lambda_R) \sin \phi - \delta_R \sin(\lambda - \lambda_R) \cos \phi] \cos \beta \quad (\text{B.13})$$

$$\Delta y_M = [\delta_R \cos(\lambda - \lambda_R) \cos \phi - \delta_R \sin(\lambda - \lambda_R) \sin \phi] \cos \beta \quad (\text{B.14})$$

$$\Delta z_M = -\delta_R \sin \beta \quad (\text{B.15})$$

(16) Position of each packet relative to the origin of M

$$x_M = -L' \cos \beta \sin \phi + \Delta x_D - \Delta x_M + \epsilon r_0 \quad (\text{B.16})$$

$$y_M = L' \cos \beta \cos \phi + \Delta y_D - \Delta y_M \quad (\text{B.17})$$

$$z_M = L' \sin \beta - \Delta z_M \quad (\text{B.18})$$

(17) M-shell of each packet:

$$M = (x_M^2 + y_M^2 + z_M^2)^{1/2} \quad (\text{B.19})$$

(18) The nominal constants used in this analysis are:

$$\eta_{\text{tilt}} = 9.8^\circ \quad (\text{B.20})$$

$$\lambda_0 = 200^\circ \quad (\text{B.21})$$

$$\delta_D = 0.12R_J \quad (\text{B.22})$$

$$\lambda_D = 149^\circ \quad (\text{B.23})$$

$$\delta_R = 0.59R_J \quad (\text{B.24})$$

$$\lambda_R = 149^\circ \quad (\text{B.25})$$

Variability of these parameters is discussed elsewhere the text.

- (19) ζ is the distance along the field line from the centrifugal equator to the atoms:

$$\zeta = \int_{\theta}^{\ell} \left((r'(\xi))^2 + \left(\frac{dr'}{d\xi} \right)^2 \right)^{1/2} d\xi \quad (\text{B.26})$$

where $r'(\xi) = L/\cos^2(\xi)$

- (20) The analytic solution to this integral is:

$$\zeta = (L \cos^4 \xi + 4 \cos^2 \xi \sin^2 \xi) \left[\frac{\tanh^{-1} \left(\frac{\sqrt{6} \sin \xi}{\sqrt{5-3 \cos(2\xi)}} \right) \sec \xi}{\sqrt{6} \sqrt{5-3 \cos(2\xi)}} + \frac{\tan \xi}{2} \right] \Bigg|_{\alpha}^{\theta} \quad (\text{B.27})$$

- (21) Several factors contribute to the electron density and temperature at the location of a packet: the M-shell, the distance off the centrifugal axis (ζ), the local time (orbital phase angle ϕ), and the System-III longitude.

- (22) $n_{e,0}$, T_e , and T_i in the centrifugal plane are given by the Voyager data (Bagenal 1994) as a function of M. The ribbon is held at a constant distance from Jupiter of $M=5.7 R_J$.

- (23) T_e is assumed to be constant along field lines.

- (24) n_e decreases as a function of the distance along the field line to the centrifugal equator:

$$n_e = n_{e,0} e^{-(\zeta/H(L))^2} \quad (\text{B.28})$$

- (25) Scale height is determined from the ions in the torus:

$$H = \left(\frac{2kT}{2m^* \Omega R_J^2} \right)^{1/2} \quad (\text{B.29})$$

$$m^* = \frac{m}{1 + Z (T_e/T_{\parallel})} \quad (\text{B.30})$$

with m and Z the masses and charges of torus ions, and $\Omega =$ Jupiter's angular velocity.

(26) Modulation of the Voyager profile is based on observations of the torus from several published sources (Schneider and Trauger 1995; Brown 1995) and observations in this thesis. There are three types of modulation employed:

- (a) Local Time Modulation: The observed East/West brightness asymmetry in the torus is indicative of local time variations in the electron density and temperature due to the changing magnetic field a packet experiences as it moves through the torus. The correction factor is normalized to western elongation ($\phi = 270^\circ$).

$$C = 1 - \frac{1-R}{2} (1 - \sin \phi) n_e = n_{e,0} \times ct_e = t_{e,0} \times c \quad (\text{B.31})$$

where R is the East/West ribbon intensity ratio, with a nominal value of R=0.92.

- (b) System-III brightness variation: Based on observations that the ribbon is brighter near $\lambda_{III} = 200^\circ$. Electron density varies with the square root of the observed intensity:

$$n_e = n_e \times (1 + A_n \cos(\lambda - \lambda_n)) \quad (\text{B.32})$$

where A_n is the amplitude of the sinusoidal variation and λ_n is the longitude of maximum intensity.

- (c) System-III scale height variation: Based on observations of the variations in ribbon scale height. Schneider and Trauger (1995) found the variation in parallel ion temperature implied by the observations. An approximate fit to these observations is used here:

$$T_{\parallel} = -A_T \cos(\lambda - \lambda_T) + T_{avg} \quad (\text{B.33})$$

where T_{avg} is the average parallel ion temperature, A_T is the amplitude of variation, and λ_T is the longitude of minimum scale height. The calculation of the scale height from T_{\parallel} is described above.

- (27) The sodium lifetime follows directly from the knowledge of n_e and T_e as is described elsewhere.